



HAL
open science

Control of a multi-terminal HVDC (MTDC) system and study of the interactions between the MTDC and the AC grids.

Samy Akkari

► **To cite this version:**

Samy Akkari. Control of a multi-terminal HVDC (MTDC) system and study of the interactions between the MTDC and the AC grids.. Other. Université Paris Saclay (COMUE), 2016. English. NNT : 2016SACLC069 . tel-01380743

HAL Id: tel-01380743

<https://theses.hal.science/tel-01380743>

Submitted on 13 Oct 2016

HAL is a multi-disciplinary open access archive for the deposit and dissemination of scientific research documents, whether they are published or not. The documents may come from teaching and research institutions in France or abroad, or from public or private research centers.

L'archive ouverte pluridisciplinaire **HAL**, est destinée au dépôt et à la diffusion de documents scientifiques de niveau recherche, publiés ou non, émanant des établissements d'enseignement et de recherche français ou étrangers, des laboratoires publics ou privés.

NNT : 2016SACL069

THÈSE DE DOCTORAT
DE
L'UNIVERSITÉ PARIS-SACLAY
PRÉPARÉE À
L'ÉCOLE CENTRALESUPÉLEC

ÉCOLE DOCTORALE 575 EOBÉ
Electrical, optical, bio-physics and engineering

Spécialité de doctorat : Génie Électrique

Par

M. Samy Akkari

CONTROL OF A MULTI-TERMINAL HVDC (MTDC) SYSTEM AND
STUDY OF ITS INTERACTIONS WITH THE AC GRIDS.

Thèse présentée et soutenue à Gif-Sur-Yvette, le 29 septembre 2016.

Composition du Jury :

E. Labouré, Professeur, CentraleSupélec, GeePs, Président du Jury
B. Marinescu, Professeur, École Centrale Nantes, IRCCyN, Examineur
T. Van Cutsem, Professeur, Université de Liège, FNRS, Rapporteur
S. Bacha, Professeur, Université Joseph Fourier, G2Elab, Rapporteur
X. Guillaud, Professeur, École Centrale Lille, L2EP, Co-encadrant
J. Dai, Enseignant Chercheur, CentraleSupélec, GeePs, Co-encadrant
M. Petit, Enseignant Chercheur, CentraleSupélec, GeePs, Directeur de thèse

Remerciements

Pour nombre de thésards, le doctorat est une aventure éprouvante et solitaire. Pour ma part, quand je regarde derrière moi pour appréhender le chemin effectué au cours de ces trois intenses années, je me rends compte que j'ai eu le plaisir et le privilège de travailler avec de nombreuses personnes, à la fois compétentes et expérimentées, mais aussi enthousiastes et chaleureuses.

Tout d'abord je tiens à remercier mes trois encadrants, en commençant par mon directeur de thèse, Marc Petit, pour m'avoir donné l'opportunité de travailler dans le domaine du HVDC à CentraleSupélec, et pour avoir suivi l'évolution du projet tout au long de ces trois années. Je remercie ensuite Jing Dai qui a été l'un des piliers de ce doctorat de par sa disponibilité et sa diligence constante tout au long de la thèse. Enfin, je remercie Xavier Guillaud qui a su toujours donner le cap et chapeauter tous les travaux grâce à son expérience et son expertise, et aussi bien sûr pour m'avoir permis de travailler avec l'équipe HVDC du L2EP de Lille.

Je remercie donc l'équipe HVDC de Lille, avec tout d'abord Khaled Almaksour et Frédéric Colas sans qui je n'aurais pas pu réaliser les essais expérimentaux sur la plate-forme MTDC de RTE. Je remercie également Moez Belhaouane avec qui j'ai beaucoup échangé et qui m'a généreusement accueilli chez lui en Tunisie. Enfin, je remercie Julian Freytes, a.k.a. "El Tractor" avec qui j'ai travaillé en binôme pendant plus de quatre mois et qui est véritablement devenu un ami.

À Supélec, je tenais d'abord à remercier Stéphanie Douesnard qui m'a accompagné dans toutes les démarches administratives aussi contraignantes qu'obscures. Et je remercie bien évidemment tous mes collègues et amis, actuellement ou anciennement thésards au département Énergie de CentraleSupélec, avec qui j'ai passé la majeure partie de ces trois années de doctorat!

Sur une note plus intime, je remercie Anne et Daniel qui m'ont suivi et accompagné à tous les stades de la thèse. Je remercie mes parents qui m'ont toujours poussé à aller de l'avant et qui m'ont toujours soutenu depuis l'autre bout de la France. Et enfin, à ma fiancée, Charlotte, qui me soutient et me supporte depuis plus de six ans, et qui m'emmène vers un futur radieux.

Abstract

High Voltage Direct Current (HVDC) transmission systems are largely used worldwide, mostly in the form of back-to-back and point-to-point HVDC, using either thyristor-based Line Commutated Converters (LCCs) or IGBT-based Voltage Source Converters (VSCs). With the recent deployment of the INELFE HVDC link between France and Spain, and the commissioning in China of a three-terminal HVDC transmission system using Modular Multilevel Converters (MMCs), a modular design of voltage source converters, the focus of the scientific community has shifted onto the analysis and control of MMC-based HVDC transmission systems.

In this thesis, the average value models of both a standard 2-level VSC and an MMC are proposed and the most interesting difference between the two converter technologies –the control of the stored energy in the MMC– is emphasised and explained. These models are then linearised, expressed in state-space form and validated by comparing their behaviour to more detailed models under Electro-Magnetic Transient (EMT) programs. Afterwards, these state-space representations are used in the modelling of HVDC transmission systems, either point-to-point or Multi-Terminal HVDC (MTDC), via a Matlab[®] routine specially designed to be capable of generating any generic HVDC transmission system regardless of its topology. A modal analysis is performed on an HVDC link, for both 2-level VSCs and MMCs. The modes of these two systems are specified and compared and the independent control of the DC voltage and the DC current in the case of an MMC is illustrated. This analysis is extended to the scope of a 5-terminal HVDC system in order to perform a stability analysis, understand the origin of the system dynamics and identify the dominant DC voltage mode that dictates the DC voltage response time. Using the Singular Value Decomposition (SVD) method on the MTDC system, the proper design of the voltage-droop gains of the controllers is then achieved so that the system operation is ensured within physical constraints, such as the maximum DC voltage deviation and the maximum admissible current in the power electronics. The impact of the DC cable models on the SVD results is studied and the classical PI model of a cable section is improved to properly reproduce the dynamics of a DC grid. Finally, a supplementary droop

–the frequency-droop control– is proposed so that MTDC systems also participate to the onshore grids frequency regulation. However, this controller interacts with the voltage-droop controller. This interaction is mathematically quantified and a corrected frequency-droop gain is proposed. This control is then illustrated with an application to the physical converters of the *Twenties* project mock-up.

This work have brought a better understanding of MMC-based HVDC systems by comparison to standard 2-level VSC systems, and furnished a tool to generate and analyse any MTDC system of any topology and any converter technology. A design methodology of the voltage-droop controller for multi-terminal HVDC systems has been developed, and a new control technique allowing the converters to participate in the AC grid frequency regulation has been proposed.

Résumé court en français

La multiplication des projets HVDC de par le monde démontre l'engouement toujours croissant pour cette technologie de transport de l'électricité. La grande majorité de ces transmissions HVDC correspondent à des liaisons point-à-point et se basent sur des convertisseurs AC/DC de type LCC ou VSC à 2 ou 3 niveaux. Les travaux de cette thèse se focalisent sur l'étude, le contrôle et la commande de systèmes HVDC de type multi-terminal (MTDC), avec des convertisseurs de type VSC à 2 niveaux ou modulaire multi-niveaux (MMC).

La première étape consiste à obtenir les modèles moyens du VSC à 2 niveaux et du MMC ainsi que leurs commandes respectives. La différence fondamentale entre ces deux convertisseurs, à savoir la possibilité pour le MMC de stocker et de contrôler l'énergie des condensateurs des sous-modules, est détaillée et expliquée. Ces modèles et leurs commandes sont ensuite linéarisés et mis sous forme de représentations d'état, puis validés en comparant leur comportement à ceux de modèles de convertisseurs plus détaillés à l'aide de logiciels de type EMTP (ElectroMagnetic Transient Program). Une fois validés, les modèles d'état peuvent être utilisés dans une routine Matlab[®] permettant de générer le modèle d'état de tout système de transmissions HVDC, qu'il soit point-à-point ou MTDC, indépendamment de la topologie du réseau DC. La comparaison d'une liaison HVDC à base de VSC 2 niveaux et d'une liaison HVDC à base de MMC est alors réalisée. Leurs valeurs propres sont étudiées et comparées, et les modes ayant un impact sur la tension DC sont identifiés et analysés. Cette étude est ensuite étendue à un système MTDC à 5 terminaux, et son analyse modale permet à la fois d'étudier la stabilité du système, mais aussi de comprendre l'origine de ses valeurs propres ainsi que leur impact sur la dynamique du système. La méthode de décomposition en valeurs singulières (SVD) permet ensuite d'obtenir un intervalle de valeurs possibles pour le paramètre de "voltage droop", permettant ainsi le contrôle du système MTDC tout en s'assurant qu'il soit conforme à des contraintes bien définies, comme l'écart maximal admissible en tension DC. L'impact du modèle des câbles DC sur les résultats de la SVD est également étudié. Enfin, une proposition de "frequency droop" ("statisme" en français), permettant aux convertisseurs de participer au réglage de la fréquence des réseaux AC auxquels ils sont connectés, est étudiée. Le frequency droop est utilisé conjointement avec le voltage droop afin de garantir le bon fonctionnement de la partie AC et de la partie DC. Cependant, l'utilisation des deux droop génère un couplage indésirable entre les deux commandes. Ces interactions sont mathématiquement quantifiées et une correction à apporter au paramètre de frequency

droop est proposée. Ces résultats sont ensuite validés par des simulations EMT et par des essais sur la plate-forme MTDC du laboratoire L2EP.

Les travaux de cette thèse ont permis une meilleure compréhension des systèmes MTDC à base de MMCs. Ils ont également permis le développement d'un outil permettant de générer et d'analyser la représentation d'état de tout système MTDC, indépendamment de la topologie de son réseau DC ou de la technologie utilisée pour ses convertisseurs. Par ailleurs, ces travaux ont conduit à la mise en place d'une méthodologie permettant l'obtention d'une plage de valeurs pour le paramètre de voltage droop des systèmes MTDC vis-à-vis de contraintes pré-définies. Enfin, une commande permettant aux convertisseurs de participer à la régulation de la fréquence du réseau AC a été proposée et validée expérimentalement.

Résumé de la thèse en français

Introduction

La multiplication des projets High-Voltage Direct Current (HVDC) de par le monde démontre l'engouement toujours croissant pour cette technologie de transport de l'électricité. Les raisons de ce succès sont multiples, les principales étant : (a) l'augmentation des besoins en terme d'interconnexions électriques entre les pays voisins; (b) la limite de distance du transport de l'énergie électrique via des câbles souterrains ou sous-marins avec la technologie High-Voltage Alternative Current (HVAC) est approximativement de 50 km. Cette limite n'existe pas avec la technologie HVDC; (c) la connexion de réseaux électriques AC asynchrones n'est possible qu'avec la technologie HVDC; (d) des pertes et coûts réduits pour le transport de l'électricité sur de longues distances par rapport à la technologie HVAC.

Cependant, alors que le HVDC sous forme de liaison point-à-point constitue maintenant une technologie arrivée à maturité et que les convertisseurs de type MMC commencent à être la norme pour les liaisons utilisant technologie VSC, la mise en place de systèmes HVDC sous forme de Multi-Terminal HVDC (MTDC) – c'est-à-dire l'interconnexion de plus de deux terminaux AC/DC par un réseau HVDC – reste aujourd'hui un enjeu majeur. En effet, seulement cinq systèmes MTDC sont aujourd'hui en activité dans le monde, et seulement pour des réseaux HVDC de topologie radiale et non pas maillée. Pour autant, un système MTDC permet de faciliter les échanges de puissance entre les différents acteurs du système, de mutualiser leurs réserves primaires, d'ajouter plus de flexibilité au système, et dans le cas des fermes éoliennes offshore, de lisser les fluctuations de production en considérant la production d'électricité offshore sur une large zone géographique.

Le développement des systèmes MTDC doit initialement passer par l'étape de leur modélisation afin de permettre leur analyse. Les travaux de cette thèse de doctorat débutent par la modélisation de convertisseurs de type Voltage Source Converter (VSC) (à la fois le VSC à deux niveaux et multi-niveaux Modular Multilevel

Convertir (MMC)) ainsi que leur commande. Ces modèles sont ensuite linéarisés, mis sous forme de représentations d'état et validés par comparaison avec la simulation Electro-Magnetic Transient (EMT) de modèles plus détaillés. Une routine Matlab[®] permet alors de générer automatiquement la représentation d'état de tout système MTDC indépendamment de la topologie de son réseau DC grâce à l'agrégation des représentations d'état des convertisseurs du système et des câbles utilisés pour les lignes de transmission DC. Le modèle d'état ainsi obtenu est ensuite étudié à l'aide d'une analyse modale et de l'utilisation de l'outil de décomposition en valeurs singulières (en anglais Singular Value Decomposition (SVD)). Finalement, une boucle de réglage de fréquence est ajoutée aux convertisseurs d'un système MTDC afin qu'ils participent au réglage de fréquence des réseau AC aux-quels ils sont connectés.

Modélisation des convertisseurs de type VSC

Dans les travaux de cette thèse de doctorat, la modélisation du convertisseur VSC à deux niveaux et de sa commande est très similaire à celle de [117]. La partie AC du convertisseur est modélisée dans le plan $dq0$ par un circuit RL correspondant au transformateur et la partie DC est associée au condensateur de sortie du convertisseur directement connectée au bus DC. Le convertisseur est considéré idéal (pas de pertes dans l'électronique de puissance) et sa commande est constituée d'une boucle de courant en cascade avec des boucles de puissance ou de tension. La boucle de courant permet le découplage de courants AC dans le plan $dq0$. Les boucles extérieures permettent le contrôle de la puissance active, de la puissance réactive, de la tension DC ou de la tension AC.

La modélisation du convertisseur de type VSC multi-niveaux (MMC) est basée sur les travaux de [50]. Au niveau de la commande du convertisseur, la boucle de courant ainsi que les boucles de puissance et/ou de tension présentes dans le VSC à deux niveaux restent inchangées. Cependant, la topologie du MMC est telle que l'énergie totale stockée dans les condensateurs des sous-modules (SMs) peut-être régulée, tandis que les VSCs à deux niveaux ne peuvent tout simplement pas stocker de l'énergie puisque leur condensateur de sortie est directement connecté au bus DC. S'impose alors la mise en place d'une boucle de courant DC en cascade avec une boucle de régulation de l'énergie stockée dans les SMs du MMC, permettant de ce fait un contrôle indépendant des variables AC et DC.

Les modèles des deux types de VSC (i.e. le VSC deux niveaux et le MMC) et leurs commandes respectives sont ensuite linéarisés sous l'hypothèse des petits signaux, puis

mis sous la forme de représentations d'état. Chaque modèle est validé à travers une comparaison avec des modèles plus détaillés lors de simulations effectuées avec des logiciels de simulation de type EMT.

Étude d'une liaison HVDC

Les représentations d'état des convertisseurs sont utilisées pour générer le modèle d'état d'une liaison HVDC pour des convertisseurs de type VSC à deux niveaux, puis pour des convertisseurs de type MMC, et dans le cas où un seul MMC partage l'énergie stockée dans les condensateurs de ses sous-modules, puis dans le cas où les deux convertisseurs partagent leur énergie stockée dans les condensateurs des SMs.

Une analyse modale permet l'identification des modes dangereux vis-à-vis de la stabilité de la liaison HVDC, et permet de mettre en avant les modes qui régissent la dynamique du courant et de la tension DC du système.

L'émulation du comportement de la liaison HVDC avec VSC deux niveaux par la liaison avec MMC – uniquement dans le cas où les deux convertisseurs partagent leur énergie stockée dans les condensateurs des Sub-Modules (SMs) avec le bus DC – est également illustrée et expliquée, mettant ainsi l'accent sur le rôle de la boucle de courant DC présente dans la commande du MMC et absente pour le VSC à deux niveaux.

Représentation d'état et analyse modale d'un système MTDC

La représentation d'état d'un système MTDC 5-terminaux à base de MMCs est obtenue à l'aide d'une routine Matlab[®] développée spécialement dans le but d'agréger automatiquement les modèles d'état de plusieurs sous-systèmes, à savoir les convertisseurs et les câbles constituant les lignes électriques, en prenant en compte les relations entre les entrées et les sorties de ces sous-systèmes.

Une fois le modèle d'état du système MTDC obtenu, une analyse modale permet d'identifier les modes qui jouent un rôle dans la dynamique des variables du système telles que le courant, la tension DC ou l'énergie stockée dans les SMs des MMCs. La stratégie de contrôle dite "voltage droop", une stratégie de contrôle permettant à plusieurs convertisseurs d'un système MTDC de participer à la régulation de la tension DC, est expliquée et illustrée. L'impact du gain des contrôleurs à voltage droop sur

les valeurs propres du système est étudié en détails afin d'expliquer la dynamique du système. En particulier, les valeurs du droop conduisant à un système instable sont identifiées et écartées.

Dimensionnement du paramètre de voltage droop par décomposition en valeurs singulières

La conception et le design des systèmes MTDC doit être tel que la tension du bus continu ne dépasse pas une déviation maximale admissible souvent fixée à $\pm 5\%$. Par conséquent, le choix du paramètre de voltage droop des convertisseurs est extrêmement important puisqu'il impacte directement à la fois la déviation en tension DC générée par les convertisseurs (point de vue statique) mais aussi l'évolution de la tension DC d'un point de vue dynamique, par exemple pendant les régimes transitoires. D'ailleurs, alors que le choix du paramètre de voltage droop peut facilement être réalisé d'un point de vue statique, il est beaucoup plus difficile de savoir si le choix de ce paramètre conduira à un respect de la contrainte d'un point de vue dynamique. L'emploi de l'outil de décomposition en valeurs singulières (SVD) permet de répondre à cette problématique.

Un système MTDC est un système à plusieurs entrées et plusieurs sorties (en anglais, Multi-Input Multi-Output (MIMO)). Ainsi, les directions des vecteurs d'entrée et de sortie influent grandement sur le gain du système, ce qui rend l'étude par fonction de transfert laborieuse et inadéquate. L'analyse de la réponse fréquentielle du système peut cependant être réalisée grâce à la méthode de décomposition en valeurs singulières (SVD), où la valeur singulière maximale exprime le gain maximum possible du système à une fréquence donnée en considérant toutes les directions possibles du système. Ainsi, en s'assurant que la valeur singulière maximale ne viole jamais la limite déterminée par la déviation maximale admissible d'une variable d'étude, le respect de la contrainte par le système est garantie. Dans le cas de l'étude de la tension DC, cette méthode conduit à un intervalle de valeurs possibles du paramètre de voltage droop qui certifie le respect de la contrainte en tension par le système.

Les résultats de la méthode SVD appliquée au réseau MTDC 5-terminaux présentement considéré sont ensuite étudiés pour différents modèles de câbles DC. Ils montrent que les câbles du réseau à courant continu ne devraient jamais être modélisés par un unique condensateur, ou même par une section RC, puisqu'une grande partie des dynamiques du système – en particulier celles résultant d'une interaction entre les éléments du réseau à courant continu et les convertisseurs – sont alors effacées. Les résultats montrent également que la modélisation des câbles DC par un modèle dit "PI-

couplé” ne donne pas de résultats satisfaisants puisque les interactions entre le réseau DC et les convertisseurs deviennent quasi-inexistantes. Enfin, l’utilisation d’une section PI classique, largement utilisée pour modéliser les câbles DC dans la littérature, donne une représentation assez précise du comportement dynamique du système MTDC, mais amplifie déraisonnablement les interactions entre le réseau DC et les convertisseurs, empêchant de ce fait l’étude du système vis-à-vis d’une contrainte donnée. Ce modèle PI classique peut cependant être amélioré par l’ajout de plusieurs branches RL en parallèle afin de permettre à l’impédance du modèle de câble de correspondre au mieux à l’impédance d’un câble de référence dit “wide-band” dans le logiciel EMTP-TV[®]. Les résultats de la SVD pour ce dernier modèle montrent que, pour le système MTDC considéré, deux intervalles distincts de paramètre de voltage droop assurent au système de respecter la déviation maximale en tension continue de $\pm 5\%$. Cependant, l’étude de stabilité réalisée lors de l’analyse modale va venir réduire davantage ces intervalles de valeurs acceptables.

Étude d’une commande dite de “frequency droop”

Après avoir rappelé le principe de fonctionnement du voltage droop pour les convertisseurs VSC-HVDC, et proposé un contrôle équivalent mais pour la fréquence des réseaux AC – dit de “frequency droop”, ou “statisme” en français – l’utilisation simultanée des deux types de droop est considérée à travers un contrôleur à double emploi. Ce contrôleur permet au convertisseur de participer à la fois à la régulation de la tension DC et au réglage de la fréquence du réseau AC auquel il est connecté.

Cependant, l’utilisation simultanée des deux types de droop génère un couplage entre les déviations de puissance qu’ils génèrent. Il est alors nécessaire de corriger le paramètre de frequency droop afin de le conformer aux exigences des Gestionnaires de Réseau de Transport (GRTs) en dépit de cette interaction entre les droops. Une étude théorique quantifie ces interactions et propose une correction du paramètre de frequency droop en fonction des paramètres de voltage droop de chaque convertisseur du système considéré. L’utilisation de ce contrôleur à double emploi prouve être une alternative viable aux contrôleurs à un seul droop puisqu’il dispose conjointement des avantages des deux droops, et conduit donc à un système plus fiable. Cependant, les interactions entre les réseaux AC et DC ne doivent pas être négligées puisqu’elles dégradent l’efficacité de ces deux droops.

Des simulations sur le logiciel de simulation EMTP-RV[®] ainsi que des essais expérimentaux sur la maquette du laboratoire L2EP d’un système MTDC démontrent

l'impact du voltage droop sur le réglage de la fréquence apporté par le frequency droop lors d'un événement AC, et valident la valeur corrigée du paramètre de frequency droop proposée, ce qui permet au convertisseur de respecter les exigences du GRT malgré les interactions indésirables entre les deux droops.

Perspectives et futurs travaux

Au niveau des convertisseurs, la commande du MMC basée sur le contrôle de l'énergie décrite dans cette thèse devrait être comparée aux commandes qui ne prennent pas en compte le contrôle de l'énergie stockée dans les condensateurs des SMs et qui commencent à bourgeonner dans la littérature. Toujours en rapport avec le contrôle de l'énergie, des études plus poussées devraient être effectuées pour savoir quand et pourquoi un MMC devrait partager son énergie avec le bus DC dans le cas d'une commande basée sur le contrôle de l'énergie.

Les travaux de cette thèse de doctorat ouvrent la voie à l'étude plus poussée de systèmes MTDC. Étant donné que le point de fonctionnement du système affecte le modèle d'état du MTDC, il serait judicieux d'aller plus loin et de réaliser une étude détaillée sur l'impact du point de fonctionnement sur la dynamique d'un système MTDC. Vis-à-vis de la sélection du paramètre de voltage droop, il serait intéressant de définir un modus operandi de sélection du paramètre de voltage droop des convertisseurs basé non seulement sur des critères de stabilité et de performances comme dans les travaux de cette thèse, mais aussi sur un critère d'optimalité.

Enfin, il serait judicieux d'améliorer le contrôleur dit de "frequency droop" proposé en ajoutant par exemple une inertie virtuelle au convertisseur. Il serait également particulièrement intéressant de s'interroger sur la possibilité pour un MMC de puiser dans ses réserves d'énergie stockée dans les SMs lors de sa participation au réglage de la fréquence, car cela permettrait de ne pas affecter la partie DC du système MTDC à travers le couplage entre les deux droops présentés dans le dernier chapitre de cette thèse.

Table of contents

List of figures	xxiii
List of tables	xxix
1 Introduction	1
1.1 Electrification History - The War of Currents	2
1.2 Today's Incentives for HVDC Systems	4
1.3 Motivations behind Multi-Terminal HVDC Systems - Example of the North Sea	7
1.4 Objective of the Thesis and Main Contributions	9
1.5 Outline of the Thesis	10
1.6 List of Publications Derived from This Work	11
2 HVDC Systems – State of the Art	13
2.1 Chapter Introduction	14
2.2 LCC-HVDC Technology	15
2.2.1 Components of LCC-HVDC	15
2.2.2 LCC-HVDC Configurations	18
2.3 VSC-HVDC Technology	19
2.3.1 Components of VSC-HVDC	19
2.3.2 Configuration and Operation of VSC-HVDC	23
2.3.3 Advantages of VSC-HVDC over LCC-HVDC	26
2.4 MMC-HVDC Technology	28
2.4.1 Components of MMC-based HVDC transmissions	28
2.4.2 Advantages of the MMC	31
2.5 Chapter Conclusion	31
3 Modelling and Control of VSC-based Converter Stations	35
3.1 Chapter Introduction	36

3.2	Modelling and Control of a VSC-HVDC Station	36
3.2.1	Modelling of the VSC	37
3.2.2	Control of the VSC	40
3.3	Modelling and Control of an MMC-HVDC Station	48
3.3.1	Modelling of the MMC	48
3.3.2	Control of the MMC	58
3.4	Chapter Conclusion	64
4	State-Space Representation and Modal Analysis of an HVDC Link	65
4.1	Chapter Introduction	66
4.2	State-Space Representation of the VSC Model	66
4.2.1	Linearisation of the VSC Model	66
4.2.2	State-Space Representation of the Linear VSC Model	70
4.2.3	Validation of the VSC Models	71
4.3	State-Space Representation of the MMC Model	76
4.3.1	Linearisation of the simplified MMC Model	76
4.3.2	State-Space Representation of the Linear MMC Model	77
4.3.3	Validation of the MMC Models	79
4.4	Modal Analyses of an HVDC Link	87
4.4.1	HVDC link with VSCs	87
4.4.2	HVDC link with MMCs	93
4.4.3	Comparison of the HVDC Systems	100
4.4.4	Comparison of two MMC-based HVDC Links with different Energy Control Strategies	105
4.5	Chapter Conclusion	108
5	SVD Analysis of a 5-Terminal MMC-Based MTDC System	111
5.1	Chapter Introduction	112
5.2	State-Space Representation of the MTDC System	113
5.2.1	Control Strategy of an MTDC System	113
5.2.2	State-Space Representation of the MTDC System	114
5.2.3	Modal Analysis of the 5-Terminal MTDC System	116
5.3	Singular Value Decomposition Analysis of the 5-Terminal MTDC System	127
5.3.1	Motivation Behind the SVD Tool	128
5.3.2	Design of the Voltage-Droop Gain using the SVD Tool	131
5.4	Impact of the DC Cable Model on the SVD Results	136
5.4.1	Wideband Model Reference	136

5.4.2	DC Cable Models Used in this Study	137
5.4.3	Comparison of the SVD Results for the 5 DC grid Models	142
5.5	Chapter Conclusion	144
6	A Frequency Droop Technique for the MTDC to Support AC Grid	
	Frequency	147
6.1	Chapter Introduction	148
6.2	MTDC Systems to Support the AC grids Frequency Regulation	149
6.2.1	Proposition for a Frequency-Droop Controller	149
6.2.2	Voltage Droop and Frequency Droop: a Dual Controller	151
6.2.3	Interactions between Voltage and Frequency Droop	152
6.2.4	Correction of the Frequency-Droop Parameter	154
6.2.5	Impact of the Droop Controller Limits	155
6.3	EMT Simulations	157
6.3.1	Considered System	157
6.3.2	Effect of an AC Frequency Variation	159
6.3.3	Effect of an AC Frequency Variation when a Controller Reaches its Limit	163
6.4	Experimental Tests	165
6.4.1	Presentation of the L2EP Lille 5-Terminal Mock-up	165
6.4.2	Experimental Conditions	167
6.4.3	Experimental Results	168
6.5	Chapter Conclusion	174
7	Conclusions and Future Perspectives	175
7.1	Conclusions	176
7.2	Future Work	179
	Bibliography	183
	Appendix A Parameters of the HVDC Transmission Systems Used	
	Throughout this Thesis	193
A.1	HVDC Link with VSCs	193
A.2	HVDC Link with MMCs	194
A.3	MTDC with VSCs	195
A.4	MTDC with MMCs	197
	Appendix B Direct-Quadrature-Zero (or dq0) Transformation	199

Appendix C Controller Tuning	203
C.1 Inner Current Loops Controller Tuning	203
C.2 DC Voltage Loop Controller Tuning	205
Appendix D State-Space Association Routine	207
D.1 State-Space Association Theoretical Principle	207
D.2 Routine Methodology for State-Space Interconnection	209

Acronyms used in this thesis

AAM	Arm Average Model
AVM	Average Value Model
BCA	Balancing Capacitor Algorithm
EMT	Electro-Magnetic Transient
GTO	Gate Turn-Off thyristor
HVDC	High-Voltage Direct Current
HVAC	High-Voltage Alternative Current
IGBT	Insulated-Gate Bipolar Transistor
LCC	Line Commutated, current source Converter
MIMO	Multi-Input Multi-Output
MMC	Modular Multilevel Converter
MTDC	Multi-Terminal HVDC
OHL	Overhead Transmission Line
PCC	Point of Common Coupling
PLL	Phase-Locked Loop
PWM	Pulse-Width Modulation
RoW	Right of Way
SISO	Single-Input Single-Output
SM	Sub-Module
SVD	Singular Value Decomposition
TSO	Transmission System Operator
UGC	Underground Cable
VSC	Voltage Source Converter

List of figures

1.1	Thomas Edison with his phonograph at age 31 (source).	3
1.2	A photograph of Nikola Tesla at age 40 (source).	3
1.3	An original Edison light bulb from 1879 from Thomas Edison's shop in Menlo Park (Source).	4
1.4	Topsy the Elephant was electrocuted by Thomas Edison's technicians at Coney Island before a crowd of thousands (Photo: Chicago Tribune).	4
1.5	ABB project comparisons that led to commissioning of the 3-terminal North-East Agra UHVDC system in 2015 [3, 4].	5
1.6	Costs against transmission distances for HVDC and HVAC systems.	6
1.7	EWEA's 20 year offshore network development master plan [45].	8
2.1	Standard HVDC converter station [17].	15
2.2	Thyristor structure and characteristics.	16
2.3	Thyristor valve arrangement for a Line-Commutated Current Source Converter.	17
2.4	Three basic LCC-HVDC configurations.	19
2.5	IGBT structure and characteristics.	20
2.6	IGBT valve arrangement for a Voltage Source Converter.	21
2.7	2-level sinusoidal PWM method with a reference (sinusoidal) signal, a carrier (triangular), the actual VSC line-to-neutral voltage waveform and its fundamental.	22
2.8	Standard configuration of a VSC-based HVDC transmission.	23
2.9	Equivalent circuit of a VSC connected to an AC system.	24
2.10	Phasor diagram corresponding to the circuit of Figure 2.9.	24
2.11	PQ diagram of a VSC. The grey area corresponds to the operation area.	26
2.12	MMC Topology.	29
2.13	Output voltage of a 9-level MMC (i.e. 8 SMs per arm).	29
2.14	Standard configuration of an MMC station.	31

3.1	Single phase diagram of the VSC without filter.	37
3.2	Circuit of the VSC model in the $dq0$ reference frame.	39
3.3	Modelling of the AC side of the VSC without its control.	39
3.4	Modelling of the DC side of the VSC without its control.	40
3.5	Modelling of both the AC and DC side of the VSC without its control.	40
3.6	Control strategy of a VSC.	41
3.7	Modelling of the Phase-Locked Loop (PLL).	42
3.8	Modelling of the inner control loop of the VSC.	44
3.9	Open-loop and closed-loop power control variants.	45
3.10	DC voltage control with an IP controller to minimise any possible overshoot when applying a reference step [84, p. 43].	45
3.11	PCC voltage control with a PI controller.	46
3.12	Block-diagram of the complete VSC station, comprising of the physical system and its control (the PLL is not represented).	47
3.13	MMC models presented in [92], successively decreasing in complexity.	48
3.14	Detailed representation of the AAM of an MMC.	50
3.15	Equivalent circuit of each AAM phase.	53
3.16	Circuit of the simplified MMC model in the $dq0$ reference frame.	55
3.17	Block diagram modelling of the AC side of an MMC in the $dq0$ reference frame.	56
3.18	Block diagram modelling of the DC side of an MMC.	56
3.19	Block diagram modelling of the stored energy of the MMC.	56
3.20	Block diagram modelling of the complete physical system of the MMC.	57
3.21	Equivalent circuits of MMC and two-level VSC.	58
3.22	Control hierarchy of a Modular Multilevel Converter [48].	59
3.23	Modelling of the AC current control loop of the MMC.	60
3.24	Modelling of the DC current control loop of the MMC.	61
3.25	Modelling of the total energy control loop of the MMC.	62
3.26	Block-diagram of the complete MMC station, comprising of the physical system and its control (the PLL is not represented).	63
4.1	Comparison of the non-linear and linearised model of the physical system of the VSC.	68
4.2	Block diagram of the linearised VSC model.	69
4.3	Interconnection constraints of the subsystems that constitute the VSC model.	70
4.4	Configuration of a VSC-based HVDC link.	72

4.5	Active power reference of the P-mode converter.	72
4.6	Reactive power reference of the P-mode converter.	72
4.7	DC voltage reference of the Vdc-mode converter.	72
4.8	Comparison of the active and reactive power responses of the P-mode converter for the state-space model, the average value model and the detailed IGBT-based model of a standard 2-level VSC.	74
4.9	Comparison of the DC voltage responses of the Vdc-mode converter for the state-space model, the average value model and the detailed IGBT-based model of a standard 2-level VSC.	75
4.10	Comparison of the non-linear and linearised model of the physical system of the MMC.	77
4.11	Block diagram of the linearised MMC model.	78
4.12	Interconnection constraints of the subsystems that constitute the MMC model.	79
4.13	Configuration of an MMC-based HVDC link.	80
4.14	Active power reference of the P-mode converter.	80
4.15	Reactive power reference of the P-mode converter.	80
4.16	DC voltage reference of the Vdc-mode converter.	81
4.17	Comparison of the active power responses of the P-mode converter for the state-space model, the simplified model, the model type 3 and the model type 2 of an MMC.	82
4.18	Comparison of the total stored energy of the P-mode converter for the state-space model, the simplified model, the model type 3 and the model type 2 of an MMC.	83
4.19	Comparison of the DC voltage of the Vdc-mode converter for the state-space model, the simplified model, the model type 3 and the model type 2 of an MMC.	84
4.20	Comparison of the DC current generated by the P-mode converter for the state-space model, the simplified model, the model type 3 and the model type 2 of an MMC.	86
4.21	Fitted PI-section of a cable [21, 22].	88
4.22	Eigenvalues representation of the VSC-based HVDC link.	91
4.23	Participation ratio of the P-mode VSC, the Vdc-mode VSC and the DC cable to the eigenvalue groups (A,B,...,G) of the complete system.	92
4.24	Eigenvalues trajectories of the VSC-based HVDC link for a sweep of the DC voltage controller response time.	92

4.25	DC voltage response to a reference step of 0.1 p.u. for different values of the 5% response time of the DC voltage controller, for the VSC-based HVDC link.	93
4.26	Participation ratio of the P-mode MMC, the Vdc-mode MMC and the DC cable to the Eigenvalues of the complete system.	95
4.27	Eigenvalues trajectories of the MMC-based HVDC link for a sweep of the power injected/withdrawn from the DC link by the P-mode MMC (i.e. for a sweep of the system operating point).	96
4.28	Eigenvalues trajectories of the MMC-based HVDC link for a sweep of the DC voltage controller response time.	96
4.29	Visualisation of the DC voltage and the stored energy of the MMCs just after the first step of -0.3 p.u. of the active power reference of the P-mode converter.	101
4.30	VSC- and MMC-based HVDC system responses to a 0.1 p.u. DC voltage reference step.	103
4.31	VSC- and MMC-based HVDC system responses to a -0.3 p.u. active power reference step.	104
4.32	VSC and MMC-based HVDC system responses for two different scenarii. Scenario 1: when only the Vdc-mode converter is sharing its energy with the DC bus. Scenario 2: when both converters are sharing their energy with the DC bus.	107
5.1	Block diagram of the voltage-droop technique.	114
5.2	Topology of the MTDC system.	115
5.3	Interconnection constraints of the subsystems of the 5-terminal MTDC system of Figure 5.2.	116
5.4	Fitted PI-section of a cable [21, 22].	117
5.5	Participation ratio of the P-mode MMCs, the Vdc-droop MMCs and the DC grid to the eigenvalues of the complete system.	118
5.6	Eigenvalue representation of the MTDC system and their dependency to either the DC grid, the P-mode MMCs or the Vdc-droop MMCs, for a voltage-droop parameter $k_v = 0.1$ p.u./p.u.	120
5.7	Eigenvalue trajectories of the MTDC system for a sweep of the voltage-droop parameter k_v	121
5.8	Comparison of the DC voltage and current of the MMC1 for an active power step of -0.2 p.u. of either the MMC4 or the MMC5.	126
5.9	Transfer function model of the considered 5-terminal MTDC system.	128

5.10	Comparison of the SVD results with the individual transfer functions of the 5-terminal MTDC system, for a voltage-droop parameter of 0.1 p.u./p.u.	131
5.11	SVD results for a sweep of the voltage-droop parameter of the MMCs.	133
5.12	SVD results, with the DC currents of the Vdc-droop MMCs as outputs and the active power reference of the P-mode converters as inputs, for different values of the voltage-droop parameter of the MMCs.	135
5.13	Underwater layout of the reference cable.	136
5.14	Representation of the 4 cable models used in this section.	138
5.15	Comparison of the cable impedances of the classical PI model, the Coupled PI model and the Fitted PI model to the impedance of a more detailed wide-band cable model.	141
5.16	SVD results, with the grid node voltages as outputs and the active power reference of the P-mode converters as inputs, for 5 different cable models and 6 different values of the voltage-droop parameter of the MMCs.	142
6.1	Control strategy of a VSC-HVDC converter	150
6.2	Block diagram of the frequency-droop technique.	151
6.3	Block diagram of the dual controller combining both the voltage- and the frequency-droop techniques.	151
6.4	Single-line diagrams of the considered system.	158
6.5	Power and voltage distribution of the VSCs, frequency of the AC grid 1 and power deviations of the droops of VSC 1	160
6.6	Impact of the interactions between the droops on the DC voltage and on the frequency of the AC grid 1	161
6.7	Frequency of the AC grid 1	163
6.8	Power reference deviations generated by the droops.	164
6.9	Effective frequency-droop parameter of VSC 1	165
6.10	Mock-up general overview [84].	166
6.11	Experimental system topology.	167
6.12	Evolution of the system variables after the tripping of a synchronous machine of the simulated AC grid connected to the VSC 2, in scenario 1, where the VSC 2 is only equipped with a voltage-droop controller.	169
6.13	Evolution of the system variables after the tripping of a synchronous machine of the simulated AC grid connected to the VSC 2, in scenario 2, where the VSC 2 is only equipped with a frequency-droop controller (contractual value).	170

6.14	Evolution of the system variables after the tripping of a synchronous machine of the simulated AC grid connected to the VSC 2, in scenario 3, where the VSC 2 is equipped with both a frequency-droop (contractual value) and a voltage-droop controller.	171
6.15	Evolution of the system variables after the tripping of a synchronous machine of the simulated AC grid connected to the VSC 2, in scenario 4, where the VSC 2 is equipped with both a frequency-droop (corrected value) and a voltage-droop controller.	172
6.16	Comparison of the DC voltage of the VSC 2 and the frequency of the AC grid 2 for the four scenarii.	173
A.1	Configuration of a VSC-based HVDC link.	193
A.2	Fitted PI-section of a cable [21, 22].	194
A.3	Configuration of an MMC-based HVDC link.	194
A.4	Detailed representation of the AAM of an MMC.	195
A.5	Single-line diagrams of the considered system.	196
A.6	Topology of the MTDC system.	197
B.1	Clarke and Park transforms.	200
C.1	System response to a step for different values of the damping ratio but for the same ω_n . The $\pm 5\%$ error band is represented in green.	204
D.1	State-space generation routine overview.	210

List of tables

1.1	List of all MTDC systems worldwide.	9
2.1	Comparison between an LCC, a 2-level VSC and an MMC [31, 32, 97, 84].	32
4.1	Component values of the fitted PI cable.	88
4.2	Eigenvalue characteristics of the VSC-based HVDC link.	90
4.3	Eigenvalue characteristics of the MMC-based HVDC link.	95
5.1	Component values of the fitted PI cable.	117
5.2	Eigenvalue characteristics of the MTDC system for a voltage-droop parameter $k_v = 0.1$ p.u./p.u.	118
5.3	Cable parameters.	136
6.1	Initial power reference values and droop coefficients of the VSC-HVDC converters	159
A.1	Base values used for the Per Unitage.	193
A.2	VSC component values and control loops response times.	194
A.3	Component values of the fitted PI cable.	194
A.4	MMC component values and control loops response times.	195
A.5	Initial operating point.	195
A.6	Base values used for the Per Unitage.	195
A.7	VSC component values and control loops response times.	196
A.8	DC cable data.	196
A.9	AC OHL data.	196
A.10	AC grid 1 generator power outputs.	196
A.11	AC grid 1 loads.	197
A.12	Generator data.	197
A.13	Transformer data.	197
A.14	Initial operating point.	198

Chapter 1

Introduction

I speak without exaggeration when I say that I have constructed 3,000 different theories in connection with the electric light, each one of them reasonable and apparently likely to be true. Yet only in two cases did my experiments prove the truth of my theory.

– T. Edison as quoted in “Talks with Edison”
by George Parsons Lathrop in *Harper’s magazine*, Vol. 80 (February 1890) [68].

Of the various branches of electrical investigation, perhaps the most interesting and immediately the most promising is that dealing with alternating currents.

– N. Tesla in *Experiments With Alternate
Currents of High Potential and High Frequency* (1904) [105].

1.1 Electrification History - The War of Currents

In our modern society, over 85% of the world's population have access to electricity [110]. Being used virtually every minute of every day, its usage is manifold, may it be for lighting, water heating, cooking, air conditioning, space heating, refrigeration, electronic devices, etc... However, this has not always been the case.

The first historical practical usage of electricity is attributed to the arc lamp (or arc light) which consists of an arc between carbon electrodes in air. It was invented by the Cornish chemist Humphry Davy in the early 1800's [40] and was widely used in several US cities starting in the late 1870's. This lighting technology needed dangerously high voltages (above 3000 volts), was maintenance intensive, buzzed, flickered and constituted a fire hazard, and hence, was only suitable for outdoor lighting.

It is in December 1879 that the inventor and businessman Thomas Edison (Figure 1.1) demonstrated his first successful light bulb model in a public demonstration at Menlo Park (see Figure 1.3). The light bulb was designed for a specific market: to bring electric lighting directly into a customer's business building or home, a niche not served by arc lighting systems. However, personal electric lighting implied bringing the electricity to each household via a transmission system non-existent at the time. To this purpose, Edison founded the *Edison Illuminating Company* that would build Thomas Edison's low voltage direct current (DC) electric distribution "utility" designed for indoor business and residential use as an alternative to gas and oil-based lighting.

At that time, the young Serbian inventor Nikola Tesla (Figure 1.2) emigrated to New York city and worked for Edison at his *Edison Machine Works* on Manhattan's Lower East Side. In 1885, Tesla was given the difficult task to redesign the Edison Company's direct current generators and successfully accomplished it, but immediately resigned when Edison refused to pay him the promised \$50,000 reward [52]. Tesla then tried to focus on his own project, an induction motor that ran on alternating current (AC). However, being penniless, he went through difficult years where he had to work at various electrical repair jobs and as a ditch digger. Along this time, he successfully convinced two men, Alfred S. Brown, a Western Union superintendent, and New York attorney Charles F. Peck to back him financially and handle his patents. In 1887, Tesla developed his induction motor that ran on alternating current, and in 1888, he seized the opportunity to demonstrate his alternating current induction motor at the American Institute of Electrical Engineers (now IEEE) which draw the attention of the businessman George Westinghouse who had been trying to secure a similar patent for some time [52].



Figure 1.1: Thomas Edison with his phonograph at age 31 (source).

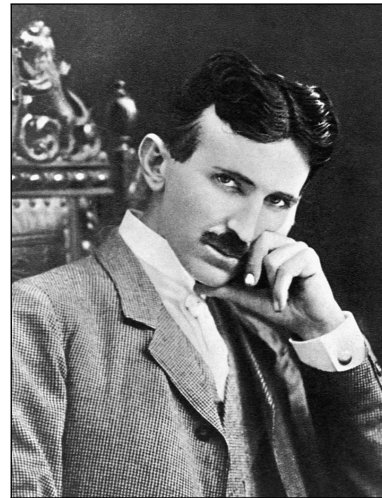


Figure 1.2: A photograph of Nikola Tesla at age 40 (source).

In July 1888, Brown and Peck negotiated a licensing deal with George Westinghouse for Tesla's induction motor design for \$60,000 and a royalty of \$2.50 per AC horsepower produced by each installed motor. Westinghouse also hired Tesla for one year for the large fee of \$2,000 per month (equivalent to \$60,000 today) to be a consultant at the *Westinghouse Electric & Manufacturing Company's* Pittsburgh labs [65].

From this point on, alternative current power systems began to gain a lot of attention. Edison, not wanting to lose the royalties he was earning from his DC current patents, began a campaign to discredit AC by spreading misinformation saying that alternating current was more dangerous, even going so far as to publicly electrocute stray or dangerous animals using alternating current to prove his point (see Figure 1.4). Despite his stance against death penalty, he even wrote, as an electrical expert, that the best method to supply electricity to the electric chair would be to use current generated by "alternating machines, manufactured principally in this country by Geo. Westinghouse" [62]. This was the height of the Current War.

In 1893, *Edison General Electric* bid to electrify the Chicago World's Fair (also known as the World's Columbian Exposition) using Edison's direct current for \$554,000, but lost the contract to George Westinghouse, who said he could power the fair for only \$399,000 using Tesla's alternating current. After this, the Niagara Falls Power Company decided to award Westinghouse the contract to generate power from Niagara Falls and dispatch it to distant cities such as Chicago, Buffalo or New York using transformers to increase the voltage and reduce losses in the lines, something that could not be achieved with direct current at the time since there were no power electronics



Figure 1.3: An original Edison light bulb from 1879 from Thomas Edison's shop in Menlo Park (Source).



Figure 1.4: Topsy the Elephant was electrocuted by Thomas Edison's technicians at Coney Island before a crowd of thousands (Photo: Chicago Tribune).

like today. At this point, Edison was dismissed from the direction board of his own company, and *Edison General Electric*, renamed as simply *General Electric*, jumped on the alternating current train, definitively abandoning DC. Alternative current had all but obliterated direct current and won the current war.

But while AC was perfectly adequate for the conditions of the day – and for much of the 20th century – the needs of the 21st century are showing its limits. And the irony is that, although Edison lost the battle in the 19th century, his direct current is making a comeback today. However, it is not a question of AC versus DC any longer, but of AC and DC working together [5].

1.2 Today's Incentives for HVDC Systems

As the electric generation resources become more and more diversified along with the rise of renewable energy sources, and that the electric consumption is changing, today's transmission system is evolving as it faces new challenges. This includes connecting offshore wind farms to the mainland grids, transmitting large amount of power over thousands of kilometres, interconnecting asynchronous AC networks, delivering bulk power via underground cables, supplying power to congested areas, and having more control over the power flows in the electric system. To achieve this, the high-voltage AC transmission system of the 20th century is slowly evolving into a hybrid transmission system that combines both HVAC and HVDC.

The use of HVDC is driven by four main incentives. The first one is the growing need at national or regional boundaries for the exchange of large amount of power, especially when the AC technology is not suitable to achieve or simply increase the required power exchange capability.

The second incentive is the increasing usage of Underground Cables (UGCs). In fact, for over a century, electrical transmission systems have been based mainly on Overhead Transmission Lines (OHLs) [87] which offer a cost advantage when compared to high-voltage UGCs. However, it is getting increasingly difficult to build additional OHLs today mainly because it is met with public resentment and political resistance as it impacts the landscape [115], generates a lot of noise [87] and requires Rights of Way (RoWs) that occupies valuable lands. For this reason, as of late, many new high-voltage transmission lines consist of UGCs. However, if there is a need for using cable transmission, the HVDC technology becomes the only technical solution even at relative short distances (50-100 km) [15, 82]. Even in the case where OHLs are preferred, an OHL-based HVDC system needs 2 to 3 times smaller RoWs than for an HVAC system of similar ratings, as illustrated by Figure 1.5.

The third incentive to mix HVDC transmissions with the AC transmission systems lies in the fact that HVDC is the only solution to connecting two asynchronous AC networks.

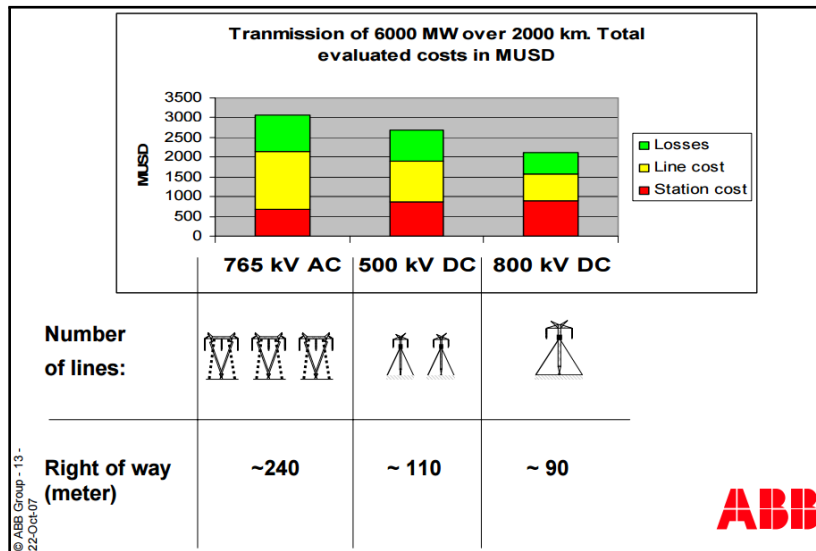


Figure 1.5: ABB project comparisons that led to commissioning of the 3-terminal North-East Agra UHVDC system in 2015 [3, 4].

Finally, the fourth incentive to develop the HVDC technology lies in the costs of the transmission systems. Indeed, even though the AC/DC stations are still onerous and

require an important initial cost, an HVDC system requires at least three times less lines than an HVAC transmission system [78, 98], and the losses in the lines are much less important. This implies that, after a break-even distance (approximately 50 km when using UGCs and 400 km when using OHLs) [101, 16, 84], an HVDC transmission system becomes always less costly than an HVAC transmission system, as illustrated by Figure 1.6.

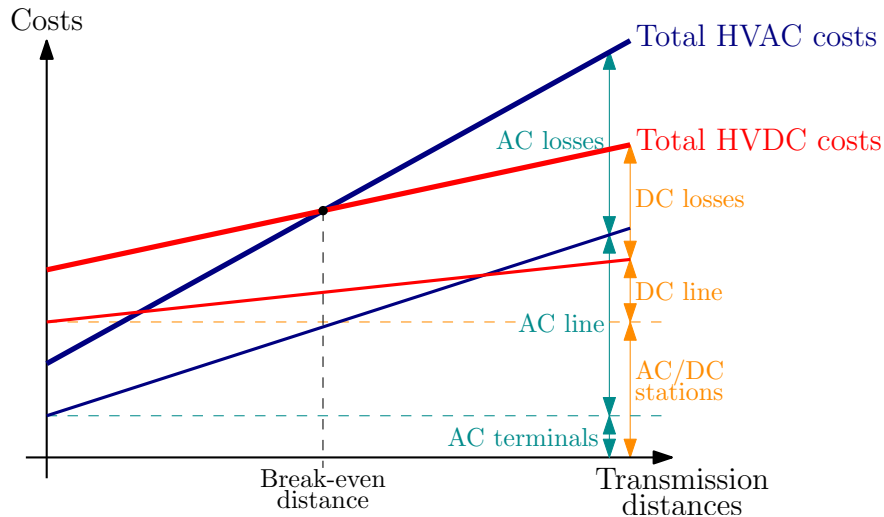


Figure 1.6: Costs against transmission distances for HVDC and HVAC systems.

Below are several applications where the HVDC technology is either advantageous over HVAC, or is the only feasible option:

- Transiting large amount of power via undersea or underground cables, e.g. the 2000 MW interconnection IFA2000 [88] between France and the United Kingdom under the English Channel.
- Providing point-to-point electrical power interconnections between asynchronous AC power networks, e.g. The HVDC back-to-back facility Shin Shinano [29, p.100-103] interconnecting Japan's western and eastern power grids whose frequencies are respectively 60 Hz and 50 Hz;
- Delivery of electrical bulk power over long distances, e.g. the 3000MW connection of the hydroelectric power station "Three Gorges Dam" to Changzhou, China, (commissioned in May 2003 [2]);
- Increasing the capacity of an existing AC transmission with an HVDC system using underground cables, which eliminates the need of new transmission RoWs,

e.g. the HVDC transmission between France and Spain using MMCs (INELFE [89]);

- Supplying power to congested load areas, where it is not possible to build new generations to meet the load demand, e.g. the connection of Majorca Island to the Spanish mainland network via an HVDC link (COMETA [99]);
- Controlling power flows. In AC networks, the power flows are subject to physical laws (Kirchhoff) since they depend on the lines impedances and on the network topology. Power marketers and system operators may need the power flow control capability provided by HVDC transmissions, e.g. the ever-fluctuating power flow between France and Spain depending on the renewable generation of Spain [89].

1.3 Motivations behind Multi-Terminal HVDC Systems - Example of the North Sea

With the proliferation of HVDC transmission lines, some geographical regions hold a high concentration of HVDC point-to-point systems. DC reinforcements, extensions and AC zone interconnections may then lead to a Multi-Terminal HVDC (MTDC) grid in the future. The North Sea is a great example of such a geographical area which possesses a high number of HVDC links.

In 2008, the European Council fixed two targets to reach by 2020, which are: (a) a reduction of at least 20% in greenhouse gas emissions by 2020; (b) a 20% share of renewable energies in EU energy consumption by 2020. These targets have been confirmed by the European Council in 2014 [109]. In order to meet them, 40 GW of offshore wind farms will be installed by 2020, and 150 GW by 2030 [45] in the shallow waters of the North Sea. Several HVDC links will dispatch the harnessed energy to the mainland grids of the area, as recommended by the European Wind Energy Association (EWEA) [45].

As depicted in Figure 1.7, some of the recommended HVDC systems are in fact MTDC systems, some of them interconnecting the three asynchronous AC grids of the area: the United-Kingdom network, the Nordic network and the European network. However, as of today, only the 3-terminal VSC-HVDC transmission system between the Oslo region (Norway) and Skåne (Sweden) with a terminal midway in Sweden has been confirmed by the ENTSO-E [44], and more will probably follow as the Cigré working group B4.52 approved the development of MTDC systems in 2013 [116].

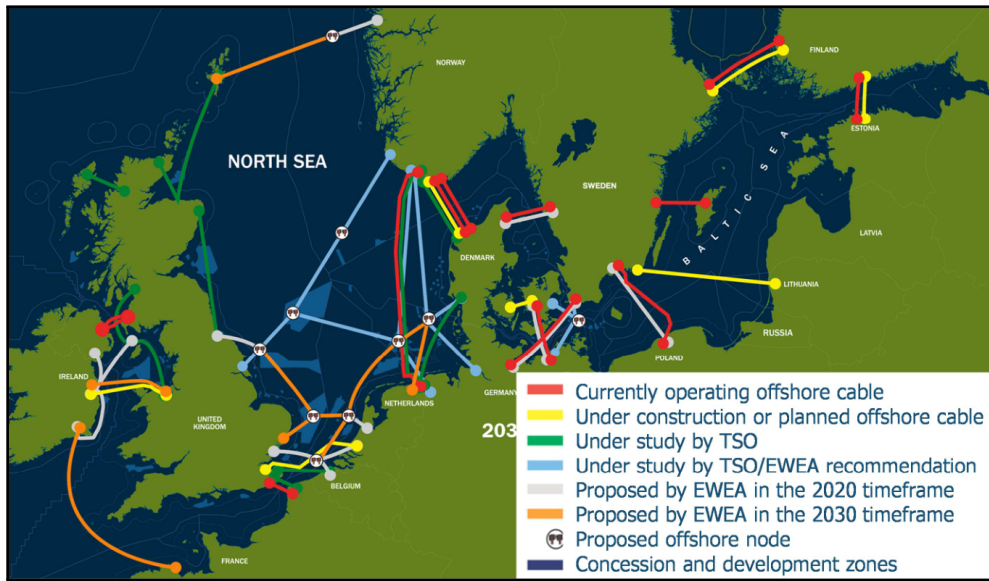


Figure 1.7: EWEA's 20 year offshore network development master plan [45].

There are only 5 MTDC systems worldwide in operation today (see Table 1.1) due to key technical challenges that still need to be tackled before MTDC systems become more accessible. These include [84]:

- Power flow and DC voltage control methods must be perfected and tested for both normal and disturbed operation conditions.
- Fast protection schemes must be elaborated to detect all possible faults before the whole MTDC system collapses.
- DC circuit breakers must be developed to physically isolate faulted parts in the DC grid.
- Standardization must be established so that devices from different manufacturers can work together for both normal and disturbed operation conditions.

Once these key challenges are dealt with, MTDC systems will become a reality and are expected to provide additional features compared to point-to-point links. These include more flexibility of power dispatch, optimised assets between wind power and trade transfer capability [70], smoothed wind power fluctuations (mitigation of wind power produced from different area) [37], frequency support to onshore grids [102] and more overall reliability (the system can operate or at least partially operate even if one of its component is out of service).

Name	Terminals	DC voltage	Power rating	Length	Commissioning year
Italy-Corsica-Sardinia project	3 LCCs	± 200 kV	300 MW	385 km (UGC)	1967 (upgraded in 1988 and 1992)
Quebec-New England project	3 LCCs	± 450 kV	2000 MW	1480 km (OHL)	1990 (upgraded in 2016)
Nan'ao-Shantou pilot	3 MMCs	± 160 kV	350 MW	32 km (OHL, UGC)	2013
Zhoushan project	5 MMCs	± 200 kV	1000 MW	129 km (UGC)	2014
North-East Agra project	4 LCCs	± 800 kV	8000 MW	1728 km (OHL)	2015

Table 1.1: List of all MTDC systems worldwide.

1.4 Objective of the Thesis and Main Contributions

The main objective of this thesis is to assess the potential and limitation of the use of VSC-HVDC in both point-to-point and multi-terminal transmissions, in particular for the MMC type of VSC. The control of such systems is elaborated and designed, and their dynamics are thoroughly apprehended and analysed.

The main contributions of the thesis are:

- The modelling of a standard 2-level VSC is recalled and then the modelling of an Average Value Model (AVM) of an MMC is derived and detailed, based on the work of [50]. Similarly, the control of a standard 2-level VSC is recalled and then the control taking into account the specificity of the MMC is derived. Additionally, the voltage-droop control strategy of an MTDC system is explained and detailed.
- The two developed models and their respective controls are linearised and put in state-space form. They are then validated by comparing their behaviour to more detailed models in an EMT simulation using the program EMTP-RV[®].
- Based on these state-space representations of the two VSC types (the standard 2-level VSC and the MMC), a methodology and a Matlab[®] routine to acquire the state-space representation of any HVDC system (point-to-point or MTDC, independently of the DC grid topology) is proposed and detailed. The newly acquired system state-space representations can then be used for modal analysis.
- Several in-depth modal analysis are performed for various systems: from a VSC-based HVDC link to an MMC-based, 5-terminal, MTDC system. The modes of these systems are studied and analysed using the participation factors among other linear control theory tools. Their dependency on some key control

parameters such as the voltage-droop parameter for an MTDC system are thoroughly investigated by studying the eigenvalue evolution of the system against parameter sweep. The main modes of the studied systems are proved to show a similar behaviour. Their respective influence on the system dynamics are fully apprehended, especially for the DC voltage.

- The design of the voltage-droop parameter with regard to the system performances is achieved by using the Singular Value Decomposition (SVD) method. This leads to a range of acceptable voltage-droop parameter values allowing the system to comply with a given maximum DC voltage deviation constraint.
- A frequency-droop controller allowing the HVDC transmission system to participate in the mainland grids frequency regulation is proposed. An EMT simulation for a 5-terminal HVDC system illustrates the behaviour of the proposed controller and experimental tests on the L2EP Lille mock-up validate the theoretical results.

1.5 Outline of the Thesis

Chapter 2 presents the two main HVDC converter technologies, namely Line Commutated, current source Converter (LCC) and Voltage Source Converter (VSC), and details the topology differences between two types of VSC: the standard 2-level VSC and the Modular Multilevel Converter (MMC). The chapter describes the structure of each converter technology, details the components of each converter station, enumerates the main HVDC configurations and lists the advantages and disadvantages of one over another.

Chapter 3 focuses on the acquisition of an AVM for both the standard 2-level VSC and the MMC. The control of the two converters is also covered and thoroughly detailed. In particular, the additional control loops of the energy-based control of the MMC are illustrated and explained.

In Chapter 4, the AVM of both the 2-level VSC and the MMC are linearised and put in state-space form. Using these state-space forms, the state-space representation of an HVDC link is acquired for both converter types. The behaviour of the HVDC link state-space models are then compared to more detailed models via simulations in an EMT programme (EMTP-RV[®]). The comparison leads to the validation of the state-space models of the converters. The state-space representation of the HVDC link is then used for an in-depth modal analysis that allows understanding and analysing the system dynamics and assessing their sensibility to some control parameters.

Chapter 5 first recalls the voltage-droop control technique used to regulate the DC voltage of an MTDC system. Then, the previous individual converter state-space models are inserted in a fully detailed Matlab[®] routine, specifically designed to automatically generate the state-space representation of a 5-terminal, MMC-based MTDC system. This state-space representation is then used for an in-depth modal analysis of the MTDC system and leads to the identification of interaction modes that play a deciding role in the DC voltage and DC current dynamics. The MTDC system state-space representation is then used to design the voltage-droop parameter by using the Singular Value Decomposition (SVD) tool. This allows narrowing the range of voltage-droop parameters to a small interval that ensures that the system never violates a 5% DC voltage deviation constraint, either in steady state or during transient. Additionally, the impact of the cable model on the SVD results is thoroughly analysed.

Chapter 6 proposes a frequency-droop controller that works in combination with the voltage droop of the converters of an MTDC system. The power deviations generated by both droops are mathematically quantified and the coupling between the two droops is exposed. A modified frequency-droop parameter is then proposed in order for the converter to still comply with the contractual value of the frequency droop agreed with the Transmission System Operator (TSO). The theoretical results are then validated by the EMT simulation of a 5-terminal MTDC system, and by the experimental results realised on the L2EP Lille MTDC system platform.

Finally, the conclusions of the work and some suggestions for future research are pointed out in Chapter 7.

1.6 List of Publications Derived from This Work

- Dai, J., Akkari, S., and Petit, M. (2013). Commande en tension dans un réseau HVDC. *Revue 3EI*, 73:pp15–20
- Akkari, S., Petit, M., Dai, J., and Guillaud, X. (2014). Modélisation, simulation et commande des systèmes VSC-HVDC multi-terminaux. In *Symposium de Génie Électrique (SGE14)*
- Akkari, S., Petit, M., Dai, J., and Guillaud, X. (2015c). Interaction between the Voltage-Droop and the Frequency-Droop Control for Multi-Terminal HVDC Systems. In *AC and DC Power Transmission, 11th IET International Conference on*, pages 1–7

- Akkari, S., Dai, J., Petit, M., and Guillaud, X. (2015a). Coupling between the frequency droop and the voltage droop of an AC/DC converter in an MTDC system. In *PowerTech, 2015 IEEE Eindhoven*, pages 1–6
- Akkari, S., Dai, J., Petit, M., Rault, P., and Guillaud, X. (2015b). Small-signal modelling for in-depth modal analysis of an MTDC system. In *Electrical Power and Energy Conference (EPEC), 2015 IEEE*, pages 233–238
- Akkari, S., Dai, J., Petit, M., and Guillaud, X. (2016a). Interaction between the voltage-droop and the frequency-droop control for multi-terminal HVDC systems. *IET Generation, Transmission Distribution*, 10(6):1345–1352
- Akkari, S., Prieto-Araujo, E., Dai, J., Gomis-Bellmunt, O., and Guillaud, X. (2016b). Impact of the DC Cable Models on the SVD Analysis of a Multi-Terminal HVDC System. In *Power Systems Computation Conference (PSCC), 2016*, pages 1–6
- Freytes, J., Akkari, S., Dai, J., Rault, P., Gruson, F., and Guillaud, X. (2016a). Small-Signal State-Space Modeling of an HVDC Link with Modular Multilevel Converters. In *2016 IEEE 17th Workshop on Control and Modeling for Power Electronics (COMPEL)*

Chapter 2

HVDC Systems – State of the Art

Edison says: After the electric light goes into general use none but the extravagant will burn tallow candles.

– Thomas Alva Edison in *Chester Daily Times* (8 January 1880) [27].

2.1 Chapter Introduction

As stated in the previous chapter, there are mainly two basic converter technologies used in modern HVDC transmission systems. The first technology one is the thyristor based Line Commutated, current source Converter (LCC) [16, 98], commonly named conventional HVDC, but also referred to as *HVDC classic* by ABB [6] and Siemens [101]. This technology has been widely used since the development of power electronics and semiconductors in the late 1960's and was considered the most reliable HVDC technology until recently.

The second HVDC technology is the Insulated-Gate Bipolar Transistor (IGBT) (or Gate Turn-Off thyristor (GTO) at lower voltage levels) based Voltage Source Converter (VSC) [115, 78], also referred to as *HVDC Light* by ABB [7] or *HVDC Plus* by Siemens [100, 101]. It was developed during the last two decades and offers several advantages over LCC-HVDC [97]. However, this technology is not suitable for HVDC systems transiting large amount of bulk power mainly because of increased losses in the converter [15]. It is only with the recent development of the Modular Multilevel Converter (MMC), a multi-level version of the standard 2-level VSC, that VSC based HVDC transmissions started to extend their reach to transmission systems with large amount of rated power, yet without attaining the higher rated power of LCC-HVDC transmissions.

Figure 2.1 portrays a standard HVDC converter station. The main difference between an LCC, a two or three-level VSC and an MMC resides mostly in the size of the shunt capacitors and harmonic filters areas, and in the size of the valve hall. The basic functioning of the converter station remains unchanged for each technology: the station is connected or disconnected from the AC network via AC breakers (in the AC switch-yard), the voltage is adapted for the converter via transformers, and finally the converter transforms the voltage from alternative to direct.

This chapter reviews these different HVDC technologies by itemizing the primary components of each technology, describing the different converter topologies and pointing out the main differences between them.

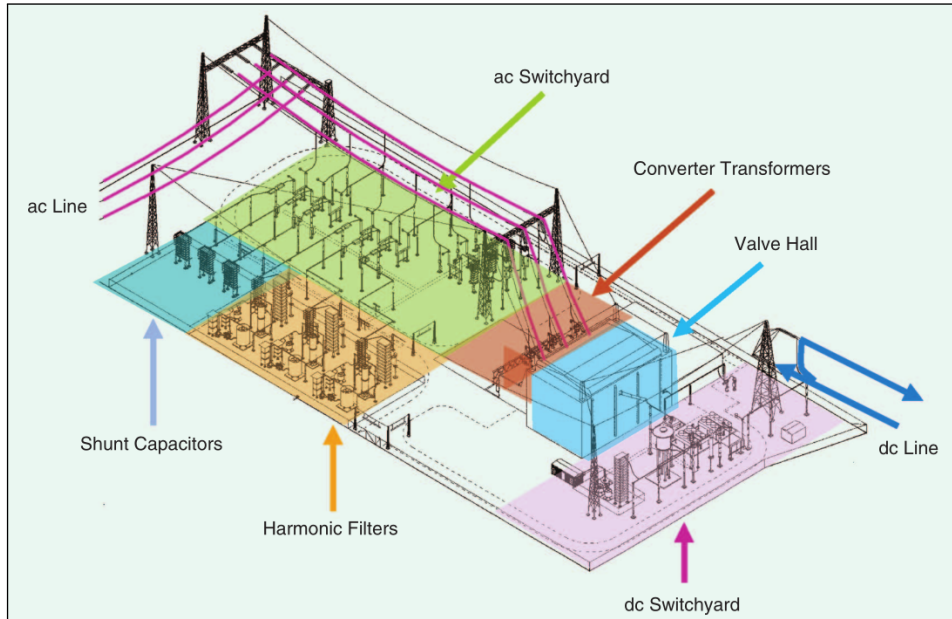


Figure 2.1: Standard HVDC converter station [17].

2.2 LCC-HVDC Technology

As the first efficient and reliable HVDC technology, LCC-HVDC has been widely used all around the world. This section describes the fundamental components of this technology, and reviews its main available configurations.

2.2.1 Components of LCC-HVDC

An LCC-based HVDC system consists of thyristor-based converters with their respective AC and DC filters, converter transformers and transmission lines.

In fact, the power thyristor is the basic component of an LCC. The thyristors used in HVDC plants today are characterized by silicon wafer diameters of up to 125 mm, a large voltage-blocking capability that can withstand up to 8 kV and current carrying capacities up to 4 kA, while the required gate power is just 40 mW [101], which makes this semiconductor device suitable for an AC/DC converter.

The basic structure of the power thyristor is an $N^+/P/N/P^+$ structure, as illustrated in Figure 2.2a. More details on the structure of the thyristor and its conception can be found in [19]. The thyristor characteristics are shown in Figure 2.2b. This semiconductor device provides both forward (BV_F) and reverse voltage-blocking (BV_R) capabilities making it well suited for AC/DC power circuit applications. When forward biased, the device can be triggered from the forward-blocking off-state to the on-state by using a

relatively small gate control current. In addition, the device automatically switches to the reverse-blocking off-state upon reversal of the voltage in an AC circuit [18].

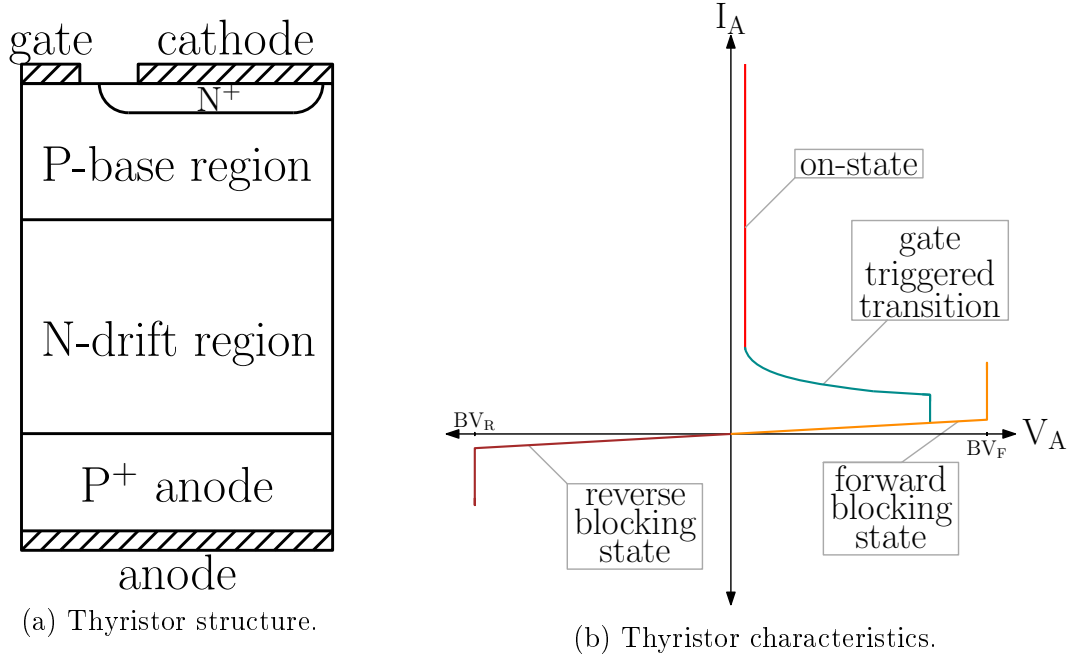


Figure 2.2: Thyristor structure and characteristics.

The LCC topology is usually comprised of two cascaded six-pulse bridges¹. Each six-pulse bridge consists of six thyristor valves and each valve consists of several series-connected thyristors² to achieve the desired DC voltage rating, as depicted in Figure 2.3a. The transformers connect the AC network to the valve bridges and adjust the AC voltage to a suitable level for the converters. The two six-pulse bridges of each converter are connected to two AC sources originating from the AC grid whose phases are shifted by 30° by means of wye-connected secondary and delta-connected secondary transformer topologies (i.e. respectively a Y-Y and a Y- Δ transformer topology). This yields a double advantage: the DC terminal can stand increased DC voltage, and some orders of AC and DC harmonics are naturally eliminated³. Operation in this manner is referred to as 12-pulse operation⁴. Depending on the converter station configuration

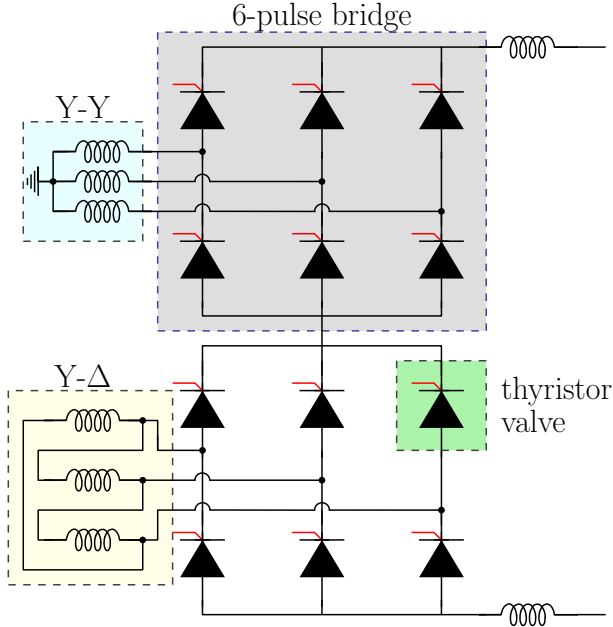
¹The six-pulse, also referred to as Graetz bridge, is a three-phase, full-wave bridge. The term six-pulse is due to six commutations or switching operations per period resulting in a characteristic harmonic ripple of six times the fundamental frequency in the DC output voltage [17].

²The thyristor valves are normally suspended from the ceiling of the valve hall for protection against earthquakes.

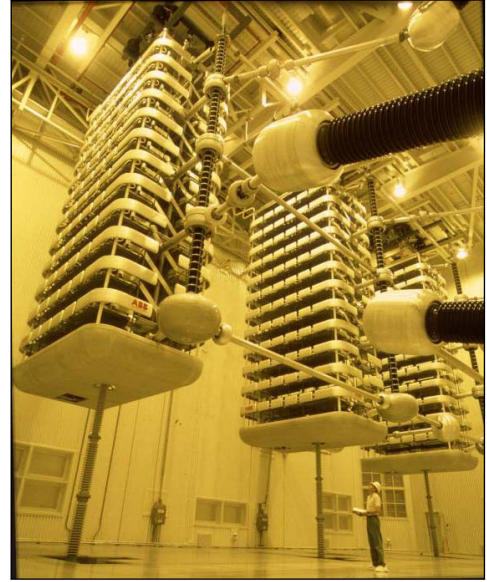
³These harmonic currents still flow through the valves and the transformer windings. However, they are 180° out of phase and cancel each other out on the primary side of the converter transformer.

⁴In 12-pulse operation, the characteristic AC current and DC voltage harmonics have frequencies of $12n \pm 1$ and $12n$, respectively.

(c.f. Section 2.2.2 below), either one or two 12-pulse bridges in series can be used to control both poles of the DC cables.



(a) 12-pulse Topology of a LC-CSC (AC filters are omitted).



(b) Quadruple thyristor valves of an LCC [28].

Figure 2.3: Thyristor valve arrangement for a Line-Commutated Current Source Converter.

By definition, LCC commutation (i.e. the transfer of current from one phase to another) is operated in a synchronized firing sequence of the thyristor valves. Since the thyristor must be forward biased before being triggered by a gate signal, the commutation can only be achieved with the AC current lagging the voltage, meaning that the converter needs reactive power to be operated. This reactive power is mostly supplied by AC filters (e.g. shunt banks or series capacitors) and the AC grid has to balance out any potential surplus or deficit of the reactive power for the converter to be operated properly.

The conversion process in an HVDC transmission system also introduces harmonic currents into the DC transmission lines. While this effect is negligible in the case of DC cable transmission lines, the DC voltage ripples have to be filtered in the case of OHLs. The DC filters can be either passive tuned filters (usually smoothing reactors [101]) or active filters [30].

2.2.2 LCC-HVDC Configurations

Depending on the application and location, a number of different HVDC station configurations can be identified [17, 98]. The most used configurations of a DC link are the back-to-back configuration, the monopolar configuration and the bipolar configuration, as displayed in Figure 2.4.

- *Back-to-back configuration:* This configuration (Figure 2.4a) is mainly used to interconnect two possibly asynchronous AC networks. In this case, the two HVDC stations are located at the same site and are directly connected without any DC transmission line.
- *Monopolar configuration:* This configuration (Figure 2.4b) is mainly used in congested areas, undersea transmissions or areas with high earth resistivity. It consists of two HVDC stations connected with a single conductor line with either a positive or a negative polarity. The return current is assured either via the ground or a relatively small metallic conductor.
- *Bipolar configuration:* This configuration (Figure 2.4c) is the most common configuration for overhead HVDC transmissions. It consists of a 12-pulse converter for each pole at each terminal. This gives two independent DC circuits, each capable of half capacity. For normal balanced operation there is no earth current. In case of outage in one pole, it is still possible to run the system as a monopolar earth-return configuration.

These configurations can easily be generalized to Multi-Terminal HVDC (MTDC) systems.

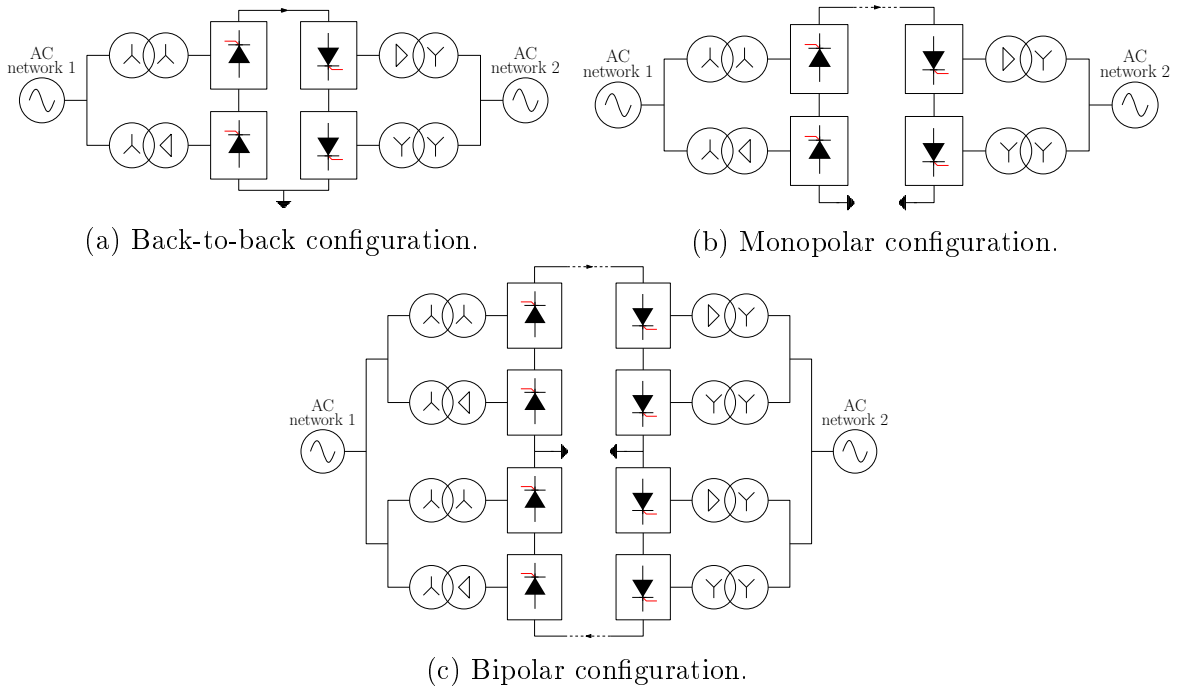


Figure 2.4: Three basic LCC-HVDC configurations.

2.3 VSC-HVDC Technology

During the last two decades, a new HVDC technology has emerged which makes use of the newly acquired IGBT semiconductor technology instead of thyristors [19]. This HVDC technology is referred to as VSC-HVDC (or VSC-based HVDC).

2.3.1 Components of VSC-HVDC

A VSC-HVDC system consists of IGBT (or GTO)-based converters, their corresponding DC capacitors, their respective AC filters, their associated transformers (also acting as phase reactors) and transmission lines.

The Insulated-Gate Bipolar Transistor (IGBT) offers a unique combination of ease of control due to its Metal Oxide Semiconductor (MOS)-gate structure, low chip cost due to its relatively high on-state current density, and exceptional ruggedness. Silicon IGBT modules are available with a blocking voltage capability up to 6.5 kV and a current handling capability of 1 kA [19], which makes them suitable, when stacked in series and parallel, for high voltage AC/DC applications.

The basic structure of the IGBT is a combination of a MOSFET ($N^+/P/N$ -base) controlled by the gate potential and a bipolar transistor (P^+ -region/ N -buffer/ N -base/ P^+), as illustrated in Figure 2.5a. The electric field in the asymmetric IGBT takes a

trapezoidal shape allowing supporting the forward blocking voltage with a thinner N-base region. This allows achieving a lower on-state voltage drop and superior turn-off characteristics than a thyristor. More details on the structure of the IGBT and its conception can be found in [19]. The IGBT characteristics are shown in Figure 2.5b. Similarly to the thyristor, the IGBT provides both forward (BV_F) and reverse ($BV_{R,S}$) voltage-blocking capabilities making it well suited for AC/DC power circuit applications. The switching of the IGBT device is performed by toggling the gate bias V_{GE} between zero and a positive bias above its threshold voltage. The IGBT structure is also capable of exhibiting an active region with the collector current saturated at a value determined by the applied gate bias V_{GE} [18], as illustrated in the figure.

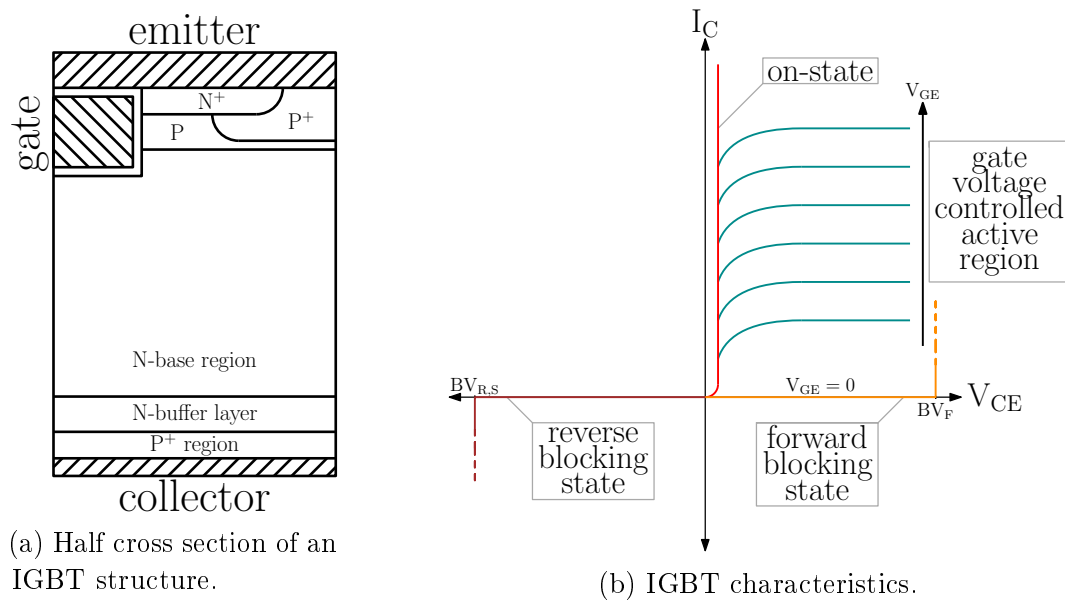


Figure 2.5: IGBT structure and characteristics.

The simplest VSC topology is the two-level three-phase bridge⁵ shown in Figure 2.6a. Similarly to the LCC thyristor valves, each conductor valve consists of several series-connected IGBTs (as shown in Figure 2.6b) for the converter to hold a higher blocking voltage capability and, hence, withstand an increased DC bus voltage. Each IGBT comes with an anti-parallel diode in order to ensure the four-quadrant operation of the converter.

The converter is commonly controlled through Pulse-Width Modulation (PWM) as shown in Figure 2.7, to create the desired voltage waveform⁶. Each phase leg

⁵A 3-level VSC can also be used, of which the functioning is very similar to the presented 2-level VSC.

⁶Through PWM control, the fundamental frequency component of the voltage can achieve any desired waveform, any phase angle and magnitude.

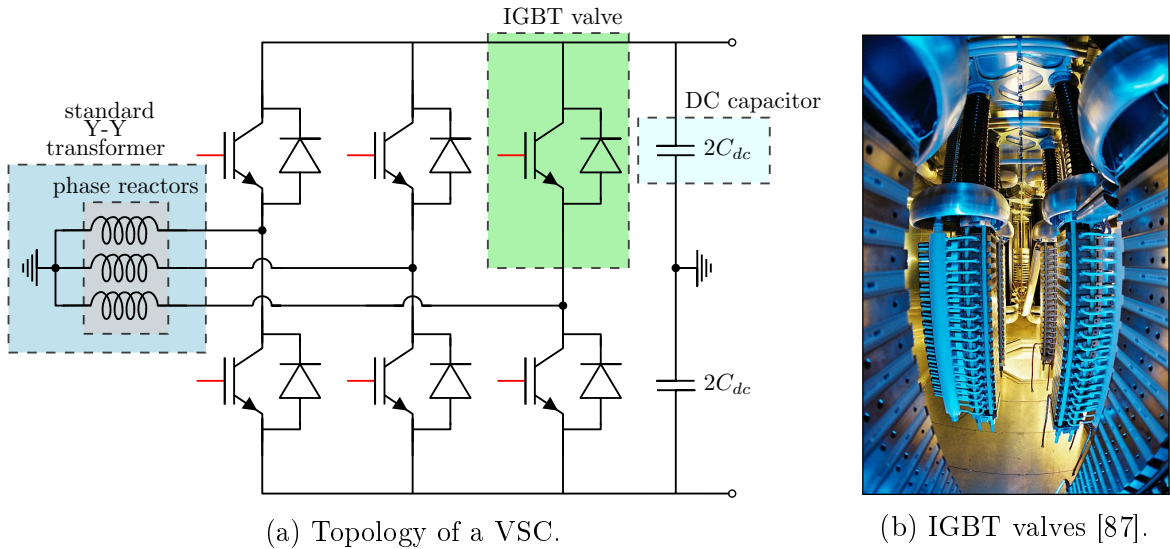


Figure 2.6: IGBT valve arrangement for a Voltage Source Converter.

of the converter is connected to the AC system through phase reactors that filters high frequencies of the voltage output of the converter. The harmonics are directly associated with the switching frequency of the converter.

The phase reactor is an inductive element with a small resistance that connects each leg of the converter to their respective phase of the AC network, hence, effectively permitting the connection of two voltage sources: the AC grid (assimilated to a voltage source) and the Voltage Source Converter (VSC). Through the control of the complex currents in the dq frame, the phase reactor enables the VSC to control the active and reactive power exchanged with the AC network. Due to its highly inductive feature, the phase reactor also acts as a low-pass filter that prevents high frequency harmonics from polluting the AC grid.

Filters in the form of shunt inductances and capacitors can also be included on the AC side to further reduce the harmonic content flowing into the AC system [39, 47]. However, thanks to the presence of the phase reactor, they are not indispensable in order to meet the typical restrictions on harmonic injection into the grid⁷ [61]. For the same reason, a standard transformer with a Y/Y or Y/ Δ topology can be used to connect the VSC to the AC network. In some cases, the inductive elements of the converter side of the transformer are large enough to be used as phase reactors, thus saving actual phase reactors between the converter and the transformer.

The DC bus capacitors act as an energy buffer by providing the required energy storage allowing the control of the power flow. They also offer filtering to reduce the

⁷Even more so in the case of a 3-level VSC.

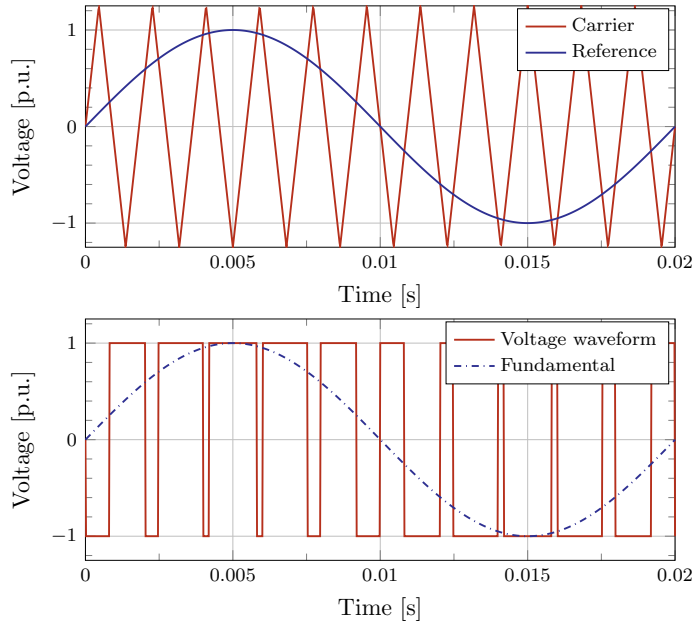


Figure 2.7: 2-level sinusoidal PWM method with a reference (sinusoidal) signal, a carrier (triangular), the actual VSC line-to-neutral voltage waveform and its fundamental.

DC voltage ripples generated by the PWM⁸. The DC capacitors are grounded at their electrical centre point to establish the earth reference potential for the transmission system.

In power systems, the inertia of a synchronous machine is commonly characterized by its inertia constant (H) to normalize the kinetic inertia of each generator with respect to their respective nominal power [67], and consequently allowing the comparison between units with different ratings. Similarly, the electrostatic energy stored in the DC capacitors of a converter can be weighted by the substation base power. This leads to an electrostatic constant homogeneous to time [84]:

$$H_c = \frac{\frac{1}{2}C_{dc}v_{dc,N}^2}{P_N} \quad (2.1)$$

where H_c is the electrostatic constant [s] of the considered converter, C_{dc} is the equivalent DC capacitor [F] of the converter, $v_{dc,N}$ is the nominal output DC voltage [V] of the converter and P_N is the nominal active power [W] of the converter station.

The electrostatic constant H_c actually corresponds to the time needed to charge the capacitors from zero to the rated voltage $v_{dc,N}$ if the converter is supplied with a

⁸Because of the PWM, the DC current contains harmonics which result in DC ripples on the DC voltage.

constant active power equal to P_N . The DC capacitor values can be calculated based on the desired electrostatic constant of the converter station.

As illustrated by (2.1), the selection of the DC capacitor values depends on the nominal power of the converter, its nominal DC voltage and its chosen electrostatic constant. Typically, the electrostatic constant H_c has a numerical value of 30-40 ms (i.e. a capacitance corresponding to a stored energy of 30-40 kJ/MW where MW refers to the converter rating) [61].

2.3.2 Configuration and Operation of VSC-HVDC

Even though all the configurations of LCC-HVDC of Figure 2.4 can be transferred to VSC-based HVDC, a standard VSC-based HVDC transmission is usually arranged with a single converter connected pole to pole rather than pole to ground, as shown in Figure 2.8.

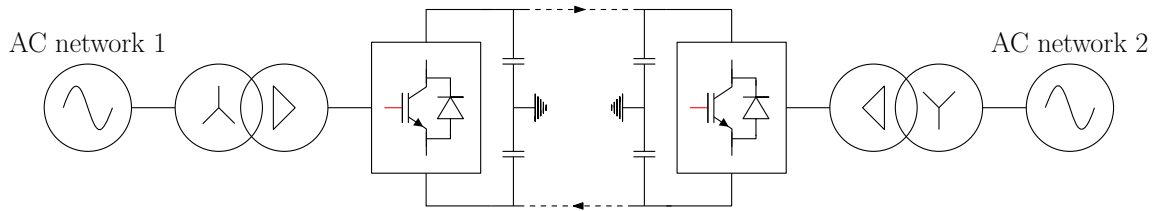


Figure 2.8: Standard configuration of a VSC-based HVDC transmission.

The transformer usually has a Y- Δ topology that connects the VSC to the AC network and guarantees a galvanic isolation between the AC system and the converter station. The AC side of the converter is connected to ground through a star point reactor to provide a reference for the AC voltage. The DC capacitors are grounded at their electrical centre point to establish the earth reference potential for the transmission system. Hence, half the converter DC voltage appears across the insulation on each of the two DC cables, one positive and the other negative.

This configuration can be generalized to Multi-Terminal HVDC (MTDC) systems. It will be the base configuration for each HVDC system considered in this thesis.

The basic operation of a VSC-HVDC is recalled below by modelling the AC side of the converter station by a controlled voltage source v_m connected to the AC grid via a phase reactor, and the DC side by a controlled current source i_{dc} , as depicted in Figure 2.9.

Assuming a sinusoidal PWM strategy (see Figure 2.7), the per-switching-cycle average AC voltage of a single phase can be controlled by simultaneously acting on the

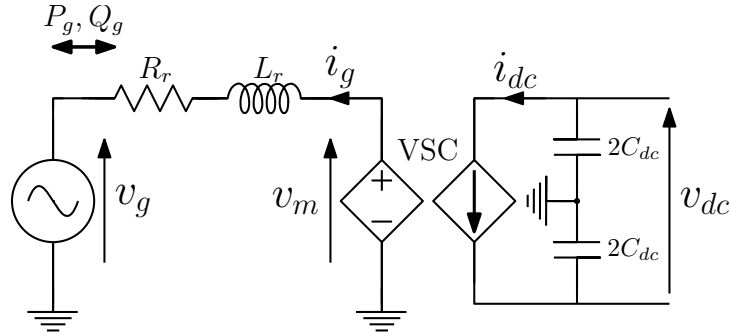


Figure 2.9: Equivalent circuit of a VSC connected to an AC system.

PWM modulation index m (defined as the ratio of the peak value of the modulating wave and the peak value of the carrier wave) which impacts the amplitude of the voltage waveform $V_m(m)$, on the angular frequency given by the Phase-Locked Loop (PLL) ω_{PLL} and on the phase shift of the output voltage δ .

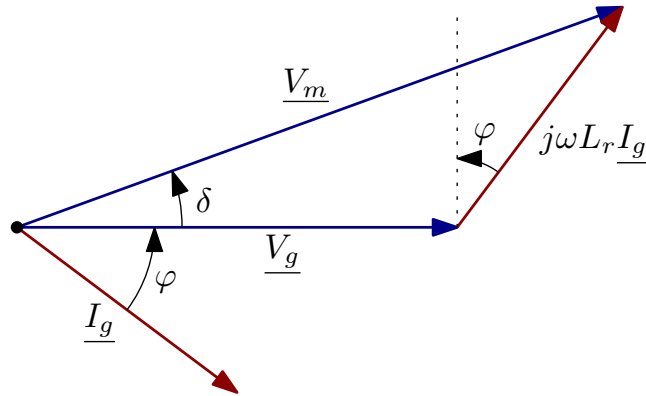


Figure 2.10: Phasor diagram corresponding to the circuit of Figure 2.9.

The phasor diagram of Figure 2.10 can be obtained for the following assumptions:

- The AC network current i_g has a quasi-sinusoidal waveform;
- The AC network voltage has a sinusoidal waveform $v_g = V_g\sqrt{2}\sin(\omega t)$;
- In steady-state, the averaged modulated voltage also has a sinusoidal waveform $v_m = v_{m,ref} = V_m(m)\sqrt{2}\sin(\omega_{PLL}t + \delta)$;
- The measured angular frequency is equal to the AC grid angular frequency $\omega_{PLL} = \omega$;
- The losses are neglected in the phase reactors and $X_r = \omega L_r$;

The active and reactive power can be expressed by the well known equations:

$$P_g = \frac{V_g V_m(m) \sin \delta}{X_r} \quad (2.2)$$

$$Q_g = \frac{V_g(V_g - V_m(m) \cos \delta)}{X_r} \quad (2.3)$$

The variables m , ω and δ are controlled by the VSC so that the voltage drop across the phase reactor is adjusted to control the active and reactive power accordingly. They can also be controlled independently: the active power flow between the AC system and the converter can be controlled by changing the phase angle δ between the fundamental frequency voltage generated by the converter v_m and the AC network voltage v_g . The reactive power can be determined by the amplitude of v_m [39].

However, even though the active and reactive power can be independently chosen, they must remain within certain limits: the operation range of a VSC-HVDC system is limited by three factors: current through the converter, DC voltage, and rating of the cable [33].

The limit corresponding to the current flowing through the power electronics of the converter depends on the switching elements of the converter, and more precisely on their maximum admissible current ratings that cannot be bypassed without hazardous consequences for the power electronic components. This first limit translates into a circle with centre at the origin and radius $V_g I_g^{\max}$ in the PQ diagram of the converter (see Figure 2.11):

$$S_g = \sqrt{P_g^2 + Q_g^2} \leq S_g^{\max} = V_g I_g^{\max} \quad (2.4)$$

The second limit comes from the limitation of the amplitude of the fundamental frequency voltage generated by the converter v_m . In fact, from (2.2) and (2.3) we have:

$$\cos^2 \delta + \sin^2 \delta = 1 = \left(\left(Q_g + \frac{V_g^2}{X_r} \right) \frac{X_r}{V_g V_m} \right)^2 + \left(\frac{P_g X_r}{V_g V_m} \right)^2$$

i.e.

$$\left(\frac{V_g V_m}{X_r} \right)^2 = P_g^2 + \left(Q_g + \frac{V_g^2}{X_r} \right)^2 \quad (2.5)$$

which is also the equation of a circle in the PQ diagram with centre $(0, -\frac{V_g^2}{X_r})$ and radius $\frac{V_g V_m}{X_r}$ (see Figure 2.11).

The third limit corresponds to the maximum admissible current through the DC cables of the HVDC transmission. It translates into two vertical lines in the PQ diagram at rated DC voltage, as depicted in Figure 2.11 where the dashed vertical lines are not actually restricting the operation area, as it is generally the case with well dimensioned systems.

$$|P_g| \leq V_{dc} I_{dc}^{\max} \quad (2.6)$$

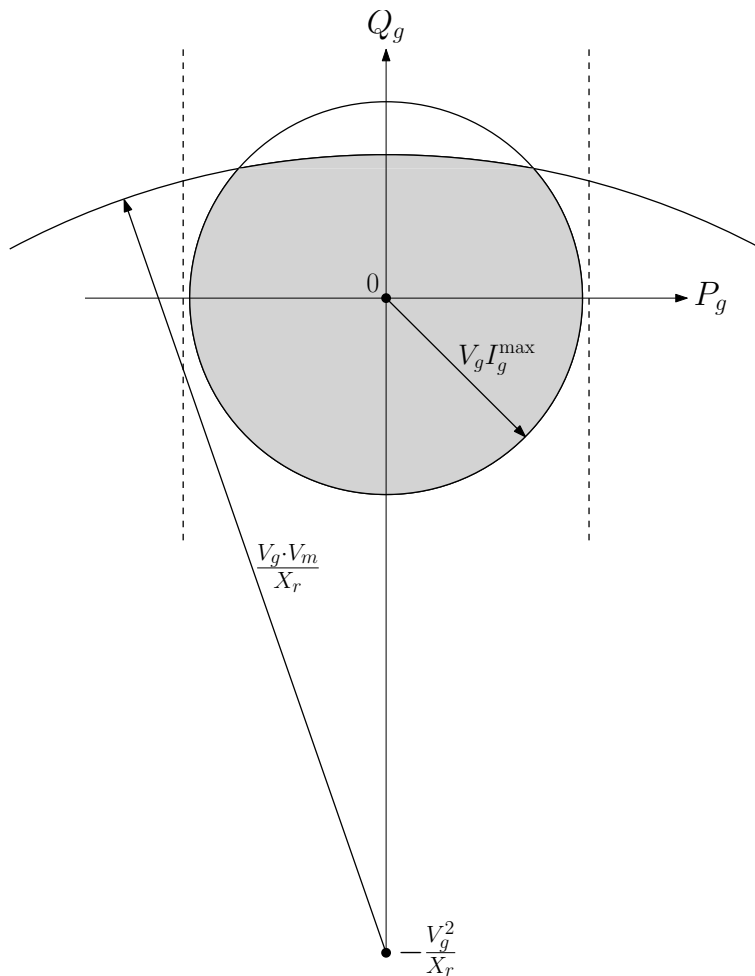


Figure 2.11: PQ diagram of a VSC. The grey area corresponds to the operation area.

2.3.3 Advantages of VSC-HVDC over LCC-HVDC

The VSC-HVDC technology has several advantages over LCC-HVDC, the main difference being the higher controllability of the former. Here is a detailed list of potential advantages [14]:

- Simpler circuitry;
- Considerably smaller footprint (i.e. occupying less space) than an equivalent LCC-HVDC station;
- No need of reactive power support via shunt banks or series capacitors, since the PWM allows the VSC to control both active and reactive power independently. The reactive power can even be used for voltage control for weak or islanded AC systems;
- Need of only harmonic filters, which can be non switchable.
- A VSC transmission has no minimum DC current limits.
- Easier power reversal: in an LCC, the current cannot be inverted through the thyristors, thus an active power transfer reversal supposes to shut-down the whole system and start it up again but with opposite voltage polarity;
- The voltage polarity on the DC side is always the same. DC cables are always exposed to the same voltage polarity, which makes the VSC technology more suitable for meshed MTDC systems.
- Possibility of *black start* for weak, islanded or passive AC systems;
- No risks of commutation failures, hence more suitable for offshore wind-farm connection: with LCC, commutation failures can happen when a valve cannot be extinguished (i.e. the flowing current is not returning to zero); e.g. case of an AC grid weakened by a short circuit.
- Possibility of operating the VSC for a very small short-circuit ratio of the connected AC grid. The least SCR which has been practically experienced by the end of year 2004 is 1.3 [31].

However, similarly to the LCC, the standard two-level VSC offers crude basic AC waveforms that often need to be filtered. More importantly, a VSC station also suffers from increased losses by comparison to its corresponding LCC station (primarily due to higher switching frequency, and secondly because of the increased number of semiconductor switches in a VSC than an LCC valve of the same rating), hence the lack of high rated power VSC-based HVDC transmissions. Additionally, DC line faults require opening of the VSC AC circuit breakers at both ends of a scheme in order to clear the DC fault, unless appropriate DC breakers are provided in the scheme.

2.4 MMC-HVDC Technology

Over the last 15 years, VSC-based HVDC has become a mature technology for HVDC transmission schemes [47]. The Modular Multilevel Converter (MMC) represents the recent development among the diverse available topologies of VSC and is allegedly the most promising solution today [69]. In fact, the MMC topology offers significant benefits compared to the traditional two-level VSC, such as lower losses, distributed storage of capacitive energy, improved scalability to higher voltage ratings, a modular design, low total harmonic distortion and, hence, the potential lack of passive filters on the AC-side of the converter [90].

2.4.1 Components of MMC-based HVDC transmissions

An MMC-based HVDC system consists of converters with thousands of cascaded bidirectional chopper-cells and their respective floating DC capacitor [58], transformers, phase reactors and transmission lines. In opposition to LCC-HVDC or even 2-level VSC-HVDC, there are neither AC nor DC filters.

The thousands of IGBTs are distributed within three legs. Each leg consists of an upper and a lower arm, and each arm consists of an inductor L_{arm} , which limits arm-current harmonics and fault currents, and N SMs. Finally, each SM consists of a half-bridge unit that includes two IGBTs with anti-parallel diodes (switches S_1 and S_2) and a floating DC capacitor C (see Figure 2.12).

The switching of these IGBTs allows a selective connection and disconnection of the floating capacitors to the AC grid. Thus, the N SMs per arm can produce a line-to-neutral voltage waveform of $N+1$ levels. Figure 2.13 shows the voltage waveform of a 9-level MMC (i.e. 8 SMs per arm) where the red curve corresponds to the reference voltage and the blue curve corresponds to the actual output AC voltage of the MMC. A higher number of the voltage waveform levels means less harmonics on the AC side. The number of levels of an MMC depends on the manufacturer, and they generally attain several hundreds.

Each SM is a half-bridge⁹ unit that includes two IGBTs with anti-parallel diodes (switches S_1 and S_2 in Figure 2.12) and a floating DC capacitor C . The IGBTs with anti-parallel diodes are fully controllable switches. Hence, each SM can have three different states:

⁹SMs in the form of a full-bridge are being more and more considered because the converter can then act as a DC breaker in case of a DC fault. However, this topology also results in additional switching losses.

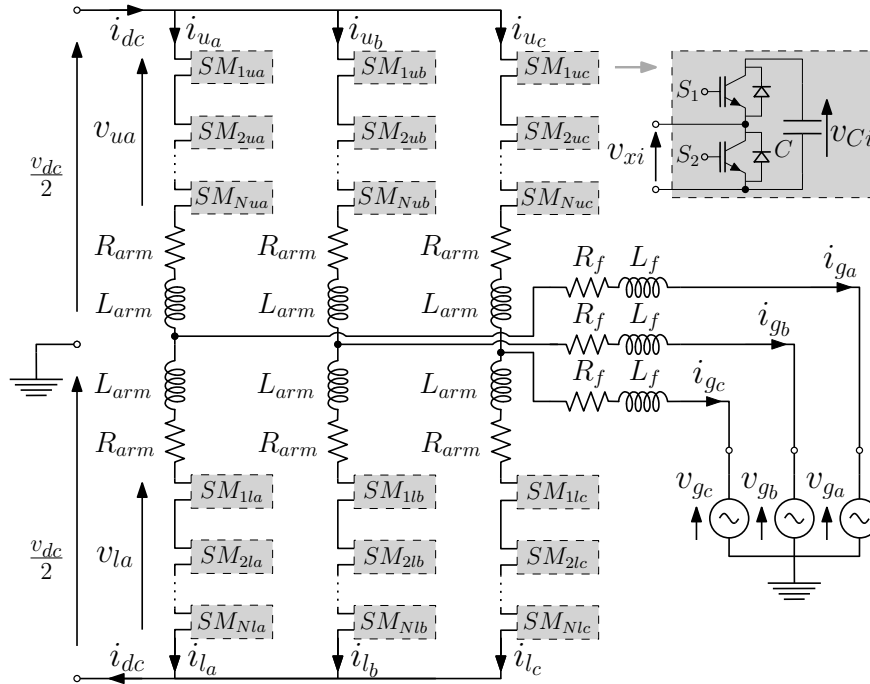


Figure 2.12: MMC Topology.

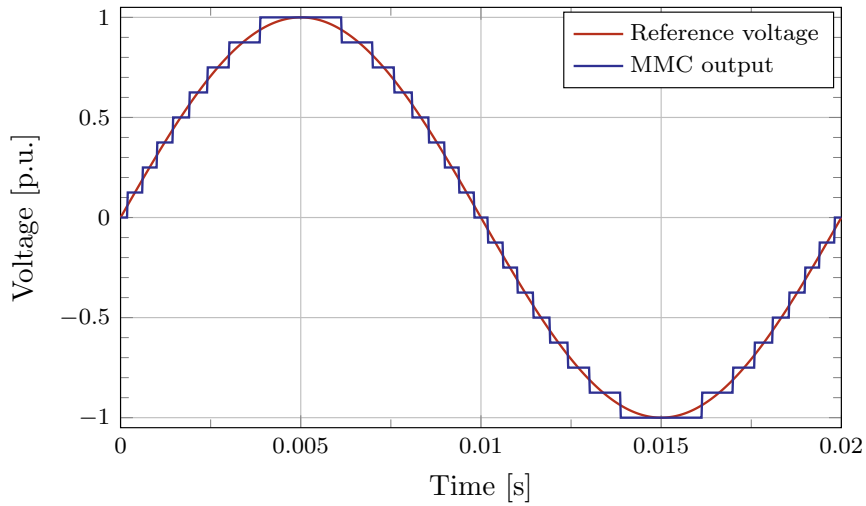


Figure 2.13: Output voltage of a 9-level MMC (i.e. 8 SMs per arm).

- If S_1 is turned on and S_2 is turned off, the SM voltage v_{x_i} is equal to the floating capacitor voltage. This SM state is called *ON*.
- If S_1 is turned off and S_2 is turned on, the SM voltage is short circuited: $v_{SM_i} = 0$. This SM state is called *OFF*.
- If both S_1 and S_2 are turned off, the SM voltage depends on the arm current: the floating capacitor can be charged through the anti-parallel diode of S_1 , but cannot be discharged. This SM state is called *Blocked*.

The SMs can have different topologies than the one shown in Figure 2.12, such as a full-bridge or a double-clamp SM [72]. However, since the half-bridge SM leads to the lowest losses and lowest cost in general (but has no DC current limitation in case of short circuit) and that it is the most used configuration as of today, it will be the one used throughout this thesis.

Since the MMC voltage rating depends on the number of SMs and that the harmonic distortion is almost non-existent for a large number of SMs, an MMC based HVDC transmission system is arranged with a single converter connected pole to pole rather than two converters in series connected pole to ground, as in Figure 2.8.

The standard layout of an MMC station is portrayed in Figure 2.14. The components of the station include [91, p15-16]:

- An AC breaker that connects or disconnects the MMC station from the AC network;
- A transformer with a Y- Δ configuration to guarantee a galvanic isolation between the AC network and the converter station. The transformer acts as a phase reactor;
- A breaker with a parallel resistor (a few k Ω) between the secondary of the transformer and the converter: the resistor limits peak currents during the start-up of the station when the distributed capacitors of the MMC are being charged. The resistor is then short-circuited by the breaker in normal operation conditions;
- A star point reactor (an inductor of a few kH in series with a resistor of a few k Ω) to stabilize the ground reference level on the secondary side of the transformer;
- An MMC whose topology can vary from one manufacturer to another.

In opposition to the LCC or the standard 2-level VSC, the MMC station is filter-less (both on the AC and the DC side).

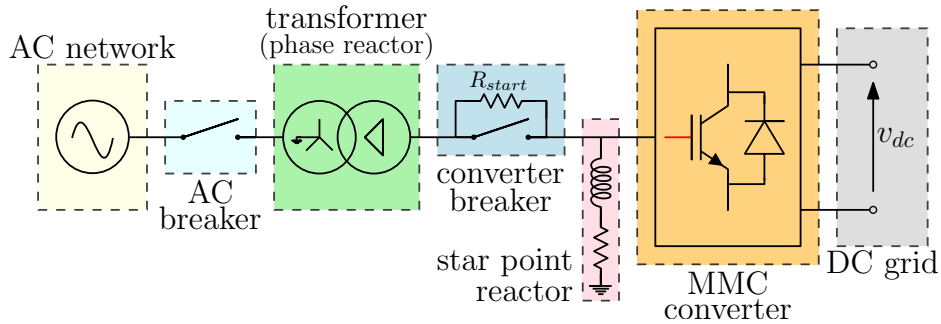


Figure 2.14: Standard configuration of an MMC station.

2.4.2 Advantages of the MMC

The MMC enjoys the benefits of a standard 2-level VSC and offers various additional advantages. These include [90]:

- Distributed storage of capacitive energy;
- Easier and better scalability to higher voltages thanks to the modular design of the converter (simple scaling by a series connection of SMs);
- Higher ratings than standard 2-level VSCs and similar ratings to LCCs;
- Low total harmonic distortion (THD) translating into a filter-less configuration once an adequate number of voltage level is reached;
- Lower switching frequency and transient peak voltages on IGBTs, hence lower converter losses;
- Simple realization of redundancy;
- Grid connection via a standard transformer, and in certain cases, transformer-less.

One disadvantage of the MMC, however, is the higher number of semiconductors and gate units. Furthermore, the total value of the distributed capacitors is distinctly higher as compared to that of a standard 2-level VSC [46].

2.5 Chapter Conclusion

This chapter reviewed the two main technologies used in modern HVDC and Table 2.1 lists their respective advantages and disadvantages.

Converter	LCC	2-level VSC	MMC
Filter requirements	Important AC and DC filters are required	Small AC filters are required	No filters are required
Overvoltages in the AC system	Sudden stop can cause fundamental frequency overvoltages	Smaller overvoltages (if any)	No overvoltages
AC fault impact	Can cause commutation failures	The converter can ride through the AC fault	The converter can ride through the AC fault
DC fault	Thyristors allow the LCC to ride through the DC fault by controlling the DC fault current	If point-to-point, the system needs to be shut down. If MTDC, the system needs DC breakers	The MMC sub-modules can block the fault current only if the SMs are full-bridges or double-clamp SMs
Active power reversal	The system must be shut down and restarted with opposite voltage polarities (requires mechanical switching operation)	Can be achieved within tens of milliseconds	Can be achieved within tens of milliseconds
Reactive power control	Not possible. The LCC must be supplied with reactive power by shunt capacitor banks and by the AC network (50% to 60% of the active power)	The converter can generate or absorb any amount of reactive power within apparent power limitation	The converter can generate or absorb any amount of reactive power within apparent power limitation
Black start capability	Not possible	Possible	Possible
AC short circuit ratio (SCR)	A strong AC grid (SCR of more than 2) is mandatory because the LCC switches through an external voltage source	No SCR required	No SCR required
Maximum power rating today	Up to 5000 MW per monopole	Up to 700 MW per monopole	Up to 1000 MW per monopole (still increasing)
Station cost (1000 MW)	90 M€±20%	90 M€±20%	125 M€±20% (will considerably decrease during the coming years)
Losses (1000 MW)	0.75%	1.75%	0.9%
Station Footprint (1000 MW each pole)	100,000m ² (100%)	25,000-40,000m ² (25-40%)	30,000-50,000m ² (30-50%)

Table 2.1: Comparison between an LCC, a 2-level VSC and an MMC [31, 32, 97, 84].

The first HVDC converter technology is the thyristor-based Line Commutated, current source Converter (LCC) also referred to as LCC-HVDC or HVDC classic. Since the advent of power electronics in the late 1960's, this technology has been widely used worldwide to transmit large amount of bulk power over long distances or via underground transmissions thanks to its numerous benefits over HVAC.

The second HVDC converter technology is the IGBT-based self commutated Voltage Source Converter (VSC) that was developed in the last two decades. It offers several advantages over LCC-HVDC, the main difference being the higher controllability of the power flows. However, this technology was not suitable for high rated power transmission systems until recently. Indeed, it is only with the recent development of a new topology of VSC, the Modular Multilevel Converter (MMC), that this technology is starting to be adopted for high rated power HVDC transmissions, but still cannot compete with LCC-HVDC for very high rated power HVDC projects.

Because it is now a mature HVDC technology, solely the VSC technology will be considered in the rest of this thesis – either a 2-level VSC or an MMC depending on the objectives of the upcoming studies. The control of those converters, which is crucial to ensure the proper functioning of an HVDC system, will be detailed in the next chapter.

Chapter 3

Modelling and Control of VSC-based Converter Stations

The universal utilization of water power and its long-distance transmission will supply every household with cheap power and will dispense with the necessity of burning fuel.

– Nikola Tesla, as told to George Sylvester Viereck,
in *Liberty Magazine* (9 February 1935) [108].

3.1 Chapter Introduction

The previous chapter presented the two main High-Voltage Direct Current (HVDC) converter technologies, namely Line Commutated, current source Converter (LCC)-HVDC and Voltage Source Converter (VSC)-HVDC. This chapter will focus on VSC-based converter stations by modelling both a standard 2-level VSC station and a Modular Multilevel Converter (MMC) station.

The station models presented in this chapter consist of both the physical and control systems of the considered converters. The equations governing the physical system are analysed and consequently wielded to allow the derivation of a non-linear model, which is presented in the form of both an equivalent electrical circuit that reproduces the system behaviour and a block diagram that describes the modelling of the system plant under control, which facilitates the control design. The control strategy of the converters is designed to decouple the d and q components of the grid currents and ensure the proper tracking of the reference signals. These can either be a DC voltage reference or an active power reference on one hand, and a reactive power reference or an AC voltage reference on the other hand.

In the case of the MMC, some simplifying assumptions are made to derive an energy-based Average Value Model (AVM) that takes into account the internal dynamics (i.e. the total energy stored in the converter) which do not exist in the 2-level VSC, as well as the AC and DC side dynamics. This additional internal dynamics implies that the control system of the converter must possess additional control loops that govern the DC current and the total amount of stored energy in the SM capacitors of the MMC. The total stored energy in the MMC is then decoupled from the DC bus, but can also be potentially shared depending on the reference signal of the energy control loop.

3.2 Modelling and Control of a VSC-HVDC Station

A large number of publications deal with the modelling and control of standard 2-level VSCs. On one hand, the cascaded control of the converters is usually preferred and the inner control (the current control loop) is generally the same. On the other hand, the outer control can greatly differ from one publication to another, depending on the situation of the studied systems. While some of them correspond to very specific circumstances, such as using the VSC to support the main grid frequency [59] or to support weak AC systems [118], many are correlated with the control strategy of MTDC systems [38, 20, 54, 25, 43] that will be detailed in the next chapter.

The VSC model derived in this section is an AVM and its control is similar to the one detailed in [117]: it is realised in the $dq0$ reference frame, implying an inner current controller that decouples the grid currents between them, and outer controllers that ensure the proper tracking of the references. The obtained model is standardised and can be used for most simulations involving a 2-level VSC.

3.2.1 Modelling of the VSC

For the sake of clarity, the reference signal of the signal x will be noted x^* for each signal in the rest of this manuscript.

In order to facilitate the acquisition of an AVM of the Voltage Source Converter (VSC), the following assumptions are made:

- The AC side of the VSC is assumed to be an ideal, fully controllable, voltage source (i.e. $v_m = v_m^*$) connected to the Point of Common Coupling (PCC) via a phase reactor L_r , as shown in Figure 3.1.
- The DC side of the VSC is assumed to be an ideal current source (i.e. $i_m = i_m^*$) connected to the DC bus in parallel with a DC capacitor C_{dc} , as shown in Figure 3.1.
- The losses in the power electronics of the VSC are neglected.
- The voltage between the neutral-point (N) of the AC side and the mid-point (O) of the DC capacitors is assumed to be equal to 0 (i.e. $v_{NO} = 0$).

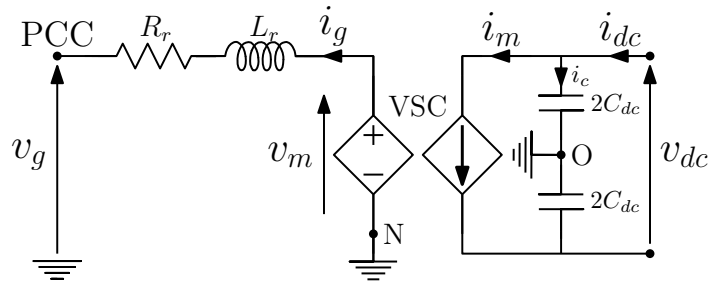


Figure 3.1: Single phase diagram of the VSC without filter.

Applying Kirchhoff's law to the AC side of the VSC, the following equation is derived for each phase j :

$$v_{m,j}(t) - v_{g,j}(t) = L_r \frac{di_{g,j}(t)}{dt} + R_r i_{g,j}(t) \quad (3.1)$$

Using the power invariant Park transformation, the three-phase equations are transformed to a rotating $dq0$ -reference frame, as described in Appendix B, where the phase a of the grid voltage v_g is aligned with the d -axis of the $dq0$ rotating frame¹, the following equations are derived (where the time dependence of each variable is voluntarily omitted for the sake of clarity, and ω_g is the AC grid angular frequency):

$$v_{m,d} - v_{g,d} = L_r \frac{di_{g,d}}{dt} + R_r i_{g,d} - \omega_g L_r i_{g,q} \quad (3.2)$$

$$v_{m,q} - v_{g,q} = L_r \frac{di_{g,q}}{dt} + R_r i_{g,q} + \omega_g L_r i_{g,d} \quad (3.3)$$

Since the DC side of the VSC is considered a current source i_m connected to the DC bus in parallel with a DC capacitor C_{dc} , the DC side of the VSC is governed by (3.4).

$$i_c = i_{dc} - i_m = C_{dc} \frac{dv_{dc}}{dt} \quad (3.4)$$

Since the losses in the power electronics of the VSC are neglected, the instantaneous active power on the AC side of the VSC strictly matches the instantaneous active power on the DC side of the VSC, as described by (3.5).

$$p_{ac} = v_{m,d} i_{g,d} + v_{m,q} i_{g,q} = v_{dc} i_m = p_{dc} \quad (3.5)$$

Thus, a new expression of i_m can be derived:

$$i_m = m_d i_{g,d} + m_q i_{g,q} \quad (3.6)$$

where the control signals m_d and m_q are defined as:

$$m_d = \frac{v_{m,d}}{v_{dc}}, \quad m_q = \frac{v_{m,q}}{v_{dc}} \quad (3.7)$$

Following the above analysis, an equivalent circuit for the VSC model based on (3.2), (3.3), (3.4) and (3.6) is derived and shown in Figure 3.2.

Block diagram modelling of the VSC

The AC side dynamics of the converter (i.e. Equations (3.2) and (3.3)) can be modelled with Laplace transformation by the block diagram of Figure 3.3.

¹The $dq0$ transform reduces three-phase AC quantities (e.g. $v_{g,a}$, $v_{g,b}$ and $v_{g,c}$) into two DC quantities (e.g. $v_{g,d}$, $v_{g,q}$). For balanced systems, the zero-sequence component is zero. The DC quantities facilitate control. In particular, it enables the use of Proportional Integer (PI) controllers.

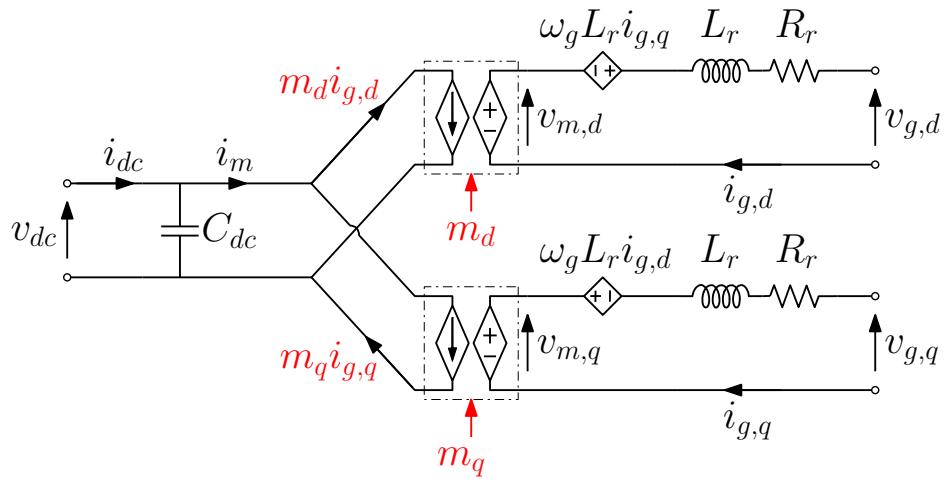


Figure 3.2: Circuit of the VSC model in the $dq0$ reference frame.

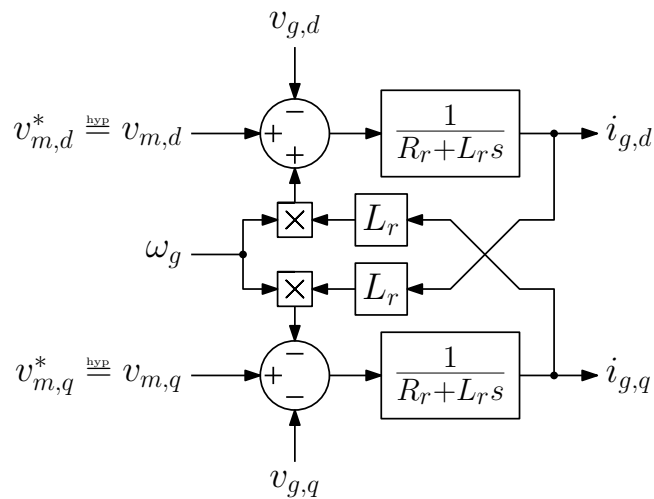


Figure 3.3: Modelling of the AC side of the VSC without its control.

The DC side dynamics of the converter (i.e. Equation (3.4)) can be modelled with Laplace transformation by the block diagram of Figure 3.4.

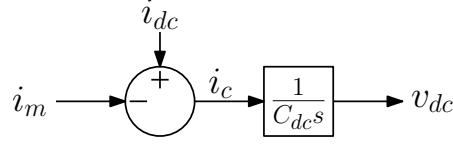


Figure 3.4: Modelling of the DC side of the VSC without its control.

The complete block diagram model of the VSC finally consists of the combination of Figures 3.3 and 3.4 by using the relation between the AC and DC instantaneous active power (i.e. Equation (3.5)) and is shown in Figure 3.5.

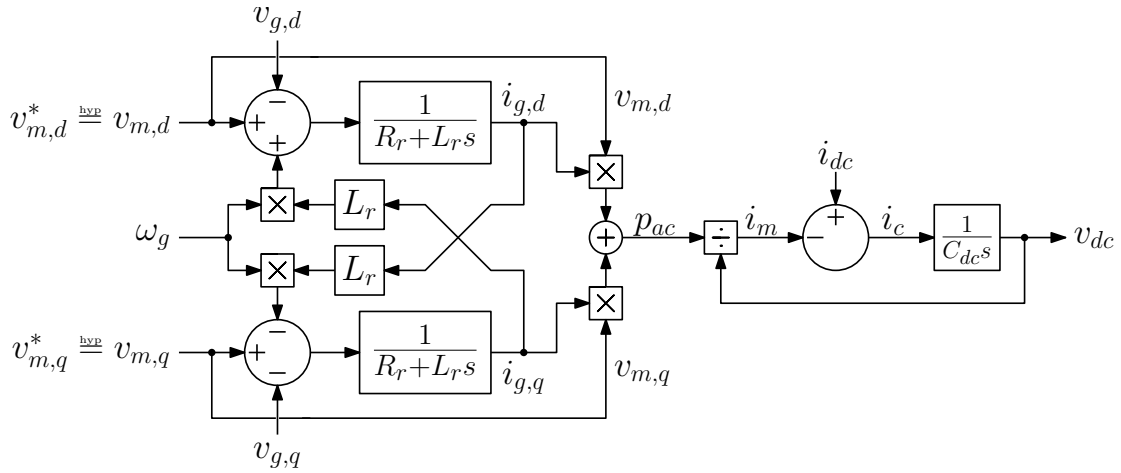


Figure 3.5: Modelling of both the AC and DC side of the VSC without its control.

3.2.2 Control of the VSC

The active and reactive power delivered or absorbed by the VSC to the AC network can be controlled by acting on both the amplitude and the phase angle of the modulated voltage v_m . This directly impacts the grid current i_g in accordance with the AC-side physical system equations described by (3.2) and (3.3), where the coupling between the dynamics of $i_{g,d}$ and $i_{g,q}$ is represented by the presence of the $\omega_g L_r$ terms.

The control strategy considered here is the commonly used vector control that consists of cascaded control loops in a $dq0$ rotating frame which is synchronised to the AC grid by means of a PLL. The first control loop, called the inner control loop, is the $dq0$ transform that allows decoupling the grid currents. The other control loops, called the outer control loops, can be used to control either the DC voltage or the

active power by controlling the d-axis of the $dq0$ reference frame, and the AC voltage or the reactive power by controlling the q-axis of the $dq0$ reference frame. The overall control strategy of a VSC is pictured in Figure 3.6 and the above-mentioned control loops are detailed throughout this section in order to be incorporated in the model of the VSC converter.

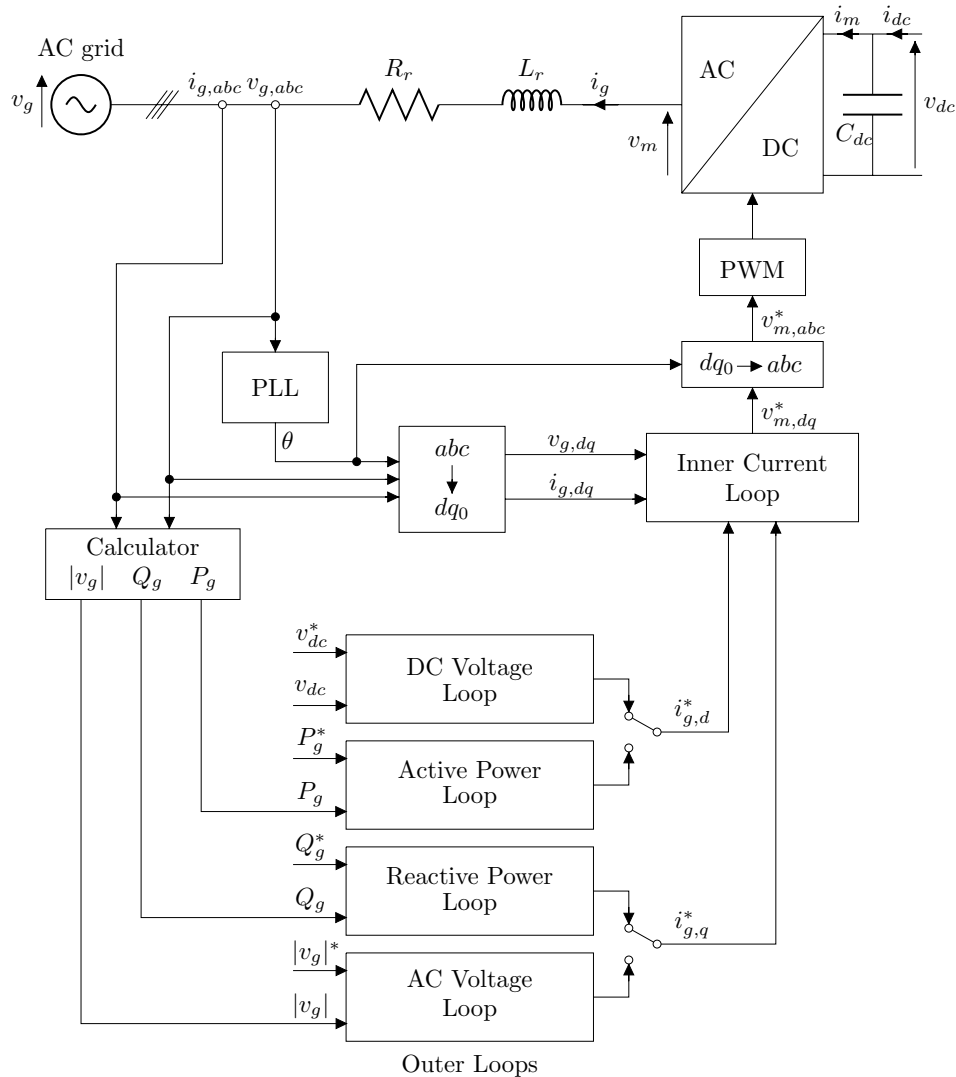


Figure 3.6: Control strategy of a VSC.

The Phase-Locked Loop (PLL)

The control of the Voltage Source Converter (VSC) is achieved in the $dq0$ reference frame which is synchronised to the grid voltage by means of a Phase-Locked Loop (PLL). The synchronization function of the PLL plays a key role in ensuring a proper energy

transfer between AC and DC grids. In fact, the control of the converter will generate voltage reference signals that need to be synchronised with the network voltage in order for the VSC to control the grid current in the phase reactor and exchange active and reactive power accordingly.

The modelling of the PLL, which is pictured in Figure 3.7, is based on the simplified PLL model of [64]: a PI controller is used to obtain the value of θ_{pll} which drives the generated voltage $v_{gq,pll}$ to the desired value $v_{gq}^* = 0$. This method not only results in the utility frequency ω_{pll} but also allows one to lock at the grid angle θ_g . The PLL can thus be considered as a non-linear control system with the voltage magnitude V_g multiplied in the feedback path, the forward path being PI controller and a simple integrator.

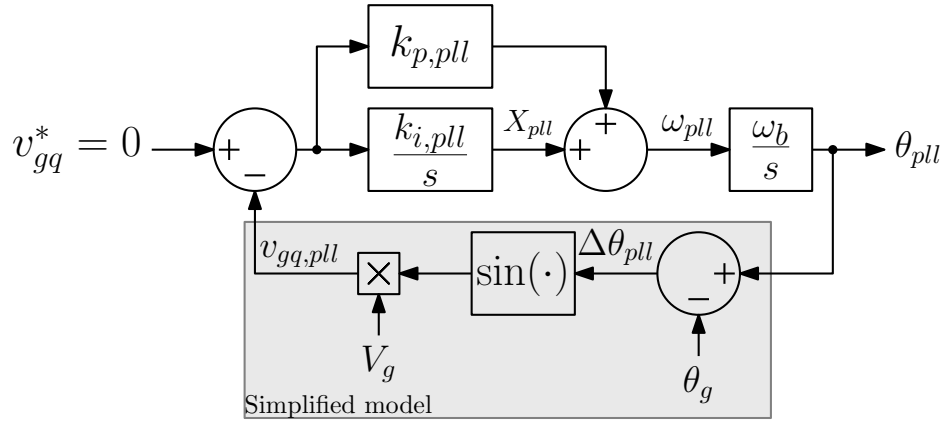


Figure 3.7: Modelling of the Phase-Locked Loop (PLL).

VSC inner control loop

A *current control loop* in the $dq0$ -frame, also called *inner control loop*, can be designed to introduce a decoupling of the currents $i_{g,d}$ and $i_{g,q}$, thus allowing the independent control of the active and reactive power absorbed or delivered by the VSC. In fact, this can be achieved by arranging the current controller so that the reference voltages $v_{m,d}^*$ and $v_{m,q}^*$ are created according to:

$$v_{m,d}^* = C(s) (i_{g,d}^* - i_{g,d}) + v_{g,d} - \omega_{PLL} L_r i_{g,q} \quad (3.8)$$

$$v_{m,q}^* = C(s) (i_{g,q}^* - i_{g,q}) + v_{g,q} + \omega_{PLL} L_r i_{g,d} \quad (3.9)$$

where $C(s)$ is the transfer function of the controller and ω_{PLL} is the angular frequency measured by the PLL.

In normal operation conditions of the VSC, it can be assumed that:

$$\omega_{PLL} = \omega_g \quad (3.10)$$

Moreover, it is assumed that the dynamics of the PWM can be neglected when considering the current loop. Hence:

$$v_{m,d} = v_{m,d}^* \quad (3.11)$$

Then, in sinusoidal steady-state and by using the Laplace transformation, injecting (3.8), (3.10) and (3.11) into (3.2) yields:

$$C(s) (i_{g,d}^* - i_{g,d}) + v_{g,d} - \omega_g L_r i_{g,q} - v_{g,d} = sL_r i_{g,d} + R_r i_{g,d} - \omega_g L_r i_{g,q} \quad (3.12)$$

i.e.

$$i_{g,d} = \frac{C(s)}{C(s) + sL_r + R_r} i_{g,d}^* \quad (3.13)$$

and similarly, injecting (3.9), (3.10) and (3.11) into (3.3) yields:

$$i_{g,q} = \frac{C(s)}{C(s) + sL_r + R_r} i_{g,q}^* \quad (3.14)$$

Equations (3.13) and (3.14) illustrate the fact that a clever generation of the reference modulated voltage $v_{m,dq}^*$ introduces a decoupling of the grid currents $i_{g,d}$ and $i_{g,q}$. This leads to a direct control of these currents by their respective control references $i_{g,d}^*$ and $i_{g,q}^*$, hence allowing the independent control of the active and reactive power absorbed or delivered by the VSC from or to the AC network.

The transfer function of the controller $C(s)$ used in this thesis is simply that of a Proportional Integer (PI) controller with the proportional gain $k_{p,i}$ and the integer gain $k_{i,i}$ tuned to achieve a response time of 10 ms, as described in Appendix C.

With regards to (3.13) and (3.14), the inner control loop can be modelled by the block diagram of Figure 3.8.

VSC outer control loops

Since the d -axis of the $dq0$ reference frame is aligned with the phase a of the grid voltage v_g , then $v_{g,q} = 0$ and the active power expression at the PCC is:

$$P_g = v_{g,d} i_{g,d} \quad (3.15)$$

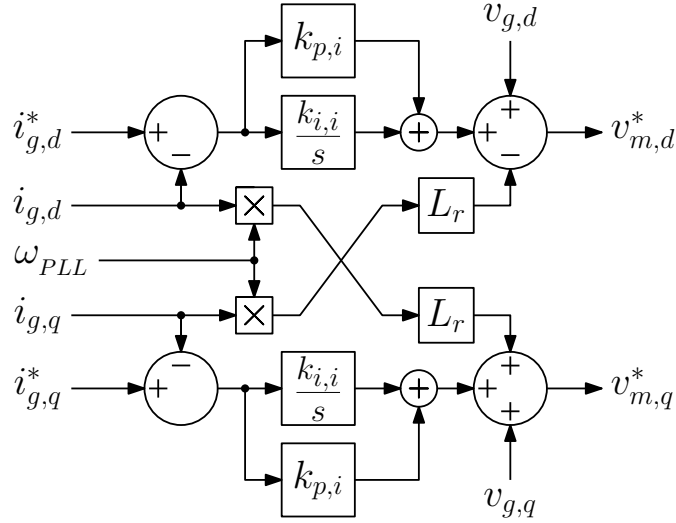


Figure 3.8: Modelling of the inner control loop of the VSC.

Now that the d and q components of the grid current, $i_{g,d}$ and $i_{g,q}$, are decoupled by the inner control loop, the active power absorbed or delivered by the VSC can be controlled by solely controlling the d -axis component of the current $i_{g,d}$.

The d -axis current reference of the inner control loop is then generated according to (3.16) and is described in Figure 3.9a. However, it can be judicious to control the active power via a closed loop using a PI controller² to reject potential disturbances and avoid dividing by $v_{g,d}$, as depicted in Figure 3.9c. A feed-forward action can even be used in parallel with the PI controller to lighten the power controller efforts by directly feeding the reference into the current controller [84, p. 31], as depicted in Figure 3.9d.

$$i_{g,d}^* = \frac{P_g^*}{v_{g,d}} \quad (3.16)$$

Similarly, the reactive power expression at the PCC is given by (3.17), which implies the reactive power absorbed or delivered by the VSC can be controlled by solely controlling the q -axis component of the current $i_{g,q}$, which leads to similar controllers as for the active power control (as shown in Figure 3.9b for the open-loop control).

$$Q_g = v_{g,d} i_{g,q} \quad (3.17)$$

²If a PI controller is used for the outer loop, it has to be considerably slower than the one used in the inner control loop. The time response of this PI can be set at 100 ms (ten times larger than the PI of the current loop).

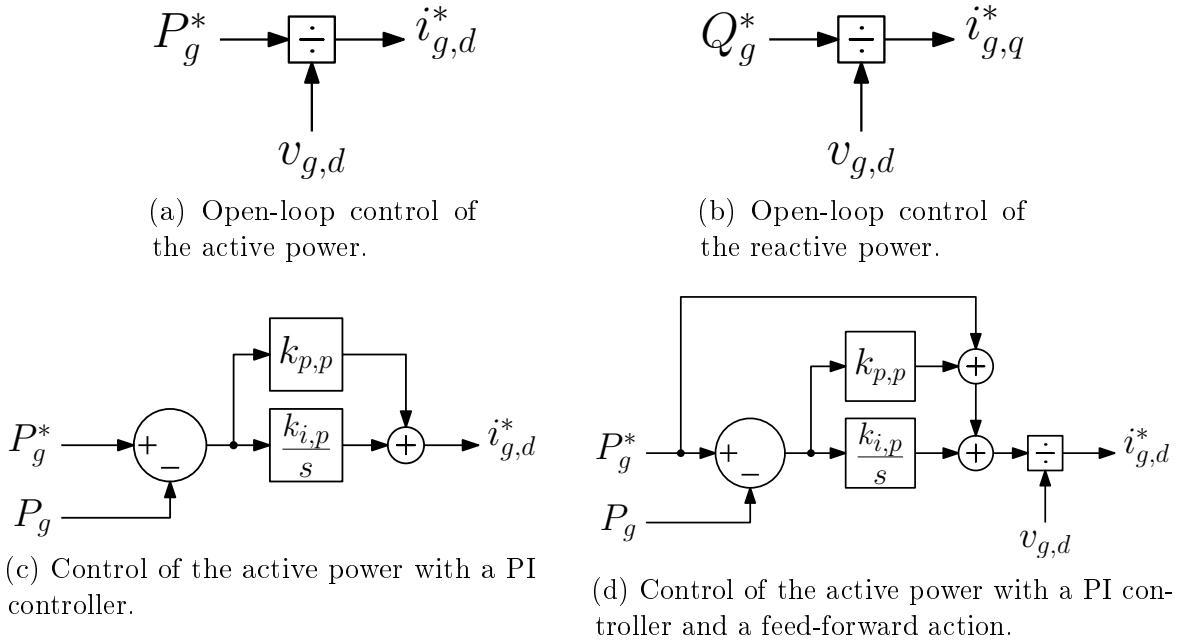


Figure 3.9: Open-loop and closed-loop power control variants.

As shown in Figure 3.6, the d -axis current reference of the VSC can be generated by a DC voltage controller instead of an active power controller, and the q -axis current reference of the VSC can be generated by an AC voltage controller instead of a reactive power controller.

By regulating the d -axis current $i_{g,d}$, and thus the active power transiting through the VSC, the DC voltage controller –depicted in Figure 3.10– allows the VSC to control the DC voltage level on the DC bus by increasing or reducing the amount of power transiting through the DC grid.

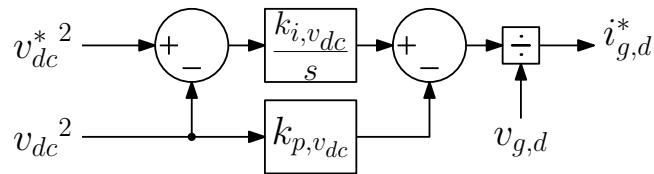


Figure 3.10: DC voltage control with an IP controller to minimise any possible overshoot when applying a reference step [84, p. 43].

By regulating the q -axis current $i_{g,q}$, and thus the reactive power transiting through the phase reactor, the AC voltage controller –depicted in Figure 3.11– allows the VSC to control the voltage drop across the phase reactor, and hence, to control the PCC voltage. This is particularly useful in the case of a VSC connected to a weak or islanded AC grid. The AC voltage controller is depicted in Figure.

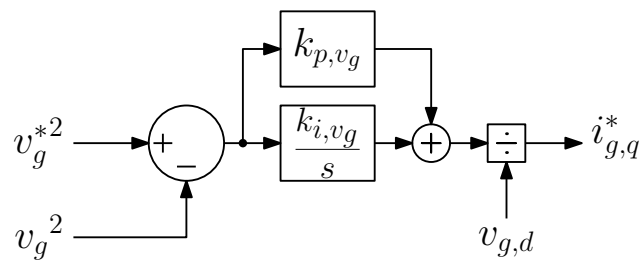


Figure 3.11: PCC voltage control with a PI controller.

The complete VSC model comprising of the physical system and its control is then described by Figure 3.12, where the external signals are highlighted in blue in the case of reference signals and red in the case of measured signals, and the internal (or generated) signals are highlighted in green.

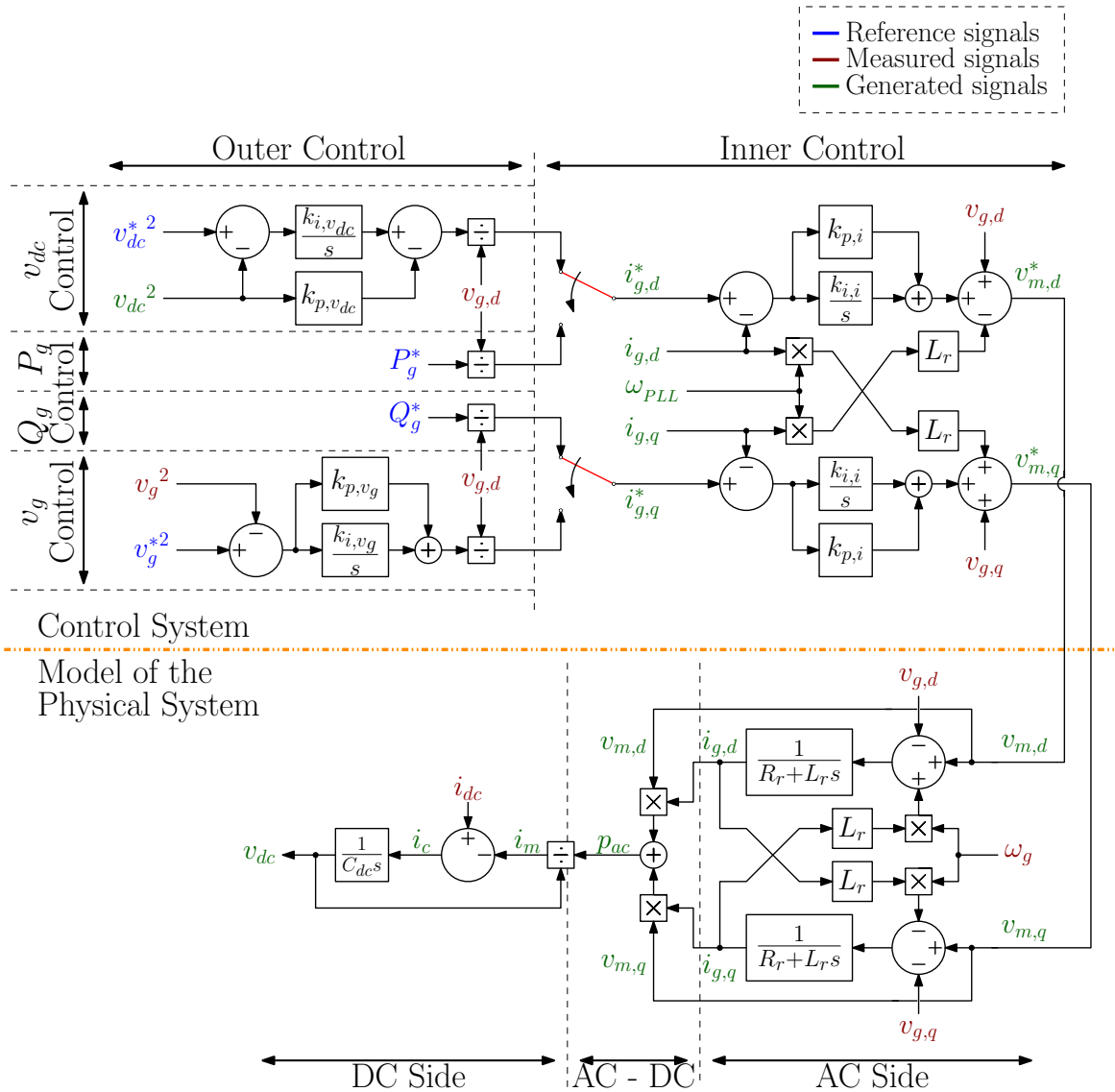


Figure 3.12: Block-diagram of the complete VSC station, comprising of the physical system and its control (the PLL is not represented).

3.3 Modelling and Control of an MMC-HVDC Station

There exist several MMC models in the literature. One of the first MMC model was presented in [104] but was too simplified to accurately represent the singularities of an MMC. Numerous recent publications have adopted a similar model for the MMC as for a standard 2 or 3-level VSC with little modifications. However, these models are either based on strong assumptions regarding the way the MMC control is implemented [93, 71] or introduce supplementary functions and resort to parameter identification techniques to reproduce its dynamic behaviour [111]. Finally, other models were presented but are only valid in steady state [63, 74].

A model able to accurately reproduce both the transient and steady-state behaviour of the MMC without reducing it to a mere 2-level VSC was first derived in [92] and will be the starting point of this section. Then [24] and [50] improved it by effectively controlling the total stored energy in the SM capacitors of the converter.

3.3.1 Modelling of the MMC

The modelling of the Modular Multilevel Converter (MMC) that is presented in this section is largely derived from the MMC models type 1, 2 and 3 of [92] and the simplified MMC model is the one presented in [50].

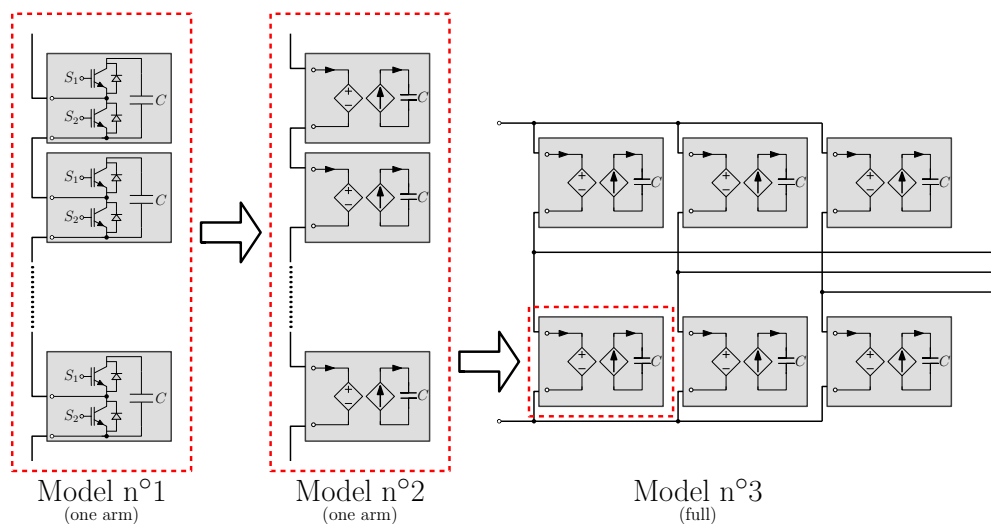


Figure 3.13: MMC models presented in [92], successively decreasing in complexity.

Reference MMC models [92]

Reference [91] presented 4 different models successively decreasing in complexity. The first 3 models are pictured in Figure 3.13 and are reviewed below. The 4th model is discarded since it oversimplifies the MMC to the point where its model becomes no different than the one of a mere 2-level VSC.

The most accurate MMC model consists of thousands of non-linear models of IGBTs and their anti-parallel diodes. Such a model, numbered *Model type 1* in [91, p.26], possesses the main advantage of reproducing the behaviour of the power electronic components as well as their losses, and allowing the use of different topologies of SMs. However, the simulation of a 401-levels MMC (i.e. 4800 ideal switches and 4800 non-linear diodes) demands a high computation effort that can only be accomplished by a powerful EMT software combined with a powerful hardware capability, and cannot be characterised by a limited set of equations. Moreover, a Balancing Capacitor Algorithm (BCA)³ needs to be implemented with this model. In order to obtain an AVM of the converter, this model is simplified to give way to the *Model type 2*.

The *Model type 2*, initially described in [53] and [91, p.27], replaces the switches of each SMs with ON/OFF resistors [53]. This allows the derivation of a Norton equivalent for each arm of the MMC, at each simulation step time, reducing considerably the number of electrical nodes, and hence, the computation effort. A BCA needs to be implemented with this model. Like the *Model type 1*, the system cannot be characterised by a set of equations: each arm model is coded with regard to an algorithm that calculates, for each simulation step time, the voltage and current of each SM capacitor. Yet again, this model is further simplified in order to obtain an AVM of the MMC.

The *Model type 3* [91, p.32], also called Arm Average Model (AAM), is an Average Value Model (AVM) that is obtained using the switching function concept of a half-bridge converter based on the assumption that all SM capacitor voltages are balanced [36]. Since there is no actual SM any longer, the SM capacitor voltages are assumed to be balanced by a BCA that needs not to be implemented in the control of this model, thus, drastically reducing the computational effort. The internal dynamics and the total energy stored in each arm of the MMC is retained. However, the information about the switching states of the SMs is lost. This model is recalled below and will be the starting point of the derivation of the simplified MMC model [50].

The topology of the AAM is detailed in Figure 3.14. The MMC overall topology is preserved in that the model still comprises of one leg for each phase, each consisting

³The Balancing Capacitor Algorithm (BCA) balances the capacitor voltages at each arm to maintain them within an acceptable range [112, 93].

of an upper and a lower arm. Since all the SM capacitor voltages are assumed to be balanced by an ideal BCA, all the SM capacitors can be replaced by a single equivalent capacitor C_{tot} which is identical for each arm. Therefore, each arm includes an arm inductance L_{arm} , an arm resistance R_{arm} and an equivalent capacitor C_{tot} in parallel with a chopper.

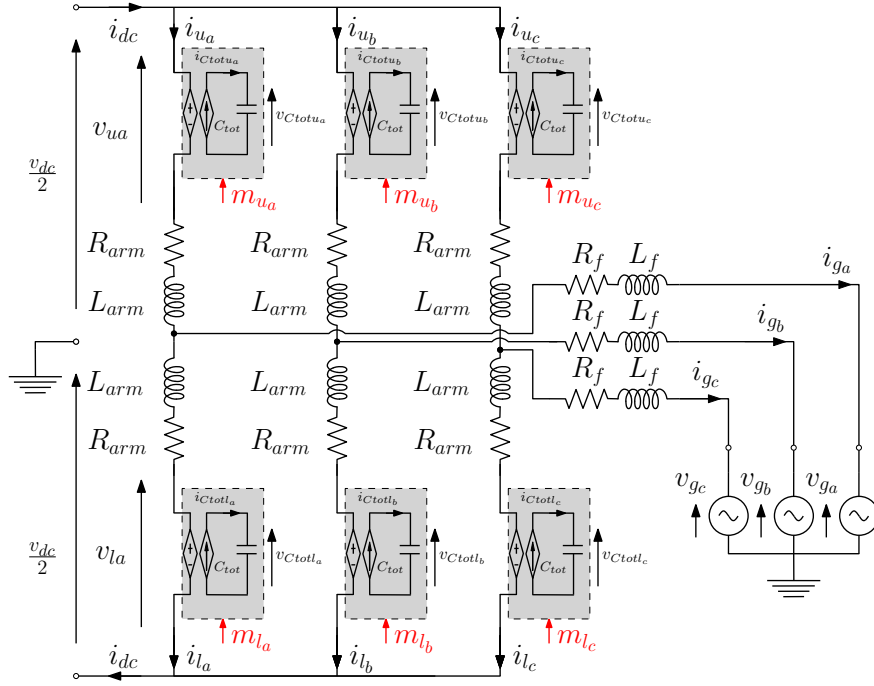


Figure 3.14: Detailed representation of the AAM of an MMC.

The voltage v_{u_j} (v_{l_j}) and the current i_{u_j} (i_{l_j}) of the upper (lower) arm of each arm j ($j = a, b, c$) is described by the following equations:

$$v_{u_j} = m_{u_j} v_{Ctotu_j}, \quad v_{l_j} = m_{l_j} v_{Ctotl_j} \quad (3.18)$$

$$i_{Ctotu_j} = m_{u_j} i_{u_j}, \quad i_{Ctotl_j} = m_{l_j} i_{l_j} \quad (3.19)$$

where v_{Ctotu_j} (v_{Ctotl_j}) is the voltage of the equivalent capacitor across the upper (lower) arm, m_{u_j} (m_{l_j}) is the corresponding instantaneous duty cycle and i_{Ctotu_j} (i_{Ctotl_j}) is the current through the upper (lower) arm capacitor. The voltage and current of the equivalent capacitor are related through the capacitor equation:

$$i_{Ctotu_j} = C_{tot} \frac{dv_{Ctotu_j}}{dt}, \quad i_{Ctotl_j} = C_{tot} \frac{dv_{Ctotl_j}}{dt} \quad (3.20)$$

At this stage, the MMC is characterised by 11 independent state variables: the six equivalent capacitor voltages and five currents (three arm currents and two phase currents).

Applying Kirchhoff's law, the following equations are derived for phase j :

$$\frac{v_{dc}}{2} - v_{u_j} - L_{arm} \frac{di_{u_j}}{dt} - R_{arm} i_{u_j} - L_f \frac{di_{g_j}}{dt} - R_f i_{g_j} - v_{g_j} = 0 \quad (3.21)$$

$$\frac{-v_{dc}}{2} + v_{l_j} + L_{arm} \frac{di_{l_j}}{dt} + R_{arm} i_{l_j} - L_f \frac{di_{g_j}}{dt} - R_f i_{g_j} - v_{g_j} = 0 \quad (3.22)$$

On the one hand, summing (3.21) and (3.22) yields:

$$v_{m_j} - v_{g_j} = L_{eq}^{ac} \frac{di_{g_j}}{dt} + R_{eq}^{ac} i_{g_j} \quad (3.23)$$

where:

$$i_{g_j} = i_{u_j} - i_{l_j} \quad (3.24)$$

$$v_{m_j} = \frac{-v_{u_j} + v_{l_j}}{2} \quad (3.25)$$

$$R_{eq}^{ac} = \frac{R_{arm} + 2R_f}{2}, \quad L_{eq}^{ac} = \frac{L_{arm} + 2L_f}{2} \quad (3.26)$$

On the other hand, subtracting (3.22) from (3.21) yields:

$$v_{dc} - v_{diff_j} = 2L_{arm} \frac{di_{diff_j}}{dt} + 2R_{arm} i_{diff_j} \quad (3.27)$$

where the differential currents i_{diff_j} and voltages v_{diff_j} are defined as:

$$i_{diff_j} = \frac{i_{u_j} + i_{l_j}}{2} \quad (3.28)$$

$$v_{diff_j} = v_{u_j} + v_{l_j} \quad (3.29)$$

These equations enable the characterisation of the AC and DC dynamics of the MMC: (3.23) describes the AC side dynamics of the AAM while (3.27) describes the DC side dynamics of the AAM.

Derivation of the simplified MMC model [50]

In order to further simplify the model, additional assumptions are made that lead to the derivation of a simplified MMC model that only has 4 independent variables instead of the 11 of the model type 3.

In normal operation conditions, it is assumed the *high level* control balances the upper and low arm voltages v_{Ctotu_j} and v_{Ctotl_j} [93], hence the simplification:

$$v_{Ctotu_j} = v_{Ctotl_j} = \bar{v}_{Ctot_j} \quad (3.30)$$

where \bar{v}_{Ctot_j} is the average of the upper and lower arm capacitor voltages of each arm of the MMC, i.e. $\bar{v}_{Ctot_j} = \frac{v_{Ctotu_j} + v_{Ctotl_j}}{2}$.

The combination of (3.30) with (3.19) and (3.20), and the summation of the upper and lower arm equations yields:

$$2C_{tot} \frac{d\bar{v}_{Ctot_j}}{dt} = m_{u_j} i_{u_j} + m_{l_j} i_{l_j} \quad (3.31)$$

At this point, two new AC and DC duty cycles are defined, following the same pattern than for (3.25) and (3.29):

$$m_{ac_j} = \frac{m_{l_j} - m_{u_j}}{2} \quad (3.32)$$

$$m_{dc_j} = m_{u_j} + m_{l_j} \quad (3.33)$$

Combining (3.30), (3.32), (3.33), (3.25) and (3.29) yields:

$$v_{m_j} = m_{ac_j} \bar{v}_{Ctot_j} \quad (3.34)$$

$$v_{diff_j} = m_{dc_j} \bar{v}_{Ctot_j} \quad (3.35)$$

Injecting (3.28), (3.32) and (3.33) in (3.31) yields:

$$2C_{tot} \frac{d\bar{v}_{Ctot_j}}{dt} = m_{dc_j} i_{diff_j} - m_{ac_j} i_{g_j} = i_{mdc_j} - i_{mac_j} \quad (3.36)$$

where the modulated DC and AC currents are introduced:

$$i_{mdc_j} = m_{dc_j} i_{diff_j}, \quad i_{mac_j} = m_{ac_j} i_{g_j} \quad (3.37)$$

While (3.23) describes the AC dynamics of the MMC and (3.27) describes the DC dynamics of the MMC, Equation (3.36) describes the internal dynamics of the converter. These equations can be combined into the equivalent circuit of Figure 3.15 for each phase.

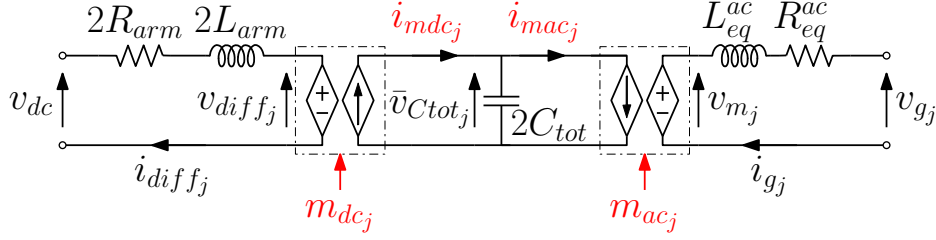


Figure 3.15: Equivalent circuit of each AAM phase.

In normal operation condition, the MMC distributes the total energy stored in the converter equally between each leg⁴. Therefore, in order to reduce the system complexity, it can be assumed that:

$$\bar{v}_{Ctot_a} = \bar{v}_{Ctot_b} = \bar{v}_{Ctot_c} = \bar{v}_{Ctot} \quad (3.38)$$

Taking (3.38) into account and summing the equations (3.36) for the three phase yields, for $C_{eq} = 6C_{tot}$:

$$C_{eq} \frac{d\bar{v}_{Ctot}}{dt} = \sum_{j=a,b,c} i_{mdc_j} - \sum_{j=a,b,c} i_{mac_j} \quad (3.39)$$

Equation (3.39) shows that the 6 arm capacitors can be replaced by an equivalent capacitance $C_{eq} = 6C_{tot}$ subject to voltage \bar{v}_{Ctot} . It also shows that the charging or discharging of that equivalent capacitor depends on the difference between the sum of the modulated DC currents and the sum of the modulated AC currents. Thus, the equivalent capacitor of the arm capacitors acts as an energy buffer between the AC side and the DC side of the converter, which are consequently decoupled (by opposition to a standard 2-level VSC where the active power on both side of the converter is directly related).

Equation (3.39) can be further simplified by assuming that the DC current i_{dc} is distributed equally among the three legs of the MMC (i.e. $m_{dc_a} = m_{dc_b} = m_{dc_c} = m_{dc}$), and taking into account that $\sum_j i_{diff_j} = i_{dc}$, the first sum in the right-hand side of (3.39) is equal to:

$$\sum_{j=a,b,c} i_{mdc_j} = m_{dc} i_{dc} \quad (3.40)$$

⁴This is achieved by the *Low Level* control of the MMC, which is described in Section 3.3.2

and by using (3.34) and (3.38), the second sum of (3.39) can be expressed as:

$$\sum_{j=a,b,c} i_{mac_j} = \frac{1}{\bar{v}_{Ctot}} \sum_{j=a,b,c} v_{m_j} i_{g_j} = \frac{p_{mac}}{\bar{v}_{Ctot}} \quad (3.41)$$

where p_{mac} is the instantaneous three-phase AC power flowing out of the MMC.

Therefore, after transformation to the $dq0$ reference frame, p_{mac} can be expressed as:

$$p_{mac} = v_{m,d} i_{g,d} + v_{m,q} i_{g,q} = (m_d i_{g,d} + m_q i_{g,q}) \bar{v}_{Ctot} \quad (3.42)$$

where the subscripts d and q indicate the d -axis and q -axis components of the corresponding variables and m_d , m_q are defined as:

$$m_d = \frac{v_{m,d}}{\bar{v}_{Ctot}}, \quad m_q = \frac{v_{m,q}}{\bar{v}_{Ctot}} \quad (3.43)$$

As a result, (3.39) becomes:

$$C_{eq} \frac{d\bar{v}_{Ctot}}{dt} = m_{dc} i_{dc} - m_d i_{g,d} - m_q i_{g,q} \quad (3.44)$$

Furthermore, similarly to the AC side equations of a standard 2-level VSC (i.e. Equations (3.2) and (3.3)), the AC dynamics equation (3.23) can be decomposed into:

$$v_{m,d} - v_{g,d} = L_{eq}^{ac} \frac{di_{g,d}}{dt} + R_{eq}^{ac} i_{g,d} - \omega_g L_{eq}^{ac} i_{g,q} \quad (3.45)$$

$$v_{m,q} - v_{g,q} = L_{eq}^{ac} \frac{di_{g,q}}{dt} + R_{eq}^{ac} i_{g,q} + \omega_g L_{eq}^{ac} i_{g,d} \quad (3.46)$$

The DC side equation of the MMC (3.27) can be expressed as:

$$v_{dc} - v_{mdc} = L_{eq}^{dc} \frac{di_{dc}}{dt} + R_{eq}^{dc} i_{dc} \quad (3.47)$$

where:

$$v_{mdc} = m_{dc} \bar{v}_{Ctot} \quad (3.48)$$

$$R_{eq}^{dc} = \frac{2R_{arm}}{3}, \quad L_{eq}^{dc} = \frac{2L_{arm}}{3} \quad (3.49)$$

Following the above analysis, a new equivalent circuit for the MMC model based on (3.44), (3.45), (3.46) and (3.47) is derived and shown in Figure 3.16.

The *simplified MMC model* only has 4 independent variables (the DC current i_{dc} , the equivalent capacitor voltage \bar{v}_{Ctot} , the d -axis AC current $i_{g,d}$ and the q -axis AC current

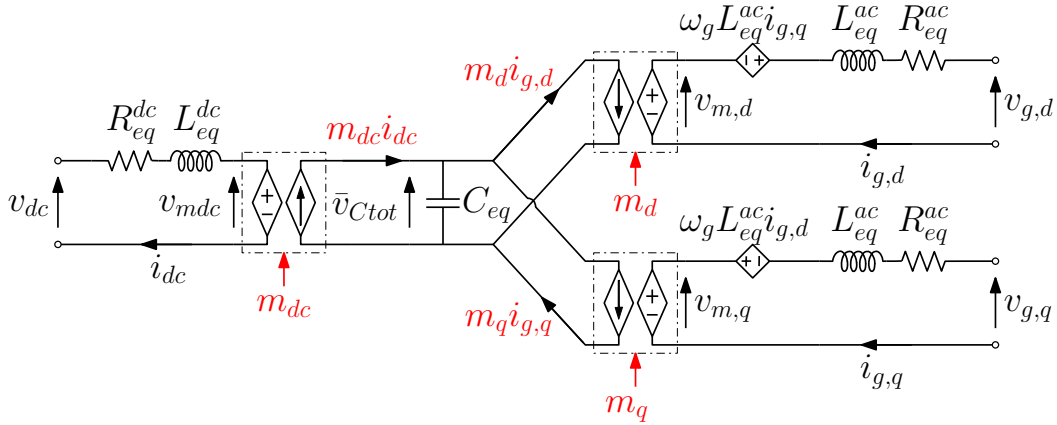


Figure 3.16: Circuit of the simplified MMC model in the $dq0$ reference frame.

$i_{g,q}$) while the *Model type 3* had 11. This reduction is explained by the fact that the six arm capacitors have been replaced by a single equivalent one, hence the replacement of the six capacitor voltages v_{Ctotu_j} and v_{Ctotl_j} in Figure 3.14 by the equivalent capacitor voltage \bar{v}_{Ctot} in Figure 3.16, reducing the number of total independent variables from 11 to 6. And since the six arms have been merged together, the three differential currents i_{diff_j} have been combined into a single DC current i_{dc} , hence reducing the number of total independent variables from 6 to a final 4.

Block diagram of the MMC model

The block diagram representation of the modelling of the AC side of the MMC, corresponding to (3.45) and (3.46), is very similar to the block diagram representation of the modelling of the AC side of a standard 2-level VSC and is pictured in Figure 3.17.

The block diagram representation of the DC side of the MMC, corresponding to (3.47), is pictured in Figure 3.18. By opposition to the DC side modelling of the 2-level VSC, there is no capacitance connected to the DC bus. However, there is an inductance and its associated resistance.

The internal dynamics of the MMC are characterised by (3.44). In order to obtain the block diagram representation of the complete MMC model, (3.43) is inserted in (3.44), which yields:

$$C_{eq}\bar{v}_{Ctot}\frac{d\bar{v}_{Ctot}}{dt} = m_{dc}i_{dc}\bar{v}_{Ctot} - v_{m,d}i_{g,d} - v_{m,q}i_{g,q} \quad (3.50)$$

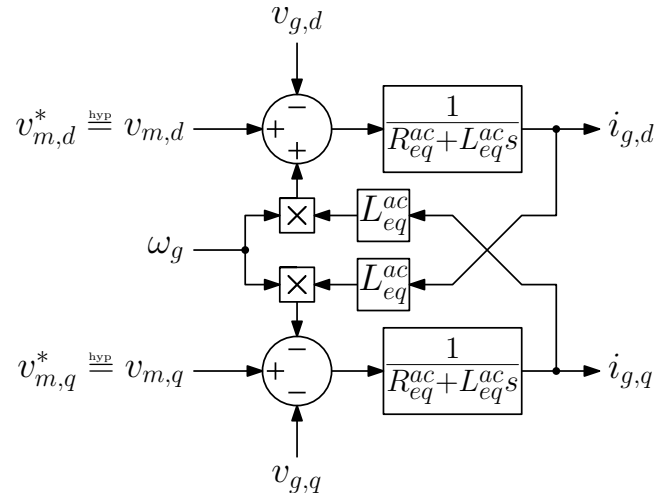


Figure 3.17: Block diagram modelling of the AC side of an MMC in the $dq0$ reference frame.

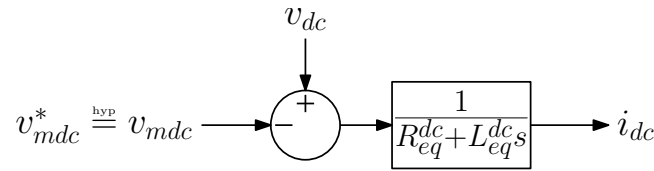


Figure 3.18: Block diagram modelling of the DC side of an MMC.

and by expressing the stored energy of the capacitor $W_{tot} = \frac{1}{2}C_{eq}\bar{v}_{Ctot}^2$ (i.e. $\frac{dW_{tot}}{dt} = C_{eq}\bar{v}_{Ctot}\frac{d\bar{v}_{Ctot}}{dt}$), and by using the fact that $m_{dc}\bar{v}_{Ctot} = v_{m,dc}$, (3.50) becomes:

$$\frac{dW_{tot}}{dt} = v_{m,dc}i_{dc} - (v_{m,d}i_{g,d} + v_{m,q}i_{g,q}) = p_{dc} - p_{ac} \quad (3.51)$$

which leads to the following block diagram:

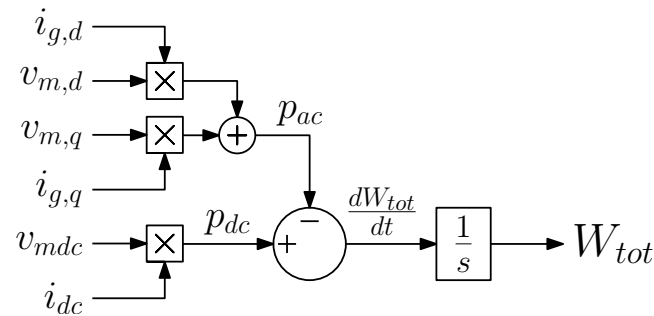


Figure 3.19: Block diagram modelling of the stored energy of the MMC.

The combination of Figures 3.17, 3.18 and 3.19 gives the block diagram of the physical system of the MMC pictured in Figure 3.20. The block-diagram modelling of the control system of the MMC will be derived in Section 3.3.2.

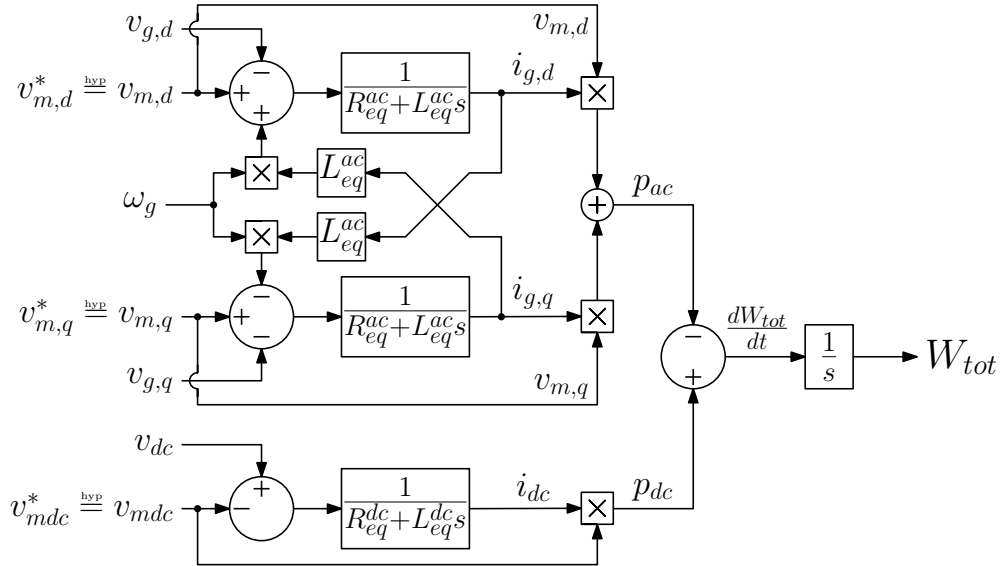


Figure 3.20: Block diagram modelling of the complete physical system of the MMC.

Comparison of the 2-level VSC model with the simplified MMC model

The comparison of the 2-level VSC equivalent circuit recalled in Figure 3.21a with the simplified MMC model circuit recalled in Figure 3.21b shows several fundamental differences due to the inherent nature of the two converters:

- The DC current i_s is an independent state variable in the simplified MMC model whereas it is *not* an independent state variable in the two-level VSC model. Therefore, it cannot be independently controlled in the latter as it can in the former.
- The DC capacitor of the VSC is *physically coupled* with the DC bus while the total capacitance of the MMC is *not* physically coupled with the DC bus [93]. This can impact the total equivalent capacitance of the DC grid and, hence, the time response of the DC voltage and current [85, 10]. Furthermore, it shows that the instantaneous active power on either side of the converter is identical in the case of a 2-level VSC (when the losses in the power electronics are not considered), but has no immediate correlation in the case of an MMC.

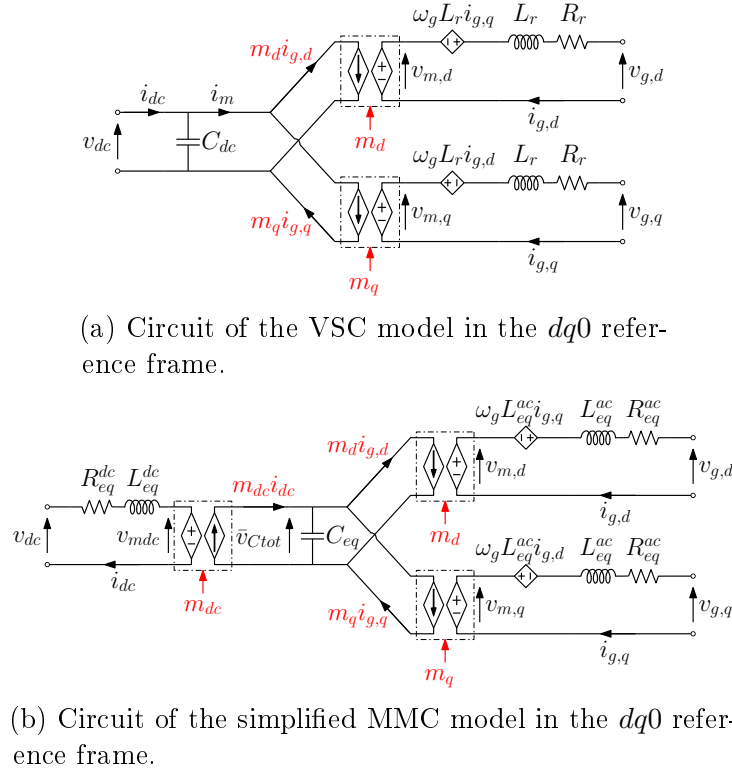


Figure 3.21: Equivalent circuits of MMC and two-level VSC.

- There is no R_{eq}^{dc} and L_{eq}^{dc} in the 2-level VSC model.
- The MMC model can mimic the behaviour of a 2-level VSC by taking $m_{dc} = 1$, $R_{eq}^{dc} = 0$ and $L_{eq}^{dc} = 0$. By taking $m_{dc} = 1$ (i.e. by forcing $v_{m_{dc}} = \bar{v}_{Ctot}$), the stored energy of the MMC is shared with the DC bus.

3.3.2 Control of the MMC

The control strategy of the MMC can be decomposed into two control levels, as depicted in Figure 3.22, the high-level control and the low-level control:

- High-Level control: This level aims at calculating the upper and lower arm voltage references (v_{uj} and v_{lj} for $j = a, b, c$) needed with regards to its design. This control level consists of cascaded loops: the inner control loops (AC and DC current control) and the outer control loops (can be an active power control, a reactive power control, a DC voltage control, an AC voltage control and an MMC total energy control). Although very similar to a 2-level VSC, the High Level control of an MMC shows some notable disparities that will be detailed

in this section. The synchronization to the AC network, however, is achieved through the same PLL than for a VSC (Figure 3.7).

- **Low-Level control:** This level has two main tasks to perform. The first one is to select and activate the correct combination of SM of which the sum of their instantaneous voltages matches with the upper and lower arm voltage references ($v_{u_j}^*$ and $v_{l_j}^*$ for $j = a, b, c$) given by the High Level Control. This can be achieved with different techniques such as Pulse Width Modulation (PWM) [58] or Nearest Level Control (NLC) [112]. The second task is to balance the capacitor voltages between them to maintain them within an similar range. This is achieved with the Balancing Capacitor Algorithm (BCA) [112, 93]. This control needs not to be implemented with the simplified MMC model presented in the previous section, and hence, will not be detailed in this thesis.

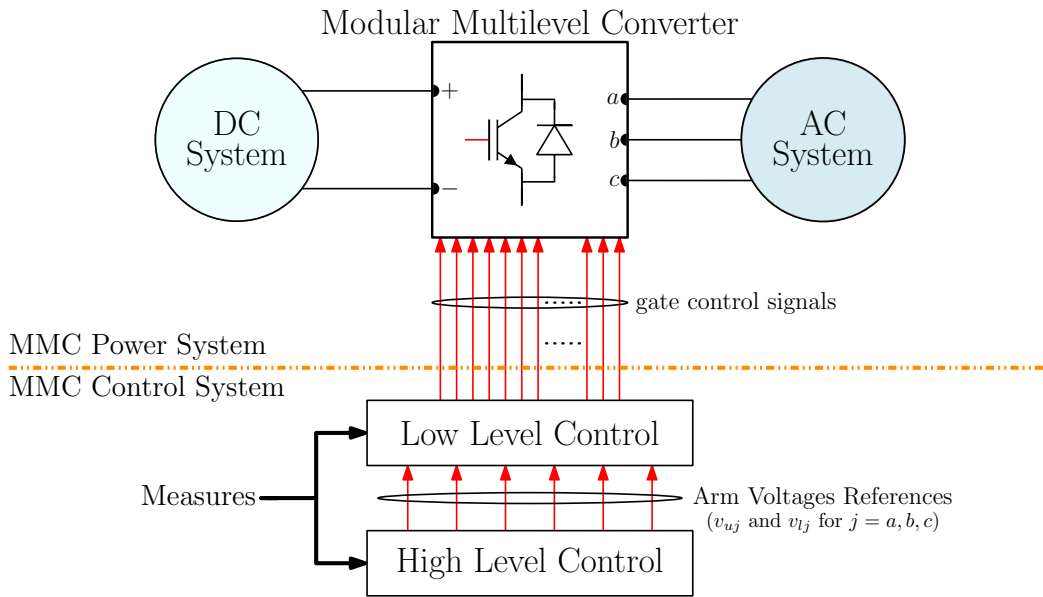


Figure 3.22: Control hierarchy of a Modular Multilevel Converter [48].

MMC current control loops

The AC side of the MMC being very similar to the AC side of a standard 2-level VSC, the control of the MMC needs to be synchronised with the AC grid through the same PLL than for a VSC (Figure 3.7), and include an AC current loop to decouple the grid currents $i_{g,d}$ and $i_{g,q}$ in the $dq0$ reference frame. The principle of this current loop, detailed in Figure 3.23, is no different than the one of a standard 2-level VSC presented

in Section 3.2.2: a PI controller tuned for a response time of 10 ms, followed by the current decoupling terms.

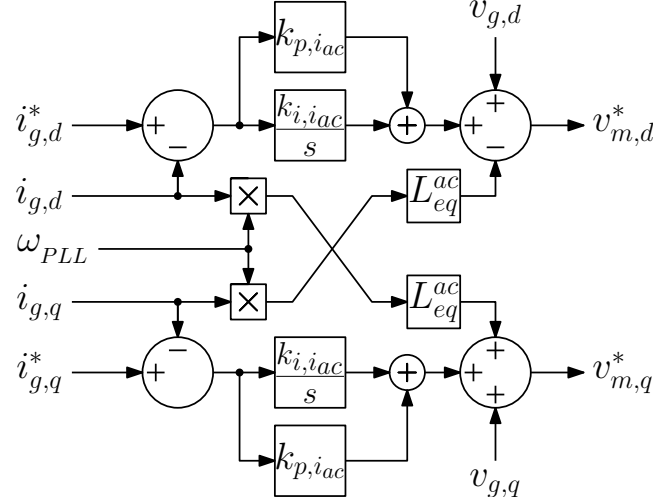


Figure 3.23: Modelling of the AC current control loop of the MMC.

As was stated in the previous section, the DC current i_{dc} is a fully controllable state-variable in the simplified MMC model. The control of the DC current is simply achieved through a PI controller tuned for a response time of 4 ms. However, in order to reduce the effort furnished by the PI controller and improve the converter DC dynamics, the output of the PI controller is subtracted to a compensation variable which is generally the measurement of v_{dc} (but can also be a constant equal to the nominal value of the DC voltage to avoid any additional perturbation to be re-injected in the control system), as shown in Figure 3.24. In fact, by doing this the output of the DC current loop becomes, with $C(s)$ as the PI controller transfer function:

$$v_{mdc}^* = v_{dc} - C(s) (i_{dc}^* - i_{dc}) \quad (3.52)$$

and the DC side equation of the MMC (3.47) becomes, assuming $v_{mdc}^* = v_{mdc}$:

$$v_{dc} - v_{dc} + C(s) (i_{dc}^* - i_{dc}) = sL_{eq}^{dc}i_{dc} + R_{eq}^{dc}i_{dc} \quad (3.53)$$

i.e.

$$i_{dc} = \frac{C(s)}{C(s) + sL_{eq}^{dc} + R_{eq}^{dc}} i_{dc}^* \quad (3.54)$$

hence the direct control of i_{dc} by its reference i_{dc}^* .

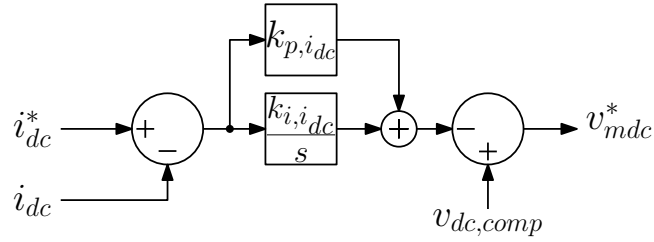


Figure 3.24: Modelling of the DC current control loop of the MMC.

MMC outer control loops

The MMC converter being a specific converter topology of VSC-HVDC systems, the four outer loops presented in the previous section in the case of a standard 2-level VSC, namely the DC voltage, the active power, the reactive power and the AC voltage control loops, are available for the outer control of an MMC. As stated previously, they each generate a grid current reference $i_{g,d}$ or $i_{g,q}$ and are cascaded with the current control loop.

In the case of an MMC, there is also a DC current loop that controls the DC current output of the converter. The reference of this second inner controller is generated by an energy control loop whose aim is to control the internal energy stored in the MMC at all times. In fact, the control of the total stored energy (W_{tot}) in the converter is based on the regulation of the exchanged energy between AC and DC sides [93]. This control can be achieved by a simple PI (or IP) controller that ensures the stored energy corresponds to the reference W_{tot}^* and whose output is commonly summed to an AC power compensation variable $P_{ac, comp}$. The stored energy signal is generally filtered to avoid interfering with the control of the energy.

If the energy reference W_{tot}^* of the controller is a constant value, as considered in [93] (upper position of the switch in Figure 3.25), then the model's equivalent capacitor C_{eq} is completely decoupled from the DC grid. However, if the energy reference is associated with the square of the DC voltage v_{dc}^2 , as considered in [94] (lower position of the switch in Figure 3.25), then the stored energy of the MMC is shared with the DC bus.

The complete MMC model comprising of the physical system and its control is then described by Figure 3.26, where the external signals are highlighted in blue in the case of the reference signals and red in the case of the measured signals, and the internal (or generated) signals are highlighted in green.

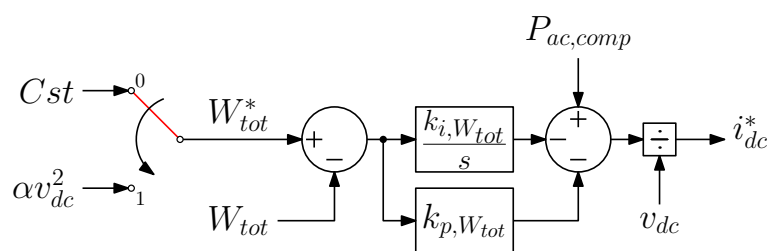


Figure 3.25: Modelling of the total energy control loop of the MMC.

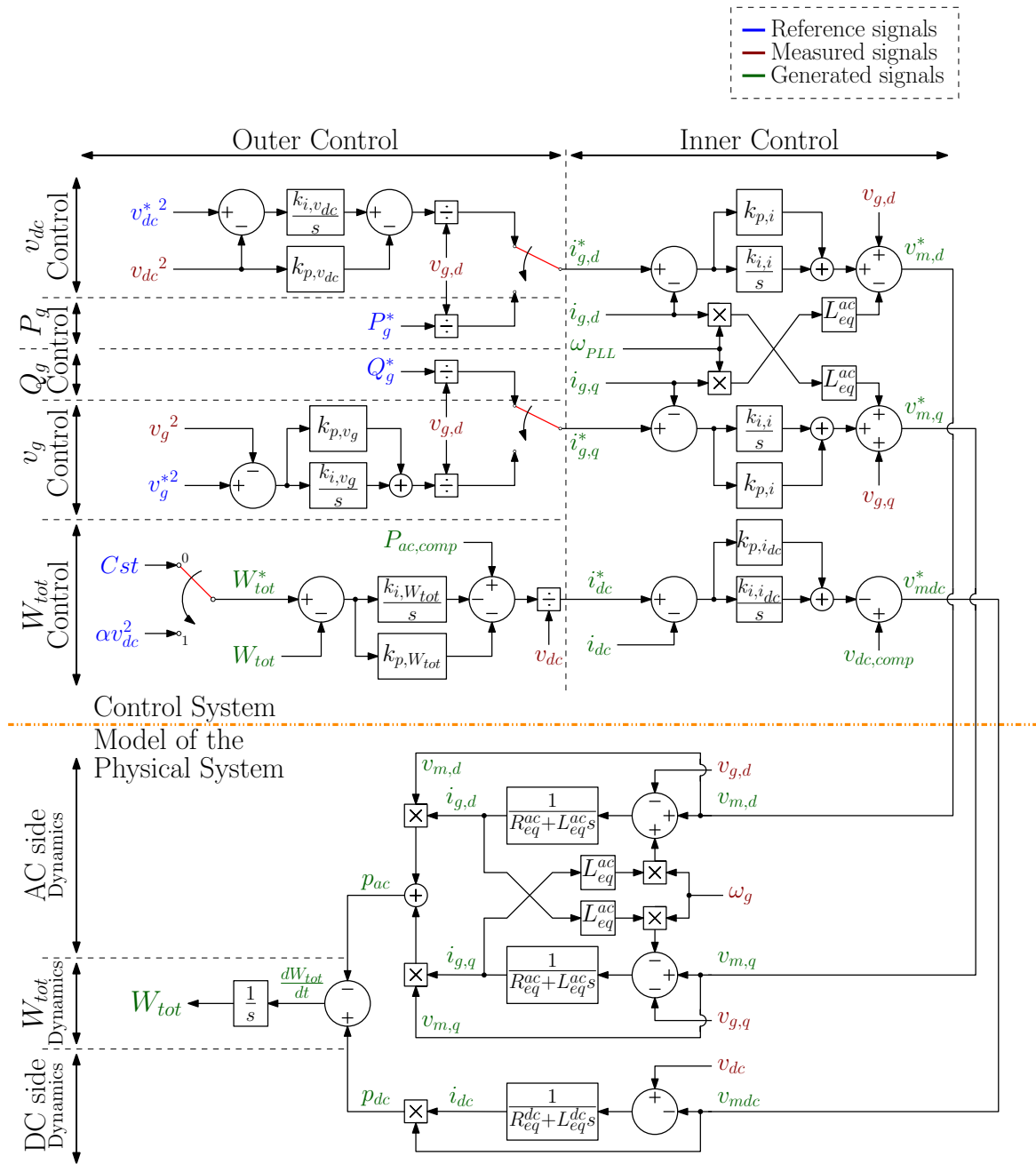


Figure 3.26: Block-diagram of the complete MMC station, comprising of the physical system and its control (the PLL is not represented).

3.4 Chapter Conclusion

This chapter described the modelling process of two VSC-based converters: the standard 2-level Voltage Source Converter (VSC) and the Modular Multilevel Converter (MMC).

The physical system of each converter was analysed and mathematically quantified in order to derive an Average Value Model (AVM) able to properly reproduce the behaviour of the converters without the incur of complex and cumbersome power electronics models by voluntarily losing the information on the switching state of the power electronic components. In the case of the MMC, the internal dynamics of the converter –corresponding to the total stored energy in the capacitors of each SM– are reproduced by the derived model, allowing the use of energy-based control techniques. The control of the two converters was explained and detailed. This includes the PLL, the inner control loop with its current decoupling design and the various outer control loops that each achieve a different purpose.

The resulting models are efficient, easy to use and require little computational effort. However they are non-linear, and thus, cannot be easily analysed. The next chapter will linearise these models and verify their validity by comparing them to detailed reference models.

Chapter 4

State-Space Representation and Modal Analysis of an HVDC Link

[...] I may state that I have obtained, by its means, spark discharges extending through more than one hundred feet and carrying currents of one thousand amperes, electromotive forces approximating twenty million volts, chemically active streamers covering areas of several thousand square feet, and electrical disturbances in the natural media surpassing those caused by lightning, in intensity. Whatever the future may bring, the universal application of these great principles is fully assured, though it may be long in coming. With the opening of the first power plant, incredulity will give way to wonderment, and this to ingratitude, as ever before. The time is not distant when the energy of falling water will be man's life energy.

– Nikola Tesla, *The Transmission of Electrical Energy Without Wires as a Means for Furthering Peace* in *Electrical World and Engineer* (7 January 1905) [106].

4.1 Chapter Introduction

The previous chapter led to the derivation of both an Average Value Model (AVM) of the Voltage Source Converter (VSC) and a simplified Modular Multilevel Converter (MMC) model, as well as their respective control strategy. However, these models and their control are non-linear and cannot be put in state-space form to use the powerful tools of the control theory for linear systems. In this chapter, they are linearised and a methodology to obtain their state-space representation is described. The procedure is based on combining the state-space equations describing the different parts of the converter. The complete state-space models are then validated by comparing their behaviour to more detailed reference models using Electro-Magnetic Transient (EMT) programs.

Once the state-space models are validated, an HVDC link using both converter technologies is studied and the modes are identified and assessed to understand the dynamics of the transmission system. The results of the VSC- and MMC-based HVDC links are finally compared and the main differences are emphasised and explained.

4.2 State-Space Representation of the VSC Model

This section presents the methodology to obtain the state-space representation of both the AVM of the VSC and its command that were derived in the previous chapter. The state-space model is then be validated by a comparison with the behaviour of a more detailed IGBT-based VSC model in an EMT program.

4.2.1 Linearisation of the VSC Model

Chapter 3 has presented the different parts that constitute a VSC station, namely, the AC physical system, the Phase-Locked Loop (PLL), the inner current control and the outer control loops. However, these individual parts, called subsystems, are non-linear and thus, prevent the use of some powerful control theory analysis tools for linear systems. For this reason, the subsystems are individually linearised around an operating point and assembled together to generate a linearised model of the AVM that was described in the previous chapter.

Each subsystem is linearised under the small-signal approximation: each variable x is expressed as $x = x_0 + \Delta x$ where x_0 is the variable value at the initial operating point, and Δx is the small deviation of the considered variable around the initial operating point.

For instance, as detailed in the previous chapter, the AC-side of the physical system of the VSC is described by the equations (4.1) and (4.2) which show a non-linearity due to the multiplication of ω_g and $i_{g,dq}$.

$$v_{m,d} - v_{g,d} = L_r \frac{di_{g,d}}{dt} + R_r i_{g,d} - \omega_g L_r i_{g,q} \quad (4.1)$$

$$v_{m,q} - v_{g,q} = L_r \frac{di_{g,q}}{dt} + R_r i_{g,q} + \omega_g L_r i_{g,d} \quad (4.2)$$

Under the small-signal assumption, $i_{g,d} = I_{g,d0} + \Delta i_{g,d}$, $i_{g,q} = I_{g,q0} + \Delta i_{g,q}$, $v_{m,d} = V_{m,d0} + \Delta v_{m,d}$, $v_{m,q} = V_{m,q0} + \Delta v_{m,q}$ and $\omega_g = \omega_{g0} + \Delta \omega_g$. Thus, (4.1) and (4.2) become:

$$\begin{aligned} V_{m,d0} + \Delta v_{m,d} - V_{g,d0} - \Delta v_{g,d} = & L_r \frac{d\Delta i_{g,d}}{dt} + R_r (I_{g,d0} + \Delta i_{g,d}) - L_r I_{g,q0} \omega_{g0} \\ & - L_r I_{g,q0} \Delta \omega_g - L_r \omega_{g0} \Delta i_{g,q} - L_r \Delta i_{g,q} \Delta \omega_g \end{aligned} \quad (4.3)$$

$$\begin{aligned} V_{m,q0} + \Delta v_{m,q} - V_{g,q0} - \Delta v_{g,q} = & L_r \frac{d\Delta i_{g,q}}{dt} + R_r (I_{g,q0} + \Delta i_{g,q}) + L_r I_{g,d0} \omega_{g0} \\ & + L_r I_{g,d0} \Delta \omega_g + L_r \omega_{g0} \Delta i_{g,d} + L_r \Delta i_{g,d} \Delta \omega_g \end{aligned} \quad (4.4)$$

which yields, with $V_{m,d0} - V_{g,d0} = R_r I_{g,d0} - L_r I_{g,q0} \omega_{g0}$ and $V_{m,q0} - V_{g,q0} = R_r I_{g,q0} - L_r I_{g,d0} \omega_{g0}$, and after neglecting the second order terms:

$$\Delta v_{m,d} - \Delta v_{g,d} = L_r \frac{d\Delta i_{g,d}}{dt} + R_r \Delta i_{g,d} - L_r I_{g,q0} \Delta \omega_g - L_r \omega_{g0} \Delta i_{g,q} \quad (4.5)$$

$$\Delta v_{m,q} - \Delta v_{g,q} = L_r \frac{d\Delta i_{g,q}}{dt} + R_r \Delta i_{g,q} + L_r I_{g,d0} \Delta \omega_g + L_r \omega_{g0} \Delta i_{g,d} \quad (4.6)$$

Equations (4.5) and (4.6) are thus the linearised version of (4.1) and (4.2).

Similarly, the DC-side physical system is governed by (4.7).

$$i_{dc} - i_m = C_{dc} \frac{dv_{dc}}{dt} \quad (4.7)$$

Under the small-signal assumption, $i_{dc} = I_{dc0} + \Delta i_{dc}$, $i_m = I_{m0} + \Delta i_m$ and $v_{dc} = V_{dc0} + \Delta v_{dc}$. Equation (4.7) becomes, after removing the steady-state terms:

$$\Delta i_{dc} - \Delta i_m = C_{dc} \frac{d\Delta v_{dc}}{dt} \quad (4.8)$$

Finally, the AC and DC sides of the converter are related by the instantaneous power which is identical at both sides of the VSC since the power electronic losses are

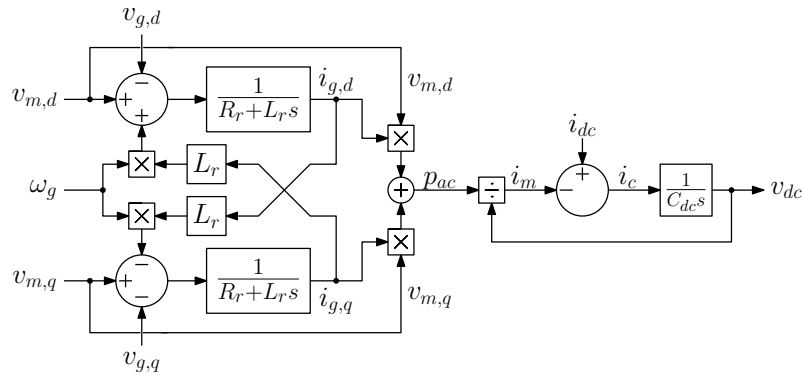
neglected. Hence:

$$p_{ac} = v_{m,d}i_{g,d} + v_{m,q}i_{g,q} = v_{dc}i_m = p_{dc} \quad (4.9)$$

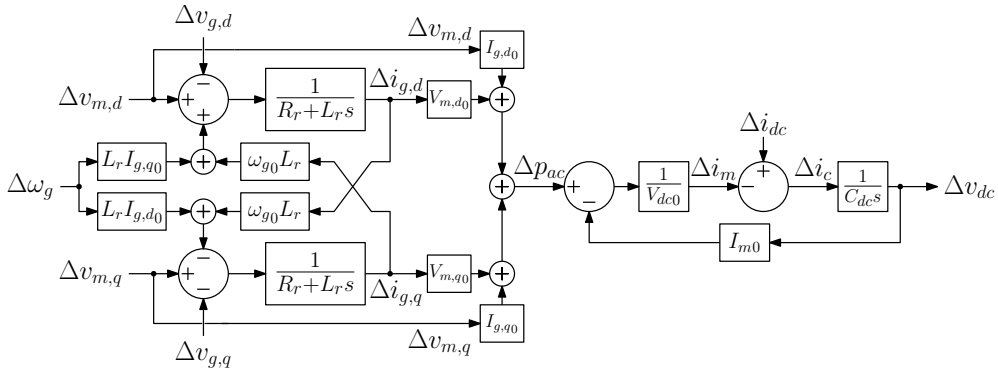
which yields, under the small-signal assumption:

$$\Delta i_m = \frac{1}{V_{dc0}} (V_{m,d0} \Delta i_{g,d} + I_{g,d0} \Delta v_{m,d} + V_{m,q0} \Delta i_{g,q} + I_{g,q0} \Delta v_{m,q} - I_{m0} \Delta v_{dc}) \quad (4.10)$$

The linear equations (4.5), (4.6), (4.8) and (4.10) correspond to the linear VSC model and lead to the block-diagram of Figure 4.1b which is to be compared with the initial non-linear model of Figure 4.1a.



(a) Non-linear model of the physical system of the VSC.



(b) Linearised model of the physical system of the VSC.

Figure 4.1: Comparison of the non-linear and linearised model of the physical system of the VSC.

Using the same linearisation principle, the linearisation of the control system is also achieved. More linearisation details of the subsystems can be found in [84]. A block-diagram representation of the complete linearised VSC model, comprising of both the physical and the control system, is obtained and pictured in Figure 4.2.

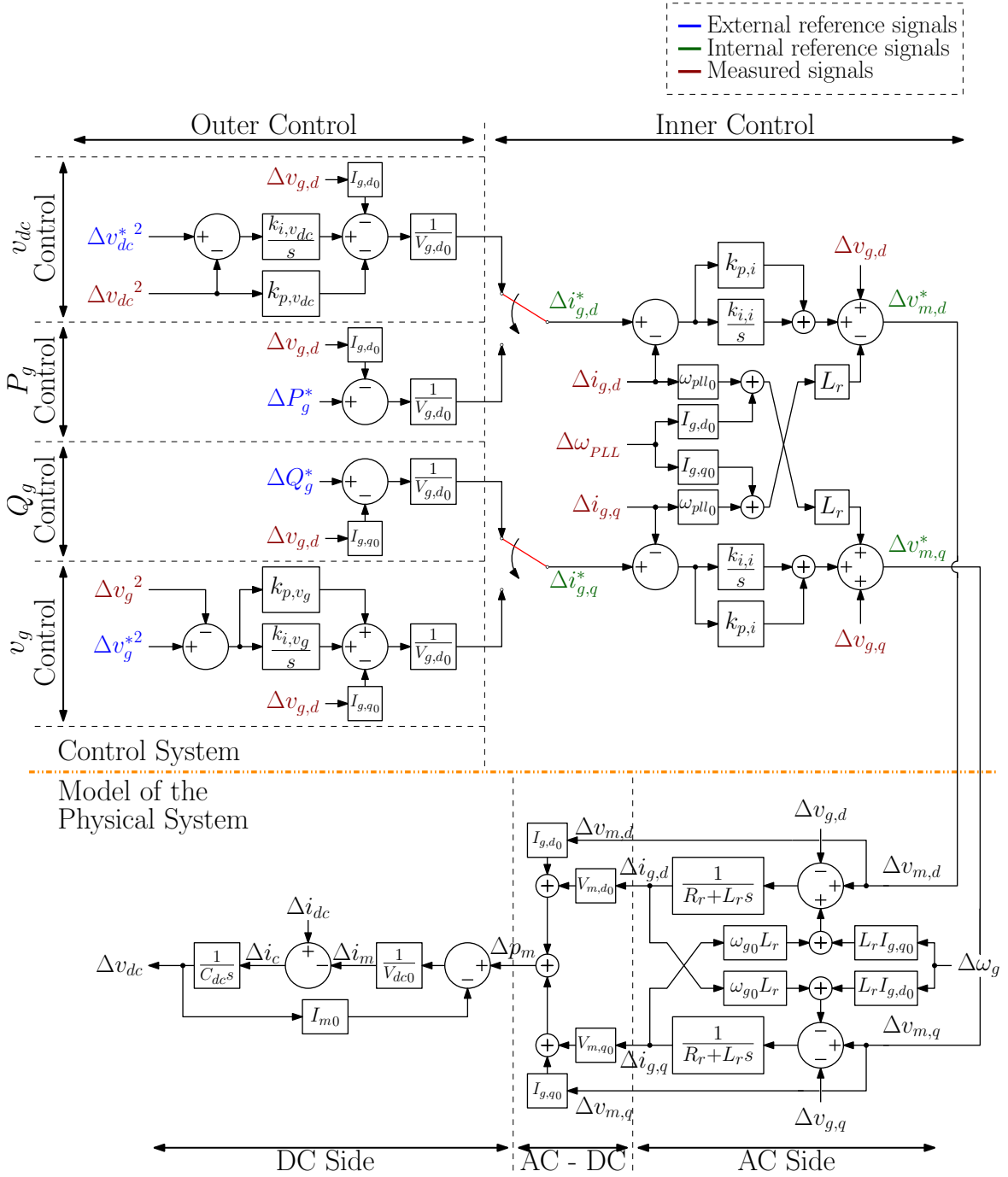


Figure 4.2: Block diagram of the linearised VSC model.

4.2.2 State-Space Representation of the Linear VSC Model

Once each one of the subsystems that were presented in the previous chapter has been linearised, they can be represented in the state-space form of (4.11).

$$\begin{aligned}\frac{d}{dt}x &= Ax + Bu \\ y &= Cx + Du\end{aligned}\quad (4.11)$$

Each subsystem is linked to the others through its inputs and outputs, as depicted in Figure 4.3. These relations between the inputs and outputs of the subsystems form the interconnection static constraints (also called network model in [77]).

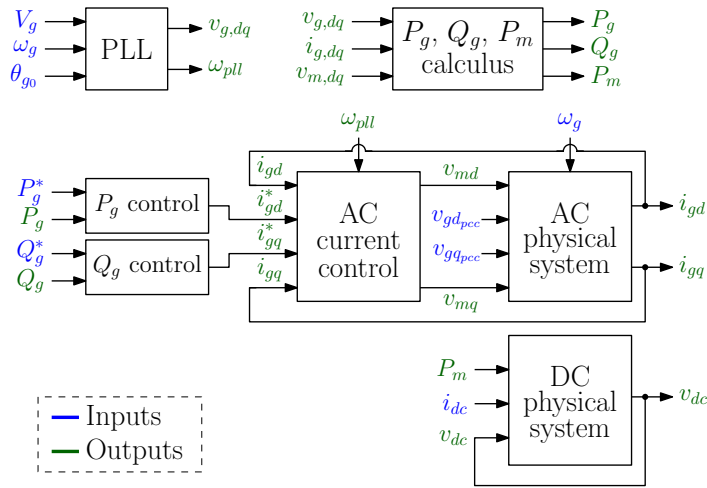


Figure 4.3: Interconnection constraints of the subsystems that constitute the VSC model.

The complete VSC state-space model is obtained by combining the N individual linearised subsystems according to the interconnection static constraints.

$$\begin{aligned}\frac{d}{dt}x_n &= A_n x_n + B_n u_n \\ y_n &= C_n x_n + D_n u_n\end{aligned}\quad (4.12)$$

with the interconnection static constraints:

$$u \triangleq [u_1 \quad \dots \quad u_N]^\top = Jy \triangleq J [y_1 \quad \dots \quad y_N]^\top \quad (4.13)$$

where x_n , u_n and y_n are column vectors for $n = 1, 2, \dots, N$, and J is the network matrix representing how the subsystems are interconnected (see Appendix D for more details).

The decomposition of the complete system into several subsystems offers both a simplicity and a commodity advantage by comparison to the small-signal modelling of the whole converter as once, as in [35]. In fact, it allows the user to easily replace a subsystem by another, hence effectively facilitating the use of variants in the subsystems (e.g. use a PI instead of a IP controller for the DC voltage loop, adding various kind of filters to the measured variables, swapping the outer control loops of a converter, etc...).

4.2.3 Validation of the VSC Models

The previous chapter proposed an AVM of a standard 2-level VSC and the previous section linearised this AVM in order to obtain a state-space representation of the system. This section now validates both the AVM and the state-space representation through a comparison with a detailed IGBT-based 2-level VSC simulated thanks to an EMT software.

Instead of going through the cumbersome process of validating individually the different models of a P-mode (i.e. power-controlled) VSC and a Vdc-mode (i.e. DC voltage-controlled) VSC, an HVDC link is used to simultaneously validate the models for the two control types. In fact, the standard *master-slave* control strategy of an HVDC link is as follows: the Vdc-mode converter, also called the *master* converter, controls the DC voltage level while the P-mode converter, also called the *slave*, controls the active power transmitted by the HVDC link.

The HVDC link configuration is illustrated in Figure 4.4. The initial operating point is as follows: the P-mode converter injects a power of 0.6 p.u. (600 MW) into the DC link and the DC voltage of the Vdc-mode converter is regulated at 1 p.u. of DC voltage (640 kV). The converter parameters are listed in Appendix A. The DC cable is a 200 km DC cable whose model is described in [21, 22]. The state-space model of the HVDC link is automatically generated by a Matlab[®] routine that uses the aggregation method described in Section 4.2.2. The validation of both the non-linear AVM and the linearised state-space model of the HVDC link is achieved by comparing their respective behaviours to a more detailed model (using the detailed IGBT-based model of a VSC).

In order to observe the system behaviours of both the AVM and the state-space model, several reference changes are scheduled during the simulation. Each quantity

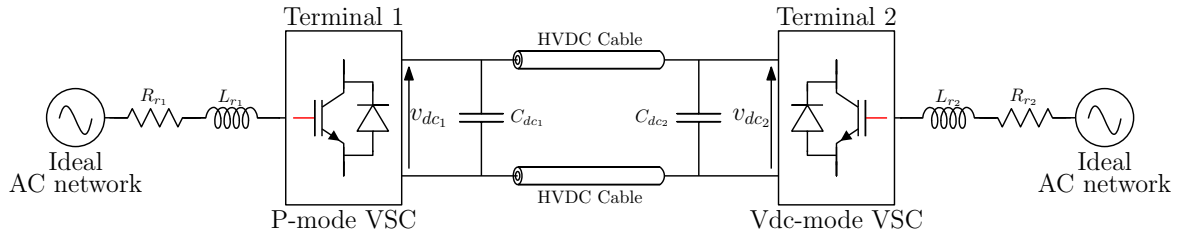


Figure 4.4: Configuration of a VSC-based HVDC link.

has two opposite reference steps so that at the end of the simulation, the HVDC system is back to its original operating point:

- Active power reference of the P-mode converter: -0.3 p.u. at $t = 1$ s and $+0.3$ p.u. at $t = 2.2$ s, as illustrated in Figure 4.5.

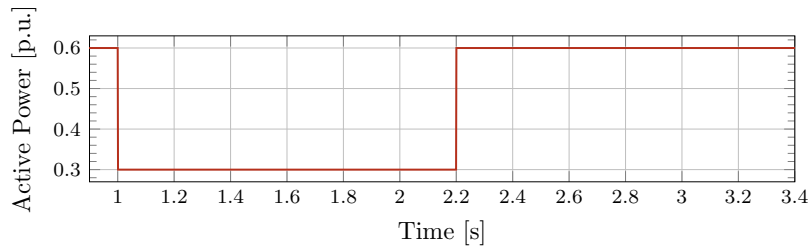


Figure 4.5: Active power reference of the P-mode converter.

- Reactive power reference of the P-mode converter: $+0.2$ p.u. at $t = 1.4$ s and -0.2 p.u. at $t = 2.6$ s, as illustrated in Figure 4.6.

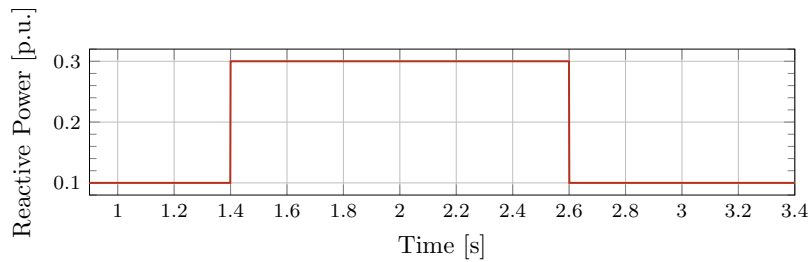


Figure 4.6: Reactive power reference of the P-mode converter.

- DC voltage reference of the Vdc-mode converter: $+0.1$ p.u. at $t = 1.8$ s and -0.1 p.u. at $t = 3$ s, as illustrated in Figure 4.7.

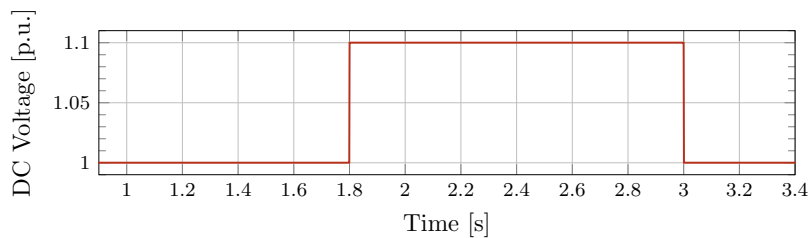
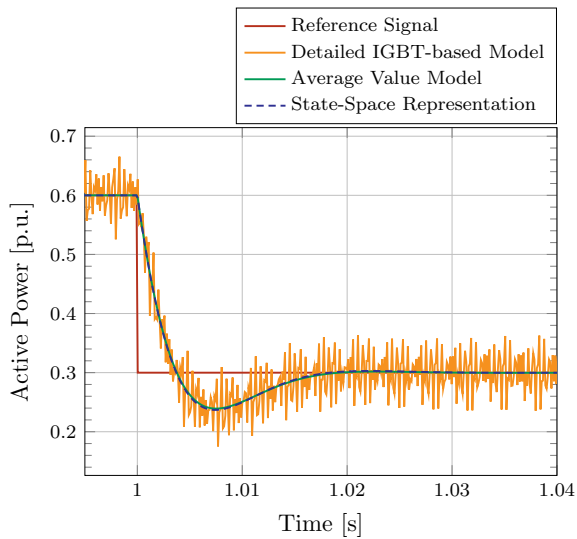


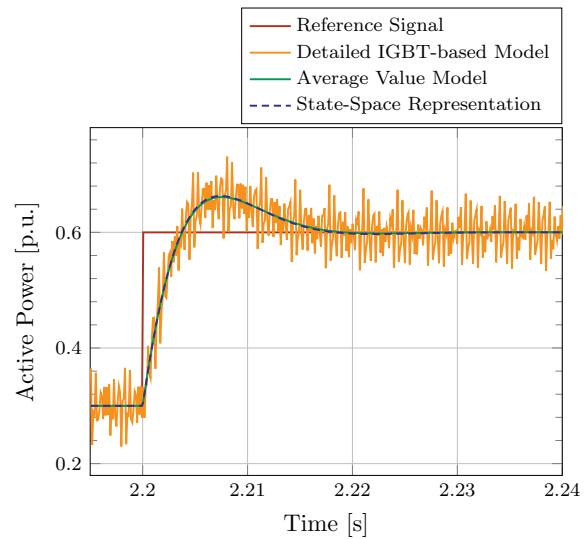
Figure 4.7: DC voltage reference of the Vdc-mode converter.

Figure 4.8 shows the active and reactive power response of the P-mode converter for the three models, namely, the AVM, the state-space model and the detailed IGBT-based model. Figures 4.8a and 4.8b offer a zoom on the active power response around the first reference step at $t = 1$ s and second step at $t = 2.2$ s, while Figures 4.8c and 4.8d offer a zoom on the reactive power response around the first reference step at $t = 1.4$ s and second reference step at $t = 2.6$ s. These figures show almost no discernible differences between the AVM and the state-space model and illustrate the fact that these two models correspond to the average value of the detailed IGBT-based model of the VSC. The response of the system is similar to the response of a second-order plant with a 5% settling time close to 10 ms, which is the 5% tuning time constant of the inner current loop controllers.

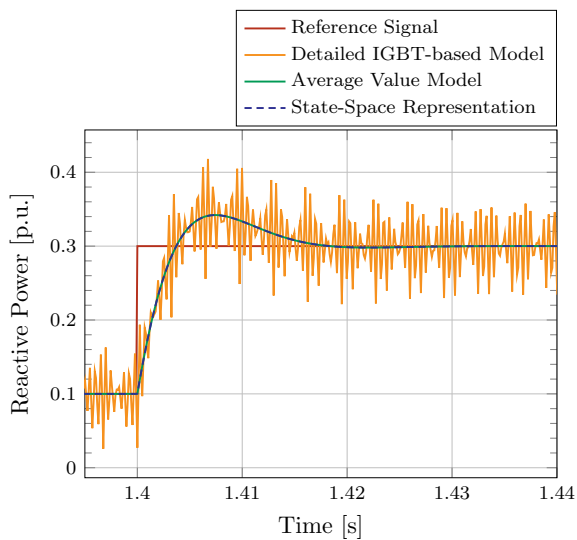
Figure 4.9a shows the DC voltage response of the Vdc-mode converter for the three models and for the entire duration of the simulation. It shows that the DC voltage is impacted by the active power reference steps at $t = 1$ s and $t = 2.2$ s while it is not impacted by the reactive power reference steps. Figure 4.9b offers a zoom on the DC voltage after the the first step of the active power reference: since the P-mode converter is injecting more power into the HVDC link, the DC voltage is increasing. However, the Vdc-mode converter controls the DC voltage to regulate it back to its reference value within a 100 ms response time. The figure shows a small difference between the AVM and the state-space model that is due to the linearisation process. However, this difference of 0.002 p.u. is negligible and the dynamics of the system are perfectly reproduced. Figure 4.9c offers a zoom on the DC voltage response around the first reference step at $t = 1.8$ s. The response of the system is similar to the response of a second order plant with a 5% response time close to the 100 ms settling time of the outer DC voltage loop controller.



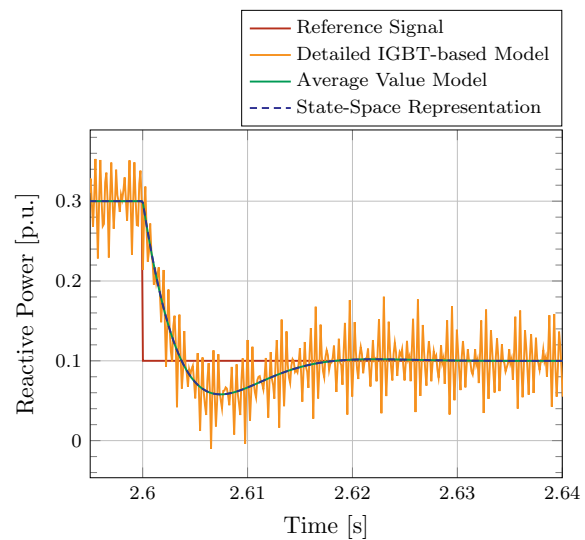
(a) Zoom on the first step of the active power reference.



(b) Zoom on the second step of the active power reference.

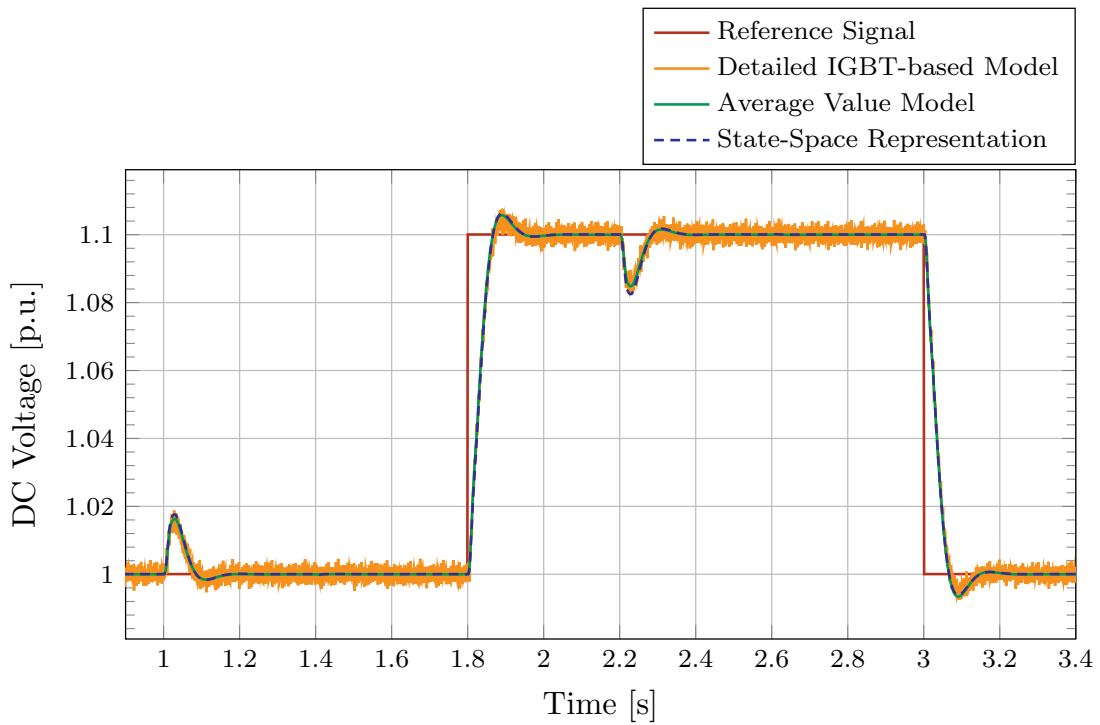


(c) Zoom on the first step of the reactive power reference.

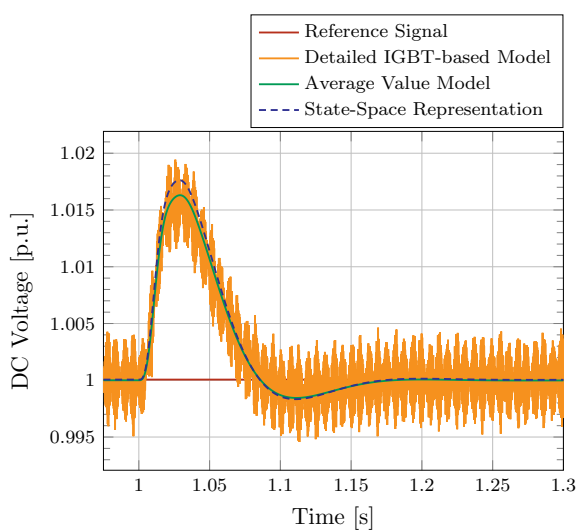


(d) Zoom on the second step of the reactive power reference.

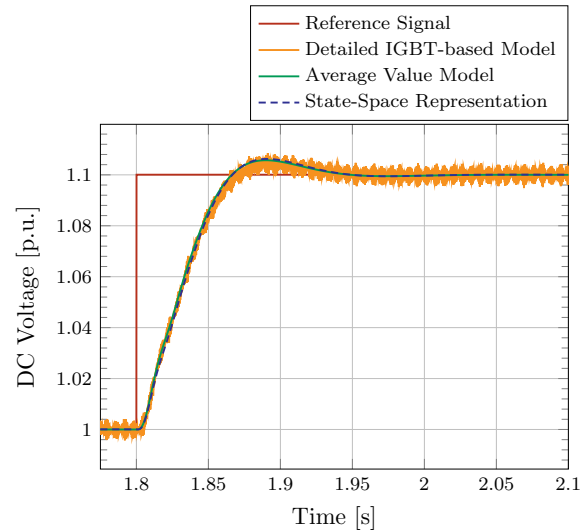
Figure 4.8: Comparison of the active and reactive power responses of the P-mode converter for the state-space model, the average value model and the detailed IGBT-based model of a standard 2-level VSC.



(a) Entire duration of the simulation.



(b) Zoom on the DC voltage behaviour just after the first step of the active power reference.



(c) Zoom on the first step of the DC voltage reference.

Figure 4.9: Comparison of the DC voltage responses of the Vdc-mode converter for the state-space model, the average value model and the detailed IGBT-based model of a standard 2-level VSC.

4.3 State-Space Representation of the MMC Model

This section presents the methodology to obtain the state-space representation of the simplified MMC model that was derived in the previous chapter. This state-space is then validated by being compared to the behaviour of two detailed MMC models.

4.3.1 Linearisation of the simplified MMC Model

The simplified MMC Model is also linearised under the small-signal assumption. Similarly to the VSC, the AC side of the MMC is described by the following equations:

$$v_{m,d} - v_{g,d} = L_{eq}^{ac} \frac{di_{g,d}}{dt} + R_{eq}^{ac} i_{g,d} - \omega_g L_{eq}^{ac} i_{g,q} \quad (4.14)$$

$$v_{m,q} - v_{g,q} = L_{eq}^{ac} \frac{di_{g,q}}{dt} + R_{eq}^{ac} i_{g,q} + \omega_g L_{eq}^{ac} i_{g,d} \quad (4.15)$$

which yield, under the small-signal assumption, after removing the steady-state terms and after neglecting the second order terms:

$$\Delta v_{m,d} - \Delta v_{g,d} = L_{eq}^{ac} \frac{d\Delta i_{g,d}}{dt} + R_{eq}^{ac} \Delta i_{g,d} - L_{eq}^{ac} I_{g,q0} \Delta \omega_g - L_{eq}^{ac} \omega_{g0} \Delta i_{g,q} \quad (4.16)$$

$$\Delta v_{m,q} - \Delta v_{g,q} = L_{eq}^{ac} \frac{d\Delta i_{g,q}}{dt} + R_{eq}^{ac} \Delta i_{g,q} + L_{eq}^{ac} I_{g,d0} \Delta \omega_g + L_{eq}^{ac} \omega_{g0} \Delta i_{g,d} \quad (4.17)$$

The DC side equation of the MMC is expressed as:

$$v_{dc} - v_{mdc} = L_{eq}^{dc} \frac{di_{dc}}{dt} + R_{eq}^{dc} i_{dc} \quad (4.18)$$

Since this equation is already linear, its small-signal counter-part is easily obtained:

$$\Delta v_{dc} - \Delta v_{mdc} = L_{eq}^{dc} \frac{d\Delta i_{dc}}{dt} + R_{eq}^{dc} \Delta i_{dc} \quad (4.19)$$

Finally, the AC and DC sides of the converter are related by the total stored energy in the flying capacitors of the SMs. In fact, it was demonstrated in the previous chapter that the voltage of the equivalent capacitor of the MMC can be expressed by:

$$C_{eq} \bar{v}_{Ctot} \frac{d\bar{v}_{Ctot}}{dt} = m_{dc} i_{dc} \bar{v}_{Ctot} - v_{m,d} i_{g,d} - v_{m,q} i_{g,q} \quad (4.20)$$

and by expressing the stored energy of the equivalent capacitor $W_{tot} = \frac{1}{2} C_{eq} \bar{v}_{Ctot}^2$ (which gives $\frac{dW_{tot}}{dt} = C_{eq} \bar{v}_{Ctot} \frac{d\bar{v}_{Ctot}}{dt}$), and by using the fact that $m_{dc} \bar{v}_{Ctot} = v_{mdc}$, (4.20)

becomes:

$$\frac{dW_{tot}}{dt} = v_{mdc}i_{dc} - (v_{m,d}i_{g,d} + v_{m,q}i_{g,q}) = p_{dc} - p_{ac} \quad (4.21)$$

which is linearised as:

$$\begin{aligned} \frac{d\Delta W_{tot}}{dt} = & I_{dc0}\Delta v_{mdc} + V_{dc0}\Delta i_{dc} - (V_{m,d0}\Delta i_{g,d} + I_{g,d0}\Delta v_{m,d} \\ & + V_{m,q0}\Delta i_{g,q} + I_{g,q0}\Delta v_{m,q}) \end{aligned} \quad (4.22)$$

The linear equations (4.16), (4.17), (4.19) and (4.22) correspond to the linear MMC model and lead to the block-diagram of Figure 4.10b which is to be compared with the initial non-linear model of Figure 4.10a.

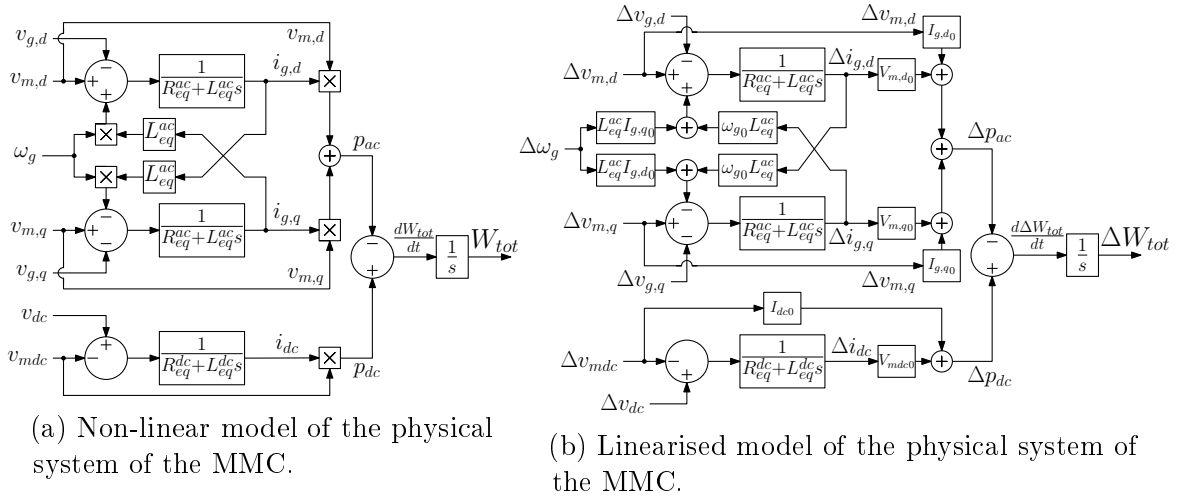


Figure 4.10: Comparison of the non-linear and linearised model of the physical system of the MMC.

Using the same linearisation principle, the linearisation of the control system is also achieved. A block-diagram representation of the complete linearised MMC model, comprising of both the physical and the control system, is obtained and pictured in Figure 4.11.

4.3.2 State-Space Representation of the Linear MMC Model

It was stated in the description of the MMC model of the previous chapter that the MMC allows controlling the energy internally stored in the SMs, and by this means, the DC current. For this reason, the MMC model consists of all the subsystems that compose the standard VSC, with the addition of an outer energy control and an inner

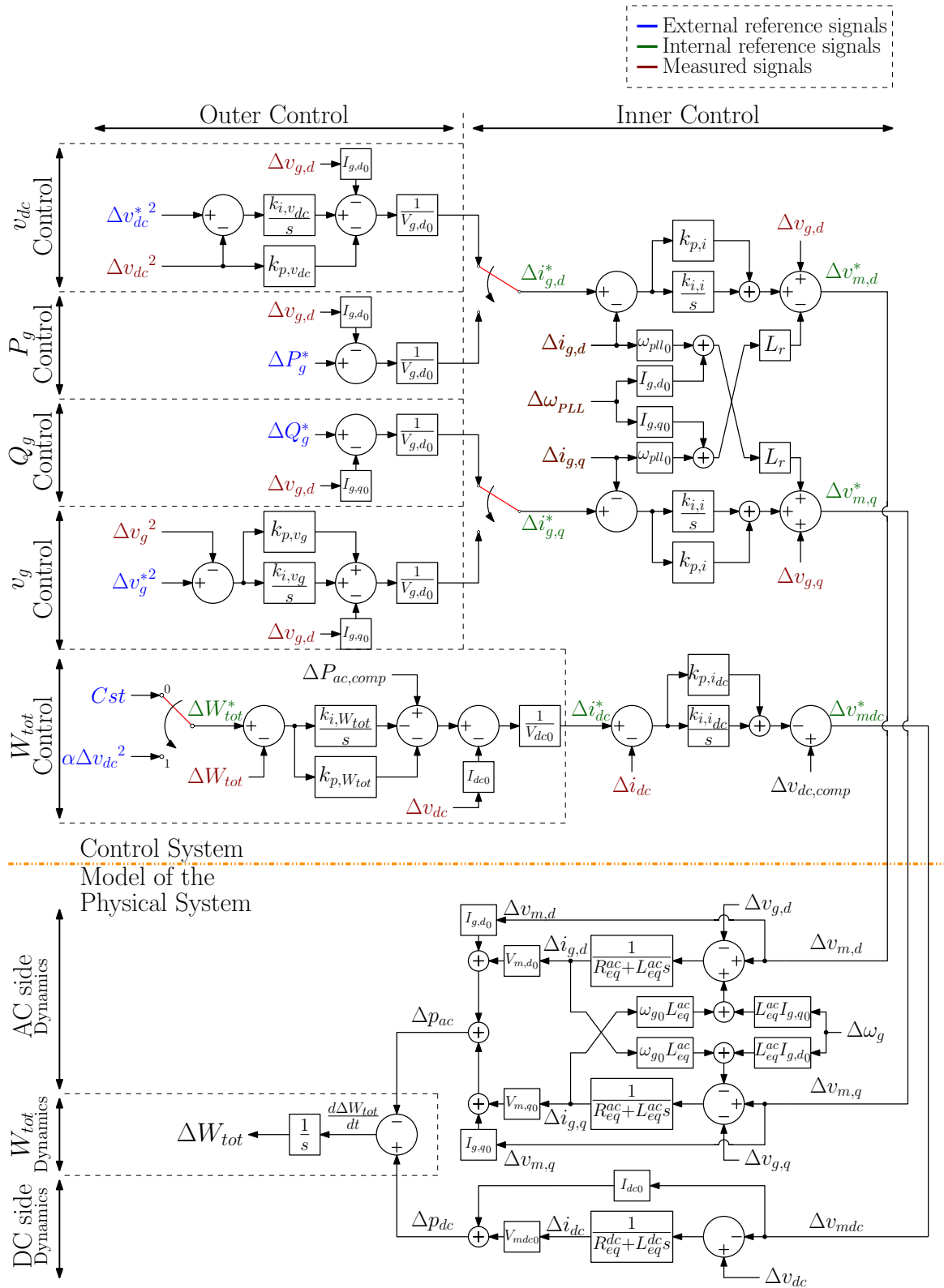


Figure 4.11: Block diagram of the linearised MMC model.

DC current control, as depicted in Figure 4.12 which shows the interconnection static constraints of the MMC subsystems.

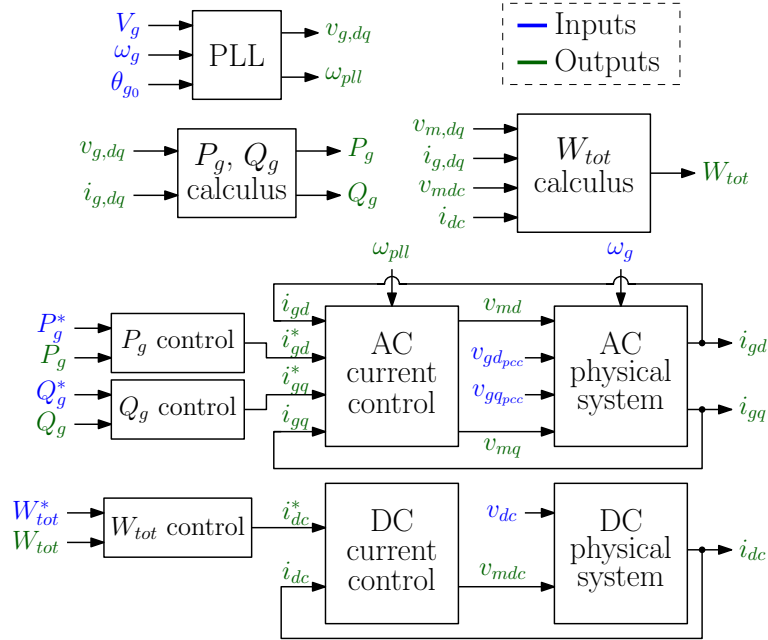


Figure 4.12: Interconnection constraints of the subsystems that constitute the MMC model.

In a similar fashion as for the VSC, the state-space model of the linearised simplified MMC model is obtained by concatenating the state-space representations of all the subsystems according to the methodology described in Appendix D.

4.3.3 Validation of the MMC Models

The simplified MMC model presented in the previous chapter and the state-space model presented in the previous section are validated by comparing their respective behaviour in an MMC-based HVDC link to the behaviour of two detailed MMC models:

- The MMC model type 2 initially presented in [53] and validated with a detailed IGBT-based MMC model in [91]
- The MMC model type 3 which is an AVM derived from the MMC model type 2 in [91, 93] and was the starting point of the derivation of the simplified MMC model presented in the previous chapter.

The HVDC link configuration is illustrated in Figure 4.13. It is to be noted that there are no DC capacitors any longer. The initial operating point is as follows: the

P-mode converter extracts a power of 0.81 p.u. (810 MW) from the DC link and the DC voltage of the Vdc-mode converter is regulated at a voltage level of 1 p.u. (640 kV). The converter parameters are listed in Appendix A. The DC cable is a 200 km DC cable whose model is described in [21, 22]. The state-space model of the HVDC link is automatically generated by a Matlab[®] routine that uses the aggregation method described in Appendix D.

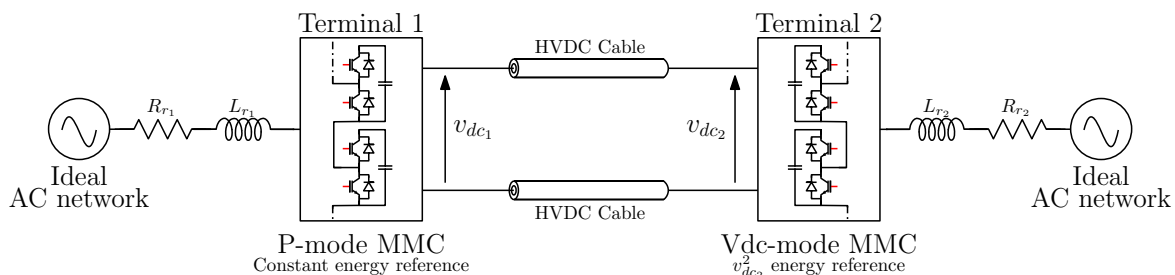


Figure 4.13: Configuration of an MMC-based HVDC link.

In order to observe the behaviour of the system for the simplified MMC model and for the state-space model, several reference changes are scheduled during the simulation. Each quantity has two opposite reference steps so that at the end of the simulation, the HVDC system is back to its original operating point:

- Active power reference of the P-mode converter: +0.2 p.u. at $t = 0.5$ s and -0.2 p.u. at $t = 0.8$ s, as illustrated in Figure 4.14.

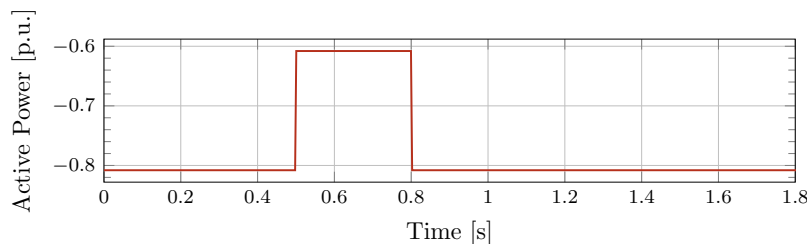


Figure 4.14: Active power reference of the P-mode converter.

- Reactive power reference of the P-mode converter: -0.1 p.u. at $t = 1$ s and +0.1 p.u. at $t = 1.8$ s, as illustrated in Figure 4.15.

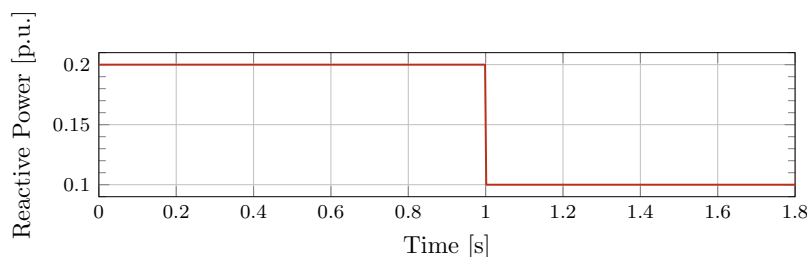


Figure 4.15: Reactive power reference of the P-mode converter.

- DC voltage reference of the Vdc-mode converter: +0.02 p.u. at $t = 1.2$ s and -0.02 p.u. at $t = 1.6$ s, as illustrated in Figure 4.16.

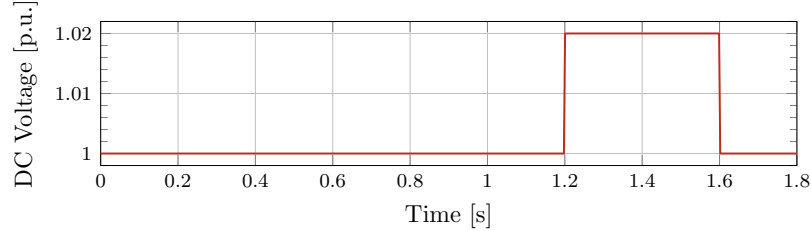
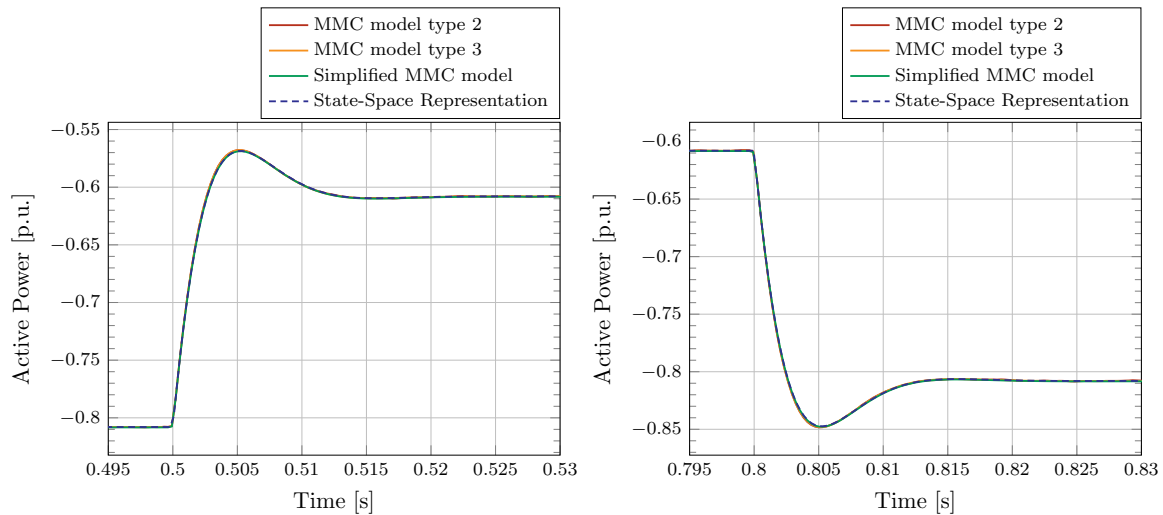


Figure 4.16: DC voltage reference of the Vdc-mode converter.

Figure 4.17 shows the active power response to the active power reference changes of the P-mode converter for the four models. Figures 4.17a and 4.17b offer a zoom on the active power response around the first reference step at $t = 0.5$ s and the second reference step at $t = 0.8$ s. These figures show almost no discernible differences between the four models (i.e. between the behaviour of the MMC-based HVDC link using the MMC model type 2, the MMC model type 3, the simplified MMC model and the state-space model for the MMCs) which validate both the simplified model and the state-space model of the MMC with regard to the active power behaviour of the system. The system 5% response time corresponds to the 100 ms tuning of the controllers of the AC current loop.

Figure 4.18a shows the total energy stored in the SMs of the P-mode converter for the four models. Figure 4.18b offers a zoom on the total stored energy just after the first step of the active power reference. The active power variation causes a fluctuation of the stored energy since the capacitors of the SMs are assuring the energy transfer between the AC and the DC side of the converter, as illustrated by (4.21). However, since the energy reference is set at a constant value of 1 p.u., the energy controller regulates the stored energy at 1 p.u. with a response time corresponding to the energy controller 5% response time tuning of 60 ms. Similarly, Figure 4.18c offers a zoom on the total stored energy just after the first step of the reactive power reference. This reactive power change induces a variation of the grid currents $i_{g,dq}$ and the AC voltages $v_{m,dq}$, hence generating a transient of the instantaneous power on the AC side of the converter, thereby impacting the total stored energy W_{tot} of the MMC according to (4.21). Once again, the difference between the state-space model and the other models is negligible (less than 0.001 p.u.) and the dynamics of the system are properly reproduced. Thus, the simplified MMC model and the state-space model are validated with regard to the total stored energy of the converters of the system.

Figure 4.19a shows the DC voltage at the Vdc-mode converter terminals for the four models. Figure 4.19b offers a zoom on the DC voltage just after the first step



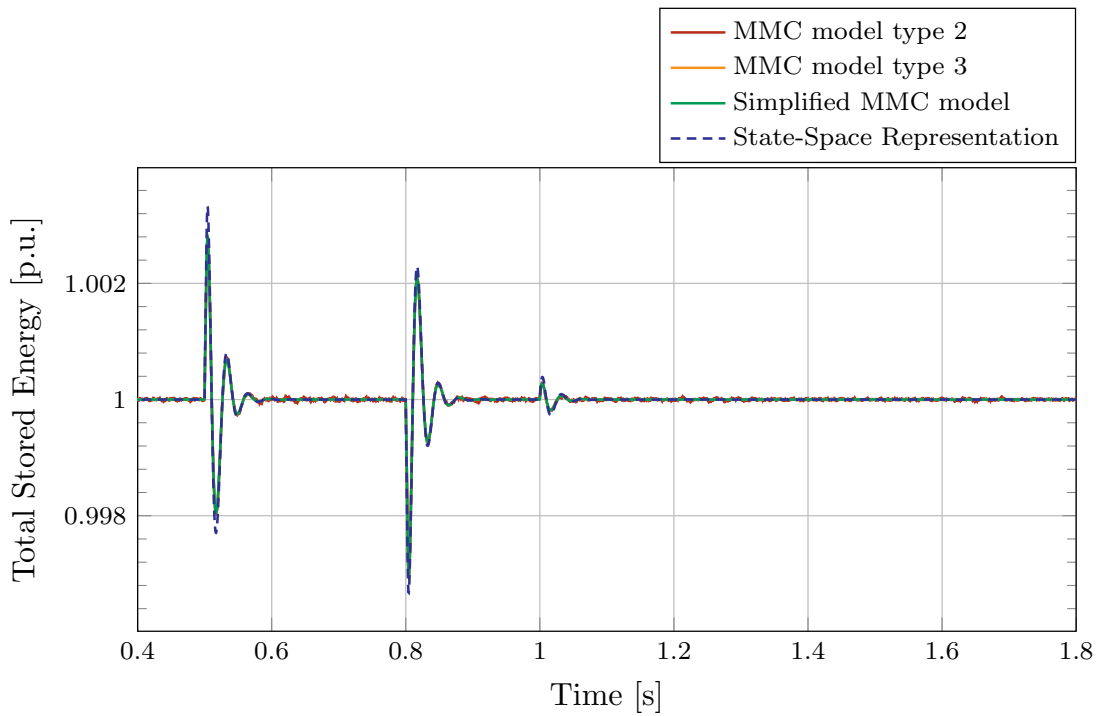
(a) Zoom on the first step of the active power reference.

(b) Zoom on the second step of the active power reference.

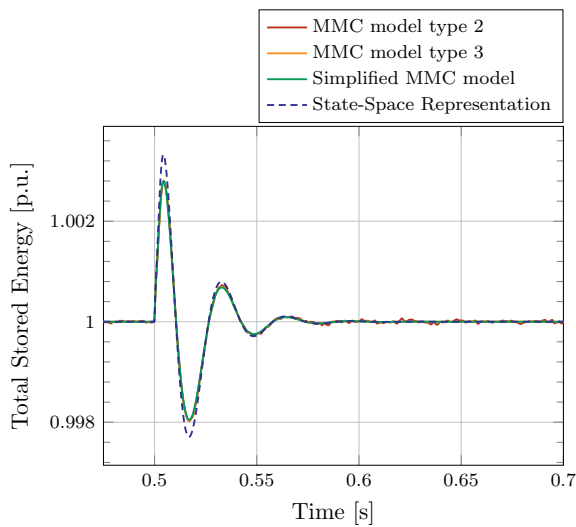
Figure 4.17: Comparison of the active power responses of the P-mode converter for the state-space model, the simplified model, the model type 3 and the model type 2 of an MMC.

of the active power reference. Since the power transiting through the HVDC link is reduced, the DC voltage level decreases before being regulated back to its nominal value by the Vdc-mode converter with a 5% response time corresponding to the 100 ms tuning of the DC voltage controller. Figure 4.19c offers a zoom on the DC voltage just after the first step of the DC voltage reference of 0.02 p.u. This time, the Vdc-mode converter regulates the DC voltage to the desired value. Once again, in both figures, the state-space model and the simplified MMC behaviours correspond to the detailed models and the dynamics of the system are properly reproduced. Thus, these models are validated with regard to the DC voltage behaviour of the system.

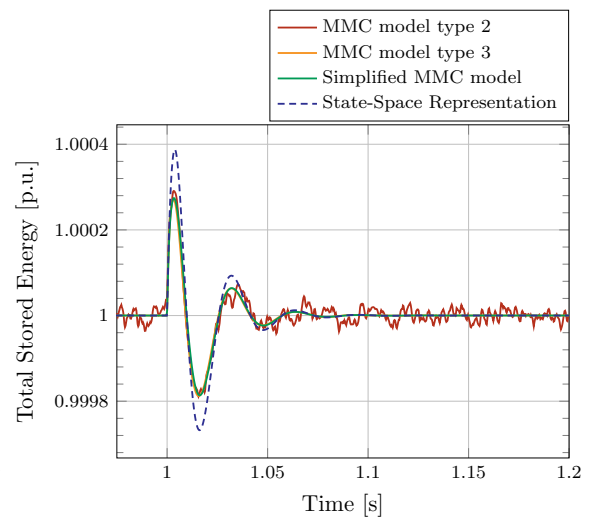
Since the DC current loop of the MMC is cascaded with the energy control loop, it is also interesting to visualise the DC current behaviour. Figure 4.20a shows the DC current output of the P-mode converter for the four models. Figure 4.20b offers a zoom on the DC current just after the first step of the active power reference. Since the power transiting through the HVDC link is being reduced while the DC voltage level is maintained at the same value, the DC current follows the active power reference step but with the transient dynamics of the DC current loop. Figure 4.20c offers a zoom on the DC current just after the first step of the DC voltage reference. This time, the DC voltage increases while the active power is regulated at a constant value, so the DC



(a) Total stored energy behaviour for the entire duration of the simulation.

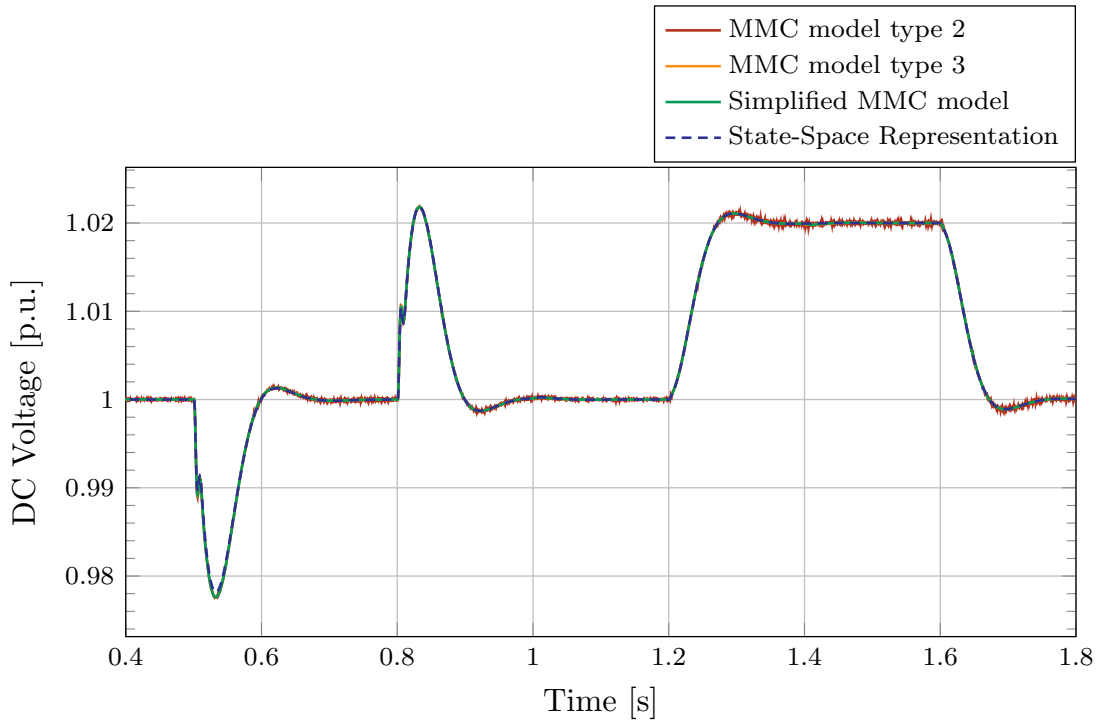


(b) Zoom on the total stored energy just after the first step of the active power reference.

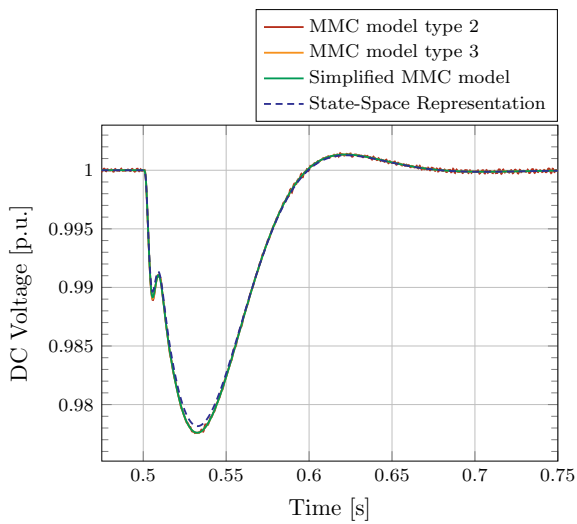


(c) Zoom on the total stored energy just after the first step of the reactive power reference.

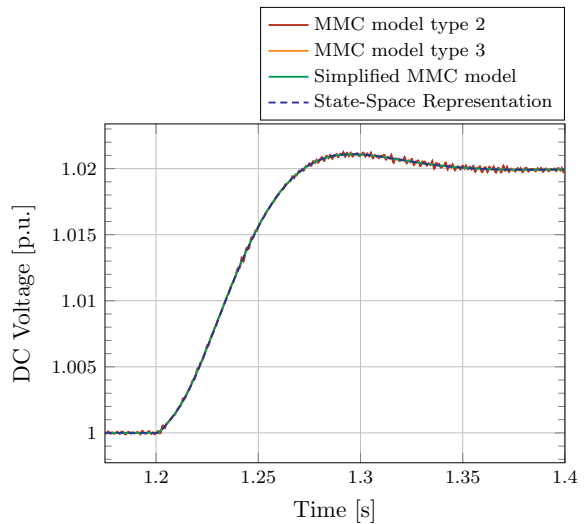
Figure 4.18: Comparison of the total stored energy of the P-mode converter for the state-space model, the simplified model, the model type 3 and the model type 2 of an MMC.



(a) DC voltage behaviour for the entire duration of the simulation.



(b) Zoom on the DC voltage just after the first step of the active power reference.

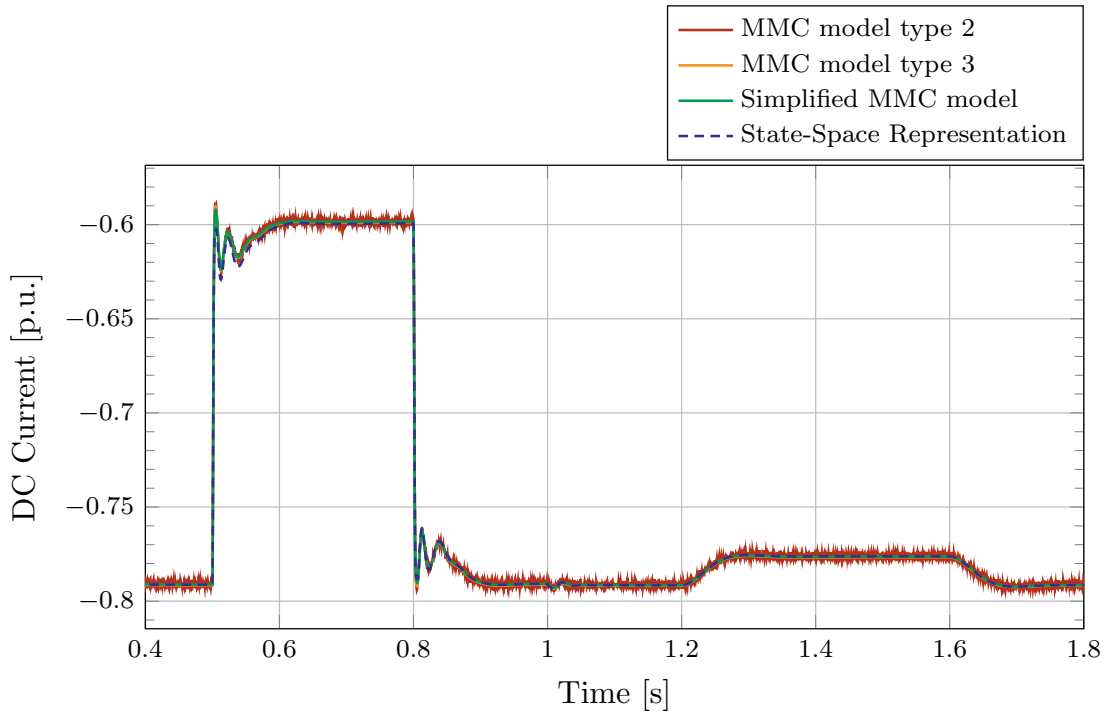


(c) Zoom on the DC voltage just after the first step of the DC voltage reference.

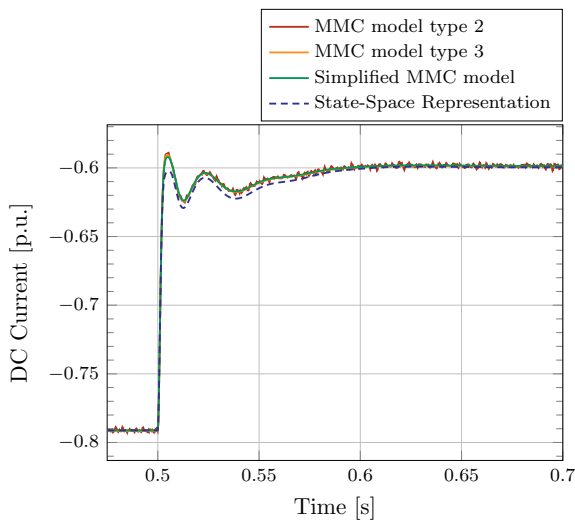
Figure 4.19: Comparison of the DC voltage of the V_{dc}-mode converter for the state-space model, the simplified model, the model type 3 and the model type 2 of an MMC.

current is decreasing to compensate for the DC voltage increase. A small deviation of the state-space model by comparison to the other models can be observed during the transient of the DC current in Figure 4.20b and is explained by the linearising process. In both figures, the state-space model and the simplified MMC behaviours correspond to the detailed models and the dynamics of the system are properly reproduced. Thus, these models are validated with regard to the DC current behaviour of the system.

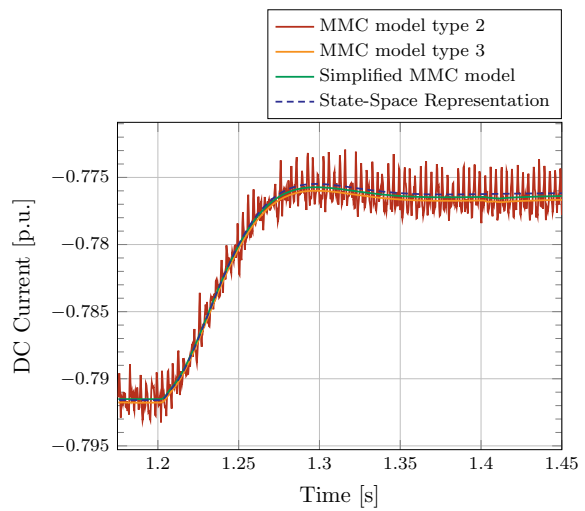
Every aspect of the HVDC link is validated, thus validating both the simplified MMC model and the state-space representation of the MMC. A particular attention has to be paid to the tuning of the controllers in order to avoid undesired oscillations. A better tuning of the controllers can be performed by observing the eigenvalues corresponding to the mode generating the undesired oscillations and stabilising the system by doing a parametric sweep of the controller gains, as illustrated in [24].



(a) DC current behaviour for the entire duration of the simulation.



(b) Zoom on the DC current just after the first step of the active power reference.



(c) Zoom on the DC current just after the first step of the DC voltage reference.

Figure 4.20: Comparison of the DC current generated by the P-mode converter for the state-space model, the simplified model, the model type 3 and the model type 2 of an MMC.

4.4 Modal Analyses of an HVDC Link

The state-space representation of both the VSC and the MMC have been validated. They can now be used to study the dynamics of an HVDC link by means of a modal analysis in order to identify and assess the impact of the different modes on the global behaviour of the HVDC transmission system. In this section, the modal analysis of both a VSC-based HVDC link and an MMC-based HVDC link are achieved and the main differences between the two are emphasised and explained.

4.4.1 HVDC link with VSCs

The considered HVDC link is identical to the HVDC link of Section 4.2.3: it consists of two converters connected to each other by two cables (one for the positive pole and one for the negative pole). One converter, the *Vdc-mode* converter, controls the DC voltage. The other converter, the *P-mode* converter, controls the active power transmitted by the HVDC transmission. The system operating point is as follows: the P-mode converter injects a power of 0.6 p.u. (600 MW) into the DC link and the DC voltage of the Vdc-mode converter is regulated at a voltage level of 1 p.u. (640 kV).

The cable model used in this section, called the Fitted PI-section of a cable, is a 200 km long, improved classical PI-section with parallel branches, as depicted in Figure 4.21 and described in [21, 22]. A judicious choice of the component values used in the parallel branches enables this simple model to fit the frequency response of a more detailed model such as the wide-band model [83]. The component values are automatically determined by a Matlab[®] fitting algorithm, depending on the number of parallel branches desired by the user [57, 56]. The component values of the three parallel branches cable model used in this section are described in Table 4.1. The impact of the cable model on the system will be thoroughly analysed in the next chapter as the impact of different cable models on the results of a Singular Value Decomposition (SVD) analysis will be studied.

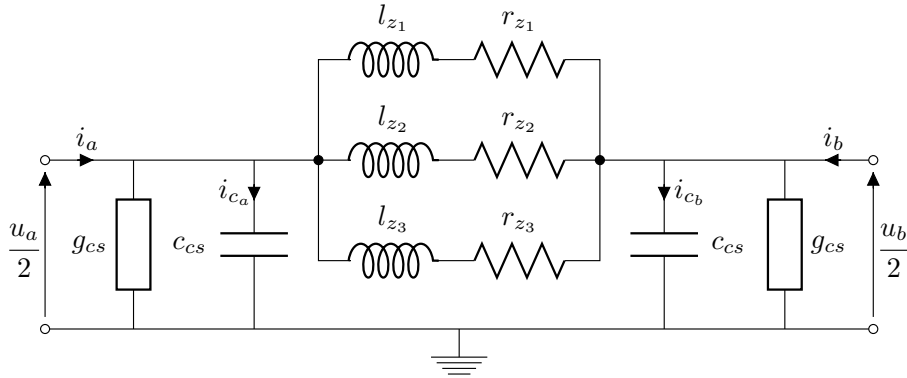


Figure 4.21: Fitted PI-section of a cable [21, 22].

$r_{z_1} = 1.1724 \cdot 10^{-1} \Omega/\text{km}$	$l_{z_1} = 2.2851 \cdot 10^{-4} \text{ H}/\text{km}$
$r_{z_2} = 8.2072 \cdot 10^{-2} \Omega/\text{km}$	$l_{z_2} = 1.5522 \cdot 10^{-3} \text{ H}/\text{km}$
$r_{z_3} = 1.1946 \cdot 10^{-2} \Omega/\text{km}$	$l_{z_3} = 3.2942 \cdot 10^{-3} \text{ H}/\text{km}$
$g_{cs} = 7.6333 \cdot 10^{-11} \text{ S}/\text{km}$	$c_{cs} = 1.9083 \cdot 10^{-7} \text{ F}/\text{km}$

Table 4.1: Component values of the fitted PI cable.

The state-space representation of a VSC-based HVDC link using the VSC state-space models derived in the previous section, and the above cable model, results in a 18×18 state matrix A , a 18×14 input matrix B , a 36×18 output matrix C and a 36×14 feed-forward matrix D . The 18 eigenvalues of the system are obtained and described in Table 4.2 where they are categorised into 7 groups (A, B, ..., G). Table 4.2 also specifies the frequency of the modes associated to the eigenvalues and their damping ratio. Finally, using the participation matrix definition of [77] and adopted in [67], which allows the identification of the relation between the eigenvalues and the state variables and to find out the most valuable state variables for certain eigenvalues, the dominant states of each group of eigenvalues are listed. In the rest of this chapter, the states $i_{z_{1,2,3}}$ correspond to the current in the parallel branches of the DC cable model, and each state defined by x_{\dots} corresponds to the output of the integral action of a controller in the state-space model (e.g. $x_{i_{gd_1}}$ corresponds to the output of the integral action of the d-axis controller of the inner current loop). The results are consistent with the work of [23].

The eigenvalues of the system are arranged into the following 7 groups:

		Eigenvalues	Freq. (Hz)	Damp. ratio	Dominant States	
• Group A:	A	$\lambda_{1,2}$	$-127.4 \pm j336.1$	53.5	0.354	$i_{z_1}, i_{z_2}, x_{v_{dc2}}, v_{dc2}, x_{i_{gd_2}}, i_{gd_2}$

The complex conjugate eigenvalues $\lambda_{1,2}$ correspond to modes that are strongly related to the power regulation in the system. They result from an interaction between the d-axis control loops of the Vdc-mode converter ($x_{v_{dc2}}$ is the integrator state variable of the DC voltage controller and $x_{i_{gd2}}$ is the integrator state variable of the d-axis inner current controller) and the DC cable. They are the determining factor in the system stability as they are the only eigenvalues that show a possible positive real part (when $tr_{5\%,v_{dc}} < 20$ ms), as illustrated by Figure 4.24. Besides, these eigenvalues are the only ones which are really dependent on the operating point of the system.

- Group B:

Eigenvalues			Freq. (Hz)	Damp. ratio	Dominant States
B	λ_3	-365.6	0	-	i_{z1}, i_{gd2}

The eigenvalue λ_3 corresponds to an interaction between the Vdc-mode converter current controller and the DC cable parallel branches (with an increased sensitivity to r_{z2}, l_{z1} and l_{z2}). This mode is moderately impacted by the parameter sweep.

- Group C:

Eigenvalues			Freq. (Hz)	Damp. ratio	Dominant States
C	$\lambda_{4,5}$	$-130.2 \pm j64.8$	10.3	0.895	$i_{z2}, i_{z3}, x_{v_{dc2}}, v_{dc1}, v_{dc2}, x_{i_{gd1}}$

In a similar fashion as $\lambda_{1,2}$, the complex conjugate eigenvalues $\lambda_{4,5}$ correspond to modes that are strongly related to the power flows in the system. They result from an interaction between the d-axis control of the P-mode converter and the DC cable, but are also influenced by DC voltage controller of the Vdc-mode converter. By opposition to $\lambda_{1,2}$, these eigenvalues can never have a positive real part with the parameter sweep. Their associated time constant is mildly impacted by the parameter sweep (except for the values that lead to an unstable system).

- Group D:

Eigenvalues			Freq. (Hz)	Damp. ratio	Dominant States
D	$\lambda_{6,7}$	$-29.5 \pm j36.9$	5.87	0.624	$i_{z2}, i_{z3}, x_{v_{dc2}}, v_{dc1}, v_{dc2}$

The complex conjugate $\lambda_{6,7}$ are strongly related to the DC voltage of each converter. In fact, they correspond to the poles of the DC voltage controller of the Vdc-mode converter and show a 5% response time of 100 ms. Their associated mode is the most influential mode on the DC voltage dynamics (i.e. these eigenvalues are the main driver behind the DC voltage dynamics, as detailed below).

- Group E:

Eigenvalues			Freq. (Hz)	Damp. ratio	Dominant States
E	λ_8	-16.3	0	-	$i_{z_1}, i_{z_2}, i_{z_3}, v_{dc_1}, v_{dc_2}$

The eigenvalue λ_8 is associated with the voltage drop across the DC line. It is not impacted at all by the parameter sweep and mostly depends on the intrinsic DC cable parameters. In fact, this eigenvalue is equal to $\frac{-R_{eq,cable}}{L_{eq,cable}}$.

- Group F:

Eigenvalues			Freq. (Hz)	Damp. ratio	Dominant States
F	$\lambda_{9,\dots,14}$	$-210.1 \pm j214.2$	34.1	0.700	$x_{i_{gd_1}}, i_{gd_1}, x_{i_{gq_1}}, i_{gq_1}, x_{i_{gq_2}}, i_{gq_2}$

The eigenvalue $\lambda_{9,\dots,14}$ correspond to the interaction between the d and q-axis outer control loops and the inner current loop of the P-mode converter, and of the q-axis outer control loops and the inner current loop of the Vdc-mode converter (the interaction between the d-axis outer loop (DC voltage control) and the inner current loop of the Vdc-mode converter being described by $\lambda_{1,2}$). Their associated 5% response time of 14.3 ms is close to the tuning of the inner control loop (tuned for 10 ms 5% response time).

- Group G:

Eigenvalues			Freq. (Hz)	Damp. ratio	Dominant States
G	$\lambda_{15,\dots,18}$	-1000	0	-	$x_{pll_1}, x_{pll_2}, \theta_{pll_1}, \theta_{pll_2}$

Finally, the eigenvalues of the group G are associated with the tuning of the PLLs.

Eigenvalues			Freq. (Hz)	Damp. ratio	Dominant States
A	$\lambda_{1,2}$	$-127.4 \pm j336.1$	53.5	0.354	$i_{z_1}, i_{z_2}, x_{v_{dc_2}}, v_{dc_2}, x_{i_{gd_2}}, i_{gd_2}$
B	λ_3	-365.6	0	-	i_{z_1}, i_{gd_2}
C	$\lambda_{4,5}$	$-130.2 \pm j64.8$	10.3	0.895	$i_{z_2}, i_{z_3}, x_{v_{dc_2}}, v_{dc_1}, v_{dc_2}, x_{i_{gd_2}}$
D	$\lambda_{6,7}$	$-29.5 \pm j36.9$	5.87	0.624	$i_{z_2}, i_{z_3}, x_{v_{dc_2}}, v_{dc_1}, v_{dc_2}$
E	λ_8	-16.3	0	-	$i_{z_1}, i_{z_2}, i_{z_3}, v_{dc_1}, v_{dc_2}$
F	$\lambda_{9,\dots,14}$	$-210.1 \pm j214.2$	34.1	0.700	$x_{i_{gd_1}}, i_{gd_1}, x_{i_{gq_1}}, i_{gq_1}, x_{i_{gq_2}}, i_{gq_2}$
G	$\lambda_{15,\dots,18}$	-1000	0	-	$x_{pll_1}, x_{pll_2}, \theta_{pll_1}, \theta_{pll_2}$

Table 4.2: Eigenvalue characteristics of the VSC-based HVDC link.

The eigenvalues listed in Table 4.2 are represented in the complex plane in Figure 4.22 and are categorised into four different entities: the eigenvalues that are more impacted by the states of the DC cable, the eigenvalues that are more influenced by the states of the P-mode converter (P-mode converter: VSC1), the eigenvalues that are more influenced by the states of the Vdc-mode converter (Vdc-mode converter: VSC2), and finally those that are not clearly influenced by a single one of the previous three. In brief, each eigenvalue has been placed in one of these four entities with regards to the states they are the more influenced by, according to the participation matrix. Figure 4.23 shows the overall participation of each entity (i.e. the DC cable, the VSC1 or the VSC2) to the eigenvalues of the system.

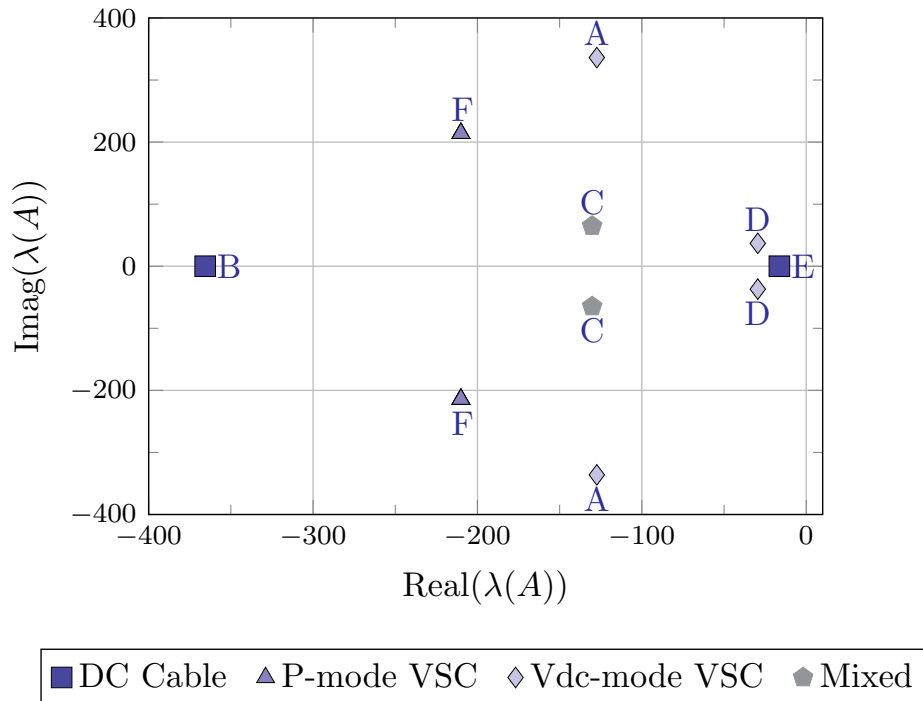


Figure 4.22: Eigenvalues representation of the VSC-based HVDC link.

In order to identify the modes that influence the most the DC voltage dynamics, a root locus of the state-space model of the VSC-based HVDC link is performed for a sweep of the DC voltage controller response time from 1 ms to 1 s (see Figure 4.24). At first, it is observed that the system is not stable when the DC voltage controller of the Vdc-mode converter is designed for a 5% DC voltage response time smaller than 15 ms, acknowledging the fact that the inner current loop controllers are designed to have a response time of 10 ms. Indeed, for smaller values of the DC voltage response time, the eigenvalues corresponding to the group A show a positive real part.

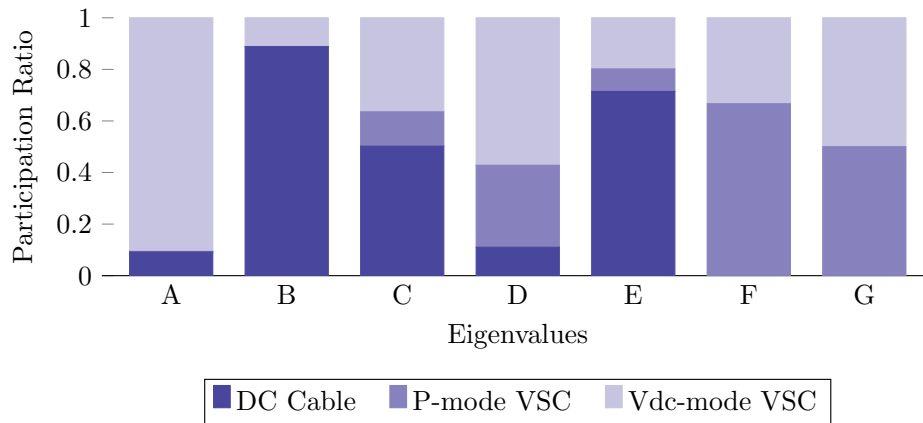


Figure 4.23: Participation ratio of the P-mode VSC, the Vdc-mode VSC and the DC cable to the eigenvalue groups (A,B,...,G) of the complete system.

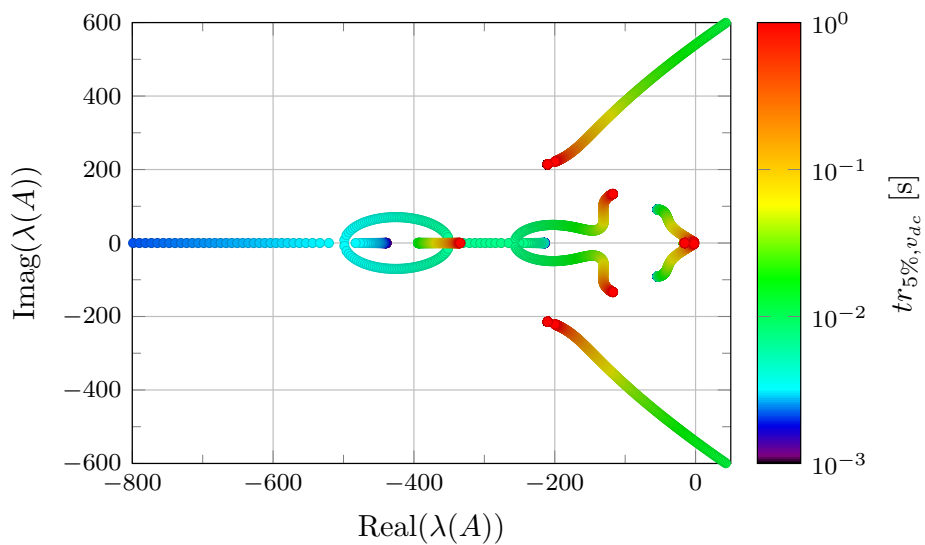


Figure 4.24: Eigenvalues trajectories of the VSC-based HVDC link for a sweep of the DC voltage controller response time.

Figure 4.25 shows the DC voltage response to a reference step for different values of the 5% response time of the DC voltage controller. For $tr_{5\%,v_{dc}} = 20$ ms, which is just above the stability threshold of 15 ms obtained in Figure 4.24, some oscillations can be observed. These oscillations have a frequency of 76.6 Hz corresponding to the frequency of the eigenvalues $\lambda_{1,2}|_{tr=20ms} = -40.8 \pm j481$ which are interacting with the main DC voltage mode. These interactions cannot be observed for greater values of the 5% response time of the DC voltage controller, validating the widely accepted presupposition that if the inner control loop is 10 times faster than the outer control loop, any undesired interaction is avoided.

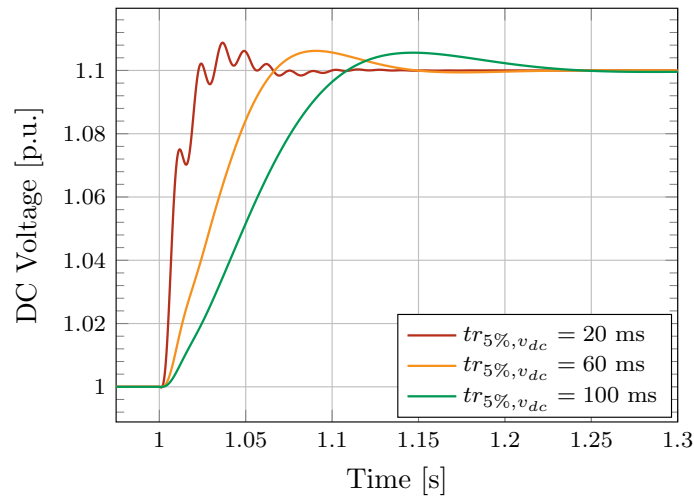


Figure 4.25: DC voltage response to a reference step of 0.1 p.u. for different values of the 5% response time of the DC voltage controller, for the VSC-based HVDC link.

4.4.2 HVDC link with MMCs

The VSC state-space models of the previous HVDC link are now replaced with the state-space models of MMCs. The control strategy remains the same: the converter 1 controls the active power transmitted by the DC link while the converter 2 regulates the DC voltage. However, the P-mode converter does not share its energy with the DC link (i.e. its stored energy reference is a constant) while the Vdc-mode converter does share its energy with the DC link (i.e. its stored energy reference is proportional to the DC voltage level). The HVDC link configuration is described by Figure 4.13 in the previous section and the system operating point is as follows: the P-mode converter injects a power of 0.6 p.u. (600 MW) into the DC link and the DC voltage of the Vdc-mode converter is regulated at a voltage level of 1 p.u. (640 kV). This results in a

30×30 state matrix A , a 30×15 input matrix B , a 44×30 output matrix C and a 44×15 feed-forward matrix D .

The 30 eigenvalues of the system are listed in Table 4.3. Their respective frequencies, damping ratios and dominant states are described as well. Once again, the eigenvalues are arranged into 15 groups ranging from A to O. Figure 4.26 shows the respective influence of the Vdc-mode converter, the P-mode converter and the DC cable on the different eigenvalue groups. Figure 4.27 is a representation of the eigenvalue trajectories for a sweep of the P-mode MMC power output (i.e. of the HVDC link operating point) from -1 p.u. to 1 p.u., which shows that some modes are not dependent on the operating point (these modes usually correspond to modes that are related to the system parameters such as the DC cable components or the control loops' gains), while others are greatly impacted by the operating point (these modes are generally related to the physics of the system). Finally, Figure 4.28 offers a representation of the eigenvalue trajectories for a sweep of the response time tuning of the DC controller of the Vdc-mode converter in order to identify the main modes that drive the system internal dynamics.

The eigenvalues of the system are arranged into the following 15 groups:

- Group A:

Eigenvalues			Freq. (Hz)	Damp. ratio	Dominant States
A	$\lambda_{1,2}$	$-172.3 \pm j1596$	254	0.107	$i_{z_1}, i_{dc_2}, i_{gd_2}, v_{dc_1}, v_{dc_2}$

This group corresponds to modes that are strongly related to the DC voltage of the Vdc-mode converter and thus with regulating the power flow in the system, and is the equivalent of the group A of the VSC-based HVDC link. These eigenvalues result from an interaction between the d-axis control loops of the Vdc-mode converter and the DC cable. They determine the system stability since they show a positive real part if the response time parameter used to tune the DC voltage controller of the Vdc-mode converter is below 20.2 ms and no other eigenvalue can have a positive real part. As shown in Figure 4.27, the eigenvalues of this group are moderately influenced by the operating point of the system.

- Group B:

Eigenvalues			Freq. (Hz)	Damp. ratio	Dominant States
B	$\lambda_{3,4}$	$-737.3 \pm j627.9$	100	0.761	$i_{z_1}, i_{dc_1}, i_{dc_2}, v_{dc_2}$

The fact that the eigenvalue pair $\lambda_{3,4}$ does not vary with the sweep of the DC voltage controller response time (see Figure 4.28) indicates that these eigenvalues correspond to the DC current loop of the P-mode converter. Because the DC current loop is cascaded with the energy control loop of the P-mode converter (whose reference is a constant), this mode is not impacted by the sweep of the

Eigenvalues			Freq. (Hz)	Damp. ratio	Dominant States
A	$\lambda_{1,2}$	$-172.3 \pm j1596$	254	0.107	$i_{z_1}, i_{dc_2}, i_{gd_2}, v_{dc_1}, v_{dc_2}$
B	$\lambda_{3,4}$	$-737.3 \pm j627.9$	100	0.761	$i_{z_1}, i_{dc_1}, i_{dc_2}, v_{dc_2}$
C	$\lambda_{5,6}$	$-661.5 \pm j410.2$	65.3	0.850	$i_{z_2}, i_{z_3}, W_{tot_2}, v_{dc_1}, x_{i_{dc_1}}, x_{i_{dc_2}}, x_{i_{gd_2}}, i_{dc_2}$
D	$\lambda_{7,8}$	$-160.5 \pm j551.0$	87.7	0.280	$i_{z_2}, i_{z_3}, W_{tot_1}, x_{W_{tot_2}}, v_{dc_1}, v_{dc_2}, x_{i_{dc_1}}, x_{i_{gd_2}}, x_{i_{dc_2}}, i_{gd_2}$
E	λ_9	-524.9	0	—	$x_{i_{gd_2}}, W_{tot_2}, x_{i_{dc_2}}, x_{W_{tot_2}}$
F	λ_{10}	-500.8	0	—	$i_{z_2}, x_{i_{dc_1}}, x_{W_{tot_1}}$
G	$\lambda_{11,12}$	$-236.4 \pm j137.0$	21.8	0.865	$i_{z_2}, x_{i_{gd_2}}, W_{tot_2}, x_{i_{dc_2}}, x_{i_{dc_1}}, x_{v_{dc_2}}, x_{W_{tot_2}}$
H	λ_{13}	-319.3	0	—	$i_{z_2}, W_{tot_1}, x_{i_{dc_1}}, x_{W_{tot_1}}, W_{tot_2}, x_{v_{dc_2}}$
I	λ_{14}	-139.6	0	—	$i_{z_3}, W_{tot_1}, x_{i_{dc_1}}, x_{W_{tot_1}}, W_{tot_2}$
J	λ_{15}	-15.7	0	—	$i_{z_2}, i_{z_3}, W_{tot_1}$
K	$\lambda_{16,17}$	$-22.2 \pm j41.3$	6.6	0.474	$W_{tot_1}, x_{i_{dc_1}}, x_{W_{tot_1}}, x_{i_{gd_2}}, W_{tot_2}, x_{i_{dc_2}}, x_{v_{dc_2}}, x_{W_{tot_2}}, W_{filt_1}$
L	$\lambda_{18,19}$	$-64.9 \pm j72.8$	11.6	0.666	W_{filt_1}, W_{filt_2}
M	λ_{20}	-46.5	0	—	W_{filt_1}, W_{filt_2}
N	$\lambda_{21,\dots,26}$	$-216.2 \pm j208.0$	33.1	0.721	$x_{i_{gd_1}}, i_{gd_1}, x_{i_{gq_1}}, i_{gq_1}, x_{i_{gq_2}}, i_{gq_2}$
O	$\lambda_{27,\dots,30}$	-1000	0	—	$x_{pll_1}, x_{pll_2}, \theta_{pll_1}, \theta_{pll_2}$

Table 4.3: Eigenvalue characteristics of the MMC-based HVDC link.

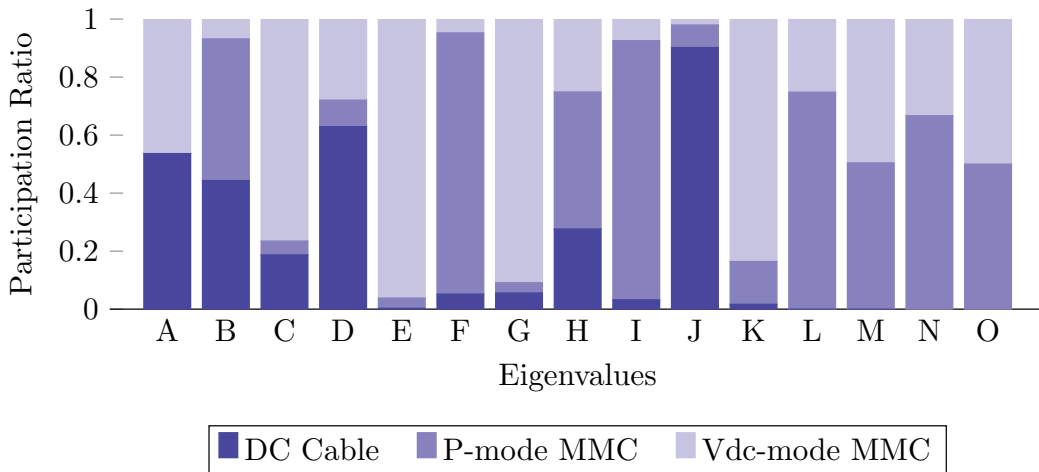


Figure 4.26: Participation ratio of the P-mode MMC, the Vdc-mode MMC and the DC cable to the Eigenvalues of the complete system.

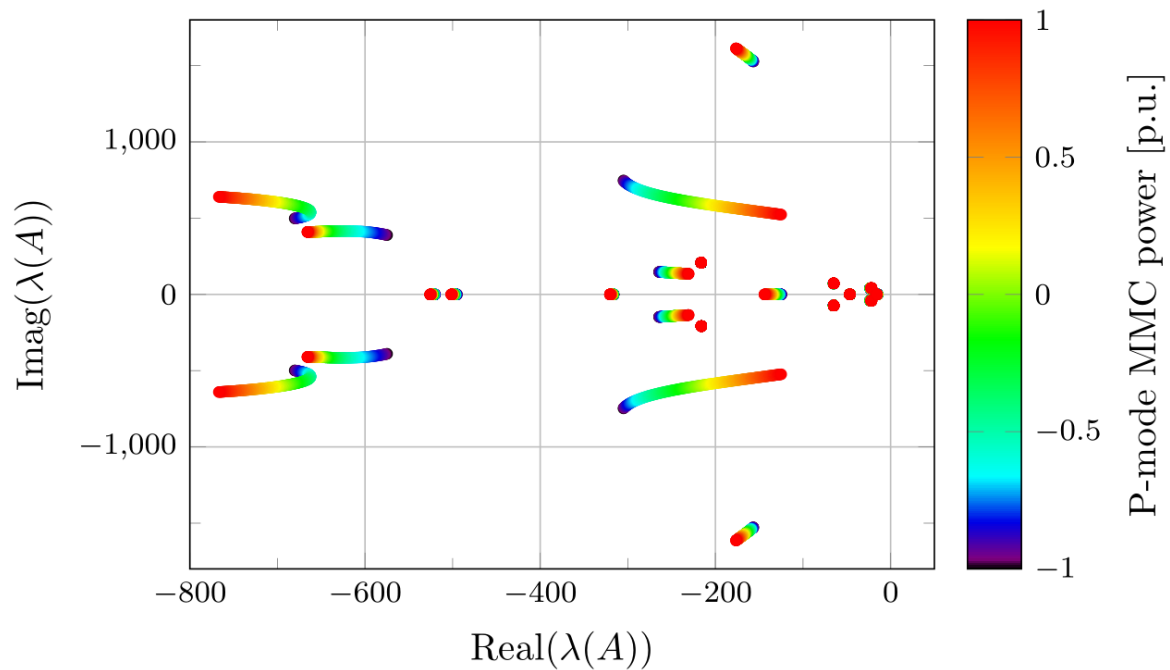


Figure 4.27: Eigenvalues trajectories of the MMC-based HVDC link for a sweep of the power injected/withdrawn from the DC link by the P-mode MMC (i.e. for a sweep of the system operating point).

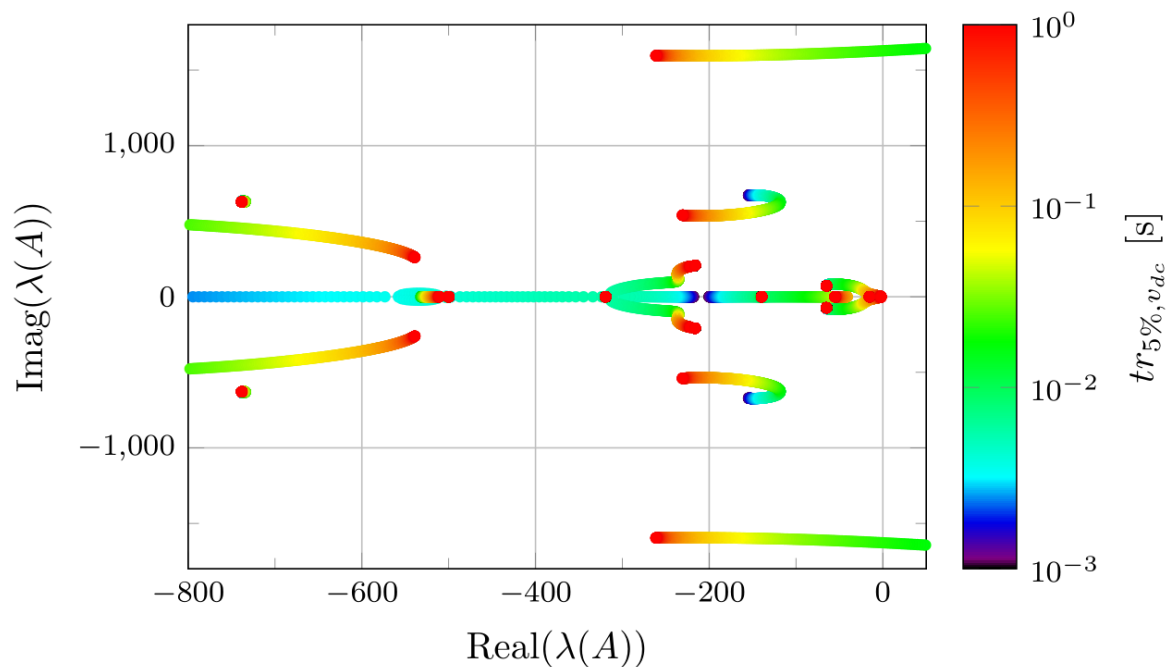


Figure 4.28: Eigenvalues trajectories of the MMC-based HVDC link for a sweep of the DC voltage controller response time.

DC voltage controller response time. In fact, its own associated response time corresponds to the 4 ms settling time of the DC current controller. However, because the stored energy is directly linked to the power output of the P-mode converter, these eigenvalues are highly dependent on the operating point of the system, as shown in Figure 4.27.

		Eigenvalues		Freq. (Hz)	Damp. ratio	Dominant States
• Group C:	C	$\lambda_{5,6}$	$-661.5 \pm j410.2$	65.3	0.850	$i_{z2}, i_{z3}, W_{tot2}, v_{dc1}, x_{idc1}, x_{idc2}, x_{igd2}, i_{dc2}$

Similarly to the eigenvalue pair of group B for the P-mode converter, $\lambda_{5,6}$ correspond to the DC current loop of the Vdc-mode converter. In fact, the 5% response time of $\lambda_{5,6}$ corresponds to the dynamics of the DC current loop, as the eigenvalues response time of 4.5 ms is close to the 4 ms settling time of the DC current controller. This eigenvalue pair is, however, greatly affected by the sweep of the DC voltage controller response time. This is explained by the reference of the energy control loop being set to the square of the DC voltage (i.e. $W_{tot}^* = v_{dc2}^2$) which is directly affected by the sweep of the DC voltage controller response time, and since the DC current loop is cascaded with the energy control loop, $\lambda_{5,6}$ is equally impacted by the parameter sweep. Additionally, since the stored energy is directly linked to the power output of the Vdc-mode converter, this mode is highly dependent on the operating point of the system, as shown in Figure 4.27.

		Eigenvalues		Freq. (Hz)	Damp. ratio	Dominant States
• Group D:	D	$\lambda_{7,8}$	$-160.5 \pm j551.0$	87.7	0.280	$i_{z2}, i_{z3}, W_{tot1}, x_{W_{tot2}}, v_{dc1}, v_{dc2}, x_{idc1}, x_{igd2}, x_{idc2}, i_{gd2}$

This group is similar to group A but for the P-mode converter: it corresponds to modes that are strongly related with the DC voltage of the P-mode converter and thus with the value of the DC current transiting through the HVDC link. This eigenvalue pair shows a curved variation with the sweep of the DC voltage controller response time but plays no role in the system stability. Figure 4.29a shows the MMC2 DC voltage behaviour just after the first step of an active power reference of MMC1. The observed oscillations at 88 Hz correspond to the frequency of $\lambda_{7,8}$, illustrating the fact that their associated modes impact the DC voltage dynamics during power variations in the DC link. Additionally, Since these eigenvalues are directly related to the power output of the P-mode MMC,

they are the most volatile eigenvalues with regard to the operating point of the system, as shown in Figure 4.27.

- Group E:

Eigenvalues			Freq. (Hz)	Damp. ratio	Dominant States
E	λ_9	-524.9	0	-	$x_{i_{gd2}}, W_{tot2}, x_{i_{dc2}}, x_{W_{tot2}}$

The mode associated to λ_9 describes the interaction between the stored energy of the Vdc-mode MMC and the AC and DC physical systems. This interaction is linked to the energy control loop using the square of the DC voltage as a reference and generating the DC current reference, hence sharing its energy with the DC bus. This is supported by the fact that Figure 4.28 shows that λ_9 increases with the sweep of the DC voltage controller response time. However, this mode is not dependent on the operating point of the system as its dynamics are related to the DC voltage controller which is not affected by the operating point.

- Group F:

Eigenvalues			Freq. (Hz)	Damp. ratio	Dominant States
F	λ_{10}	-500.8	0	-	$i_{z2}, x_{i_{dc1}}, x_{W_{tot1}}$

Similarly, the mode associated to λ_{10} describes the interaction between the stored energy of the P-mode MMC and the AC and DC physical systems. However, since the P-mode MMC does not share its stored energy with the DC bus (its energy reference is a constant), this eigenvalue is not affected by the parameter sweep, as illustrated in Figure 4.28. Additionally, this mode is not dependent on the operating point of the system as the P-mode MMC stored energy dynamics are dissociated from the rest of the system.

- Group G:

Eigenvalues			Freq. (Hz)	Damp. ratio	Dominant States
G	$\lambda_{11,12}$	$-236.4 \pm j137.0$	21.8	0.865	$i_{z2}, x_{i_{gd2}}, W_{tot2}, x_{i_{dc2}}, x_{i_{dc1}}, x_{v_{dc2}}, x_{W_{tot2}}$

The eigenvalues of this group are associated to the d-axis AC current control of the Vdc-mode converter and their corresponding 5% response time is close to the 10 ms tuning of the inner AC current loop. As shown in Figure 4.27, the eigenvalues of this group are moderately influenced by the operating point of the system.

- Groups H and I:

Eigenvalues			Freq. (Hz)	Damp. ratio	Dominant States
H	λ_{13}	-319.3	0	-	$i_{z2}, W_{tot1}, x_{i_{dc1}}, x_{W_{tot1}}, W_{tot2}, x_{v_{dc2}}$
I	λ_{14}	-139.6	0	-	$i_{z3}, W_{tot1}, x_{i_{dc1}}, x_{W_{tot1}}, W_{tot2}$

The modes associated to λ_{13} and λ_{14} correspond to interactions between the DC current control loop of the P-mode MMC (and also, but to a lower extent, the DC current control loop of the Vdc-mode MMC) and the parallel branches of the DC cable. As shown in Figure 4.28, they are not impacted by the parameter sweep because the P-mode converter is not impacted by the parameter sweep as it is not sharing its energy with the DC bus and injects a constant power into the HVDC link. Because these eigenvalues only depend on the system physical components and the control loop parameters, they are not affected by the operating point of the HVDC link.

- Group J:

Eigenvalues			Freq. (Hz)	Damp. ratio	Dominant States
J	λ_{15}	-15.7	0	-	$i_{z_2}, i_{z_3}, W_{tot_1}$

The eigenvalue λ_{15} has almost the same value as λ_8 in the VSC-based HVDC link. It is associated with the voltage drop across the DC line and is not impacted at all by the parameter sweep. It mostly depends on the intrinsic DC cable parameters. In fact, this eigenvalue is equal to $\frac{-R_{eq,cable}}{L_{eq,cable}}$. Because this eigenvalue only depends on the system physical components, it is not affected by the operating point of the HVDC link.

- Group K:

Eigenvalues			Freq. (Hz)	Damp. ratio	Dominant States
K	$\lambda_{16,17}$	$-22.2 \pm j41.3$	6.6	0.474	$W_{tot_1}, x_{idc1}, x_{W_{tot_1}}, x_{igd_2}, W_{tot_2}, x_{idc2}, x_{vdc2}, x_{W_{tot_2}}, W_{filt_1}$

The complex conjugate of group K are the equivalent of the complex conjugate of group D in the VSC-based HVDC link: they are strongly related to the DC voltage of the Vdc-mode converter and their associated 5% response time roughly corresponds to the settling time of the DC voltage controller. These eigenvalues are greatly influenced by the parameter sweep and are associated to the most influential mode on the DC voltage dynamics (i.e. they are the main driver behind the DC voltage dynamics for acceptable values of the DC voltage controller). Because these eigenvalues only depend on the system control loop parameters, they are not affected by the operating point of the HVDC link.

- Group L:

Eigenvalues			Freq. (Hz)	Damp. ratio	Dominant States
L	$\lambda_{18,19}$	$-64.9 \pm j72.8$	11.6	0.666	W_{filt_1}, W_{filt_2}

These eigenvalues are mainly related to the energy controller of the Vdc-mode converter whose reference is the square of the DC voltage (W_{filt} is the measured energy after behind filtered by a notch filter). Their characteristic response time

of 46 ms corresponds to the 40 ms tuned response time of the energy controllers and is illustrated in Figure 4.29b where the total stored energy of the Vdc-mode converter shows damped oscillations at 6.6 Hz (corresponding to the group K which impacts the DC voltage and thus, the energy reference of the energy controller) and a 5% response time of 46 ms. Because these eigenvalues only depend on the system control loop parameters, they are not affected by the operating point of the HVDC link.

- Group M:

Eigenvalues			Freq. (Hz)	Damp. ratio	Dominant States
M	λ_{20}	-46.5	0	-	W_{filt_1}, W_{filt_2}

Similarly, λ_{20} is mainly related to the energy controller of the P-mode converter whose reference is a constant of 1 p.u. Because this eigenvalue only depends on the system control loop parameters, it is not affected by the operating point of the HVDC link.

- Group N:

Eigenvalues			Freq. (Hz)	Damp. ratio	Dominant States
N	$\lambda_{21, \dots, 26}$	$-216.2 \pm j208.0$	33.1	0.721	$x_{igd_1}, i_{gd_1}, x_{igq_1}, i_{gq_1},$ x_{igq_2}, i_{gq_2}

The eigenvalues of the group N correspond to the interaction between the d and q-axis outer control loops and the inner current loop of the P-mode converter, and of the q-axis outer control loops and the inner current loop of the Vdc-mode converter (the interaction between the d-axis outer loop (DC voltage control) and the inner current loop of the Vdc-mode converter being described by $\lambda_{11,12}$). Their associated response time of 13.9 ms is close to the tuning of the inner control loop (tuned for 10 ms response time). Because these eigenvalues only depend on the system control loop parameters, they are not affected by the operating point of the HVDC link.

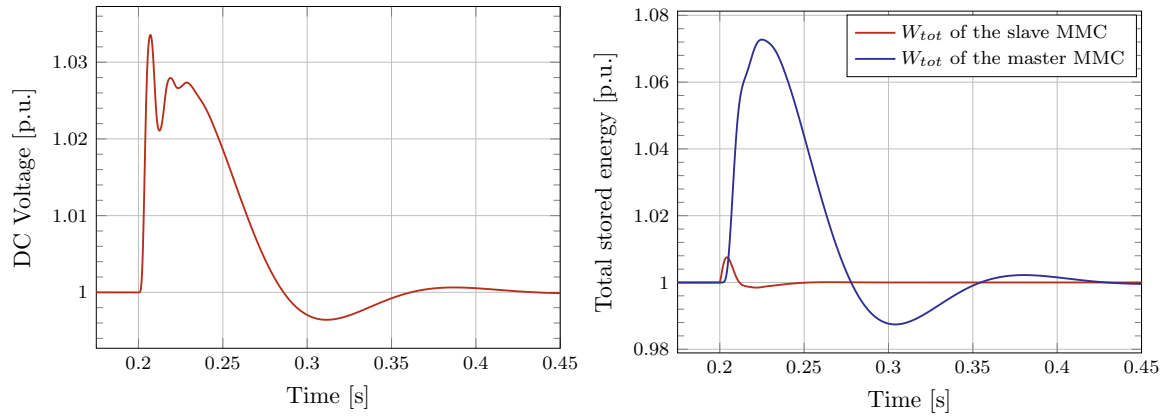
- Group O:

Eigenvalues			Freq. (Hz)	Damp. ratio	Dominant States
O	$\lambda_{27, \dots, 30}$	-1000	0	-	x_{pll_1}, x_{pll_2} $\theta_{pll_1}, \theta_{pll_2}$

The eigenvalues of the group O are associated with the tuning of the PLLs. Because these eigenvalues only depend on the system control loop parameters, they are not affected by the operating point of the HVDC link.

4.4.3 Comparison of the HVDC Systems

It can be observed that the main modes of the system behave in a similar fashion for both the VSC and the MMC-based HVDC link:



(a) Influence of $\lambda_{7,8}$ on the Vdc-mode converter DC voltage behaviour just after the first step of -0.3 p.u. of the active power reference of the P-mode converter.

(b) The P-mode converter has a constant energy reference while the Vdc-mode converter has an energy reference equal to the square of the DC voltage.

Figure 4.29: Visualisation of the DC voltage and the stored energy of the MMCs just after the first step of -0.3 p.u. of the active power reference of the P-mode converter.

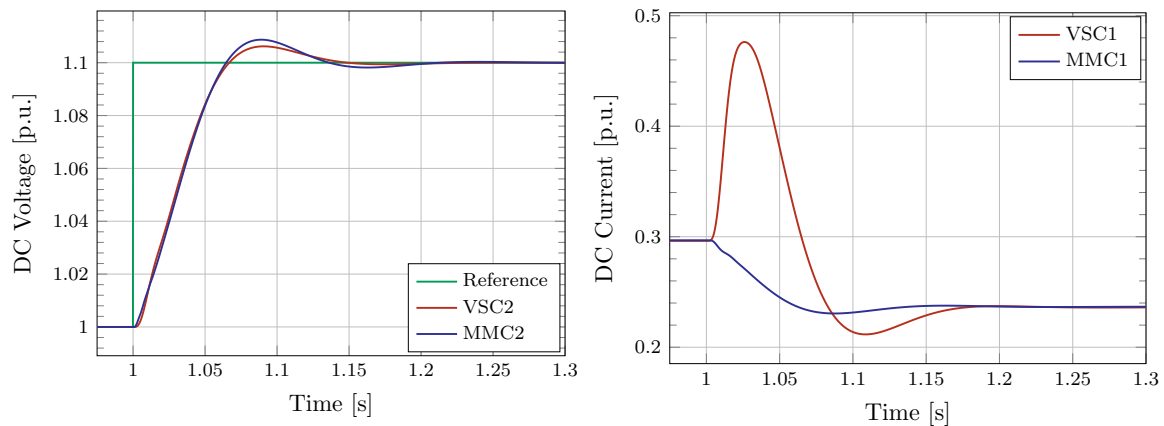
- The modes associated to the power flows –group A for both modal analyses– have broadly the same behaviour in the two systems: (a) they are directly related to the system stability as their associated eigenvalues are the only ones that can show a positive real part (for a settling time parameter of the PI controller of the DC voltage loop of $tr_{5\%,v_{dc}} = 15$ ms in the case of the VSC-based HVDC link, and $tr_{5\%,v_{dc}} = 20.2$ ms in the case of the MMC-based HVDC link); (b) as illustrated in Figure 4.28, the slower the DC voltage controller is, the more stable the system becomes.
- The modes associated to the DC voltage behaviour –group D for the MMC-based HVDC link, group K for the MMC-based HVDC link– which characterises the DC voltage dynamics, are roughly the same and depends mostly on the DC voltage control loop. Naturally, the slower the the DC voltage control is, the longer is the associated response time corresponding to the eigenvalues of these modes. On a side note, it is to be noted that the DC voltage dynamics of the MMC-based system can be entirely changed by the reference of the energy control loops, as illustrated in the next section.

Some notable differences can also be observed: while the VSC-based system does not have eigenvalues with a real part smaller than -400 (disregarding the eigenvalues associated with the PLL), the MMC-based system have 6 such eigenvalues. These eigenvalues are correlated with the dynamics of the DC currents which are tuned

for a very short response time of 4 ms. None of the control loops of the VSCs has such a small response time, hence the lack of eigenvalues with real parts below -400. Moreover, it can be noticed that the impact of the DC cable on the system modes is more pronounced in the case of the MMC-based HVDC link. This is explained by the lack of DC capacitors at both ends of the cable in the case of the MMC-based system, enabling additional interactions between the cable and the internal dynamics of the MMCs.

These observations with regards to the modal analyses of the VSC- and the MMC-based HVDC link are confirmed by the time-domain simulations of Figures 4.30 and 4.31, which illustrate both the similarities and the differences between the two systems:

- Figure 4.30 shows a comparison of the DC voltage and the DC current of both systems for a DC voltage reference step of 0.1 p.u. at the Vdc-mode converter terminals. The dynamics of the DC voltage response to the reference step (Figure 4.30a) are similar for both systems and the 5% response time is mainly influenced by the eigenvalue group D in the case of the VSC-based HVDC link and the eigenvalue group K in the case of the MMC-based HVDC link. The pseudo-period of the system responses have a value of respectively 5.9 Hz and 6.6 Hz, corresponding once again to the eigenvalue group D in the case of the VSC-based HVDC link and the eigenvalue group K in the case of the MMC-based HVDC link.
- In opposition to the similitude between the behaviour of the DC voltage of both HVDC links, the dynamics of the DC current responses to the voltage reference step (Figure 4.30b) greatly differ. In the case of the VSC-based HVDC link, the DC current shows an important peak during its transient before stabilising at its steady state value. This transient is related to the power flow variation between the two converters and the 5.9 Hz oscillation frequency corresponds to the frequency of the eigenvalues of the group D. This peak and these oscillations are non-existent in the case of the MMC-based HVDC link because the P-mode converter is not sharing its energy with the DC bus, hence enabling a fast and independent control of the current by its DC current loop.
- Figure 4.31 shows a comparison of the active power, the DC voltage and the DC current of both systems for an active power reference step of -0.3 p.u. of the P-mode converter. The active power responses (Figure 4.31a) of both systems



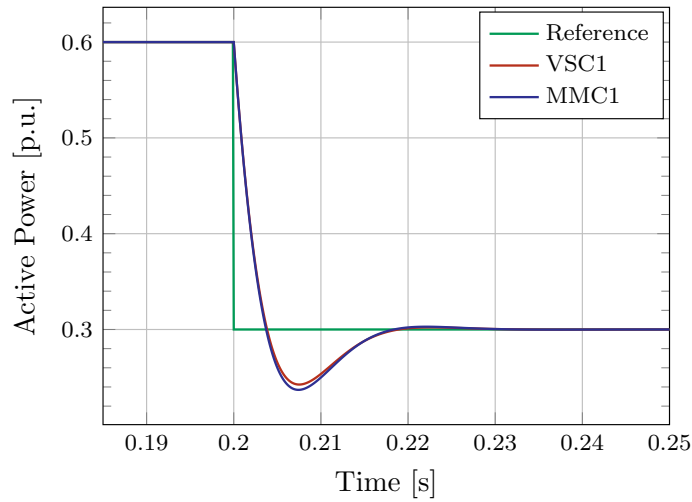
(a) VSC- and MMC-based HVDC system DC voltage responses to a 0.1 p.u. DC voltage reference step.

(b) VSC- and MMC-based HVDC system DC current responses to a 0.1 p.u. DC voltage reference step.

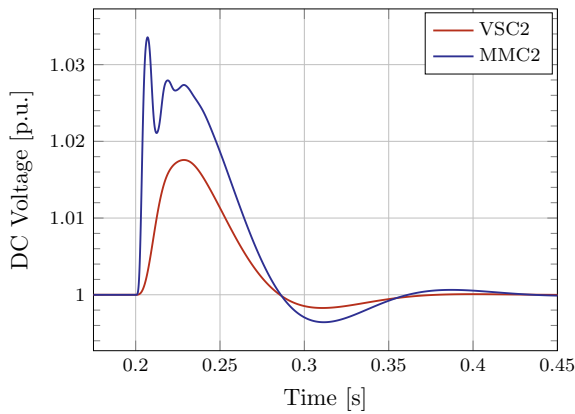
Figure 4.30: VSC- and MMC-based HVDC system responses to a 0.1 p.u. DC voltage reference step.

are very similar and correspond respectively to the 14.3 ms 5% response time of the eigenvalue group F for the VSC-based HVDC link and the 13.9 ms 5% response time of the eigenvalue group N for the MMC-based HVDC link which represents the d-axis control of the P-mode converter. They show extremely damped oscillations at a frequency of 34 and 33 Hz respectively (frequencies associated to the group F and N respectively).

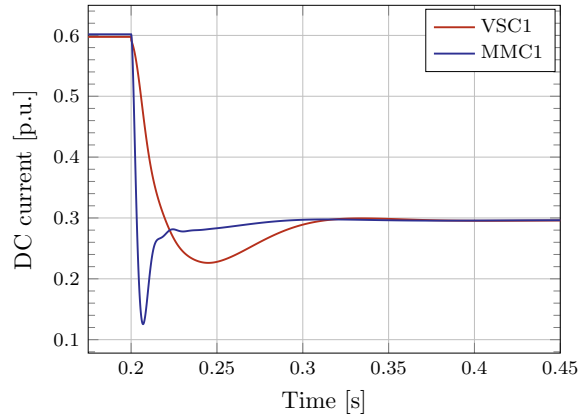
- The DC current (shown in Figure 4.31c) of the MMC-based HVDC link suffers from a transient peak due to the fast control of the DC current loop which has a 4 ms response time. This peak is not present for the VSC-based HVDC since there is no DC current loop. In turn, and in opposition to the smooth DC voltage behaviour after a DC voltage reference step, the DC voltage behaviour of the MMC-based HVDC link after the active power reference step shows some undesired oscillations at 88 Hz (related to the group D, which is linked to the stored energy in the MMCs and to the power flows of the system) with an initial voltage peak. This peak is indirectly generated by the DC current loop that operates a fast control of the DC current (4 ms time response setting) which naturally impacts the DC voltage. However, the overall behaviour (time response and frequency) is still imposed by the eigenvalues of the group K. The DC voltage behaviour of the VSC-based HVDC does not show any different dynamics than in Figure 4.30a.



(a) VSC- and MMC-based HVDC system active power responses to a -0.3 p.u. active power reference step.



(b) VSC- and MMC-based HVDC system DC voltage responses to a -0.3 p.u. active power reference step.



(c) VSC- and MMC-based HVDC system DC current responses to a -0.3 p.u. active power reference step.

Figure 4.31: VSC- and MMC-based HVDC system responses to a -0.3 p.u. active power reference step.

4.4.4 Comparison of two MMC-based HVDC Links with different Energy Control Strategies

In the previous chapter, the description of the control system of the MMC led to an energy control loop with two possible reference signals, enabling two different energy control strategies. The constant energy reference signal (upper position of the switch in Figure 3.25) allows the MMC to store a constant amount of energy in the SM capacitors independently of the DC and AC system behaviours. The αv_{dc}^2 energy reference signal (lower position of the switch in Figure 3.25) allows the MMC to share its stored energy with the DC bus by having an energy reference signal proportional to the square of the DC voltage of the DC bus, hence virtually coupling the SM capacitors to the DC bus.

The MMC-based HVDC link studied above is operated such that the Vdc-mode converter shares its energy with the DC bus while the P-mode converter does not. This enables a fast DC current control that is independent of the DC voltage level of the transmission system. The MMC-based HVDC system is capable of reproducing the behaviour of the VSC-based HVDC link by forcing the P-mode converter to share its energy with the DC bus by changing its stored energy reference from a constant to the square value of the DC voltage. Figure 4.32 shows a comparison of the MMC-based HVDC system behaviour for the two scenarii:

- Scenario 1: The Vdc-mode converter shares its energy with the DC bus but not the P-mode converter, enabling a fast control of the DC current independent of the DC voltage level.
- Scenario 2: Both the Vdc-mode and the P-mode converters share their energy with the DC bus, artificially coupling the DC voltage and the DC current, and thus reproducing the behaviour of a VSC-based HVDC link.

Figure 4.32a shows that a proper tuning of the DC voltage controller¹ leads to a similar DC voltage dynamics for the two scenarii in the event of a DC voltage reference change. However, since the DC current is artificially coupled to the DC voltage when the P-mode converter is sharing its energy with the DC bus, the DC current presents the transient that was observed in Figure 4.30b with the VSC-based system after a

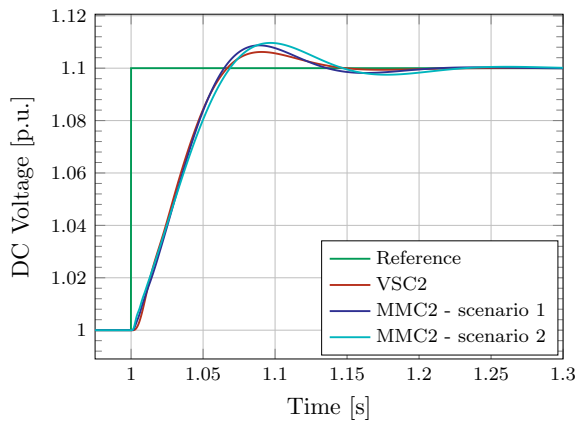
¹When only one converter is sharing its energy with the DC bus, the equivalent capacitor value used in the tuning of the DC voltage PI controller (see Appendix C) is the sum of the cable intrinsic capacitor and the MMC equivalent capacitor of the converter sharing its energy with the DC bus. When both converters are sharing their energy with the DC bus, the equivalent capacitor value used in the tuning of the DC voltage PI controller is the sum of the cable intrinsic capacitor and the two MMC equivalent capacitors.

voltage reference step whereas in the scenario 1, the DC current does not show any oscillations, as shown in Figure 4.32b.

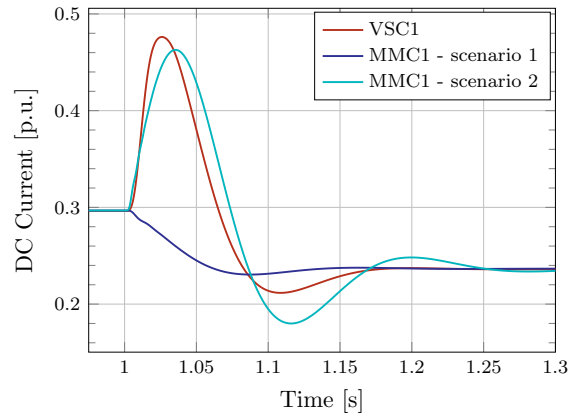
As detailed above, in the scenario 1, the fast and independent DC current control caused both a DC current and a DC voltage transient peak in the case of an active power reference step. This peak is not observed when the P-mode converter shares its energy with the DC bus as its total stored energy reference is now the square value of the DC voltage, and hence, the DC current dynamics correspond to the DC voltage dynamics. And since the DC voltage dynamics is 10 times slower than the DC current dynamics, there is no DC current transient peak any longer and the behaviour of the system corresponds to the behaviour of a VSC-based HVDC link, as shown in Figures 4.32c and 4.32d.

The comparison of Figures 4.30 and 4.31 with Figure 4.32 illustrates the fact that the P-mode MMC actually mimics the behaviour of a VSC in the scenario where its energy reference is the square of the DC voltage (i.e. the converter is sharing its stored energy with the DC bus). However, by doing so, the DC current is artificially coupled to the DC voltage, hence wasting the additional DC current control offered by the MMC by comparison to a standard VSC.

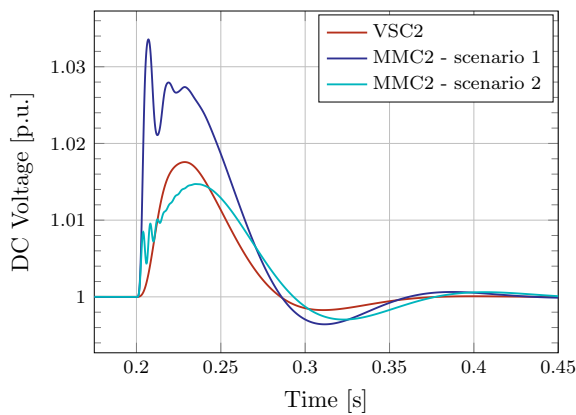
The fact that the DC voltage behaves in a similar fashion for the VSC and MMC-based HVDC link in Figure 4.32a confirms the results of the modal analysis which showed that these modes had a similar behaviour. Figure 4.32b also shows that when the DC voltage is naturally (case of the VSC-based system) or artificially (case of the MMC-based system scenario 2) coupled to the DC current, a pseudo-oscillation is noticed on the current after the DC voltage reference change. The frequency of this pseudo-oscillation corresponds to the associated frequency of the main DC voltage mode (group D in the modal analysis of the VSC-based HVDC link) and is assimilated to the charging of the capacitor (or of the flying capacitors of the SMs in the case of the MMC-based system with scenario 2) of the Vdc-mode converter. In the case of the MMC-based system with scenario 1, the DC current dynamics –group B of the modal analysis of the MMC-based HVDC link– is fully controlled by the DC current controllers and is dissociated from the DC voltage dynamics. The same conclusions can be reached with Figures 4.32c and 4.32d for a step of the active power reference instead of the DC voltage reference.



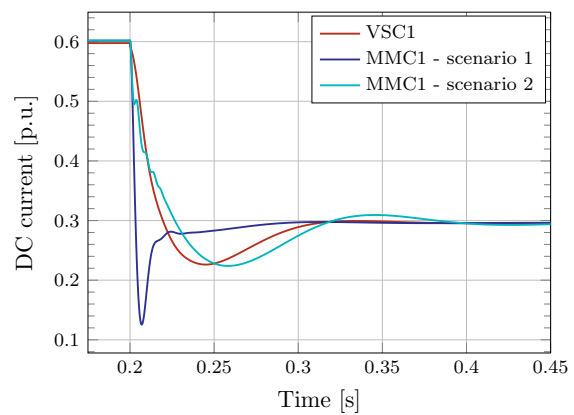
(a) VSC and MMC-based HVDC system DC voltage responses to a 0.1 p.u. DC voltage reference step.



(b) VSC and MMC-based HVDC system DC current responses to a 0.1 p.u. DC voltage reference step.



(c) VSC and MMC-based HVDC system DC voltage responses to a -0.3 p.u. active power reference step.



(d) VSC and MMC-based HVDC system DC current responses to a -0.3 p.u. active power reference step.

Figure 4.32: VSC and MMC-based HVDC system responses for two different scenarios. Scenario 1: when only the Vdc-mode converter is sharing its energy with the DC bus. Scenario 2: when both converters are sharing their energy with the DC bus.

4.5 Chapter Conclusion

This chapter presented a methodology to derive the state-space model from both the AVM of a standard 2-level VSC and the simplified MMC model that were described in the previous chapter. The state-space models of both converter have been validated for two different control strategies (the active power control or the DC voltage control) by comparing the behaviour of the state-space representation of an HVDC link to the behaviour of more detailed reference models, using EMT programs. This methodology can easily be generalised to Multi-Terminal HVDC (MTDC) systems, as described in the next chapter.

Once the state-space models of the two converter technologies have been validated, the modal analysis of both a VSC- and MMC-based HVDC link was performed in order to identify and assess the impact of the different modes on the global behaviour of the two transmission systems. The results show that the modes related to the power flow in the HVDC link have the same behaviour against the parameter sweep and determine the stability for both systems. Similarly, the main DC voltage mode is overall very similar for both systems because it mostly depends on the DC voltage controller. The additional control loops of the MMCs can generate some damped parasite oscillations of the DC voltage response after an active power reference step and can cause an undesired transient peak of the DC voltage and of the DC current. However, the fast and independent control of the DC current by the P-mode converter eliminates the observed transient oscillations of the DC current caused by the DC voltage dynamics after a DC voltage reference change.

The modal analyses significantly improve the understanding of the system dynamics overall. These dynamics can also be witnessed via EMTP simulations, however depending on the studied disturbance of the system, some of them can easily be omitted whereas the modal analyses affectively list them all. However, the participation factors are to be handled with caution as they can lead to false interpretation, especially in HVDC systems where the converters possess several cascading control loops that interact with each other and with the DC cable.

Finally, another control strategy of the MMC-based HVDC link where both converters share their energy with the DC bus is studied. The behaviour of the MMC-based HVDC link is then very similar to the one of the VSC-based HVDC link: the DC current and the DC voltage are not independent any longer and the overall dynamics are mainly influenced by the dynamics of the DC voltage. Eventually, the control of an MMC-based HVDC link requires a thorough understanding of the interaction between

the subsystems but also gives more control over the DC voltage and the DC current of the transmission system.

The state-space models developed in this chapter can now be used in larger HVDC transmission systems such as MTDC systems. They represent a fast and reliable way to include any system in a bigger electrical system without having to resort to powerful computational resources. This includes the visualisation of an MTDC system behaviour in case of an AC fault or simply the observation of the impact of a power reference change on the DC voltage of an MTDC system. The next chapter will use the state-space model of the MMC in order to design a 5-terminal MTDC system.

Chapter 5

SVD Analysis of a 5-Terminal MMC-Based MTDC System

I have not failed. I have just found 10,000 ways that won't work.

– T. A. Edison, as quoted by: J. L. Elkhorne in *The Fabulous Drone* (March 1967) [42].

If Edison had a needle to find in a haystack, he would proceed at once with the diligence of the bee to examine straw after straw until he found the object of his search. [...] I was a sorry witness of such doings, knowing that a little theory and calculation would have saved him ninety per cent of his labour.

– N. Tesla, as quoted by: J. L. Elkhorne in *The Fabulous Drone* (March 1967) [42].

5.1 Chapter Introduction

The proliferation of point-to-point HVDC transmission systems will probably give rise to several DC links located in the same geographical zone; DC reinforcements, extensions and AC zone interconnections may then lead to a Multi-Terminal HVDC (MTDC) grid in the future.

The control of HVDC grids is mandatory to maintain the stability of the system. The *master-slave* control strategy of a DC link is not suitable for MTDC systems since the single AC bus connected to the master converter would have to provide all the balancing power and that the loss of this master converter would mean the loss of the whole system. To remedy this problem, the *voltage droop* control technique described in [38, 20, 41, 12], where several VSCs participate in the DC voltage regulation at the same time, is probably the most adequate control strategy to safely and reliably operate any MTDC system.

However, in those references, the voltage-droop parameter is either selected from a static point of view, or simply arbitrarily chosen equal to 0.05 p.u./p.u. In this chapter, a power-based droop control is designed to tolerate a maximum DC voltage deviation of the MTDC grid, both in steady state and during transients. This can be achieved by using the multi-variable frequency analysis based on the Singular Value Decomposition (SVD).

The SVD tool was first applied to MTDC systems to design the voltage-droop gain in [80], where the converters were modelled as simple current injectors with a current-based voltage droop and the DC lines by classical PI sections. Reference [43] then used the SVD tool with a different objective: to minimize the impact of AC-side disturbances. Finally, Reference [81] improved the work of [80] by including the dynamics of the control loops of the DC grid converters in the frequency analysis for the voltage-droop gain selection. The difference between the results in [80] and [81, 79] is not negligible, implying that the level of complexity of the component models, such as the control loops or the DC cable model, highly impacts the results of the SVD study and thus the design of the voltage-droop gain.

In this chapter, a modal analysis is performed on a 5-terminal MMC-based MTDC system in order to understand the provenance of the different modes of the system and provide a stability study with regard to the voltage-droop parameter. Then, since References [80, 43, 81, 79] are, to the author's knowledge, the only references that applied the SVD tools to HVDC systems, the basic principle of this method is recalled and further explained in this chapter. Also, the SVD is used to design the voltage-droop parameter of the MMC of the considered MTDC system. Finally, this chapter intends

to show the impact of four basic DC cable models on the frequency response of the MTDC system obtained in the SVD analysis, and thus, on the voltage-droop gain selection.

5.2 State-Space Representation of the MTDC System

Using the state-space representation of the MMC and the DC cable model described in the previous chapter, a Matlab[®] routine is used to automatically generate the state-space representation of a 5-terminal MTDC system. The control strategy of the MTDC system is described and a modal analysis is performed in order to identify the system modes and assess the stability limitations on the controller gains.

5.2.1 Control Strategy of an MTDC System

A Multi-Terminal HVDC (MTDC) system results from the interconnection of several AC networks via an HVDC grid. The fast and efficient power flow control offered by the AC/DC converters combined with the low power losses in the DC grid are attractive features that may lead to the democratisation of MTDC systems in the future. These MTDC system will most probably use the *voltage-droop* control technique described in [38, 20, 41, 12], where several VSCs participate in the DC voltage regulation at the same time, because it is probably the most adequate control strategy to safely and reliably operate such systems.

The principle of the voltage-droop control is as follows. If a DC voltage variation is detected by a converter equipped with a voltage droop, this controller will generate a proportional deviation of the power reference of the converter that helps balance the power on the DC grid, thus preventing large deviations of the DC voltage.

Several methods of voltage-droop control are proposed in the literature. The one described in [11, 20, 84] seems to be the best feasible solution thanks to its simplicity and efficiency. With this solution, a converter equipped with a voltage-droop controller modifies its power reference according to the DC voltage level by moving its operating point along a droop characteristic line, as defined in (5.1) and illustrated in the block diagram of Figure 5.1,

$$\Delta P_{v_i}^* = \frac{1}{k_{v_i}} \Delta v_{dc_i} \quad (5.1)$$

where:

- $\Delta P_{v_i}^*$ is the power reference deviation generated by the voltage-droop controller of the i^{th} VSC-HVDC converter. A positive $\Delta P_{v_i}^*$ corresponds to a power injection from the DC grid to the AC grid.
- k_{v_i} is the voltage-droop parameter of the i^{th} converter, $k_{v_i} < 0$. It defines the droop characteristic line slope, which is $\frac{1}{k_v}$.
- $\Delta v_{dc_i} = v_{dc_i}^* - v_{dc_i}$.

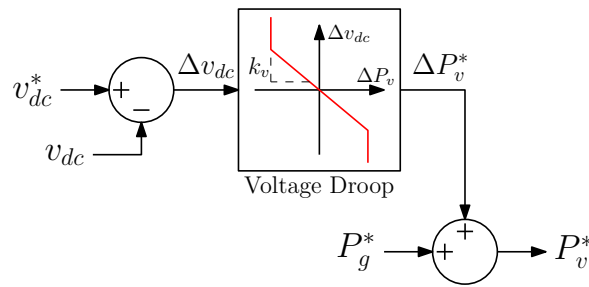


Figure 5.1: Block diagram of the voltage-droop technique.

Additionally, each voltage-droop controller provides limits that prevent the converter from moving too far away from its original operating point, as an excessive deviation from the operating point may lead to harmful operation conditions.

5.2.2 State-Space Representation of the MTDC System

The system studied in this chapter is pictured in Figure 5.2. It is a 5-terminal, MMC-based, MTDC system where the first three converters are equipped with the voltage-droop controller (called Vdc-droop converters) of Figure 5.1 and the other two are P-mode converters that inject a constant amount of power into the DC grid. The three Vdc-droop MMCs share their total stored energy with the DC bus (i.e. their energy reference signal is the square value of the DC voltage), while the two P-mode MMCs do not share their stored energy (i.e. their energy reference signal is a constant). The DC grid consists of six DC lines interconnected in a pentagon, plus one additional DC line corresponding to one diagonal of the pentagon, which adds flexibility to the system. The system parameters are listed in Appendix A.

Using the state-space model of the MMC and the Fitted PI-section cable that was used in the previous chapter and that is recalled below, a Matlab[®] routine is used to automatically generate any MTDC system for any desired topology of the HVDC grid

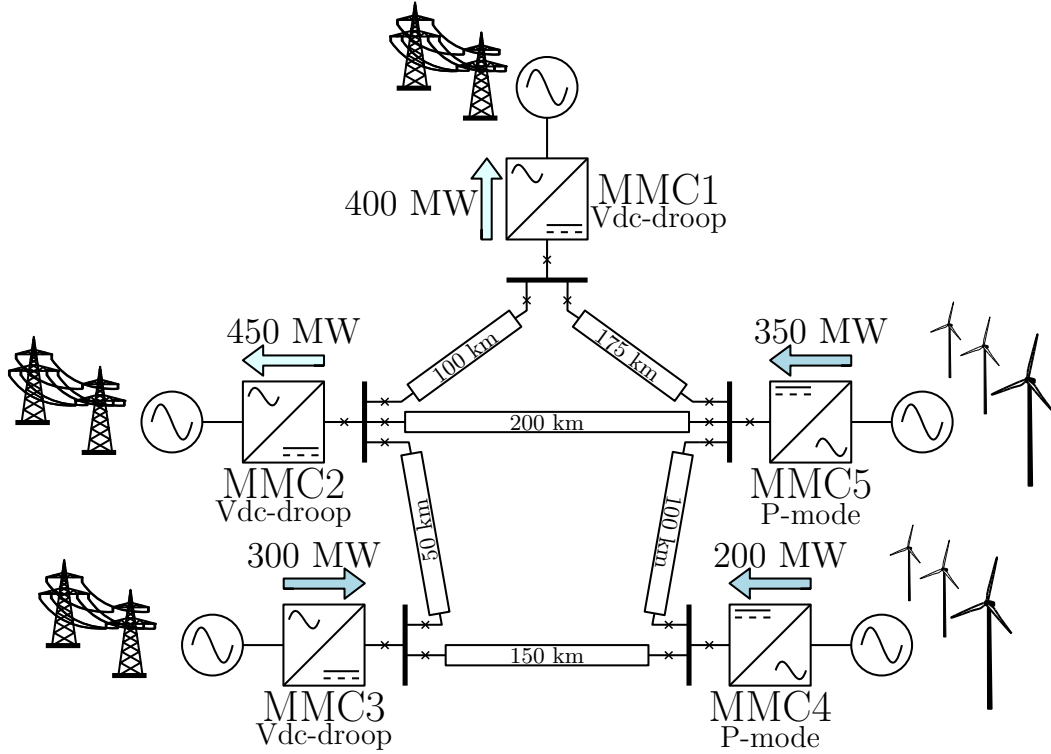


Figure 5.2: Topology of the MTDC system.

by concatenating the individual state-space model of each subsystem. In the case of the 5-terminal MTDC system of Figure 5.2, the complete system is broken down into 16 subsystems (i.e. the 5 MMCs, the 5 corresponding DC grid nodes and the 6 DC lines) where each subsystem is represented in state-space form as in (5.2). Then, by taking into account the interconnection static constraints (also called network model in [77]) that bounds the subsystems altogether, as depicted in Figure 5.3, the complete MTDC system state-space representation is obtained by combining the $N = 16$ individual state-space together.

$$\begin{aligned} \frac{d}{dt}x_n &= A_n x_n + B_n u_n \\ y_n &= C_n x_n + D_n u_n \end{aligned} \quad (5.2)$$

according to the interconnection static constraints:

$$u \triangleq [u_1 \ \dots \ u_N]^\top = Jy \triangleq J [y_1 \ \dots \ y_N]^\top \quad (5.3)$$

where x_n , u_n and y_n are column vectors for $n = 1, 2, \dots, N$, and J is the network matrix representing how the subsystems are interconnected (see Appendix D for more details).

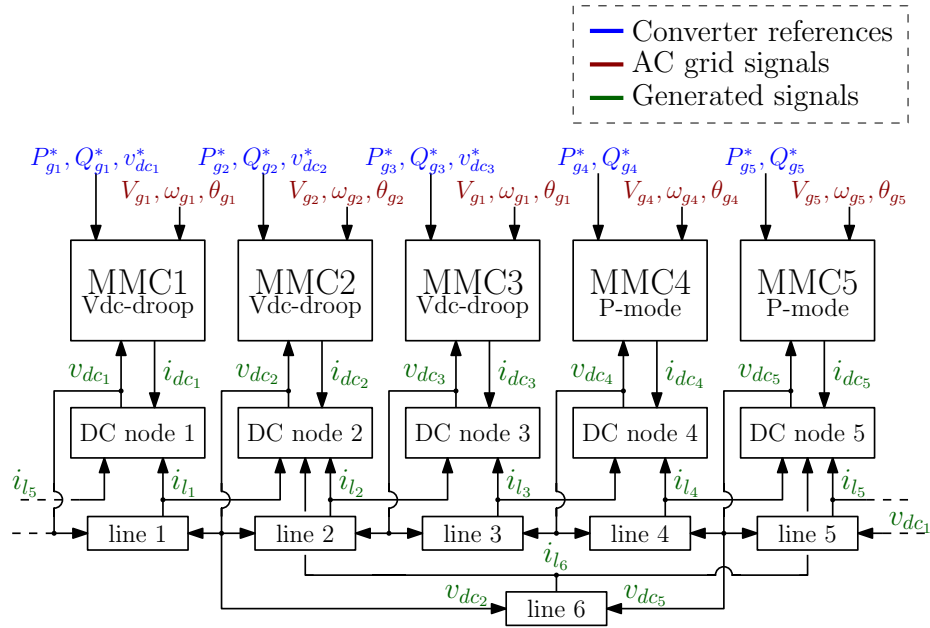


Figure 5.3: Interconnection constraints of the subsystems of the 5-terminal MTDC system of Figure 5.2.

The DC cable model used for the DC lines is an improved classical PI-section with parallel branches, as depicted in Figure 5.4 and described in [21, 22]. A judicious choice of the component values in the parallel branches enables this simple model to fit the frequency response of a more detailed model such as the wide-band model [83]. The component values are automatically determined by a fitting algorithm, depending on the number of parallel branches desired by the user [57, 56]. The component values of the three parallel branches cable model used in this section are described in Table 5.1. The impact of the cable model on the system will be thoroughly analysed using the SVD method in the last section of this chapter.

The state-space representation of the complete MTDC system results in a 73×73 state matrix A , a 73×40 input matrix B , a 117×73 output matrix C and a 117×40 feed-forward matrix D . A modal analysis can now be performed to study the behaviour of the system.

5.2.3 Modal Analysis of the 5-Terminal MTDC System

Eigenvalue study

The 73 eigenvalues of the system are obtained and described in Table 5.2 where they are categorised into 11 groups ranging from A to K, depending on their origin and

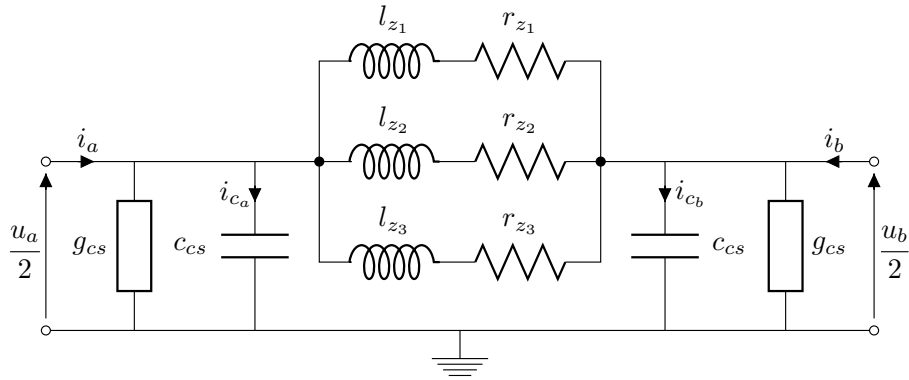


Figure 5.4: Fitted PI-section of a cable [21, 22].

$r_{z_1} = 1.1724 \cdot 10^{-1} \Omega/\text{km}$	$l_{z_1} = 2.2851 \cdot 10^{-4} \text{ H}/\text{km}$
$r_{z_2} = 8.2072 \cdot 10^{-2} \Omega/\text{km}$	$l_{z_2} = 1.5522 \cdot 10^{-3} \text{ H}/\text{km}$
$r_{z_3} = 1.1946 \cdot 10^{-2} \Omega/\text{km}$	$l_{z_3} = 3.2942 \cdot 10^{-3} \text{ H}/\text{km}$
$g_{cs} = 7.6333 \cdot 10^{-11} \text{ S}/\text{km}$	$c_{cs} = 1.9083 \cdot 10^{-7} \text{ F}/\text{km}$

Table 5.1: Component values of the fitted PI cable.

their impact on the system behaviour (i.e. on the dynamics of the DC voltages and the DC currents). Table 5.2 also specifies the frequency of the modes associated to the eigenvalues and their damping ratio. Finally, using the participation matrix definition of [77] and adopted in [67], which allows to quantify the contribution of each state variable to each eigenvalue, the dominant states of each eigenvalue group are listed. In the rest of this chapter, the states $i_{j,z_{1,2,3}}$ correspond to the current in the parallel branches of the DC cable j ($j = 1, \dots, 6$), and each state defined by x_{\dots} corresponds to the output of the integral action of a controller in the state-space model (e.g. $x_{i_{gd_1}}$ corresponds to the output of the integral action of the d-axis controller of the inner current loop).

The eigenvalues listed in Table 5.2 are then represented in the complex plane in Figure 5.6 and are categorised into four different entities: the eigenvalues that are more impacted by the states of the DC grid, the eigenvalues that are more influenced by the states of the P-mode converters (MMC4 and MMC5), the eigenvalues that are more influenced by the states of the Vdc-droop converters (MMC1, MMC2 and MMC3), and finally those that are not clearly influenced by a single one of the previous three. In brief, each eigenvalue has been placed in one of these four entities with regards to the states they are the most influenced by, according to the participation factors.

Eigenvalues			Freq. (Hz)	Damp. ratio	Dominant States
A	$\lambda_{1,2}$	$-179.7 \pm j4132$	657.6	0.043	$i_{2,z1} i_{3,z1} v_{dc2} v_{dc3} i_{dc3}$
A	$\lambda_{3,4}$	$-167.6 \pm j2577$	410.2	0.065	$i_{1,z1} i_{3,z1} v_{dc1} v_{dc2} v_{dc4} i_{dc1} i_{dc2}$
A	$\lambda_{5,6}$	$-154.3 \pm j1966$	312.9	0.078	$i_{2,z1} i_{3,z1} i_{5,z1} v_{dc1} v_{dc2} v_{dc4} i_{dc1} i_{dc2}$
A	$\lambda_{7,8}$	$-187.9 \pm j1798$	286.2	0.104	$i_{1,z1} i_{3,z1} i_{4,z1} i_{6,z1} v_{dc2} v_{dc4} v_{dc5} i_{dc3}$
A	$\lambda_{9,10}$	$-177.0 \pm j853.4$	135.8	0.203	$i_{3,z1} i_{5,z1} i_{6,z1} v_{dc1} v_{dc2} v_{dc4} v_{dc5} i_{dc1} i_{dc3}$
B	$\lambda_{11,12}$	$-544.1 \pm j499.3$	79.5	0.737	$i_{1,z1} v_{dc1} x_{idc1} i_{gd1} i_{gd3}$
B	$\lambda_{13,14}$	$-511.9 \pm j547.2$	87.09	0.683	$i_{2,z1} i_{2,z2} v_{dc2} W_{tot2} x_{idc2} i_{dc2} i_{gd2} x_{idc3} i_{dc3} i_{gd3}$
B	$\lambda_{15,16}$	$-484.6 \pm j586.8$	93.39	0.637	$i_{3,z2} v_{dc5} i_{gd1} i_{gd2} i_{gd3} i_{dc4} W_{tot5} x_{idc5} i_{dc5}$
B	$\lambda_{17,18}$	$-481.9 \pm j579.9$	92.28	0.639	$i_{3,z2} i_{4,z2} W_{tot4} x_{idc4} i_{dc4} W_{tot5} x_{idc5} i_{dc5}$
C	$\lambda_{19,20}$	$-460.7 \pm j264.0$	42.02	0.868	$i_{3,z2} x_{igd1} x_{igd2} x_{igd3} i_{gd1} i_{gd2} i_{gd3} x_{idc5}$
D	$\lambda_{21,22}$	$-222.8 \pm j194.4$	30.93	0.754	$i_{2,z2} x_{idc2} i_{gd2} i_{gd3} x_{igd2} x_{igd3}$
D	$\lambda_{23,24}$	$-235.8 \pm j175.6$	27.95	0.802	$i_{1,z2} i_{2,z2} x_{igd1} i_{gd1} W_{tot1} x_{idc1} x_{igd3} i_{gd3} x_{idc3}$
E	λ_{25}	-279.1	0	—	$x_{idc1} x_{Wtot1} x_{idc2} x_{Wtot2} x_{idc3} x_{Wtot3}$
F	$\lambda_{26,27}$	-513.0	0	—	$i_{1,z1} i_{3,z1} i_{4,z1} i_{5,z1} i_{6,z1}$
G	λ_{28}	-106.5	0	—	$i_{1,z2} i_{2,z2} x_{igd1} W_{tot1} x_{idc1} x_{igd3} x_{idc3}$
G	λ_{29}	-118.2	0	—	$i_{1,z2} i_{2,z2} x_{igd2} W_{tot2} x_{idc2} x_{igd3} x_{idc3}$
G	λ_{30}	-129.9	0	—	$i_{3,z2} i_{5,z2} i_{6,z2} x_{idc4} W_{tot5} x_{idc5}$
G	λ_{31}	-127.2	0	—	$i_{3,z2} i_{4,z2} W_{tot4} x_{idc4}$
H	$\lambda_{32,33}$	$-48.4 \pm j53.7$	8.50	0.670	$x_{idc1} x_{Wtot1} x_{Wtot3} W_{tot1} x_{idc1} W_{tot3} x_{idc3}$
I	$\lambda_{34,35}$	$-41.4 \pm j36.7$	5.84	0.749	$x_{Wtot1} x_{Wtot2} x_{Wtot3} W_{tot1} W_{tot2} W_{tot3} x_{idc3}$
H	$\lambda_{36,37}$	$-51.2 \pm j53.6$	8.52	0.691	$x_{idc2} x_{Wtot2} x_{Wtot3} W_{tot2} x_{idc2} x_{Wtot2} W_{tot3} x_{idc3}$
F	λ_{38}	-14.5	0	—	$i_{1,z3} i_{2,z3} i_{5,z3}$
F	λ_{39}	-15.0	0	—	$i_{1,z3} i_{2,z2} i_{2,z3}$
F	$\lambda_{40,41}$	-15.4	0	—	$i_{3,z3} i_{4,z3} i_{5,z3} i_{6,z3}$
H	$\lambda_{42,43}$	$-52.7 \pm j53.2$	8.47	0.704	$x_{idc5} x_{Wtot5} W_{tot5}$
H	$\lambda_{44,45}$	$-52.7 \pm j53.2$	8.47	0.704	$x_{idc4} x_{Wtot4} W_{tot4}$
F	$\lambda_{46,47}$	-3.6	0	—	$i_{1,z3} i_{4,z3} i_{5,z3} i_{6,z3}$
F	$\lambda_{48,49}$	-52.9	0	—	$i_{1,z2} i_{3,z2} i_{4,z2} i_{5,z2} i_{6,z2}$
J	$\lambda_{50,63}$	$-216.2 \pm j208.0$	33.1	0.721	$x_{igq1} i_{gq1} x_{igq2} i_{gq2} x_{igq3} i_{gq3} x_{igq4} i_{gq4} x_{igq4} i_{gq4}$ $x_{igq5} i_{gq5} x_{igq5} i_{gq5}$
K	$\lambda_{64,73}$	-1000	0	—	$\theta_{pll1} x_{pll1} \theta_{pll2} x_{pll2} \theta_{pll3} x_{pll3} \theta_{pll4} x_{pll4} \theta_{pll5} x_{pll5}$

Table 5.2: Eigenvalue characteristics of the MTDC system for a voltage-droop parameter $k_v = 0.1$ p.u./p.u.

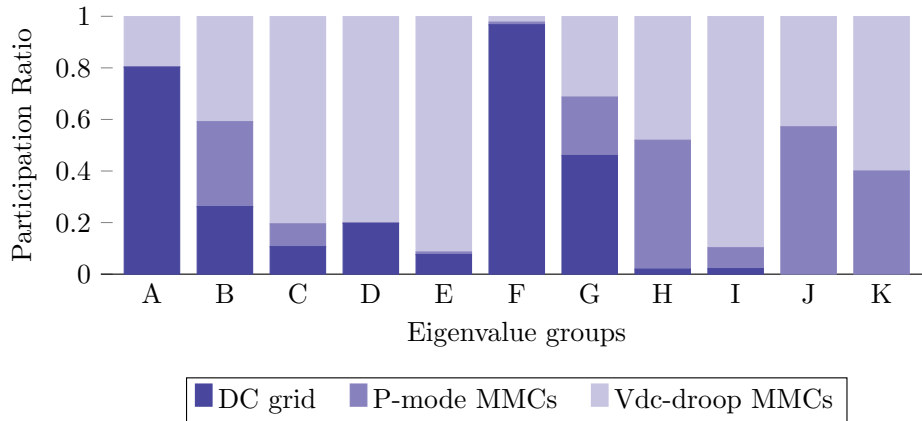


Figure 5.5: Participation ratio of the P-mode MMCs, the Vdc-droop MMCs and the DC grid to the eigenvalues of the complete system.

Figure 5.5 shows the overall participation of each entity (i.e. the DC cable, the VSC1 or the VSC2) to the eigenvalue groups of Table 5.2 in order to supply an additional understanding tool to the reader on the origin of each mode of the system.

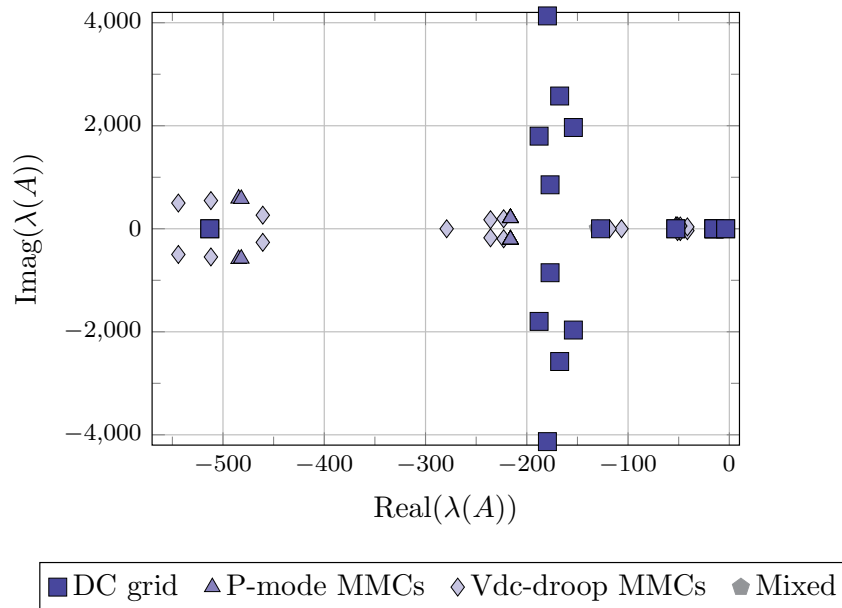
Finally, a sweep of the voltage-droop parameter k_v is performed and its impact on the system eigenvalues is illustrated in Figure 5.7. The parameter sweep starts from $|k_v| = 10^{-3}$ p.u./p.u. and increases to $|k_v| = 1$ p.u./p.u. Most eigenvalues are largely affected by the parameter sweep, implying that the voltage-droop parameter plays a major role in the MTDC system dynamics.

Using the data of Table 5.2 as well as the additional information conferred by Figures 5.5 and 5.6, combined with the eigenvalue behaviours during the voltage-droop parameter sweep of Figure 5.7, the eigenvalue groups of the system are individually studied:

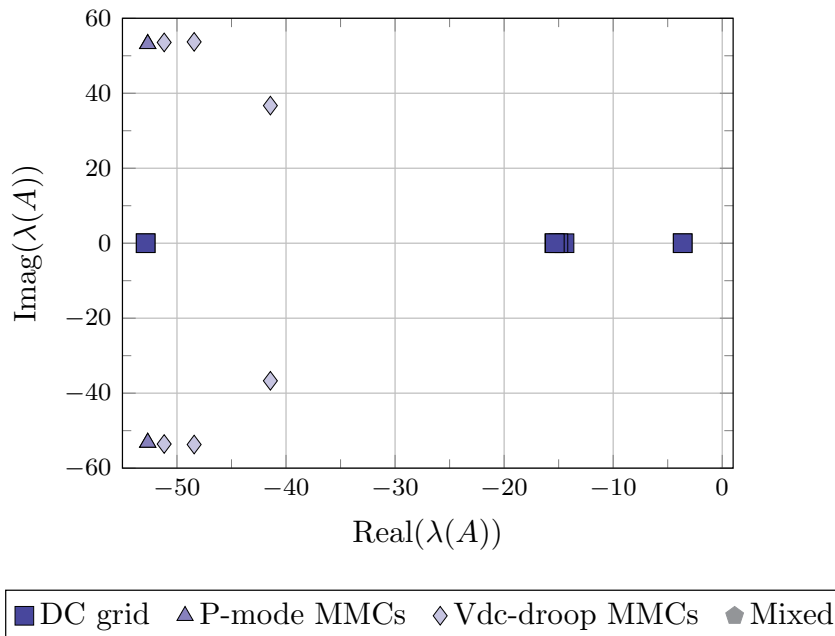
Eigenvalues		Freq. (Hz)	Damp. ratio	Dominant States	
• Group A:	$\lambda_{1,2}$	$-179.7 \pm j4132$	657.6	0.043	$i_{2,z1} i_{3,z1} v_{dc2} v_{dc3} i_{dc3}$
	$\lambda_{3,4}$	$-167.6 \pm j2577$	410.2	0.065	$i_{1,z1} i_{3,z1} v_{dc1} v_{dc2} v_{dc4} i_{dc1} i_{dc2}$
	$\lambda_{5,6}$	$-154.3 \pm j1966$	312.9	0.078	$i_{2,z1} i_{3,z1} i_{5,z1} v_{dc1} v_{dc2} v_{dc4} i_{dc1} i_{dc2}$
	$\lambda_{7,8}$	$-187.9 \pm j1798$	286.2	0.104	$i_{1,z1} i_{3,z1} i_{4,z1} i_{6,z1} v_{dc2} v_{dc4} v_{dc5} i_{dc3}$
	$\lambda_{9,10}$	$-177.0 \pm j853.4$	135.8	0.203	$i_{3,z1} i_{5,z1} i_{6,z1} v_{dc1} v_{dc2} v_{dc4} v_{dc5} i_{dc1} i_{dc3}$

This group corresponds to modes that are strongly related with the power flows in the system and is the equivalent of the group A of the MMC-based HVDC link in the previous chapter. Its eigenvalues result from an interaction between the outer loop control of the converters, their respective d-axis AC current control and the DC grid. $\lambda_{1,\dots,6}$ correspond to 3 pairs of conjugate eigenvalues that are linked to the DC voltage of the 3 MMCs equipped with voltage-droop controllers. These eigenvalue pairs dominate the system stability as they are the only ones to show a possible positive real part. In fact, the eigenvalue pairs $\lambda_{1,2}$, $\lambda_{3,4}$ and $\lambda_{5,6}$ show a positive real part for $k_v < 0.01787$ p.u./p.u., $k_v < 0.02496$ p.u./p.u. and $k_v < 0.03450$ p.u./p.u. respectively. The 2 pair of conjugate eigenvalues $\lambda_{7,8}$ and $\lambda_{9,10}$ are linked to the DC voltage of the two P-mode MMCs and show a curved variation with the parameter sweep but do not threaten the system stability. They are however responsible for the oscillations observed on both the DC current and the DC voltage response to a power reference step in Figure 5.8 for small values of the voltage-droop parameter. All these eigenvalues are dependent on the system operating point.

Eigenvalues		Freq. (Hz)	Damp. ratio	Dominant States	
• Group B:	$\lambda_{11,12}$	$-544.1 \pm j499.3$	79.5	0.737	$i_{1,z1} v_{dc1} x_{idc1} i_{gd1} i_{gd3}$
	$\lambda_{13,14}$	$-511.9 \pm j547.2$	87.09	0.683	$i_{2,z1} i_{2,z2} v_{dc2} W_{tot2} x_{idc2} i_{dc2} i_{gd2} x_{idc3} i_{dc3} i_{gd3}$
	$\lambda_{15,16}$	$-484.6 \pm j586.8$	93.39	0.637	$i_{3,z2} v_{dc5} i_{gd1} i_{gd2} i_{gd3} i_{dc4} W_{tot5} x_{idc5} i_{dc5}$
	$\lambda_{17,18}$	$-481.9 \pm j579.9$	92.28	0.639	$i_{3,z2} i_{4,z2} W_{tot4} x_{idc4} i_{dc4} W_{tot5} x_{idc5} i_{dc5}$

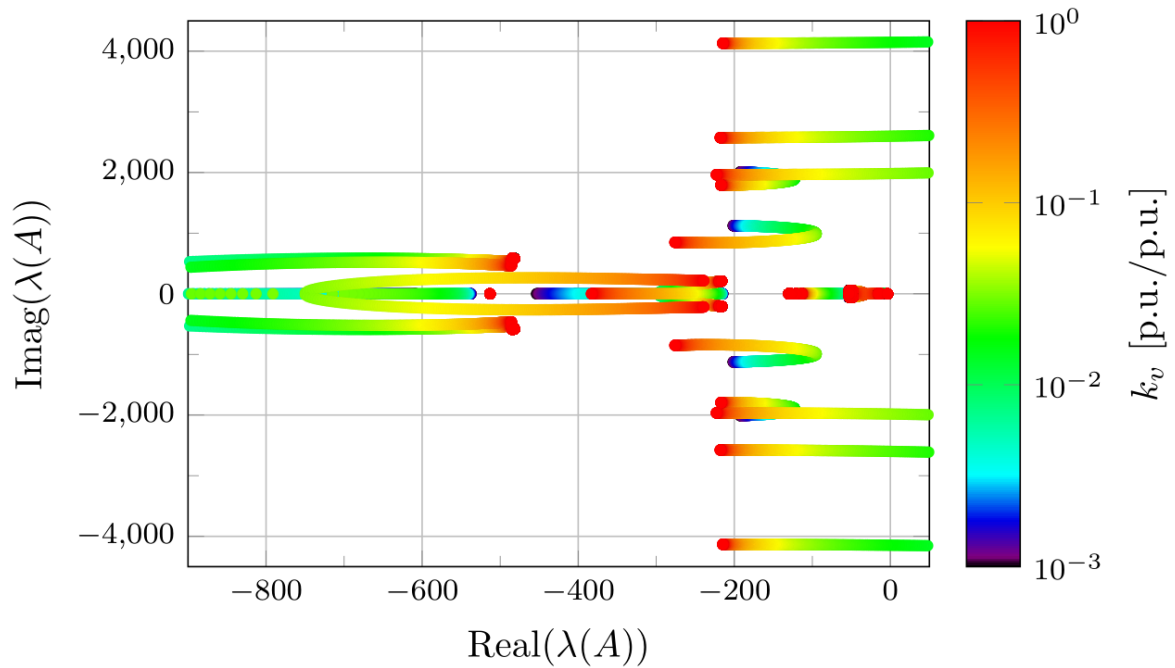


(a) Eigenvalue representation of the MTDC system and their dependency to either the DC grid, the P-mode MMCs or the Vdc-droop MMCs.

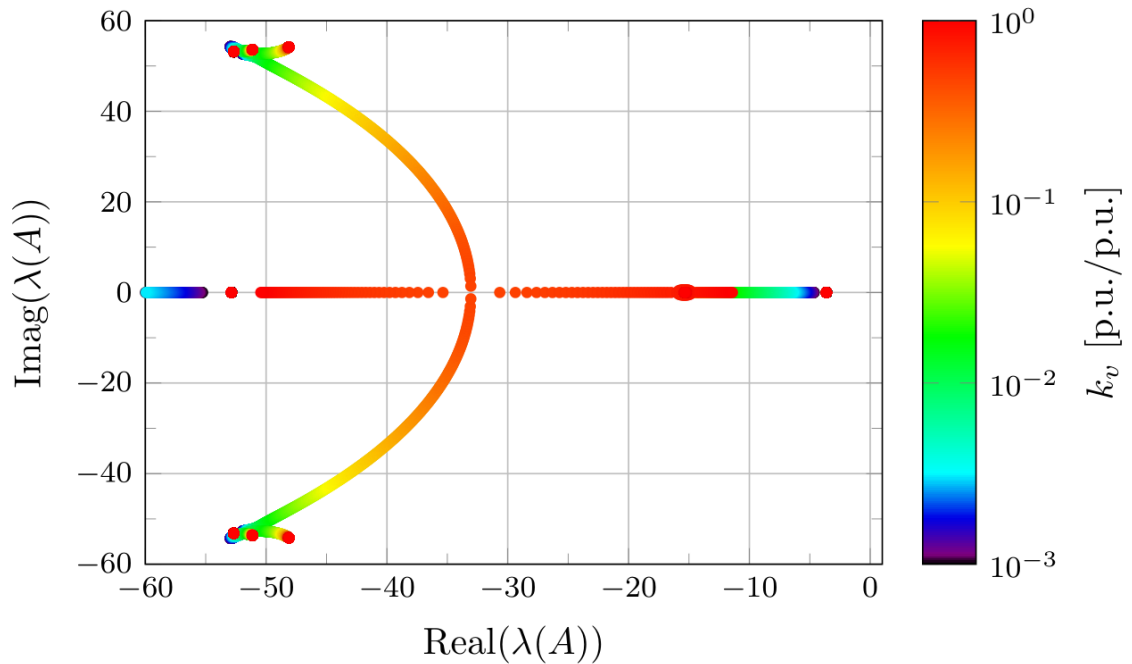


(b) Zoom on the eigenvalue representation of the MTDC system and their dependency to either the DC grid, the P-mode MMCs or the Vdc-droop MMCs.

Figure 5.6: Eigenvalue representation of the MTDC system and their dependency to either the DC grid, the P-mode MMCs or the Vdc-droop MMCs, for a voltage-droop parameter $k_v = 0.1$ p.u./p.u.



(a) Eigenvalue trajectories of the MTDC system for a sweep of the voltage-droop parameter k_v .



(b) Zoom on the eigenvalue of the MTDC system for a sweep of the voltage-droop parameter k_v .

Figure 5.7: Eigenvalue trajectories of the MTDC system for a sweep of the voltage-droop parameter k_v .

This group is strongly related to the DC current control of the MMCs and the 5% response time constant of its eigenvalues is close to the 4 ms settling time of the DC current control loop. On the one hand, $\lambda_{15,16}$ and $\lambda_{17,18}$ correspond to the dynamics of the DC current control of the two P-mode MMCs as they are not impacted at all by the voltage-droop parameter sweep of Figure 5.7a. This is coherent since the two P-mode converters do not share their energy with the DC bus, and hence, fully control their DC current output independently of the DC voltage dynamics and thus independently of the voltage-droop parameter. On the other hand, $\lambda_{11,12}$, $\lambda_{13,14}$ and $\lambda_{19,20}$ correspond to the dynamics of the DC current control of the 3 MMCs equipped with voltage-droop controllers. Since these controllers do share their total stored energy with the DC bus (i.e. their energy reference is the square of the DC voltage at their respective terminals), the dynamics of their DC current outputs are coupled to the dynamics of the DC voltage, hence their heavy dependency on the voltage-droop parameter, as shown by the voltage-droop parameter sweep of Figure 5.7a. However, the behaviour of $\lambda_{19,20}$ is different than for $\lambda_{11,12}$ and $\lambda_{13,14}$ during the voltage-droop parameter sweep, as this eigenvalue actually results from an interaction between the group B and the group D. This is why this eigenvalue has been classified in its own group, the group C. Because the stored energy of the MMCs is directly linked to the power flows of the transmission system, these eigenvalues are highly dependent on the system operating point.

- Group C:

Eigenvalues		Freq. (Hz)	Damp. ratio	Dominant States
$\lambda_{19,20}$	$-460.7 \pm j264.0$	42.02	0.868	$i_{3,z_2} x_{i_{gd_1}} x_{i_{gd_2}} x_{i_{gd_3}} i_{gd_1} i_{gd_2} i_{gd_3} x_{i_{dc_5}}$

As explained in the previous paragraph $\lambda_{19,20}$ is related to the dynamics of the DC current control of the MMCs equipped with voltage-droop controllers. However, this eigenvalue is also largely influenced by the states of the AC current loops of the Vdc-droop MMCs. In fact, since the Vdc-droop MMCs are sharing their energy with the DC bus, their respective AC side is virtually coupled to their DC side as in a standard Voltage Source Converter (VSC). The eigenvalue pair $\lambda_{19,20}$ then relates the interaction between the AC and DC currents, i.e. between the group B and the group D. These complex conjugate eigenvalues are even more impacted by the operating point than the ones of group B.

- Group D:

Eigenvalues		Freq. (Hz)	Damp. ratio	Dominant States
$\lambda_{21,22}$	$-222.8 \pm j194.4$	30.93	0.754	$i_{2,z_2} x_{i_{dc_2}} i_{gd_2} i_{gd_3} x_{i_{gd_2}} x_{i_{gd_3}}$
$\lambda_{23,24}$	$-235.8 \pm j175.6$	27.95	0.802	$i_{1,z_2} i_{2,z_2} x_{i_{gd_1}} i_{gd_1} W_{tot_1} x_{i_{dc_1}} x_{i_{gd_3}} i_{gd_3} x_{i_{dc_3}}$

The eigenvalues $\lambda_{19,20}$, $\lambda_{21,22}$ and $\lambda_{23,24}$ are associated to the AC currents control of the Vdc-droop MMCs and their corresponding 5% response time is close to the 10 ms tuning of the inner AC current loop. The eigenvalue pair $\lambda_{19,20}$, however, show a different behaviour than the other two eigenvalue pairs, as described above. They are moderately impacted by the operating point.

- Group E:

Eigenvalues		Freq. (Hz)	Damp. ratio	Dominant States
λ_{25}	-279.1	0	-	x_{idc_1} $x_{W_{tot1}}$ x_{idc_2} $x_{W_{tot2}}$ x_{idc_3} $x_{W_{tot3}}$

The eigenvalue λ_{25} corresponds to the dynamics of the DC current in the DC grid as imposed by the Vdc-droop MMCs. Indeed, this eigenvalue-associated 5% response time corresponds to the 5% response time of the DC current of Figures 5.8b and 5.8d ($\lambda_{25|k_v=0.05} = -248.9$, $\lambda_{25|k_v=0.10} = -279.1$, $\lambda_{25|k_v=0.20} = -325.0$ and $\lambda_{25|k_v=0.40} = -362.0$ which yield $tr_{5\%|k_v=0.05} = 12.1$ ms, $tr_{5\%|k_v=0.10} = 10.7$ ms, $tr_{5\%|k_v=0.20} = 9.2$ ms and $tr_{5\%|k_v=0.40} = 8.3$ ms). Ultimately, this mode represents the dynamics of the DC current following the reference generated by the energy controllers of the Vdc-droop MMCs (whose own reference signals are proportional to the square of the DC voltage at each converter terminals). This mode is also highly impacted by the operating point of the MTDC system.

- Group F:

Eigenvalues		Freq. (Hz)	Damp. ratio	Dominant States
$\lambda_{26,27}$	-513.0	0	-	$i_{1,z1}$ $i_{3,z1}$ $i_{4,z1}$ $i_{5,z1}$ $i_{6,z1}$
λ_{38}	-14.5	0	-	$i_{1,z3}$ $i_{2,z3}$ $i_{5,z3}$
λ_{39}	-15.0	0	-	$i_{1,z3}$ $i_{2,z2}$ $i_{2,z3}$
$\lambda_{40,41}$	-15.4	0	-	$i_{3,z3}$ $i_{4,z3}$ $i_{5,z3}$ $i_{6,z3}$
$\lambda_{46,47}$	-3.6	0	-	$i_{1,z3}$ $i_{4,z3}$ $i_{5,z3}$ $i_{6,z3}$
$\lambda_{48,49}$	-52.9	0	-	$i_{1,z2}$ $i_{3,z2}$ $i_{4,z2}$ $i_{5,z2}$ $i_{6,z2}$

The eigenvalues of this group are not impacted by the voltage-droop parameter sweep and correspond to DC resonances within the DC grid. In fact, the pole of the first RL branch of the DC cable model is equal to $-\frac{r_{z1}}{l_{z1}} = -513.0$ ($\lambda_{26,27}$); the pole of the second RL branch of the DC cable model is equal to $-\frac{r_{z2}}{l_{z2}} = -52.9$ ($\lambda_{48,49}$); and the pole of the third RL branch of the DC cable model is equal to $-\frac{r_{z3}}{l_{z3}} = -3.6$ ($\lambda_{46,47}$). Finally, the eigenvalues $\lambda_{38,\dots,41}$ are not impacted by the parameter sweep which implies a dependency on the DC grid only. Because these eigenvalues only depend on the system physical components, they are not affected by the operating point of the MTDC system.

- Group G:

Eigenvalues		Freq. (Hz)	Damp. ratio	Dominant States
λ_{28}	-106.5	0	-	$i_{1,z2}$ $i_{2,z2}$ x_{igd1} W_{tot1} x_{idc1} x_{igd3} x_{idc3}
λ_{29}	-118.2	0	-	$i_{1,z2}$ $i_{2,z2}$ x_{igd2} W_{tot2} x_{idc2} x_{igd3} x_{idc3}
λ_{30}	-129.9	0	-	$i_{3,z2}$ $i_{5,z2}$ $i_{6,z2}$ x_{idc4} W_{tot5} x_{idc5}
λ_{31}	-127.2	0	-	$i_{3,z2}$ $i_{4,z2}$ W_{tot4} x_{idc4}

The eigenvalues of this group are associated with the energy transfer between the MMCs and the DC grid. λ_{30} and λ_{31} are related to the P-mode MMCs and are

independent of the voltage-droop parameter sweep because the energy references of these converters are constants. λ_{25} , λ_{28} and λ_{29} are related to the Vdc-droop MMCs and are impacted by the voltage-droop parameter sweep because the energy references of these converters are proportional to the square of the DC voltage, which is directly influenced by the droop-parameter value. However, λ_{25} shows a very different behaviour with the parameter sweep as it also governs the dynamics of the DC current in the DC grid (see group E). Additionally, these modes are independent from the operating point of the system as they mostly depends on the converter capacitors and the controller gains which are not affected by the operating point.

• Group H:

Eigenvalues		Freq. (Hz)	Damp. ratio	Dominant States
$\lambda_{32,33}$	$-48.4 \pm j53.7$	8.50	0.670	$x_{idc1} x_{W_{tot1}} x_{W_{tot3}} W_{tot1} x_{idc1} W_{tot3} x_{idc3}$
$\lambda_{36,37}$	$-51.2 \pm j53.6$	8.52	0.691	$x_{idc2} x_{W_{tot2}} x_{W_{tot3}} W_{tot2} x_{idc2} x_{W_{tot2}} W_{tot3} x_{idc3}$
$\lambda_{42,43}$	$-52.7 \pm j53.2$	8.47	0.704	$x_{idc5} x_{W_{tot5}} W_{tot5}$
$\lambda_{44,45}$	$-52.7 \pm j53.2$	8.47	0.704	$x_{idc4} x_{W_{tot4}} W_{tot4}$

The eigenvalues of the group H are mainly related to the energy controllers of the MMCs and show a 5% time response similar to the 40 ms settling time of the energy controllers. On the one hand, $\lambda_{42,43}$ and $\lambda_{44,45}$ correspond to the energy controllers of the P-mode converters: they are not impacted by the voltage-droop parameter sweep as the energy references of the P-mode converters are independent of the DC voltage. On the other hand, $\lambda_{32,33}$, $\lambda_{34,35}$ and $\lambda_{36,37}$ correspond to the the energy controllers of the Vdc-droop MMCs. Even though all three eigenvalue pairs are influenced by the voltage-droop parameter sweep, only the pair $\lambda_{34,35}$ is largely impacted by the parameter sweep and has a singular behaviour. This is why this eigenvalue has been classified in its own group, the group I. Because these eigenvalues only depend on the system control loop parameters, they are not affected by the operating point of the MTDC system.

• Group I:

Eigenvalues		Freq. (Hz)	Damp. ratio	Dominant States
$\lambda_{34,35}$	$-41.4 \pm j36.7$	5.84	0.749	$x_{W_{tot1}} x_{W_{tot2}} x_{W_{tot3}} W_{tot1} W_{tot2} W_{tot3} x_{idc3}$

$\lambda_{34,35}$ is associated to the DC voltage, and thus, to the total stored energy of the Vdc-droop MMCs, and is largely impacted by the parameter sweep. In fact, this eigenvalue pair governs the MTDC system DC voltage overall dynamics by being directly related to the DC voltage response time. Indeed, this eigenvalue pair response time corresponds to the response time of the DC voltage of Figures 5.8a and 5.8c ($\lambda_{34,35}|_{k_v=0.05} = -45.46 \pm j43.99$, $\lambda_{34,35}|_{k_v=0.10} = -41.44 \pm j36.71$, $\lambda_{34,35}|_{k_v=0.20} = -37.21 \pm j26.27$ and $\lambda_{34,35}|_{k_v=0.40} = -33.73 \pm j10.76$ which yield $tr_{5\%|k_v=0.05} = 66.0$ ms, $tr_{5\%|k_v=0.10} = 72.4$ ms, $tr_{5\%|k_v=0.20} = 80.6$ ms

and $tr_{5\%|k_v=0.40} = 88.9$ ms). Ultimately, the eigenvalue pair $\lambda_{34,35}$ is the main driver behind the DC voltage time response of the system. Because these eigenvalues only depend on the MMC control parameters, they are not affected by the operating point of the MTDC system.

• Group J:

Eigenvalues		Freq. (Hz)	Damp. ratio	Dominant States
$\lambda_{50,63}$	$-216.2 \pm j208.0$	33.1	0.721	$x_{i_{gq1}} \ i_{gq1} \ x_{i_{gq2}} \ i_{gq2} \ x_{i_{gq3}} \ i_{gq3} \ x_{i_{gd4}} \ i_{gd4} \ x_{i_{gq4}} \ i_{gq4}$ $x_{i_{gd5}} \ i_{gd5} \ x_{i_{gq5}} \ i_{gq5}$

The eigenvalues of the group J correspond to the interaction between the d and q-axis outer control loops and the inner AC current loops of the P-mode converters, and of the q-axis outer control loops and the inner AC current loops of the Vdc-droop converters (the interaction between the d-axis outer loops (voltage droop) and the inner AC current loops of the Vdc-droop converters being described by the group D). Their associated 5% response time of 13.9 ms is close to the desired 10 ms settling time of the inner AC current loops of the MMCs. Because these eigenvalues only depend on the MMC control parameters, they are not affected by the operating point of the MTDC system.

• Group K:

Eigenvalues		Freq. (Hz)	Damp. ratio	Dominant States
$\lambda_{64,73}$	-1000	0	-	$\theta_{pll1} \ x_{pll1} \ \theta_{pll2} \ x_{pll2} \ \theta_{pll3} \ x_{pll3} \ \theta_{pll4} \ x_{pll4} \ \theta_{pll5} \ x_{pll5}$

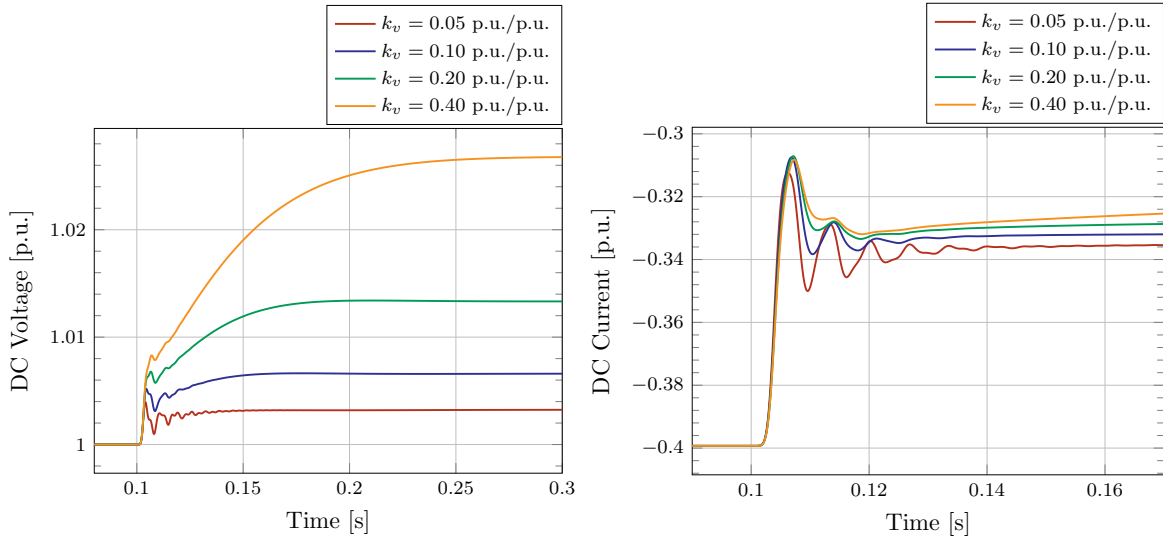
The eigenvalues of the group K are associated with the tuning of the PLL of each MMCs. Because these eigenvalues only depend on the MMC control parameters, they are not affected by the operating point of the MTDC system.

DC voltage and current responses to a power variation

The complete system state-space representation is now used to visualise the DC voltage (Figures 5.8a and 5.8c) and the DC current (Figures 5.8b and 5.8d) behaviour at the MMC 1 terminals for 4 different voltage-droop parameters and for two distinct scenarios:

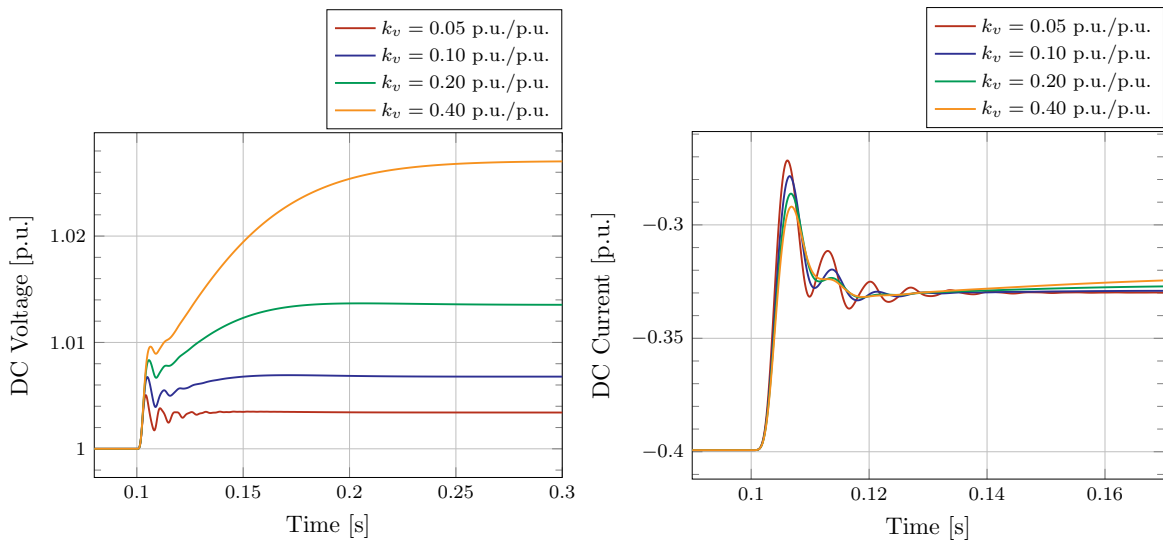
- Scenario 1: the MMC 4 starts injecting more power into the DC grid: -0.2 p.u. power reference step of the MMC 4 at $t = 0.1$ s.
- Scenario 2: the MMC 5 starts injecting more power into the DC grid: -0.2 p.u. power reference step of the MMC 5 at $t = 0.1$ s.

The fact that the power variation is generated by two different converters in the two scenarios induces a very different power flux distribution in the DC grid. This in turn greatly impacts the transient –and to a much lesser extent, the steady state value– of the DC voltage and current behaviours of the MTDC system.



(a) DC voltage output at the MMC1 terminals for an active power step of -0.2 p.u. of the MMC4.

(b) DC current output at the MMC1 terminals for an active power step of -0.2 p.u. of the MMC4.



(c) DC voltage output at the MMC1 terminals for an active power step of -0.2 p.u. of the MMC5.

(d) DC current output at the MMC1 terminals for an active power step of -0.2 p.u. of the MMC5.

Figure 5.8: Comparison of the DC voltage and current of the MMC1 for an active power step of -0.2 p.u. of either the MMC4 or the MMC5.

In fact, the transient of the DC voltage response of Figure 5.8a shows the superposition of two oscillation modes at a frequency of 135 Hz and 286 Hz respectively, which are especially visible for small values of the voltage-droop parameter. These frequencies correspond respectively to the eigenvalues $\lambda_{9,10}$ and $\lambda_{7,8}$ of the Table 5.2, related to the interaction between the d-axis control of the P-mode MMCs and the DC grid. The influence of the eigenvalue $\lambda_{7,8}$ on the DC voltage is still present but much less important in Figure 5.8c. Let aside the oscillations at the beginning of the transient, the behaviour of the DC voltage can be associated to a second order plant with a high damping ratio, or even to a first order plant for higher values of k_v . This transient is governed by the eigenvalue $\lambda_{34,35}$, as explained above. In fact, the response times for all values of k_v correspond to the response times observed in Figures 5.8a and 5.8c. Additionally, the complex conjugate eigenvalue pair $\lambda_{34,35}$ dissociates into two real eigenvalues as k_v increases, as shown in Figure 5.7b. This explains why the DC voltage behaviour corresponds to the one of a first order plant for higher values of k_v .

Since the three converters equipped with a voltage-droop controller are sharing their stored energy with the DC bus, their respective energy reference is varying with the square of the DC voltage, which, in turn, impacts the current reference of the inner DC current loop. This is why the dynamics of the DC voltage are reproduced for the DC current, hence the visualisation of oscillations at a frequency of 135 Hz –and to a lesser extent, 286 Hz.

Finally, the steady state values of the DC voltage are very similar for the two scenarii since the step is identical in both cases, albeit not applied to the same converters. This means that, neglecting the losses, since there are three converters that are equipped with voltage-droop controllers, the DC voltage deviation is equal to $\frac{-k_v \Delta P_g^*}{3}$ in both scenarii, i.e. $\Delta v_{dc1|k_v=0.05} = 0.0033$ p.u., $\Delta v_{dc1|k_v=0.10} = 0.0067$ p.u., $\Delta v_{dc1|k_v=0.20} = 0.0133$ p.u. and $\Delta v_{dc1|k_v=0.40} = 0.0267$ p.u., which correspond to the steady state values of Figures 5.8a and 5.8c.

5.3 Singular Value Decomposition Analysis of the 5-Terminal MTDC System

As illustrated by the modal analysis, the choice of the voltage-droop parameter of the converters plays a major role in the stability and the dynamics of an MTDC system. Moreover, the system must generally be designed in such way that its behaviour does not violate some given constraints on the maximum admissible DC voltage and current at all time. The Singular Value Decomposition (SVD) method offers a reliable way

to design the voltage-droop parameter by ensuring that the system does comply with these constraints both during transient and in steady state. In this section, the SVD method is applied to the MTDC system of Figure 5.2 to narrow the range of possible voltage-droop parameter candidates with regard to DC voltage and current constraints.

5.3.1 Motivation Behind the SVD Tool

a) Transfer Matrix of the Multi-Variable MTDC System

The considered 5-terminal MTDC system of Figure 5.2 is a MIMO system. The first SVD study focuses on the evolution of the DC voltage deviation of the 5 DC grid nodes (5 outputs: Δv_{dc_1} , Δv_{dc_2} , Δv_{dc_3} , Δv_{dc_4} and Δv_{dc_5}) when the system is excited by the power-reference deviations of the P-mode converters (2 inputs: $\Delta P_{g_4}^*$ and $\Delta P_{g_5}^*$). Thus, as portrayed in Figure 5.9, the basic transfer function model is $y(s) = G(s)u(s)$, where y is a 5×1 output vector, u is a 2×1 input vector and $G(s)$ is a 5×2 transfer function matrix.

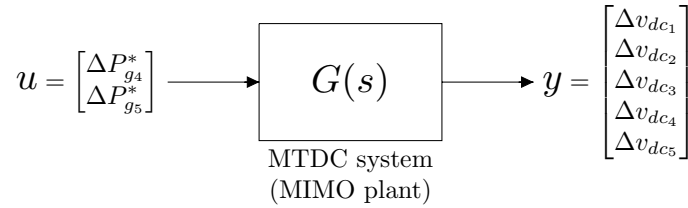


Figure 5.9: Transfer function model of the considered 5-terminal MTDC system.

The study aims at determining an range of voltage-droop gains that constrain the DC voltage deviation of each DC grid node (the outputs) within an interval of $\pm 5\%$, for any power-reference change of the P-mode converters (the inputs), from both a static and a dynamic point of view.

As the analysed system is a MIMO system, a change in one power reference of the converters, for example MMC 4, $\Delta P_{g_4}^*$, affects the DC voltage level of each node of the DC grid (the outputs Δv_{dc_1} , Δv_{dc_2} , Δv_{dc_3} , Δv_{dc_4} and Δv_{dc_5}). Hence, even if different power reference deviation input vectors (i.e. vectors of the form $u = \begin{bmatrix} \Delta P_{g_4}^* & \Delta P_{g_5}^* \end{bmatrix}^T$) have the same norm, they can have very distinct impacts on the DC voltage deviation output vectors (i.e. vectors of the form $y = \begin{bmatrix} \Delta v_{dc_1} & \Delta v_{dc_2} & \Delta v_{dc_3} & \Delta v_{dc_4} & \Delta v_{dc_5} \end{bmatrix}^T$). This illustrates the main difference between a Single-Input Single-Output (SISO) system and a MIMO system: the presence of *directions* in the latter that impacts the *gain* of the plant [103].

In fact, the gain matrix of the system $G(s)$ between the input signal $u(\omega)$ and the induced output $y(\omega)$ is given by, in terms of the L^2 norm:

$$\begin{aligned} \frac{\|y(\omega)\|_2}{\|u(\omega)\|_2} &= \frac{\|G(j\omega)u(\omega)\|_2}{\|u(\omega)\|_2} \\ &= \frac{\sqrt{\Delta v_{dc1}^2 + \Delta v_{dc2}^2 + \Delta v_{dc3}^2 + \Delta v_{dc4}^2 + \Delta v_{dc5}^2}}{\sqrt{\Delta P_{g4}^{*2} + \Delta P_{g5}^{*2}}} \\ &= \frac{\sqrt{\sum_{j=1}^5 (\sum_{k=1}^2 g_{jk} \Delta P_{g_k}^*)^2}}{\sqrt{\Delta P_{g4}^{*2} + \Delta P_{g5}^{*2}}} \end{aligned} \quad (5.4)$$

where g_{jk} is the gain of the system for the output j in the direction of the input k .

Equation (5.4) shows that the gain of the system depends on the frequency ω , and since the system is linear, it is independent of the input magnitude $\|u(\omega)\|_2$. However, the gain depends on the *direction* of the input u .

Frequency Response of an MTDC System

The singular value decomposition technique can be considered as an expansion of the Bode frequency representation for multi-variable systems, in the sense that the SVD takes into account the input and output directions of the system.

The singular values of the system transfer function matrix $G(j\omega)$ at the pulsation ω are given by:

$$\sigma_i(G(j\omega)) = \sqrt{\lambda_i(G^\top(j\omega)G(j\omega))} \quad (5.5)$$

where $\lambda_i(\cdot)$ is the i -th eigenvalue of the matrix $G^\top G$.

Since the gain depends on the direction of the input vector, which can significantly change with the pulsation ω , the gain in different directions of the system at any pulsation ω must be considered by extracting the maximum gain among all the possible input vectors. The singular values obtained with (5.5) express the gain of each input direction in the output directions of the system (see [103] for more details).

The maximum singular value $\bar{\sigma}(G(j\omega))$ is defined as the largest gain for *any* input direction $u(\omega)$ at pulsation ω :

$$\bar{\sigma}(G(j\omega)) \triangleq \max_{u \neq 0} \frac{\|G(j\omega)u(\omega)\|_2}{\|u(\omega)\|_2} \quad (5.6)$$

The maximum allowable voltage deviation and the maximum possible power-reference change of the converters can then be represented as a gain boundary in the multi-variable frequency response of the MTDC system. In fact, by ensuring that the maximum singular value does not bypass the gain boundaries corresponding to the DC voltage deviation, the MTDC system is assured to comply with the imposed constraint.

It is to be noted that the SVD analysis cannot see any stability problem due to the definition of (5.5): the multiplication of the system matrix G by its transposed matrix G^\top (i.e. $G^\top G$) induces a loss of information on the sign of the real part of the eigenvalues of G as the eigenvalues of $G^\top G$ are equal to the square of the eigenvalues of G . This is why the SVD tool must always be used together with a stability study to prevent any misleading results. The use of both the modal analysis and the SVD tool to study a system is then coherent as the two methods complement one another.

Comparison between the SVD and the Transfer Functions

The SVD representation is a useful tool that allows the quantification of the maximum gain of the system, a task that can not be achieved by solely studying its transfer function. In fact, the individual study of all the transfer functions is not only heavy (as their number grows rapidly with that of inputs and outputs of the system), but also misleading since the gain of the MIMO system depends on the direction of the input vector, and hence this gain can not be assessed by studying separately the transfer function between each input-output pair of the system.

Figure 5.10 shows a comparison between the SVD representation and the 10 transfer functions of the 5-terminal MTDC system whose input and output vectors are respectively $u = [\Delta P_{g_4}^* \quad \Delta P_{g_5}^*]^\top$ and $y = [\Delta v_{dc_1} \quad \Delta v_{dc_2} \quad \Delta v_{dc_3} \quad \Delta v_{dc_4} \quad \Delta v_{dc_5}]^\top$.

The SVD representation corresponds to the maximum possible gain of the system, that is, the system gain in the most amplified direction of the output vector at any pulsation ω . Hence, the maximum gain of the system is always bigger than the maximum of all the individual transfer function gains, as illustrated in Figure 5.10. And since the maximum of the singular values depends on the root mean square of the DC voltage deviations $\Delta v_{dc_1}, \Delta v_{dc_2}, \Delta v_{dc_3}, \Delta v_{dc_4}$ and Δv_{dc_5} , the SVD shape follows the pattern of the transfer function with the biggest gain (especially when one of the outputs is more amplified than the others).

The results of the SVD analysis provide an easy and simple way of studying the frequency response of the MIMO system with regard to its multiple inputs. However, since it basically takes into account all possible transfer functions as well as the impact

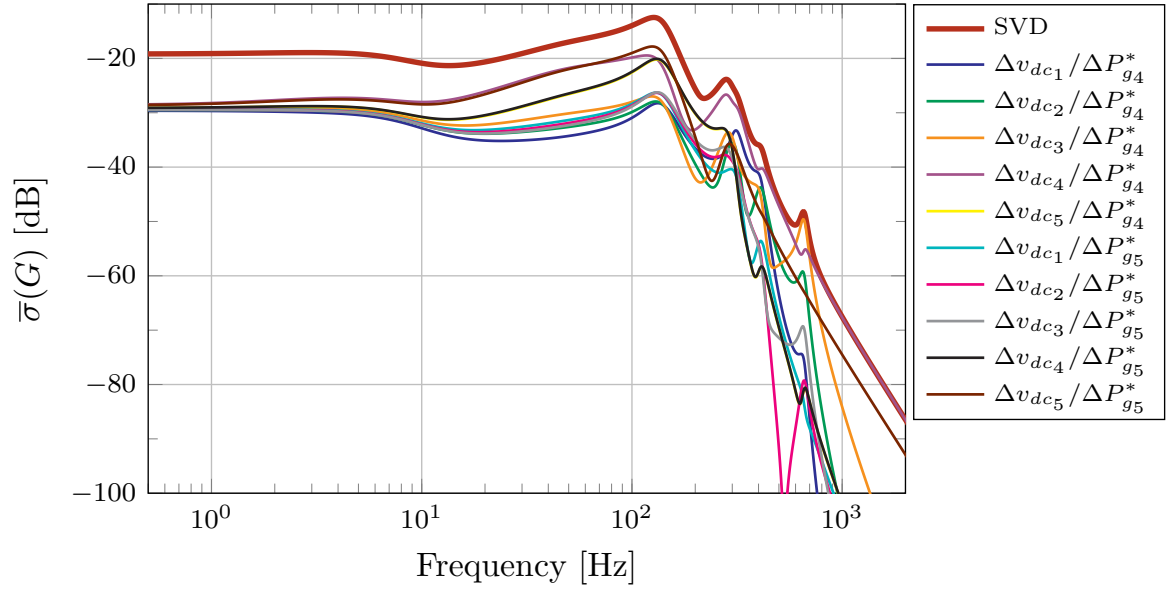


Figure 5.10: Comparison of the SVD results with the individual transfer functions of the 5-terminal MTDC system, for a voltage-droop parameter of 0.1 p.u./p.u.

of the direction of the input vector on the plant, these results are often very conservative and can lead to unreasonable parameter tuning of real life system controls.

5.3.2 Design of the Voltage-Droop Gain using the SVD Tool

The selection of the value of the voltage-droop parameter k_v is crucial to ensuring the proper behaviour of the MTDC system since this parameter highly impacts the DC voltage level of the HVDC grid (both in transient and steady state) and thus the conformity of the system to the maximum allowable DC voltage constraint of $\pm 5\%$.

The impact of the voltage-droop parameter on the MTDC system can easily be assessed from a static point of view, as in [12] and [8], where a power reference modification ΔP_g^* of one of the converters generates a computable DC voltage deviation. However, from a dynamic point of view, it is necessary to investigate how the voltage-droop parameter impacts the system transient, or its behaviour when excited by oscillatory inputs, like the output power of the WFC, or poorly-damped power oscillations generated by the AC grids.

a) The DC Voltage Constraint

The DC voltage constraint of $\pm 5\%$ can be represented as a constant boundary and compared to the frequency response of the maximum singular values of the MTDC

system. Since this constant boundary is determined from the maximum possible input, then if the maximum singular values does not exceed this constraint boundary at any pulsation ω , the DC voltages of every node of the DC grid of the MTDC system are guaranteed to satisfy the maximum DC voltage constraint.

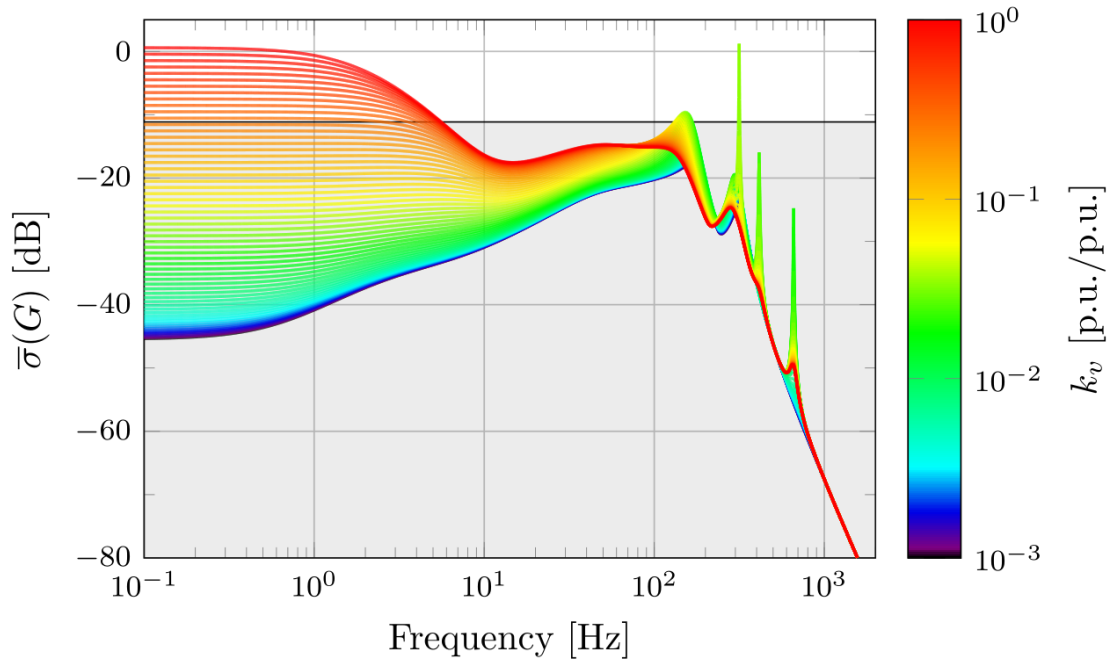
The power reference of the 3 Vdc-droop MMCs is assumed to be fixed at a given operating point by the TSOs of their respective AC grids (the system operating point is illustrated by Figure 5.2) hence their possible power reference deviation is null (i.e. $\Delta P_{g_{1,2,3}}^* = 0$). The possible power reference deviation of the 2 P-mode MMCs can go as high as $\Delta P_{g_4}^* = 0.2$ p.u. and $\Delta P_{g_5}^* = 0.35$ p.u. for the MMC 4 and 5 respectively (corresponding to the power reference deviation needed by the converters to go from their operating point to zero). This means that, for the frequency response of the DC voltage deviation output vector $y = [\Delta v_{dc_1} \ \Delta v_{dc_2} \ \Delta v_{dc_3} \ \Delta v_{dc_4} \ \Delta v_{dc_5}]^\top$ with regards to the power-reference deviations input vector $u = [\Delta P_{g_4}^* \ \Delta P_{g_5}^*]^\top$, the $\pm 5\%$ maximum DC voltage constraint (i.e. ± 0.05 p.u.) becomes:

$$\begin{aligned} & 20 \log_{10} \left(\frac{\sqrt{5 \cdot \Delta v_{dc_{\max}}^2}}{\sqrt{\Delta P_{g_{4\max}}^{*2} + \Delta P_{g_{5\max}}^{*2}}} \right) \\ &= 20 \log_{10} \left(\frac{\sqrt{5 \cdot (0.05)^2}}{\sqrt{((0.2)^2 + (0.35)^2)}} \right) \\ &= -11.14 \text{ dB} \end{aligned} \tag{5.7}$$

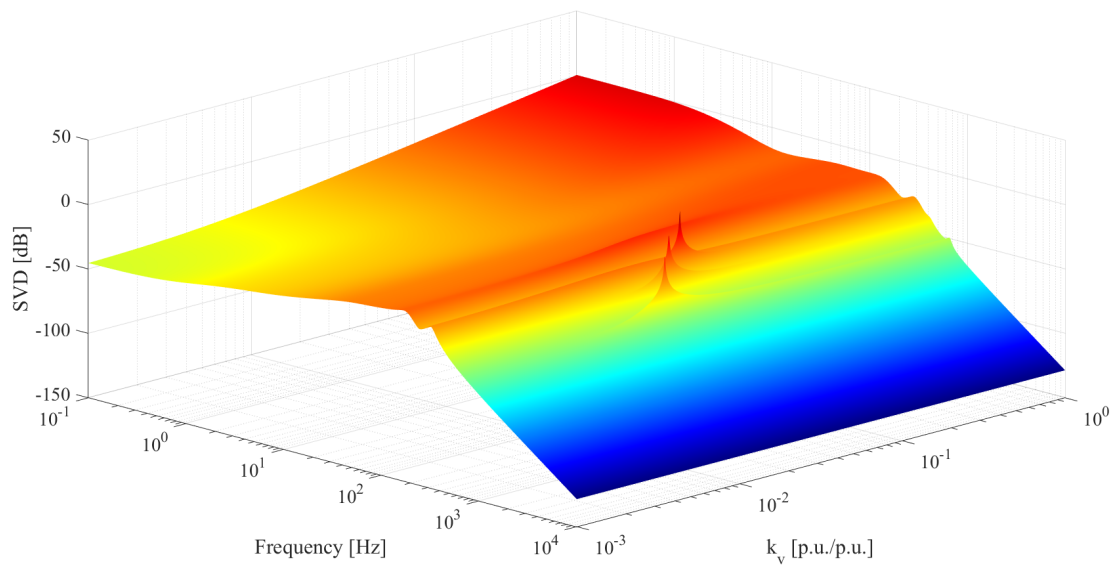
The value -11.14 dB determines the constant boundary that is not to be violated by the frequency response of the system.

b) SVD Analysis of the 5-Terminal HVDCs System

To simplify the study, the three voltage-droop parameters of the three Vdc-droop MMCs are assumed to be equal at all times. Figures 5.11a and 5.11b show the maximum singular value $\bar{\sigma}(G)$ for different values of the voltage-droop parameter of the three Vdc-droop MMCs when the DC cables are modelled by a fitted PI section. In order to satisfy the $\pm 5\%$ voltage deviation constraint, the maximum of the singular values must not bypass the constraint boundary computed in (5.7), i.e. must be strictly located in the grey area of Figure 5.11a. Figure 5.11b shows a 3D representation of the SVD results that gives a better understanding of the evolution of the maximum of the singular value with increasing values of the voltage-droop parameter.



(a) SVD results, with the grid node voltages as outputs and the active power reference of the P-mode converters as inputs, for different values of the voltage-droop parameter of the MMCs.



(b) 3D representation of the SVD results for a sweep of the voltage-droop parameter of the MMCs.

Figure 5.11: SVD results for a sweep of the voltage-droop parameter of the MMCs.

In steady state (i.e. for very low frequencies of the SVD), Figure 5.11a shows that the DC voltage constraint of a maximum $\pm 5\%$ deviation is violated for a wide range of the voltage-droop parameter: when $k_v \in [0.2586; 1]$. This is consistent with the theoretical results in first approximation, when neglecting the voltage drop in the DC lines: $k_{v,\max} = 3 \cdot \Delta v_{dc,\max} / (\Delta P_{g4,\max}^* + \Delta P_{g5,\max}^*) = 3 \cdot 0.05 / (0.2 + 0.35) = 0.2727$. However, this is not the only limitation on the voltage-droop parameter selection as the dynamics of the system can cause the system to bypass the DC voltage constraint. In fact, resonance peaks are observed at relatively low frequencies. These resonances can violate the maximum allowable DC voltage deviation imposed on the MTDC system during the transient, for example when the P-mode MMCs power references excite the system at those frequencies.

The first resonance peak around 140 Hz is related to the eigenvalue $\lambda_{9,10}$ of Table 5.2 and is the most harmful mode with regard to the DC voltage deviation of the system as it is present for every voltage-droop parameter. However, only the SVD results for the range of voltage-droop parameter $k_v \in [0.01743; 0.06339]$ do bypass the DC voltage constraint because of this mode. The second resonance peak at 285 Hz is related to the eigenvalue $\lambda_{7,8}$ and shows the same behaviour albeit with a lesser gain. As a consequence, this second mode does not result in any SVD bypassing the constraint. As explained in the previous section, these two resonances result from modes corresponding to an interaction between the d-axis current control of the two P-mode converters and the DC grid.

The three resonance peaks at 310 Hz, 410 Hz and 650 Hz correspond to the eigenvalue pairs $\lambda_{5,6}$, $\lambda_{3,4}$ and $\lambda_{1,2}$ respectively. These resonances result from an interaction between the d-axis current control of the Vdc-droop MMCs and the DC grid. They are present for a very narrow range of the voltage-droop parameter, and only the first resonance can be harmful for the system with regard to the DC voltage constraint. In fact, the maximum singular value bypasses the DC voltage constraint only for $k_v \in [0.03174; 0.03673]$ because of this 310 Hz resonance.

As a result of both the steady state and transient behaviour of the 5-terminal MTDC system, the only voltage-droop parameter values (k_v) that strictly satisfy the DC voltage constraint for *any frequency* are located between 0 and 1.74% and then between 6.33 and 25.86% (i.e. $k_v \in]0; 0.01743[\cup]0.06339; 0.2586[$). However, the stability study brought by the modal analysis of the previous section showed that the system is not stable for voltage-droop parameter smaller than $k_v < 0.03450$ p.u./p.u., which leads to the final possible range of voltage-droop parameters $k_v \in]0.06339; 0.2586[$.

Some complementary studies with different constraints, such as the maximum current amplitude in the IGBT of the converters, will then narrow further the possible range of the droop value [80, 81, 79]. However, in the case of this specific MTDC system, the SVD results of the DC current deviation with regard to the power reference deviation of the P-mode converters do not add any more restriction to the voltage-droop parameter range, as depicted in Figure 5.12. This is explained by the fairly low amount of power transmitted by the converters of the MTDC system, and hence the small value of the DC current transiting through the IGBT valve in normal operation conditions, by comparison to the maximum admissible current of an IGBT valve.

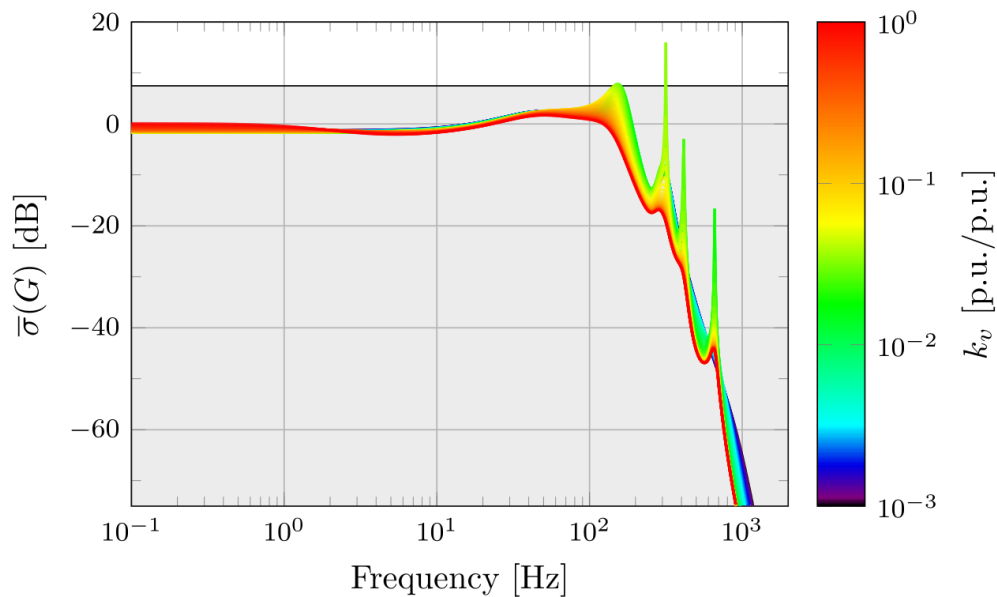


Figure 5.12: SVD results, with the DC currents of the Vdc-droop MMCs as outputs and the active power reference of the P-mode converters as inputs, for different values of the voltage-droop parameter of the MMCs.

When sizing the controller gains using the SVD tool, one has to bear in mind that the SVD results are very conservative in the sense that the system can never violate the considered constraint, even for a very short period of time. This can lead to unrealistic parameters that would never be used in reality, where compromises can yield much smaller costs for both the vendor or the TSO of the system.

5.4 Impact of the DC Cable Model on the SVD Results

The previous section showed that the dynamics of the system can play a determining role in complying with the DC voltage constraint. Because of the numerous dynamics induced by the converter control loops, particular attention must be paid to the frequency domain validity of the linear cable models used to compute the state-space representation of the MTDC system. In this section, four very basic cable models are presented and then used to generate the DC grid in order to assess their impact on the dynamics of the MTDC system.

5.4.1 Wideband Model Reference

The *wideband* cable model is an accurate, frequency-dependent cable model [66] that is available in the EMTP-RV[®] library, and is used as the reference for the state-space cable models.

The cables are designed for a transmissible power of 1000 MW, with an XLPE insulation for 320 kV and a cable length of 300 km. Their geometrical and electrical data are shown in Figure 5.13 and Table 5.3. These data are inserted in an EMTP-RV[®] routine which generates the wideband model of the cable from its geometrical and physical specifications. In the next section, the impedance of the state-space cable models is to be compared with the impedance of this accurate cable model in order to give an appreciation of the difference between the models.

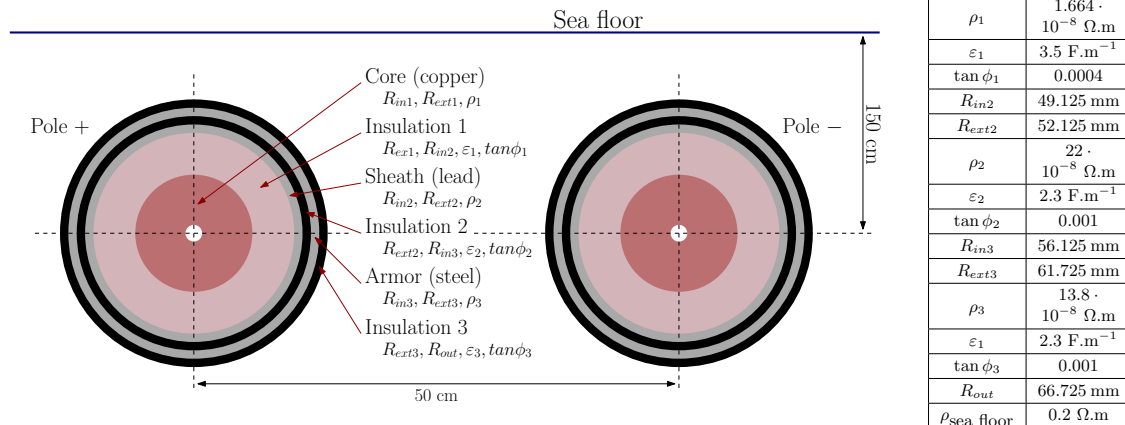


Figure 5.13: Underwater layout of the reference cable.

Table 5.3: Cable parameters.

5.4.2 DC Cable Models Used in this Study

The four cable models used in this study are illustrated in Figure 5.14. Their respective state-space models are described below.

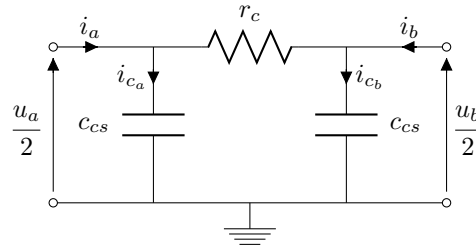
Since the DC capacitors have a strong impact on the DC voltage, the first DC cable model is simply a resistor-capacitor (RC) section as depicted in Figure 5.14a. Its state-space representation is recalled by (5.8).

$$\begin{aligned} \frac{d}{dt} \begin{bmatrix} u_a \\ u_b \end{bmatrix} &= \begin{bmatrix} \frac{-1}{r_c c_{cs}} & \frac{1}{r_c c_{cs}} \\ \frac{1}{r_c c_{cs}} & \frac{-1}{r_c c_{cs}} \end{bmatrix} \begin{bmatrix} u_a \\ u_b \end{bmatrix} + \begin{bmatrix} \frac{2}{c_{cs}} & 0 \\ 0 & \frac{2}{c_{cs}} \end{bmatrix} \begin{bmatrix} i_a \\ i_b \end{bmatrix} \\ \begin{bmatrix} u_a \\ u_b \end{bmatrix} &= \begin{bmatrix} 1 & 0 \\ 0 & 1 \end{bmatrix} \begin{bmatrix} u_a \\ u_b \end{bmatrix} + \begin{bmatrix} 0 & 0 \\ 0 & 0 \end{bmatrix} \begin{bmatrix} i_a \\ i_b \end{bmatrix} \end{aligned} \quad (5.8)$$

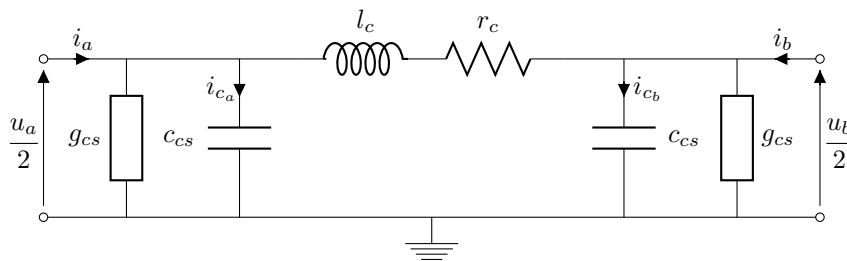
The second model is the classical PI section model used in [80] and [81] and depicted in Figure 5.14b. Its state-space representation is recalled by (5.9).

$$\begin{aligned} \frac{d}{dt} \begin{bmatrix} u_a \\ u_b \\ i_{rl} \end{bmatrix} &= \begin{bmatrix} \frac{-g_{cs}}{c_{cs}} & 0 & \frac{-2}{c_{cs}} \\ 0 & \frac{-g_{cs}}{c_{cs}} & \frac{2}{c_{cs}} \\ \frac{1}{2l_c} & \frac{-1}{2l_c} & \frac{-r_c}{l_c} \end{bmatrix} \begin{bmatrix} u_a \\ u_b \\ i_{rl} \end{bmatrix} + \begin{bmatrix} \frac{2}{c_{cs}} & 0 \\ 0 & \frac{2}{c_{cs}} \end{bmatrix} \begin{bmatrix} \dot{i}_a \\ \dot{i}_b \end{bmatrix} \\ \begin{bmatrix} u_a \\ u_b \end{bmatrix} &= \begin{bmatrix} 1 & 0 & 0 \\ 0 & 1 & 0 \end{bmatrix} \begin{bmatrix} u_a \\ u_b \\ i_{rl} \end{bmatrix} + \begin{bmatrix} 0 & 0 \\ 0 & 0 \end{bmatrix} \begin{bmatrix} i_a \\ i_b \end{bmatrix} \end{aligned} \quad (5.9)$$

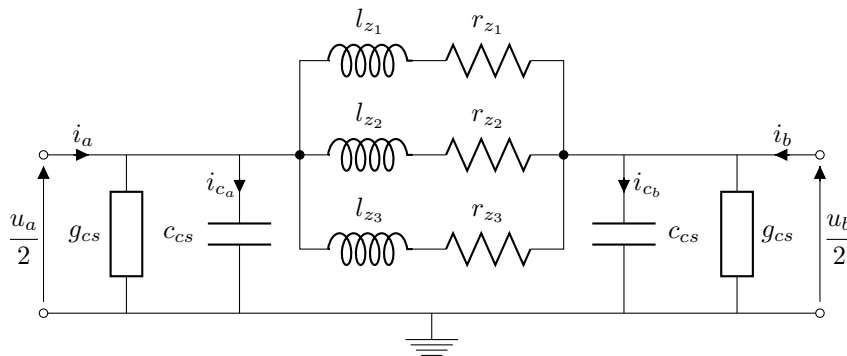
The third DC cable model is the one that was used in the previous sections. It is basically an improved classical PI-section with parallel branches, as depicted in Figure 5.14c and described in [21, 22]. A judicious choice of the component values in the parallel branches enables this simple model to fit the frequency response of a more detailed model such as the wide-band model [83]. The component values are automatically determined by a MATLAB fitting algorithm, depending on the number of parallel branches desired by the user [57, 56]. In this case, a model with three parallel branches is adopted. Its state-space representation is described by (5.10).



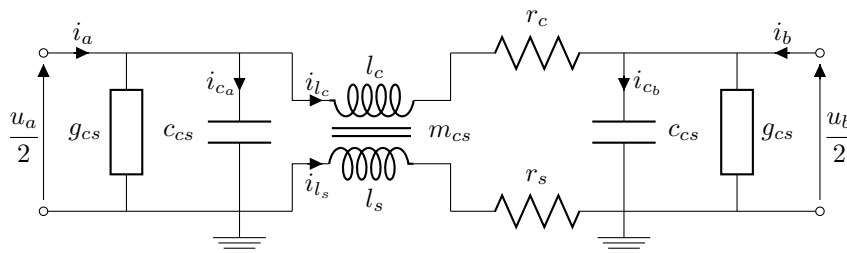
(a) RC model of a DC cable.



(b) Classical PI model of a DC cable.



(c) Fitted PI model of a DC cable.



(d) Coupled PI model of a DC cable.

Figure 5.14: Representation of the 4 cable models used in this section.

$$\begin{aligned}
\frac{d}{dt} \begin{bmatrix} u_a \\ u_b \\ i_{z1} \\ i_{z2} \\ i_{z3} \end{bmatrix} &= \begin{bmatrix} \frac{-g_{cs}}{c_{cs}} & 0 & \frac{-2}{c_{cs}} & \frac{-2}{c_{cs}} & \frac{-2}{c_{cs}} \\ 0 & \frac{-g_{cs}}{c_{cs}} & \frac{2}{c_{cs}} & \frac{2}{c_{cs}} & \frac{2}{c_{cs}} \\ \frac{1}{2l_{z1}} & \frac{-1}{2l_{z1}} & \frac{-r_{z1}}{l_{z1}} & 0 & 0 \\ \frac{1}{2l_{z2}} & \frac{-1}{2l_{z2}} & 0 & \frac{-r_{z2}}{l_{z2}} & 0 \\ \frac{1}{2l_{z3}} & \frac{-1}{2l_{z3}} & 0 & 0 & \frac{-r_{z3}}{l_{z3}} \end{bmatrix} \begin{bmatrix} u_a \\ u_b \\ i_{z1} \\ i_{z2} \\ i_{z3} \end{bmatrix} + \begin{bmatrix} \frac{2}{c_{cs}} & 0 \\ 0 & \frac{2}{c_{cs}} \\ 0 & 0 \\ 0 & 0 \\ 0 & 0 \end{bmatrix} \begin{bmatrix} \dot{i}_a \\ \dot{i}_b \end{bmatrix} \\
\begin{bmatrix} u_a \\ u_b \end{bmatrix} &= \begin{bmatrix} 1 & 0 & 0 & 0 & 0 \\ 0 & 1 & 0 & 0 & 0 \end{bmatrix} \begin{bmatrix} u_a \\ u_b \\ i_{z1} \\ i_{z2} \\ i_{z3} \end{bmatrix} + \begin{bmatrix} 0 & 0 \\ 0 & 0 \end{bmatrix} \begin{bmatrix} i_a \\ i_b \end{bmatrix}
\end{aligned} \tag{5.10}$$

Finally, the fourth DC cable model is an improved PI section where the coupling between the core and the screen of the cable is represented by a mutual inductance between the two [84, p. 52], as pictured in Figure 5.14d. This coupling generates a current that flows through the resistance of the screen, and since this resistance is significant, the transient state of the current is better damped overall than when the screen is totally neglected (as with a classical PI section).

According to Figure 5.14d, the Kirchhoff's current law gives:

$$\begin{aligned}
i_{c_a} &= i_a - i_c - g_{cs} \frac{u_a}{2}, \\
i_{c_b} &= i_b + i_c - g_{cs} \frac{u_b}{2}
\end{aligned} \tag{5.11}$$

and the Kirchhoff's voltage law gives:

$$\begin{aligned}
u_{l_c} &= \frac{u_a}{2} - \frac{u_b}{2} - r_c i_c, \\
u_{l_s} &= -r_s i_s
\end{aligned} \tag{5.12}$$

and the evolution of the capacitor voltages obeys:

$$\begin{aligned}
\frac{du_a}{dt} &= \frac{2}{c_{cs}} i_{c_a}, \\
\frac{du_b}{dt} &= \frac{2}{c_{cs}} i_{c_b}
\end{aligned} \tag{5.13}$$

while the evolution of the inductance currents obeys:

$$\begin{cases} \Phi_c = l_c i_{l_c} + m_{cs} i_{l_s} \\ \Phi_s = l_s i_{l_s} + m_{cs} i_{l_c} \end{cases} \quad (5.14)$$

i.e.

$$\begin{cases} u_{l_c} = \frac{d\Phi_c}{dt} = l_c \frac{di_{l_c}}{dt} + m_{cs} \frac{di_{l_s}}{dt} \\ u_{l_s} = \frac{d\Phi_s}{dt} = l_s \frac{di_{l_s}}{dt} + m_{cs} \frac{di_{l_c}}{dt} \end{cases} \quad (5.15)$$

which yields:

$$\begin{cases} \frac{di_{l_c}}{dt} = \frac{-l_s}{l_c l_s - m_{cs}^2} u_{l_c} + \frac{m_{cs}}{l_c l_s - m_{cs}^2} u_{l_s} \\ \frac{di_{l_s}}{dt} = \frac{m_{cs}}{l_c l_s - m_{cs}^2} u_{l_c} - \frac{l_c}{l_c l_s - m_{cs}^2} u_{l_s} \end{cases} \quad (5.16)$$

hence the state-space:

$$\begin{aligned} \frac{d}{dt} \begin{bmatrix} u_a \\ u_b \\ i_{l_c} \\ i_{l_s} \end{bmatrix} &= \begin{bmatrix} \frac{-g_{cs}}{c_{cs}} & 0 & \frac{-2}{c_{cs}} & 0 \\ 0 & \frac{-g_{cs}}{c_{cs}} & \frac{2}{c_{cs}} & 0 \\ \frac{-l_s}{2(m_{cs}^2 - l_c l_s)} & \frac{l_s}{2(m_{cs}^2 - l_c l_s)} & \frac{-r_c l_s}{m_{cs}^2 - l_c l_s} & \frac{-m_{cs} r_s}{m_{cs}^2 - l_c l_s} \\ \frac{m_{cs}}{2(m_{cs}^2 - l_c l_s)} & \frac{-m_{cs}}{2(m_{cs}^2 - l_c l_s)} & \frac{-m_{cs} r_s}{m_{cs}^2 - l_c l_s} & \frac{r_s l_c}{m_{cs}^2 - l_c l_s} \end{bmatrix} \begin{bmatrix} u_a \\ u_b \\ i_{l_c} \\ i_{l_s} \end{bmatrix} + \begin{bmatrix} \frac{2}{c_{cs}} & 0 \\ 0 & \frac{2}{c_{cs}} \\ 0 & 0 \\ 0 & 0 \end{bmatrix} \begin{bmatrix} i_a \\ i_b \end{bmatrix} \\ \begin{bmatrix} u_a \\ u_b \end{bmatrix} &= \begin{bmatrix} 1 & 0 & 0 & 0 \\ 0 & 1 & 0 & 0 \end{bmatrix} \begin{bmatrix} u_a \\ u_b \\ i_{l_c} \\ i_{l_s} \end{bmatrix} + \begin{bmatrix} 0 & 0 \\ 0 & 0 \end{bmatrix} \begin{bmatrix} i_a \\ i_b \end{bmatrix} \end{aligned} \quad (5.17)$$

Figure 5.15 shows a comparison between the modelled cable impedances during a frequency scan and pictures the wideband reference cable model impedance. It can be observed that both the classical PI section and the coupled PI section show a resonance between 30-50 Hz that is not present in the reference wideband model, and thus can be detrimental to the study of the MTDC system dynamics. The impedance of the fitted PI section, however, reproduces the wideband cable impedance with a better fidelity (up to 300 Hz). This can even be improved by adding additional parallel branches to the cable model [21, 22].

It is to be noted that none of the cable models proposed above reproduces the behaviour of the wideband reference cable at higher frequencies where they act as low-pass filters instead. This needs to be taken into account when studying the system's

behaviour at high frequencies. For instance, the modal analysis of the previous section showed there were a few eigenvalues with a corresponding frequency above 300 Hz so their impact on the system may be underestimated by the SVD method.

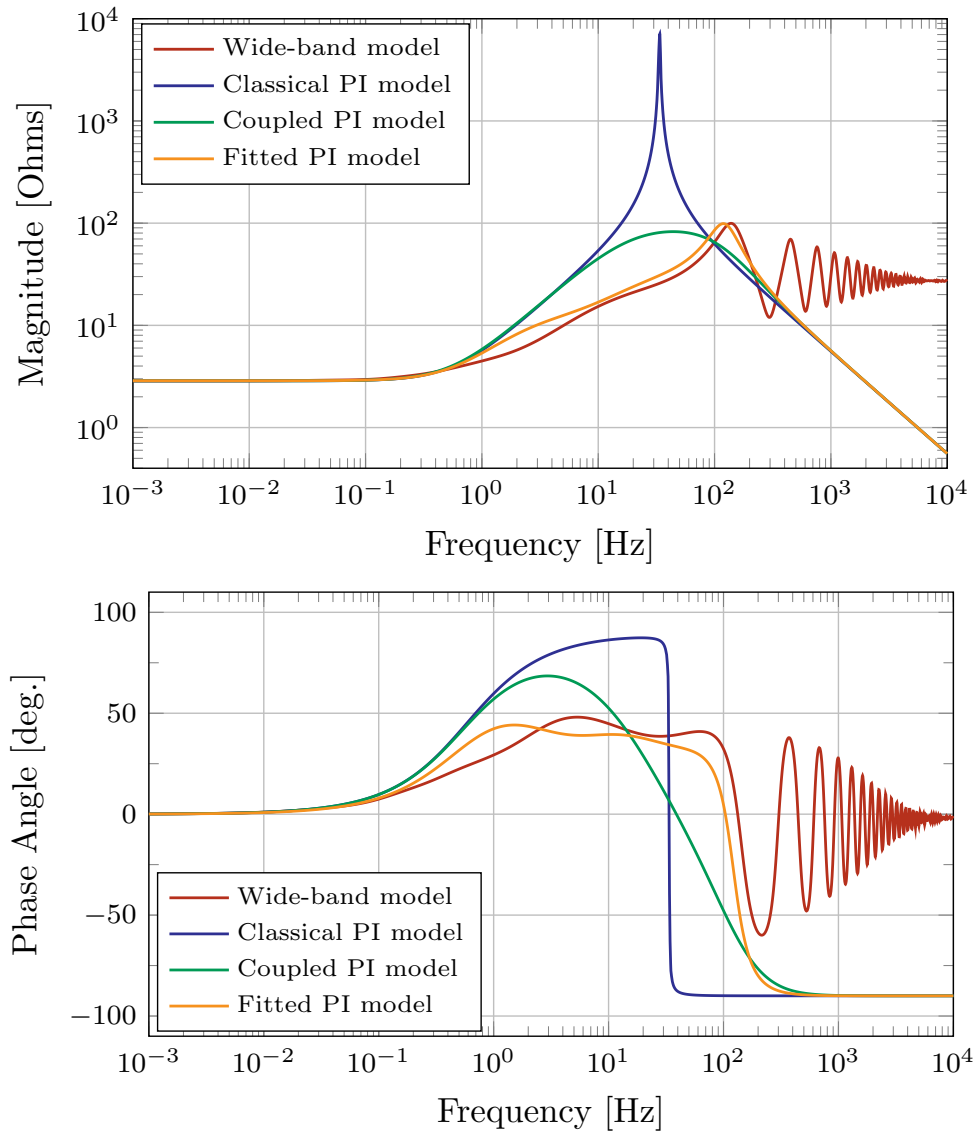


Figure 5.15: Comparison of the cable impedances of the classical PI model, the Coupled PI model and the Fitted PI model to the impedance of a more detailed wide-band cable model.

5.4.3 Comparison of the SVD Results for the 5 DC grid Models

Figure 5.16 shows the frequency response of the MTDC system when the DC grid is modelled as an equivalent DC capacitor, and then with the four DC cable models of Figure 5.14 (i.e. when the DC cables are modelled by a simple RC section, a classical PI section, a fitted PI section and a coupled PI section), for voltage-droop parameter values (k_v) of 0.001 p.u./p.u., 0.004 p.u./p.u., 0.016 p.u./p.u., 0.063 p.u./p.u., 0.25 p.u./p.u. and 1.00 p.u./p.u. (chosen arbitrarily).

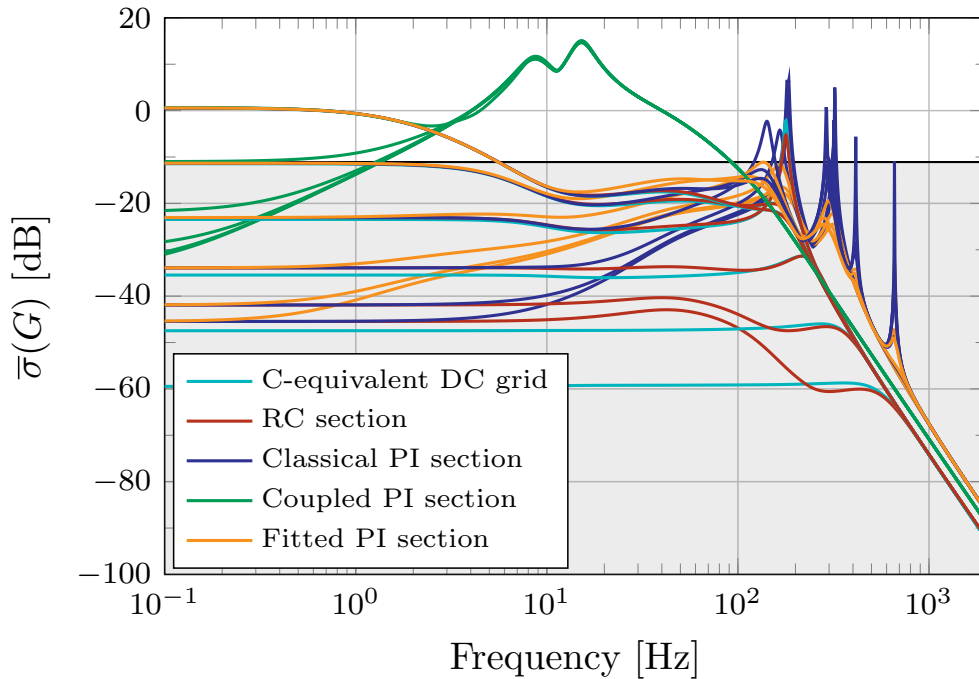


Figure 5.16: SVD results, with the grid node voltages as outputs and the active power reference of the P-mode converters as inputs, for 5 different cable models and 6 different values of the voltage-droop parameter of the MMCs.

In steady state, the five DC grid models have the same behaviour and their respective SVD satisfy the maximum allowable voltage-deviation constraint until $k_v = 0.25$ p.u./p.u., which is consistent with the theoretical results of the static study. The only singularity between the different DC grid models is the capacitor equivalent model for very small value of the voltage-droop parameter. This is caused by the voltage drop across the cables (due to their resistance) which is then of the same order of magnitude as the voltage deviation of the voltage-droop, while this is not an issue for the capacitor equivalent DC grid since the resistor of the lines have been omitted.

At high frequencies (>1 kHz), the system acts as a low-pass plant: as illustrated by Figure 5.15, the cable models act as low-pass filters. Thankfully, the modal analysis

showed there was no eigenvalue with a frequency above 700 Hz so there is no resonance peaks omitted by the modelling of the DC grid. Finally, the SVD results for the capacitor equivalent, the RC section, the classical PI section and the fitted PI section show some similarities while the results for the coupled PI section shows a very different behaviour.

In fact, from a dynamic point of view, it appears that the use of both a capacitor equivalent and a RC section results in a single resonance peak around 160 Hz corresponding to the mode associated to the interaction between the power flows in the system and the DC grid, i.e. the main driver behind the dynamics of the DC voltage (corresponding to the dominant DC voltage mode identified in [51]). Similarly, this mode is also found with both the classical PI and the fitted PI sections as their respective SVD results present a first resonance peak around 140 Hz (corresponding to the eigenvalue $\lambda_{9,10}$ of Table 5.2), even though this resonance peak is greatly attenuated with the fitted PI section. These two models then show 4 additional resonances which are once again much more attenuated in the case of the fitted PI section than for the classical PI section. This total of 5 resonance peaks results from the interaction between the additional components of the DC cables (i.e. the inductances and the conductances of the cables) and the power flows of the 5 converters, which implies that the modelling of the cable by a mere equivalent capacitor or by an RC circuit is not precise enough to represent the interaction between the DC grid and the converters. Finally, the coupled PI section presents two resonance peaks at 8 and 14 Hz corresponding to resonances within the DC grid that are not impacted at all by the voltage-droop parameter. With this cable model, the high-frequency dynamics induced by the converters are invisible.

With regard to the DC voltage constraint of $\pm 5\%$, the DC cable model clearly impact the results of the SVD. The modelling of the DC grid as an equivalent capacitor, or with cables modelled by RC sections, lead to a system that does not take into account all the interactions between the DC grid and the converters, which is detrimental to the study of the system. Similarly, the use of the coupled PI section is not recommended as the DC grid acts as a firewall between the different converters, hence preventing any possible interactions between the subsystems of the MTDC system. Finally, the use of a classical PI section reproduces the interaction between the converters and the DC grid but with unreasonable resonances that cause the SVD to unnecessarily bypass the DC voltage constraint. The use of a fitted PI section seems to be the best solution to study the system and a greater number of parallel branches of the cable model could even lead to more precise results.

5.5 Chapter Conclusion

The design of MTDC systems should ensure that the DC voltage does not exceed a maximum allowable DC voltage deviation constraint. Hence, the choice of the voltage-droop parameter of the converters is extremely important because it impacts the DC voltage behaviour of the system. Yet, while the choice of the droop parameter from a static point of view can easily be achieved, its range must be narrowed even further in order for the system to also comply with the DC voltage constraint from a dynamic point of view.

As in the previous chapter, the modal analysis of the system provides its dynamic properties and allows the thorough analysis of the system modes. As for an HVDC link, the modes associated to the power flows in the DC grid determine the stability of the system. They are associated to three complex conjugate pairs of eigenvalues, each corresponding to one converter participating in the DC voltage regulation via the voltage-droop control technique. Similarly to the HVDC link, a mode that primarily drives the DC voltage behaviour can also be identified.

An MTDC system is a MIMO plant. Thus, its input and output vectors have directions that greatly impact the gain of the system, making the study of the transfer functions inadequate. The frequency response analysis can still be performed thanks to the Singular Value Decomposition (SVD) method, where the maximum of the singular values expresses the maximum possible gain of the system at any pulsation ω . In this chapter, the SVD analysis leads to a set of acceptable voltage-droop parameters that allow the system to comply with a maximum DC voltage deviation constraint both in steady-state (static point of view) and during transient (dynamic point of view). The SVD tool and the modal analysis perfectly complement one another as they give a complete and thorough understanding of the system dynamic behaviour. However, one has to keep in mind that the results of the SVD study can be very conservative, and certain constraints can be relaxed for a short period in the time domain in real-life system in order to loosen the restrictions on the parameters of the system.

The SVD representations of the 5-terminal, MMC-based MTDC system are obtained for different DC cable models. They show that the DC grid should not be modelled as an equivalent capacitor, or with DC cables modelled as RC sections because some of the system dynamics resulting from an interaction between the DC grid components and the converters are then omitted. They also show that modelling the DC cables with a coupled PI section is not adequate as it cannot reflect any possible interaction between the DC grid and the converters. Finally, the use of a classical PI section, generally used to model the DC cables, gives a rather accurate representation of the

dynamic behaviour of the MTDC system, but causes unreasonable resonance peaks that prevent the study the system behaviour with regards to a given constraint. The use of an improved PI section model of the DC cables (called fitted PI section) gives a more accurate representation of the SVD of the MTDC system, and shows that, for the MTDC system in pentagon shape of this paper, two separate ranges of voltage-droop parameter values allow the system to comply with the DC voltage constraint. However, the stability study brought by the modal analysis narrowed it further by eliminating the first range of voltage-droop parameter.

The SVD tool can easily be computed for any system whose state-space representation is known. While this study focused on a pentagon-shaped, 5-terminal, MMC-based MTDC system, this work can easily be reproduced for any MTDC system with any DC grid topology and any converter technology.

Chapter 6

A Frequency Droop Technique for the MTDC to Support AC Grid Frequency

Only thru annihilation of distance in every respect, as the conveyance of intelligence, transport of passengers and supplies and transmission of energy will conditions be brought about some day, insuring permanency of friendly relations.

– N. Tesla in *My Inventions, Chapter 5 : The Influences That Shape Our Destiny* (February-June and October 1919) [107].

6.1 Chapter Introduction

The share of Renewable Energy Sources (RES) in the global electricity generation is gradually increasing in every nation worldwide. However, in opposition to conventional generation units, RES do not participate in the frequency regulation of AC grids as of today, even though it is being increasingly discussed. As a result, primary reserve sharing between AC networks and participation of the AC/DC converters in the onshore grids frequency regulation is under consideration. Development of a new control technique is now required to allow the AC/DC converters of the MTDC to participate in the primary frequency regulation of the AC systems. This can be achieved through the power electronics of the converters by using a frequency-droop controller based on the same principle as the frequency regulation controllers used in conventional generation units in AC grids [60, 86, 26, 73]. The power deviation generated by the frequency droop of the converter must correspond to a precise value with regards to the frequency deviation of the grid, and in compliance with the AC grid codes.

The previous chapter presented the voltage-droop control technique that provides an efficient way of controlling the DC voltage and the power flows in an MTDC system. This chapter considers a control strategy that combines both the voltage-droop and the frequency-droop control techniques. This dual control enforces the stability of the DC grid thanks to the DC voltage droop, and at the same time allows the MTDC system to participate in the frequency regulation of the different AC grids interconnected by the meshed HVDC grid thanks to the frequency droop of the converters. Only a few papers used the two droop controls at the same time on a single VSC-HVDC converter. While [26] focuses on the eigenvalues of the system and [114] describes the use of a dead-band control for both droops, those two papers do not discuss interactions between the two droops. Without going into further details, [60] reports that the frequency droop does not give the desired value for a given frequency deviation. Reference [86] deeply surveys the interactions between the AC grids and the DC grid through a modal analysis, whose conclusion was that the use of both droops resulted in a modification of the DC voltage dynamics and smaller frequency deviations. Finally, [73] observed the interaction between the two droops through the evolution pattern of the frequency of each AC area, but did not propose a correction of the droop parameters to account for this interaction.

The present chapter reveals the existence of a coupling between the two droops of the dual controller that degrades their overall performances. The interactions between the frequency droop and the voltage droop are mathematically quantified and

a correction of the frequency-droop parameter is proposed so that the frequency droop still fulfils the agreement with the TSO despite the coupling between the two droops. A simulation using the software EMTP-RV[®] is run to validate the theoretical study. Finally, the dual controller is implemented on the real mock-up MTDC system of the L2EP Lille laboratory.

6.2 MTDC Systems to Support the AC grids Frequency Regulation

This section explains the working principle of both the voltage-droop and the frequency-droop control. Then, it considers a control strategy combining the advantages of the two techniques.

The modelling and the control of the VSC-HVDC converter has already been covered in the previous chapters. The overall command strategy is depicted in Figure 6.1. The two droops directly modify the power reference of the active power loop of the converter.

In this section, the i^{th} converter of a n -converter MTDC system is considered.

6.2.1 Proposition for a Frequency-Droop Controller

The primary frequency control is currently used by conventional generation units in AC grids. If the frequency drops below (respectively rises above) its nominal value, the conventional units inject more (resp. less) power into the AC grid in order to stabilise the frequency of the system.

The frequency droops proposed in [60, 86, 26, 73] are based on a similar principle: a frequency deviation generates a proportional power deviation response of the converter. The main differences between these papers lie in the global control of the VSC-HVDC (see Figure 6.1 for the global control of the converter used in this thesis) and the expected use of the proposed controller. Reference [75] proposed a more complex controller able to emulate the behaviour of a conventional generation unit when participating in the frequency regulation. However, the proposed frequency-droop controller completely negates the action of any eventual voltage-droop controller and relies on activating/deactivating different control loops depending on the present event.

The solution adopted in the present chapter is the same as [86]. Its operating principle is very similar to the one of the voltage droop. A converter equipped with a frequency-droop control participates in the frequency regulation of the AC grid it

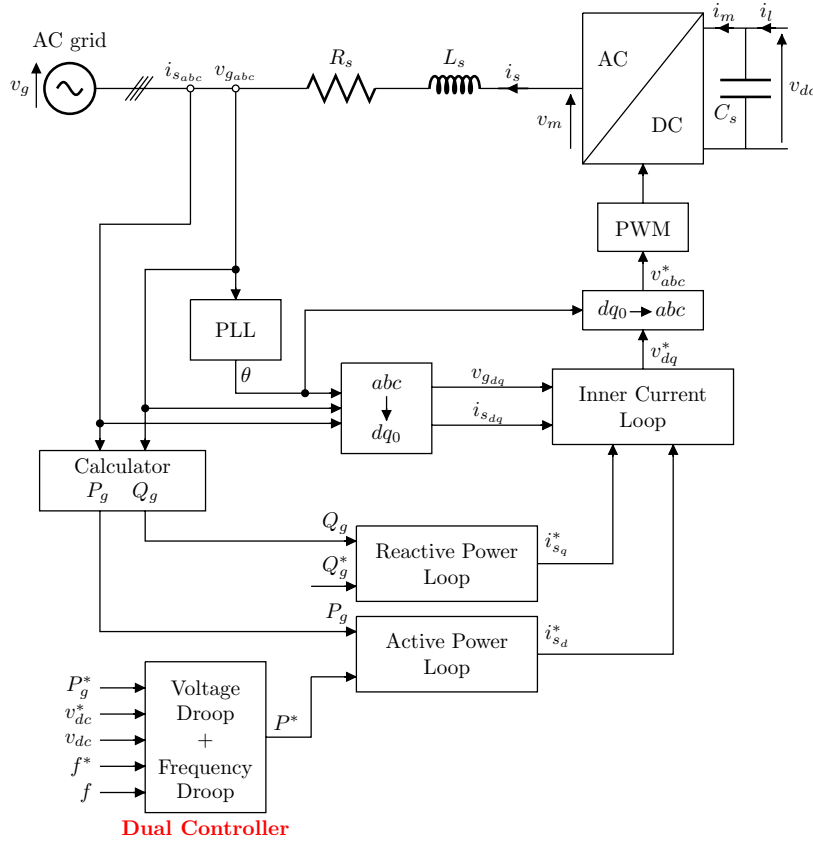


Figure 6.1: Control strategy of a VSC-HVDC converter

is connected to and modifies its power reference by following the characteristic line whose slope is $\frac{1}{k_f}$, where k_f is to the frequency-droop parameter:

$$\Delta P_{f_i}^* = \frac{1}{k_{f_i}} \Delta f_i \quad (6.1)$$

where:

- $\Delta P_{f_i}^*$ is the power reference deviation generated by the frequency-droop controller of the i^{th} VSC-HVDC converter. A positive $\Delta P_{f_i}^*$ corresponds to a power injection from the DC grid to the AC grid.
- k_{f_i} is the frequency-droop parameter of the i^{th} converter, $k_{f_i} > 0$.
- $\Delta f_i = f_i^* - f_i$.

Each controller has limits that prevent the converter from moving too far away from its original operating point. The frequency-droop controller can also be equipped with a dead-band of ± 10 mHz corresponding to the standard frequency dead-band

used by ENTSO-E [96]. However, since the dead-band has a small impact on the MTDC system, and to simplify the mathematical expressions in the next section, the dead-band is not considered in this work.

The block diagram of the frequency-droop control technique is depicted in Figure 6.2.

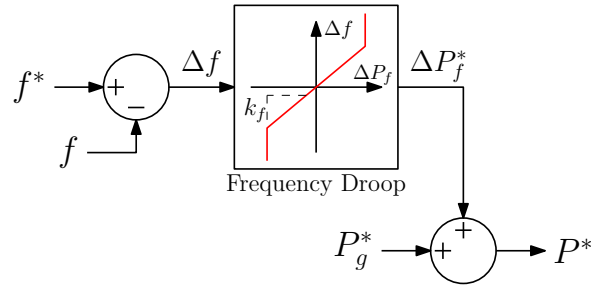


Figure 6.2: Block diagram of the frequency-droop technique.

6.2.2 Voltage Droop and Frequency Droop: a Dual Controller

The voltage-droop control technique provides a strong and reliable DC grid, while the frequency-droop control technique provides assistance to the interconnected AC grids. An ideal MTDC system should have both: a strong and reliable DC grid as well as a good support to the interconnected AC grids.

The combination of those two control techniques leads to a dual controller (Figure 6.3) that enjoys both their respective advantages. However, the combination of the two droops also leads to undesirable side-effects which will be further discussed in the next section.

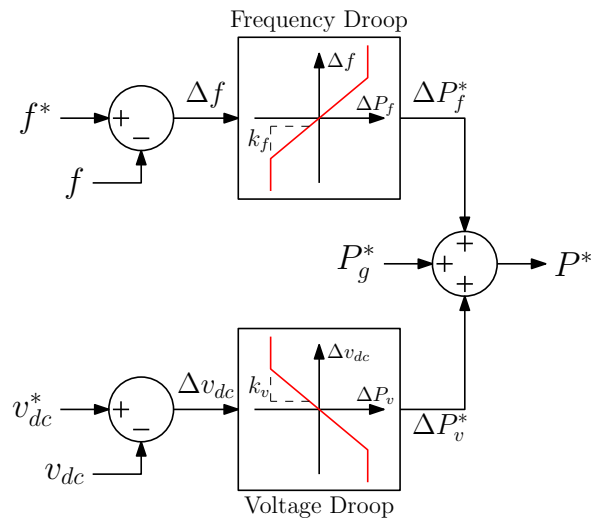


Figure 6.3: Block diagram of the dual controller combining both the voltage- and the frequency-droop techniques.

With this dual controller each converter operating point does not move along a single line any longer but obeys (6.2). If the considered converter i is not equipped with a voltage-droop and/or a frequency-droop controller then $k_{v_i} = -\infty$ and/or $k_{f_i} = \infty$.

$$\begin{aligned}\Delta P_i^* &= \Delta P_{v_i}^* + \Delta P_{f_i}^* \\ &= \frac{1}{k_{v_i}} \Delta v_{dc_i} + \frac{1}{k_{f_i}} \Delta f_i\end{aligned}\quad (6.2)$$

6.2.3 Interactions between Voltage and Frequency Droop

As stated above, there exists a coupling between the two droops used in the dual controller. For example, if the DC voltage decreases (resp. increases), the voltage droop modifies the amount of power injected/withdrawn by the converter so that there is either less (resp. more) power withdrawn from the DC grid or more (resp. less) power injected into the DC grid. This, in turn, decreases (resp. increases) the frequency of the AC grid connected to the converter and the frequency droop opposes the action of the voltage droop, resulting in unintended interactions between the AC grids and the DC grid.

This coupling is problematic since it degrades the performances of both the voltage droop and the frequency droop, as detailed in the following section. However, when the AC grid needs frequency support, priority should be given to the frequency droop since the TSO of the concerned AC grid expects a rigorous value of the frequency droop for the VSC-HVDC converter. This means the impact of the voltage droop on the frequency droop must be quantified and the frequency-droop parameter must be corrected in order to comply with the TSO requirements.

In this subsection, the limits of each droop controllers are discarded to facilitate study and understanding. An additional and more complex theoretical study taking into account the limits of each controller is detailed in the last subsection of this segment.

In order to simplify the equations, the following simplifying assumption is made: the DC voltage *variations* are identical at all nodes of the HVDC grid. This is equivalent to neglecting the evolution of the power losses in the DC grid, without neglecting the power losses themselves since they are accounted for in the initial operating point of the MTDC system. This assumption is mathematically described by (6.3) and is validated in Section 6.3 by the EMTP-RV[®] simulations.

Hence, for an MTDC system with n converters:

$$\forall j \in \{1, \dots, n\}, \quad \Delta v_{dc_j} = \Delta v_{dc} \quad (6.3)$$

After an AC event such as the loss of a generation unit or a load change, the effective power deviation of each converter obeys its reference described by (6.2), which gives:

$$\forall j \in \{1, \dots, n\}, \quad \Delta P_j = \frac{1}{k_{v_j}} \Delta v_{dc} + \frac{1}{k_{f_j}} \Delta f_j \quad (6.4)$$

The sum of the n equations (6.4) gives:

$$\sum_{j=1}^n \Delta P_j = \sum_{j=1}^n \frac{1}{k_{v_j}} \Delta v_{dc} + \sum_{j=1}^n \frac{1}{k_{f_j}} \Delta f_j \quad (6.5)$$

Since the possible variation of the power losses is neglected and that the power on the DC grid is balanced by the converters equipped with a voltage droop, we have $\sum_{j=1}^n \Delta P_j = 0$. Thus (6.5) becomes:

$$\sum_{j=1}^n \frac{1}{k_{v_j}} \Delta v_{dc} = - \sum_{j=1}^n \frac{1}{k_{f_j}} \Delta f_j \quad (6.6)$$

which leads to a new expression of Δv_{dc} :

$$\Delta v_{dc} = \frac{-1}{\sum_{j=1}^n \frac{1}{k_{v_j}}} \sum_{j=1}^n \frac{1}{k_{f_j}} \Delta f_j \quad (6.7)$$

Let us now consider the i^{th} converter of the MTDC system. Replacing Δv_{dc} in (6.4) by (6.7) yields:

$$\Delta P_i = \frac{-1}{k_{v_i} \sum_{j=1}^n \frac{1}{k_{v_j}}} \left(\sum_{j=1}^n \frac{1}{k_{f_j}} \Delta f_j \right) + \frac{1}{k_{f_i}} \Delta f_i \quad (6.8)$$

Equation (6.8) shows that the power deviation of the i^{th} converter consists of:

- ▷ The power deviation created by the sum of the frequency droops of every converter on the DC grid weighted by $\frac{-1}{k_{v_i} \sum_{j=1}^n \frac{1}{k_{v_j}}}$. This coefficient depends on the contribution of each converter participating in the DC voltage regulation of the DC grid (voltage-droop parameters k_{v_j}).
- ▷ The power deviation created by the frequency droop of the i^{th} converter.

Since the maximum power deviation of an AC/DC converter is limited and that the total power transmitted through a converter is usually small compared to the AC grid total active power, then if there is no AC fault occurring at the same time on the other AC grids, their respective frequency deviations Δf are negligible. In the case

where several VSCs (e.g. the p first VSCs with $p < n$) are connected to the faulty AC grid, and assuming the frequency is identical everywhere in a synchronous AC grid on the time scale of frequency control, then when summing the power deviations of all the converters connected to the faulty AC grid, Equation (6.8) becomes:

$$\Delta P_{AC_{grid}} = \sum_{i=1}^p \Delta P_i = \sum_{i=1}^p \left(\frac{-\sum_{j=1}^p \frac{1}{k_{f_j}}}{k_{v_i} \sum_{j=1}^n \frac{1}{k_{v_j}}} + \frac{1}{k_{f_i}} \right) \Delta f_{AC_{grid}} \quad (6.9)$$

6.2.4 Correction of the Frequency-Droop Parameter

In order to facilitate the understanding of the method, only the case where a single VSC is connected to the faulty AC grid (i.e. $p = 1$) is considered in the rest of this section. However, the methodology remains the same and can be easily generalised for $p > 1$. For $p = 1$, Equation (6.9) becomes:

$$\Delta P_i = \frac{1}{k_{f_i}} \left(1 - \frac{1}{k_{v_i} \sum_{j=1}^n \frac{1}{k_{v_j}}} \right) \Delta f_i \quad (6.10)$$

Because of the interaction between the frequency droop and the voltage droop, the actual relation between the AC grid frequency and the converter connected to this grid is now described by (6.10). This means the effective frequency-droop value, k'_{f_i} (ratio of the frequency and the power extracted or withdrawn from the AC grid), is not equal to the initial frequency-droop value k_{f_i} ; in fact $k'_{f_i} = \frac{\Delta f_i}{\Delta P_i} = \frac{k_{f_i}}{\left(1 - \frac{1}{k_{v_i} \sum_{j=1}^n \frac{1}{k_{v_j}}} \right)}$.

In order for the effective frequency droop to satisfy the contractual frequency-droop value $k_{f_{i_{contractual}}}$ required by the TSO, the initial frequency-droop parameter k_{f_i} must be corrected such that the corrected value takes into account the voltage-droop parameter of each converter of the DC grid:

$$k_{f_i} = k_{f_{i_{contractual}}} \left(1 - \frac{1}{k_{v_i} \sum_{j=1}^n \frac{1}{k_{v_j}}} \right) \quad (6.11)$$

Equation 6.11 expresses the fact that the power deviation of a converter equipped with the dual controller combining the voltage and the frequency droop is proportional to the frequency deviation of the AC grid the converter is connected to and depends on: (a) the frequency-droop parameter of the considered converter; (b) the voltage-droop parameters of each converter of the MTDC system.

In this case, the effective frequency-droop value (k'_{f_i}) is actually equal to the contractual frequency-droop value ($k_{f_i\text{contractual}}$) agreed with the TSO.

6.2.5 Impact of the Droop Controller Limits

In this subsection, the limits of the controllers are taken into account: both droop controllers have limits that prevent the power deviation generated by each droop of the i^{th} VSC from becoming higher than $\pm\Delta P_{v_{i\text{max}}}$ for the voltage-droop controller, and $\pm\Delta P_{f_{i\text{max}}}$ for the frequency-droop controller. The expressions of ΔP_{v_i} and ΔP_{f_i} are now:

$$\begin{aligned}\Delta P_{v_i} &= -\sigma(\Delta u_s) \min \left\{ \left| \frac{1}{k_{v_i}} \Delta u_s \right|, \Delta P_{v_{i\text{max}}} \right\} \\ \Delta P_{f_i} &= \sigma(\Delta f_i) \min \left\{ \left| \frac{1}{k_{f_i}} \Delta f_i \right|, \Delta P_{f_{i\text{max}}} \right\}\end{aligned}\quad (6.12)$$

where $\sigma(\cdot)$ is defined as follows for $x \in \Re$:

$$\sigma(x) = \begin{cases} 1 & \text{if } x > 0 \\ 0 & \text{if } x = 0 \\ -1 & \text{if } x < 0 \end{cases}\quad (6.13)$$

In non-critical operation conditions of the HVDC grid (i.e. when at least one VSC of the MTDC system has not reached its maximum allowed deviation with regard to the DC voltage $\Delta P_{v_{i\text{max}}}$), Equation (6.4) becomes:

$$\Delta P_j = -\sigma(\Delta u_s) \min \left\{ \left| \frac{1}{k_{v_j}} \Delta u_s \right|, \Delta P_{v_{j\text{max}}} \right\} + \sigma(\Delta f_j) \min \left\{ \left| \frac{1}{k_{f_j}} \Delta f_j \right|, \Delta P_{f_{j\text{max}}} \right\}\quad (6.14)$$

Similarly to the previous subsection, Equation (6.6) becomes:

$$\sigma(\Delta u_s) \sum_{j=1}^n \min \left\{ \left| \frac{1}{k_{v_j}} \Delta u_s \right|, \Delta P_{v_{j\text{max}}} \right\} = \sum_{j=1}^n \sigma(\Delta f_j) \min \left\{ \left| \frac{1}{k_{f_j}} \Delta f_j \right|, \Delta P_{f_{j\text{max}}} \right\}\quad (6.15)$$

Let us assume the VSCs are numbered such that the m first VSCs are those which have already reached their respective $\Delta P_{v_{\text{max}}}$ and the $n - m$ VSCs left are operating in normal conditions (i.e. they have not reached their respective $\Delta P_{v_{\text{max}}}$). Then the

new expression of Δu_s is:

$$\Delta u_s = \frac{1}{\sum_{j=m+1}^n \frac{1}{|k_{v_j}|}} \left[-\sigma(\Delta u_s) \sum_{j=1}^m \Delta P_{v_{j\max}} + \sum_{j=1}^n \sigma(\Delta f_j) \min \left\{ \left| \frac{1}{k_{f_j}} \Delta f_j \right|, \Delta P_{f_{j\max}} \right\} \right] \quad (6.16)$$

Let us now consider the i^{th} converter of the MTDC system ($i > m$). Since $k_{v_j} < 0$ and $k_{f_j} > 0$, inserting (6.16) in (6.14) yields:

$$\Delta P_i = \frac{-1}{k_{v_i} \sum_{j=m+1}^n \frac{1}{k_{v_j}}} \left[-\sigma(\Delta u_s) \sum_{j=1}^m \Delta P_{v_{j\max}} + \sum_{j=1}^n \sigma(\Delta f_j) \min \left\{ \frac{1}{k_{f_j}} |\Delta f_j|, \Delta P_{f_{j\max}} \right\} \right] + \sigma(\Delta f_i) \min \left\{ \frac{1}{k_{f_i}} |\Delta f_i|, \Delta P_{f_{i\max}} \right\} \quad (6.17)$$

If there is no AC fault occurring at the same time on the other AC grids, Δf_j for $j \neq i$ are negligible. In the case where the i^{th} VSC's maximum allowed power deviation with regard to the frequency is not reached, then (6.17) becomes:

$$\Delta P_i = \frac{1}{k_{f_i}} \left(1 - \frac{1}{k_{v_i} \sum_{j=m+1}^n \frac{1}{k_{v_j}}} \right) \Delta f_i + \frac{\sigma(\Delta u_s)}{k_{v_i} \sum_{j=m+1}^n \frac{1}{k_{v_j}}} \sum_{j=1}^m \Delta P_{v_{j\max}} \quad (6.18)$$

In order for the effective frequency droop to satisfy the contractual frequency-droop value, the implemented frequency-droop parameter must be dynamically modified every time a VSC of the HVDC grid reaches its maximum allowed power deviation with regard to the DC voltage. The dynamically changed frequency-droop parameter takes into account the fact that a VSC of the DC grid does not participate in the voltage droop of the DC voltage any longer since it has reached its limit.

The dynamic frequency-droop parameter must be:

$$k_{f_i\text{contractual}} \left(1 - \frac{1}{k_{v_i} \sum_{j=m+1}^n \frac{1}{k_{v_j}}} \right) \quad (6.19)$$

hence the power reference deviation created by the frequency-droop controller becomes:

$$\Delta P_i = \frac{1}{k_{f_i\text{contractual}}} \Delta f_i \quad (6.20)$$

Remarks:

- While communication between VSCs is not needed for the static frequency-droop controller of (6.11) in the previous subsection, the dynamic frequency-droop controller needs communication between the VSCs in order to know which controller of the DC grid converters has reached its upper or lower limit (i.e. the value of m) so that the new frequency-droop parameter can be computed accordingly to (6.19). The communication speed is not necessarily fast since the evolution of the AC grids frequencies is slow in comparison to the usual communication delay between HVDC terminals (which is smaller than 100 ms), and thus the effect of the delay caused by the communication system is very small.
- Dynamically modifying the frequency-droop parameter also impacts the value of the voltage-droop parameter because of the aforementioned coupling between the two droops, and thus can induce a modification of the dynamics of the MTDC system DC voltage, as detailed in [12]. However, since the dynamic frequency-droop controller is designed such that the effective value of the frequency-droop parameter corresponds to the contractual value at all times, the impact on the voltage droop and thus on the DC dynamics is very limited.

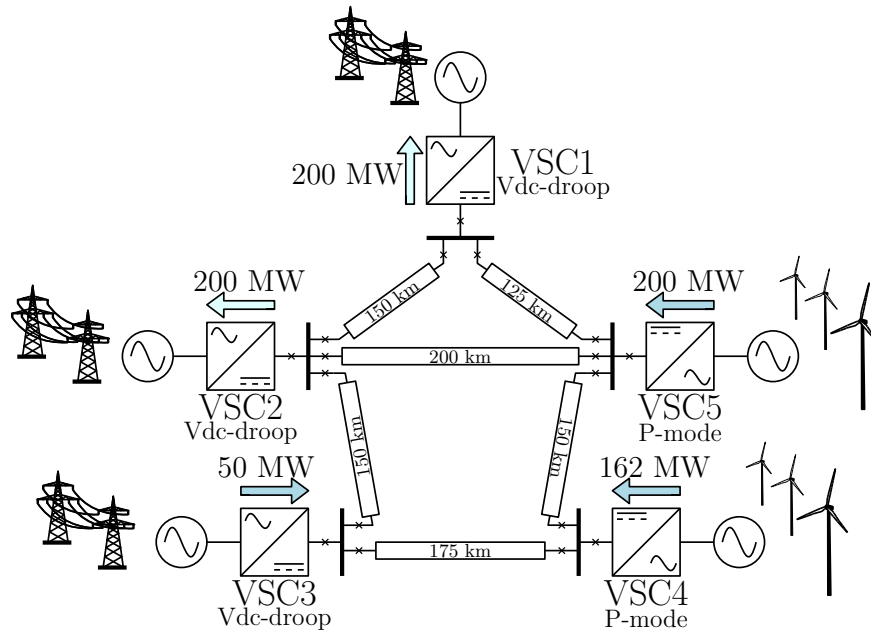
6.3 EMT Simulations

This section illustrates the behaviour of the 5-terminal MTDC system used in [95] with the same topology than the MTDC system of the previous chapter. It interconnects two offshore wind farms and three asynchronous AC grids after a disturbance. Simulations are run with the electromagnetic transients program EMTP-RV[®].

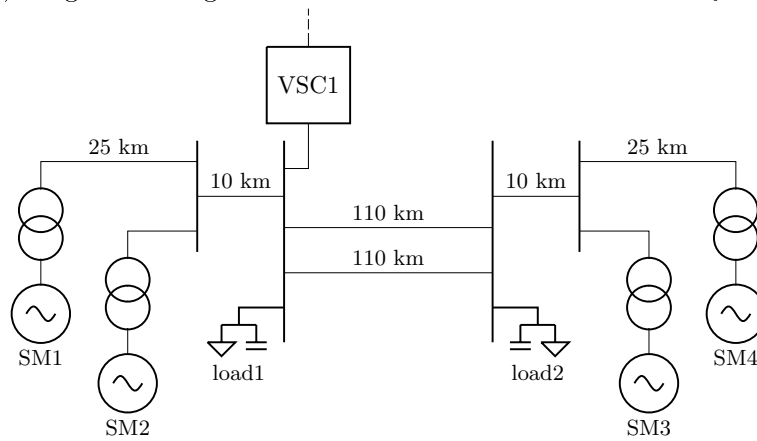
6.3.1 Considered System

The considered MTDC system is a pentagon shaped, VSC-based, 5-terminal HVDC transmission system interconnecting three asynchronous AC networks and two offshore wind farms. The DC grid includes six DC lines whose topology is depicted in Figure 6.4a, and the AC grid 1 used in this simulation is the classic Kundur grid [67] as shown in Figure 6.4b. All grid parameters are listed in Appendix A Section A.3.

The VSC 1 is the only converter equipped with a dual controller (frequency droop and voltage droop), meaning only the frequency of the AC grid 1 is supported by the MTDC system.



(a) Single-line diagram of the studied 5-terminal MTDC system.



(b) Single-line diagram of the AC grid 1 [67].

Figure 6.4: Single-line diagrams of the considered system.

Converters 2 and 3 are only equipped with a voltage-droop controller, so that they participate in the DC voltage regulation (along with the converter 1) but they do not support the frequency regulation of their AC grids. Converters 4 and 5 are offshore converters and are connected to wind farms. Since the time lapse of this study is small (shorter than a minute), the power output of the wind farms can be supposed constant. Converters 4 and 5 always inject into the DC grid the maximum output power of the wind farms, without any droop controller.

The modelling and the control of the VSCs remains identical to the description of Figure 6.1. The initial power reference of each VSC as well as their droop coefficients are listed in Table 6.1, where 1 p.u. of power is 300MW (a negative P_g^* corresponds to power extracted from the AC grid), 1 p.u. of DC voltage is 640kV and 1 p.u. of frequency is 50Hz.

Converter	1	2	3	4	5
P_g^* (p.u.)	0.667	0.667	-0.167	-0.540	-0.667
k_v (p.u./p.u.)	-0.05	-0.05	-0.05	$-\infty$	$-\infty$
k_f (p.u./p.u.)	0.05	∞	∞	∞	∞

Table 6.1: Initial power reference values and droop coefficients of the VSC-HVDC converters

6.3.2 Effect of an AC Frequency Variation

At $t = 3$ s, a 1 p.u. power plant is tripped in the AC grid 1 (SM2 in Figure 6.4b) and the frequency of the AC system drops. In this simulation, the voltage-droop and the frequency-droop controllers never reach their respective limits of ± 0.4 p.u.

The power distribution of the VSCs of the HVDC grid as well as the DC voltage at their respective terminals are represented in Figure 6.5a and 6.5b: initially the power distribution corresponds to Table 6.1, but after the fault the VSC 1 starts extracting more power from the DC grid to stabilise to frequency of the AC grid 1 (as shown in Figure 6.5c), and the VSCs 2 and 3 respectively extract less power and inject more power into the DC grid in order to stabilise the DC voltage.

Interaction between the frequency droop and the voltage droop

Figure 6.5d shows the power reference modification of VSC 1 due to the voltage droop and the frequency droop. The power deviation of the frequency droop is generated by the frequency decrease of the AC grid after the fault: the frequency-droop controller

extracts more power from the DC grid to participate in the frequency regulation, along with the conventional generation units of the AC grid. Since the frequency droop is proportional to Δf_1 , the shape of the frequency droop mimics the shape of the frequency.

The fact that the VSC 1 is extracting more power from the DC grid leads to a power imbalance on the MTDC system that decreases the DC voltage. In turn, this creates a reactionary power deviation, generated by the voltage droop of the VSC 1, which partially counterbalances the power deviation of the frequency-droop controller. This reactionary power deviation illustrates the interaction between the AC and the DC grid: the voltage droop prevents the frequency droop from operating at its full efficiency.

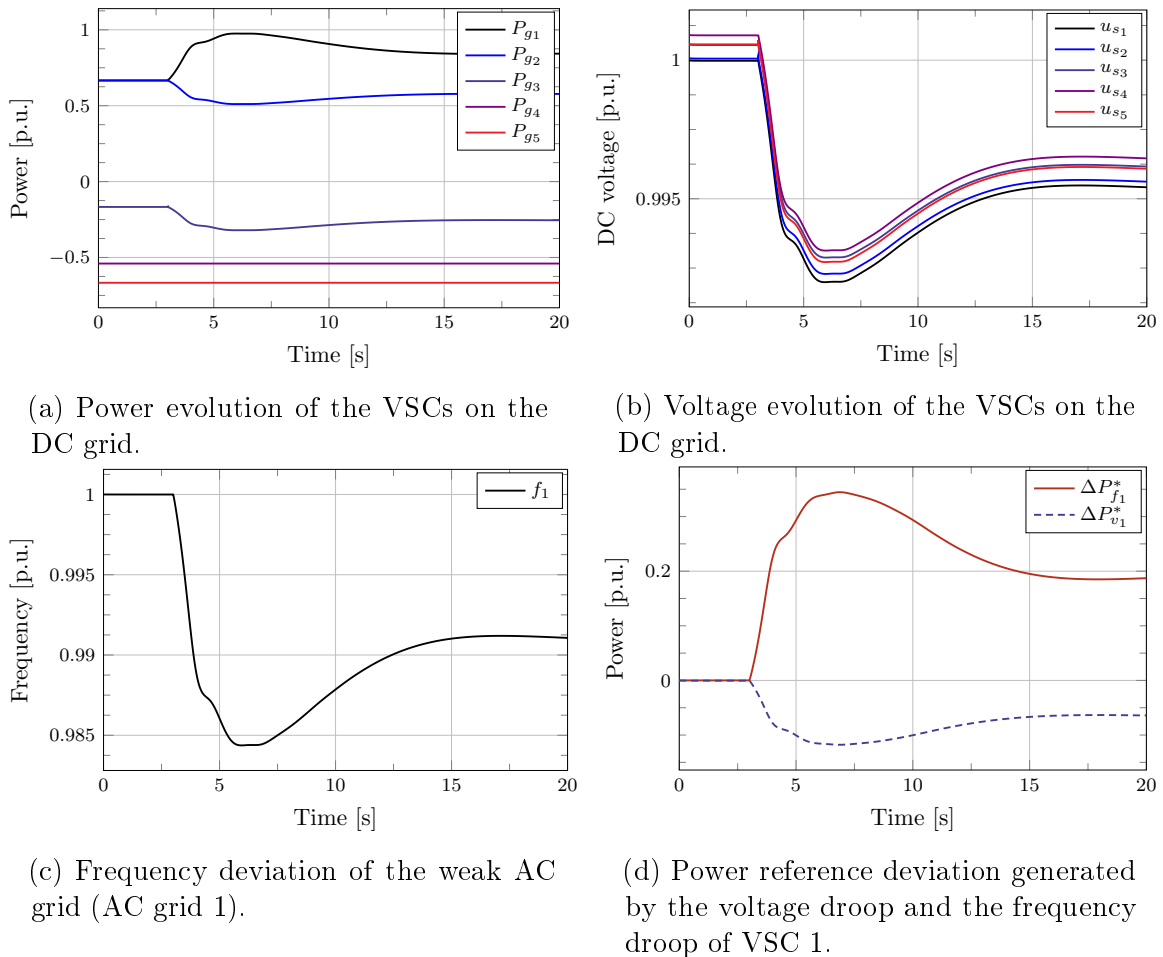
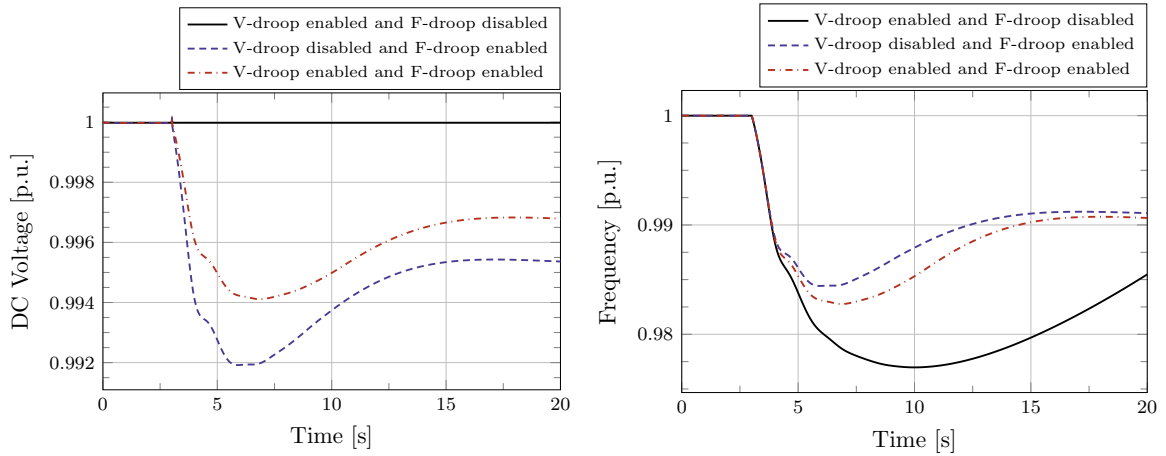


Figure 6.5: Power and voltage distribution of the VSCs, frequency of the AC grid 1 and power deviations of the droops of VSC 1

Impact of each droop on the MTDC system

Figures 6.6a and 6.6b respectively show the voltage of the DC grid and the frequency of the AC grid 1 in three different scenarios with regards to the dual controller of the VSC 1:

1. The voltage-droop controller is enabled but the frequency-droop controller is disabled (solid black curve).
2. The voltage-droop controller is disabled but the frequency-droop controller is enabled (dashed blue curve).
3. The dual controller is fully enabled (dashdotted red curve).



(a) DC Voltage at the converter 1 terminal.

(b) Frequency of the AC grid 1.

Figure 6.6: Impact of the interactions between the droops on the DC voltage and on the frequency of the AC grid 1

Figure 6.6a indicates that the DC voltage remains unchanged when the frequency-droop controller is deactivated (solid black curve): the DC grid does not participate in the frequency regulation of AC grid 1 hence does not extract more power from the DC grid. When the dual controller is fully activated (dashdotted red curve), the DC voltage does not drop as low as when the voltage-droop is deactivated (dashed blue curve) because the voltage-droop controller tries to limit the voltage decrease. However, in this case the activation of the voltage-droop controller is not desired because it hampers the functioning of the frequency droop, and is solely caused by the interactions between the DC and the AC grid.

Figure 6.6b shows that the dual controller participates in the frequency regulation (dashdotted red curve) and stabilises the frequency at a level above the scenario where

the frequency droop is deactivated (solid black curve). However, the frequency droop is not as efficient as it is in the scenario where the voltage droop is deactivated (dashed blue curve). This dashed blue curve corresponds exactly to the agreement with the TSO since the implemented frequency-droop parameter is the contractual value agreed with the TSO and there are no interaction with the voltage droop since it is disabled. However because of this, the VSC 1 does not participate in the DC voltage regulation of the DC grid.

Correction of the frequency droop

In accordance with the agreement signed with the TSO, the VSC-HVDC must participate in the frequency regulation with a contractual frequency-droop parameter of 0.05 p.u./p.u. Because of the interaction between the two droops, the actual relation between the power deviation of the converter and the frequency deviation of the AC grid at $t = 20$ s is $\frac{\Delta f_1}{\Delta P_1} = \frac{0.00936}{0.123} = 0.0759$ p.u./p.u. Hence the frequency droop does not meet the requirements agreed with the TSO and needs to be corrected to take into account the unintended interactions between the frequency droop and the voltage droop.

Equation (6.11) indicates that the relation between the AC grid frequency and the total power deviation of the VSC 1 is, after interaction between the droops:

$$\Delta P_1 = \frac{1}{k_{f_1}} \left(1 - \frac{1}{k_{v_1} \sum_{j=1}^5 \frac{1}{k_{v_j}}} \right) \Delta f_1 \quad (6.21)$$

The original engagement with the TSO was for the frequency droop to obey (6.22):

$$\Delta P_1 = \frac{1}{k_{f_1 \text{contractual}}} \Delta f_1 \quad (6.22)$$

To fulfil the TSO requirements, the frequency-droop parameter k_{f_1} cannot simply be equal to $k_{f_1 \text{contractual}}$. Instead, the implemented value of k_{f_1} must be:

$$k_{f_1} = k_{f_1 \text{contractual}} \left(1 - \frac{1}{k_{v_1} \sum_{j=1}^5 \frac{1}{k_{v_j}}} \right) \quad (6.23)$$

In order to take into account the interaction between the two droops, k_{f_1} has been rescaled by $1 - \frac{1}{k_{v_1} \sum_{j=1}^5 \frac{1}{k_{v_j}}}$ which corresponds to 67% of the contractual frequency-droop parameter, according to the data of Table 6.1.

Figure 6.7 shows that, initially, the converter equipped with a dual controller does not meet the requirements imposed by the TSO: the dash-dotted black curve does not fit the dash blue curve (case where there are no interaction between the droop since the voltage droop is disabled). However, with the corrected value of the frequency droop, the dual controller allows the converter to fulfil the TSO requirements (the solid red curve perfectly fits the dashed blue curve) while still participating in the voltage regulation of the DC grid through an active voltage droop, ensuring the MTDC system's stability in the event of a DC fault.

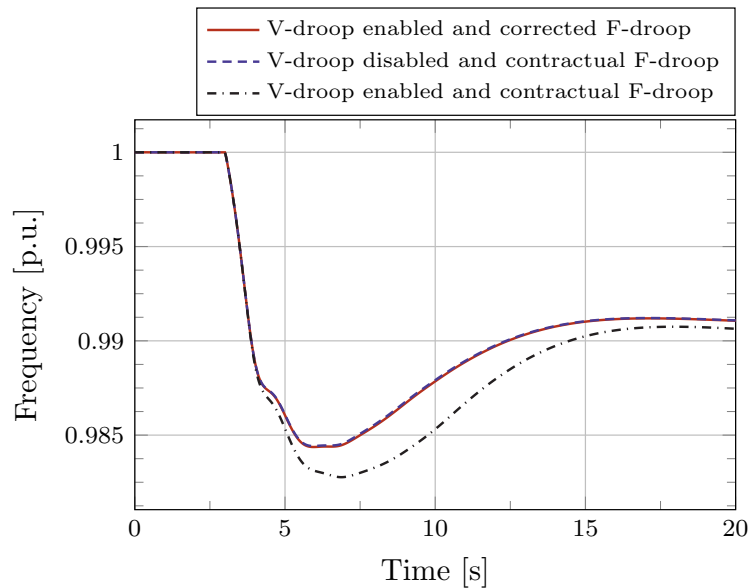


Figure 6.7: Frequency of the AC grid 1

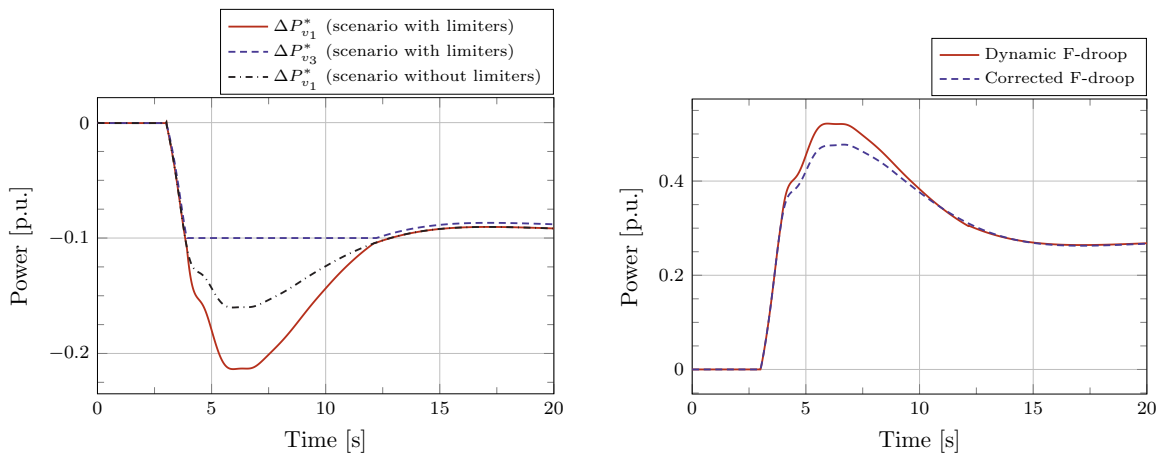
6.3.3 Effect of an AC Frequency Variation when a Controller Reaches its Limit

Similarly to the previous subsection, in this simulation the AC grid 1 loses a generating station of 1 p.u. (generator 2 of Figure 6.4b) at $t = 3$ s, and the frequency of the AC system starts to drop. This time however, the VSC 3 voltage droop reaches its lower limit (set at -0.1 p.u.), modifying the overall behaviour of the MTDC system. The frequency-droop parameter of VSC 1 is dynamically adjusted each time a VSC reaches its upper or lower limit, as described by (6.19).

Figure 6.8a illustrates the lower power limit of the voltage droop of VSC 3: the dashed blue curve shows that the voltage droop of the VSC 3 is limited to -0.05 p.u., hence cannot fully participate in the voltage droop of the DC voltage and must be

compensated by the voltage droops of the other VSCs. This is why the voltage droop of the VSC 1 has to make a bigger effort in the simulation with limits (solid red curve) than in the previous simulation without limits (dashdotted black curve). It can be noted that as soon as the VSC 3 is not operating at its lower limit any longer, the voltage droop of VSC 1 fits the one of the previous simulation again (normal conditions operations).

Figure 6.8b shows that the dynamic frequency-droop parameter allows the VSC 1 to compensate the extra power deviation of its voltage droop generated by the saturation of the voltage-droop controller of VSC 3 by comparison to the fixed corrected frequency-droop parameter of the previous section.



(a) Power reference deviations generated by the voltage droops. (b) Power reference deviations generated by the frequency droop of the first VSC.

Figure 6.8: Power reference deviations generated by the droops.

Figure 6.9 illustrates the impact of the saturation of the voltage droop of VSC 3 on the frequency of the AC grid 1. It shows the effective frequency droop for three different scenarios. According to Figure 6.8a, the VSC 3 reaches its lower limit around $t = 3.5$ s, hence the difference between the different curves of Figure 6.9.

If the frequency-droop parameter of VSC 1 is the fixed corrected droop parameter of the previous section, the effective frequency droop has deviated from the 0.05 p.u./p.u. contractual value agreed with the TSO: the dashed blue curve shows a deviation of the effective frequency droop when VSC 3 is saturated. However, with the use of a dynamically adjusted frequency-droop parameter, the saturation of VSC 3 is taken into account and the frequency droop corresponds at all time to the contractual value agreed with the TSO: the solid red curve fits the dashdotted black curve with a minor

(1.5%) error caused by the approximation of the simplifying assumption described by (6.3).

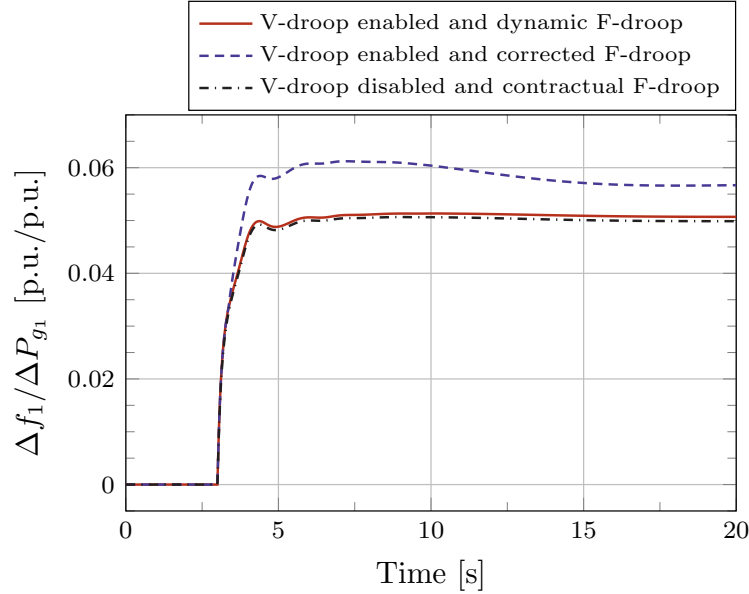


Figure 6.9: Effective frequency-droop parameter of VSC 1

6.4 Experimental Tests

The dual controller presented in the previous section is now tested on the L2EP laboratory mock-up consisting in a 5-terminal MTDC system, partially funded by the company RTE (Réseau de Transport d'Électricité, France) and the European Union within the *Twenties* European project.

6.4.1 Presentation of the L2EP Lille 5-Terminal Mock-up

A general overview of the platform is depicted in Figure 6.10. The mock-up comprises two main parts: the first one is the physical part (in the centre of the figure) and the second one is the virtual part implemented in a real-time simulator (highlighted in blue in the figure). The interface between the physical devices and the analogue outputs of the real-time simulator is achieved by several high-bandwidth AC or DC power amplifiers (number 4 in Figure 6.10). It should be noted, that power amplifiers are either dealing with AC quantities (buses 2 and 5) or DC quantities (buses 1, 3 and 4).

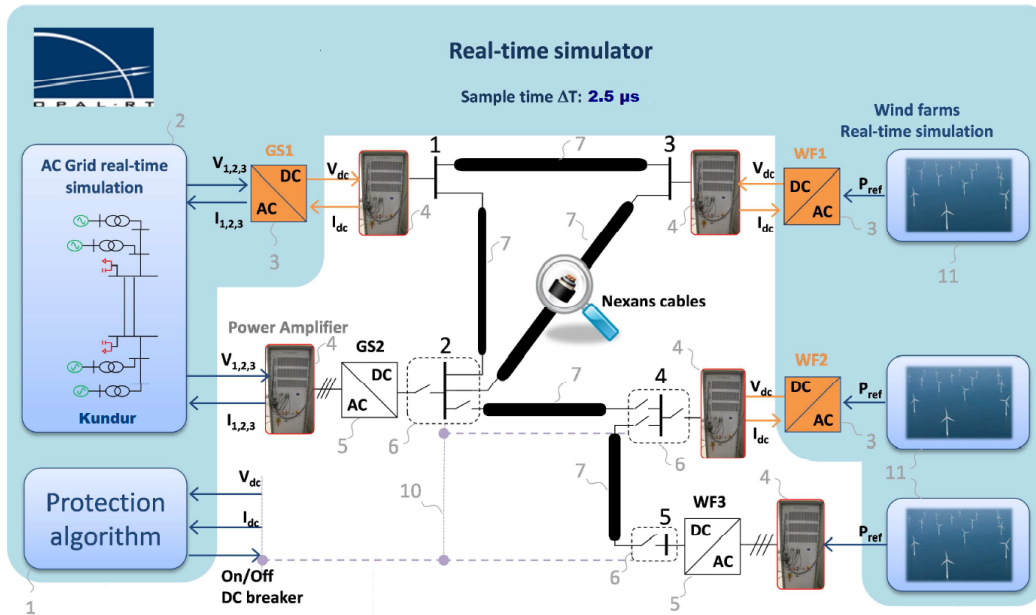


Figure 6.10: Mock-up general overview [84].

The physical components are: two physical VSCs (number 5), five low voltage DC cables composed of two symmetrical poles (number 7) and five DC low voltage breakers (number 6). There are several virtual components simulated in an Opal-RT[®] real-time simulator: three virtual VSCs (number 3), one simulated Kundur AC grid (number 2) and three simulated wind farms (number 11). The protection algorithm (number 1) is embedded in another real-time simulator in order to guarantee separate operation between the protection algorithm and the simulation. The communication between DC breakers (number 6) and the protection algorithm is provided by an independent medium (number 10). Finally the MTDC system is supervised and controlled by a SCADA system receiving data from the VSCs and the real-time simulator and monitoring their set-points (see [84] for more details).

The simulated AC grid is the Kundur AC grid of Figure 6.4b. It is a 4-synchronous machine system, representative of two AC areas linked together by two long AC lines [67]. The signals generated by the simulated AC grid, – namely, the frequency, the AC voltages and the AC currents – are transmitted to the physical system after being scaled down by the power amplifiers: the nominal value 230 kV is scaled down to 200 V (i.e. a voltage ratio of $\frac{1}{1150}$) and 1 MW of power in the virtual AC grid is scaled down to 3 W in the physical system (i.e. a power ratio of $3 \cdot 10^{-6}$). The DC grid nominal voltage is 400 V. Finally, it is to be noted that the physical converters and their control show a precision of ± 3 V and ± 20 W around their respective operating point.

6.4.2 Experimental Conditions

In order to assess the impact of the voltage droop, the frequency droop and the dual controller on the system, some tests are realised on the L2EP mock-up presented above for different scenarii. In this batch of tests, only the real VSCs are used and the topology of the mock-up is described by Figure 6.11. It is rearranged as follows: (a) a real VSC is connected to the node 1 of the DC grid (called VSC 1 from now on) and is connected to an infinite AC bus; (b) the real VSC which is connected to the node 2 of the DC grid (called VSC 2 from now on) is connected to the Kundur AC grid whose frequency is the main variable of interest of this study; (c) a DC power source is connected to the node 3 of the DC grid and injects a constant amount of power into the DC grid; (d) the DC lines between nodes 2 and 4 and between nodes 4 and 5 are disconnected and nodes 4 and 5 are not considered in this study.

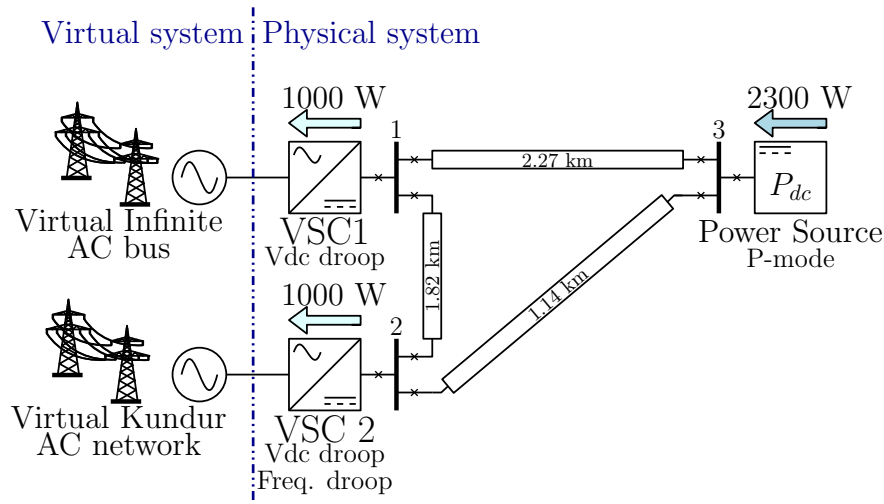


Figure 6.11: Experimental system topology.

The DC power source injects a constant power of 2300 W into the DC grid while each one of the two VSCs initially extracts 1000 W (meaning that 300 W is lost in the DC grid). The VSC 1 is equipped with a voltage-droop controller with a voltage-droop parameter of 0.82 p.u./p.u. while the VSC 2 is equipped with different types of controllers, depending on the considered scenario.

The tests are realised for the following four scenarii. In each scenario, the total active power generation of the AC grid is 2160 MW (the synchronous machines 1, 2 and 3 produce 615 MW each and the synchronous machine 4 produces 315 MW), which is equivalent to 6480 W when scaled down to the physical system. The disturbance is

the trip of the synchronous machine 4 of the virtual AC grid (which is connected to the VSC 2) at $t = 1.5$ s.

- Scenario 1: The VSC 2 is only equipped with a voltage-droop controller (no frequency droop).
- Scenario 2: The VSC 2 is only equipped with a frequency-droop controller (no voltage droop).
- Scenario 3: The VSC 2 is equipped with the dual controller (which consists of both the voltage and the frequency droops), but for the contractual value 0.05 p.u./p.u. of the frequency droop.
- Scenario 4: The VSC 2 is equipped with the dual controller, but for the corrected value 0.025 p.u./p.u. of the frequency droop (according to (6.11)).

6.4.3 Experimental Results

Scenario 1: Voltage droop only.

In this test, the VSC 2 is only equipped with a voltage-droop controller (no frequency droop) with a voltage-droop parameter of 0.82 p.u./p.u.

Figure 6.12 shows: (a) the power outputs of the AC grid synchronous machines; (b) the frequency of the AC grid connected to the VSC 2; (c) the power output of the VSC 1 and 2 (a negative value corresponds to power extracted from the DC grid and injected into their respective AC grids); (d) the DC voltage of the 3 VSCs.

Since the VSC 2 is not equipped with a frequency-droop controller, it does not react to the tripping of the synchronous machine 4 of the AC grid. In fact, the frequency of the AC grid shows a nadir of 48.933 Hz and is stabilised at 49.602 Hz by the conventional generation units while the converter does not participate in the frequency regulation since its output power remains still at -982.2 W. Because the converter output power does not vary, the DC voltage of the MTDC system remains around 400 V and is not impacted by the AC event, except for some minor oscillations generated by the control system of the converter (more specifically by the PLL locking onto the phase angle to permit the control in the $dq0$ frame).

Scenario 2: Frequency droop only.

In this test, the VSC 2 is only equipped with a frequency-droop controller (no voltage droop) with a frequency-droop parameter of 0.05 p.u./p.u. As for the previous scenario, Figure 6.13 shows the evolution of the system variables.

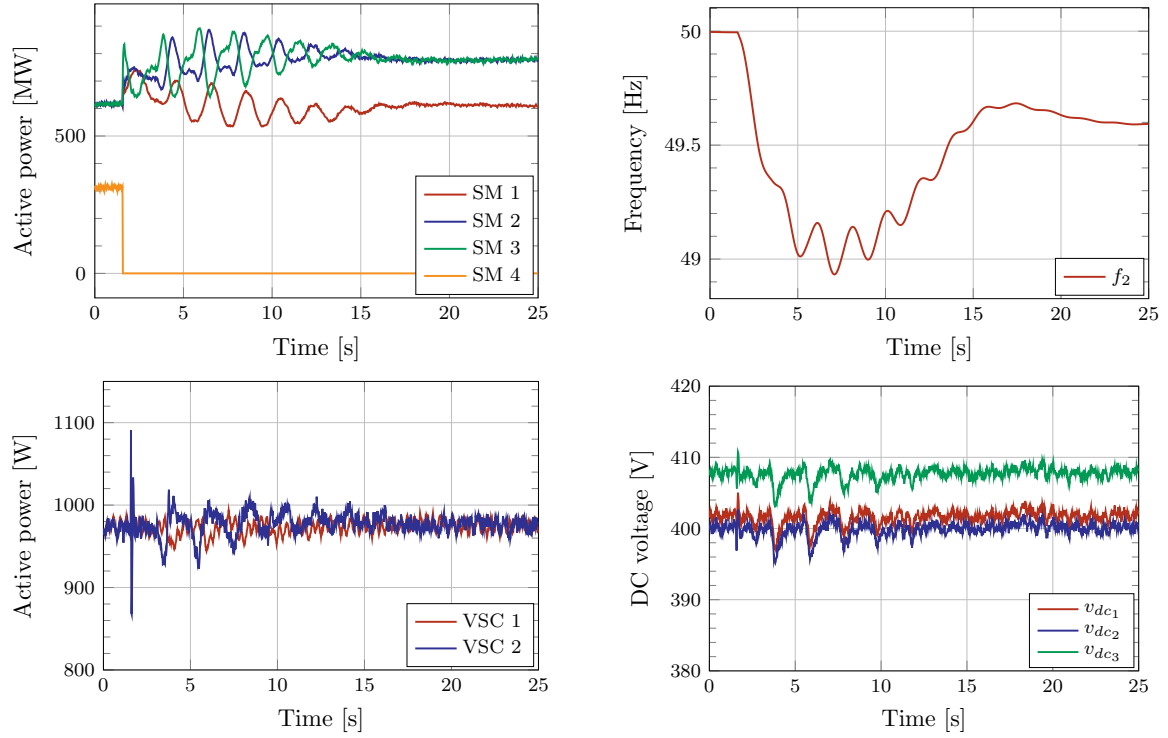


Figure 6.12: Evolution of the system variables after the tripping of a synchronous machine of the simulated AC grid connected to the VSC 2, in scenario 1, where the VSC 2 is only equipped with a voltage-droop controller.

Since the VSC 2 is equipped with a frequency-droop controller, it does react to the tripping of the synchronous machine 4 of the AC grid. In fact, the frequency of the AC grid shows a nadir of 49.562 Hz and is stabilised at 49.732 Hz by both the conventional generation units and the converter. As a result, the VSC 2 output power drops from -973 W to -1290 W (i.e. $\Delta P_f = 317$ W). Because the converter extracts more power from the DC grid, the DC voltage of the MTDC system drops from 400 V to 362 V (i.e. $\Delta v_{dc2} = 38$ V).

The power deviation induced by the frequency droop is coherent with the theoretical computation: $\Delta P_{VSC2} = \frac{P_{pu}}{f_{pu}} \cdot \frac{\Delta f_2}{k_{f,pu}} = \frac{3000}{50} \cdot \frac{50-49.732}{0.05} = 321.6$ W which is equal to the observed power deviation of the VSC 2 (taking into account the physical system error margin of ± 20 W on the power output of the converters).

Scenario 3: Dual controller with contractual value of the frequency droop.

In this test, the VSC 2 is equipped with a dual controller (both frequency and voltage droop), with a frequency-droop parameter of 0.05 p.u./p.u. (contractual value agreed

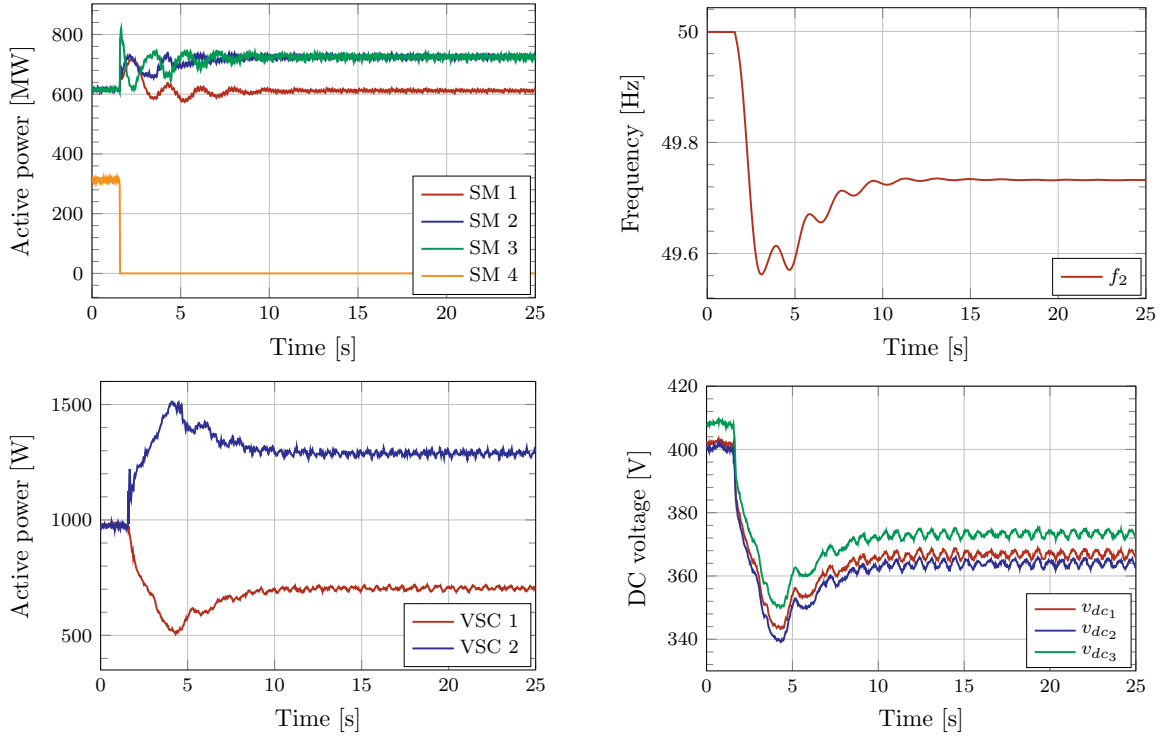


Figure 6.13: Evolution of the system variables after the tripping of a synchronous machine of the simulated AC grid connected to the VSC 2, in scenario 2, where the VSC 2 is only equipped with a frequency-droop controller (contractual value).

with the TSO) and a voltage-droop parameter of 0.82 p.u./p.u. As for the previous scenarii, Figure 6.14 shows the evolution of the system variables.

Since the VSC 2 is equipped with a frequency-droop controller, it participates in the frequency regulation after the tripping of the synchronous machine 4 of the AC grid. In fact, the frequency of the AC grid shows a nadir of 49.415 Hz and is stabilised at 49.681 Hz by both the conventional generation units and the converter. As a result, the VSC 2 output power drops from -976 W to -1164 W (i.e. $\Delta P_{vsc2} = 188$ W). Because the converter extracts more power from the DC grid, the DC voltage of the MTDC system drops from 400 V to 378 V (i.e. $\Delta v_{dc2} = 22$ V).

The power deviation $\Delta P_{vsc2} = 188$ W induced by the sum of the voltage droop and the frequency droop is coherent with the theoretical computation (taking into account the physical system error margin of ± 20 W on the power output of the converters):

- $\Delta P_{f-droop} = \frac{P_{pu}}{f_{pu}} \cdot \frac{\Delta f_2}{k_{f,pu}} = \frac{3000}{50} \cdot \frac{50-49.681}{0.05} = 382.8$ W.
- $\Delta P_{v-droop} = \frac{P_{pu}}{v_{dc,pu}} \cdot \frac{\Delta v_{dc2}}{k_{v,pu}} = \frac{3000}{400} \cdot \frac{400-378}{-0.82} = -201.2$ W.
- $\Delta P_{VSC2} = \Delta P_{f-droop} - \Delta P_{v-droop} = 181.6$ W

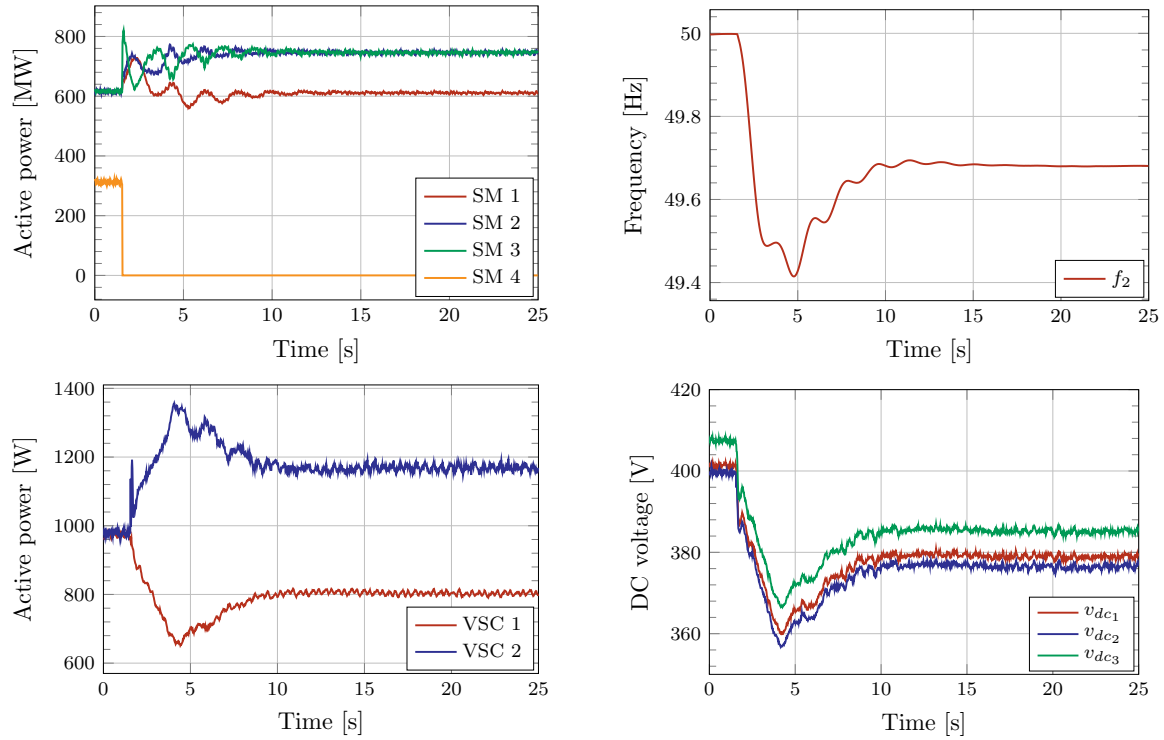


Figure 6.14: Evolution of the system variables after the tripping of a synchronous machine of the simulated AC grid connected to the VSC 2, in scenario 3, where the VSC 2 is equipped with both a frequency-droop (contractual value) and a voltage-droop controller.

However, it does not correspond to the 0.05 p.u./p.u contractual value of the frequency droop any longer: $k_{f, effective} = \frac{P_{pu}}{f_{pu}} \frac{\Delta f_2}{\Delta P_{VSC2}} = \frac{3000}{50} \frac{50-49.681}{188} = 0.108 \neq 0.05$ p.u./p.u. In order to fulfil the engagement with the TSO, the frequency-droop parameter must be corrected according to (6.11).

Scenario 4: Dual controller with corrected value of the frequency droop.

In this test, the VSC 2 is also equipped with a dual controller (both frequency and voltage droop), but with a frequency-droop parameter of 0.025 p.u./p.u. (corrected value that leads to an effective frequency droop corresponding to the contractual value of 0.05 p.u./p.u., as described by (6.11)) and a voltage-droop parameter of 0.82 p.u./p.u. As for the previous scenarii, Figure 6.15 shows the evolution of the system variables.

Since the VSC 2 is equipped with a frequency-droop controller, it participates in the frequency regulation after the tripping of the synchronous machine 4 of the AC grid. In fact, the frequency of the AC grid shows a nadir of 49.575 Hz and is stabilised at 49.737 Hz by both the conventional generation units and the converter. As a result, the

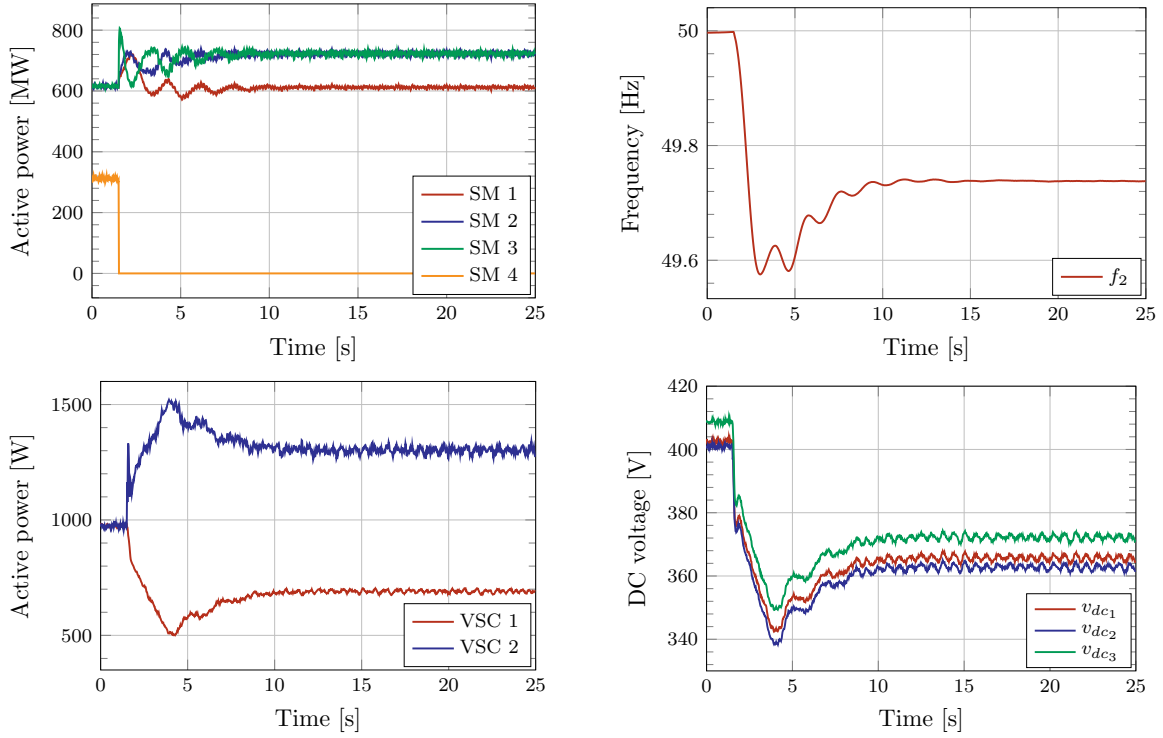


Figure 6.15: Evolution of the system variables after the tripping of a synchronous machine of the simulated AC grid connected to the VSC 2, in scenario 4, where the VSC 2 is equipped with both a frequency-droop (corrected value) and a voltage-droop controller.

VSC 2 output power drops from -980 W to -1293 W (i.e. $\Delta P_{vsc2} = 317$ W). Because the converter extracts more power from the DC grid, the DC voltage of the MTDC system drops from 400 V to 363 V (i.e. $\Delta v_{dc2} = 37$ V).

The power deviation $\Delta P_{vsc2} = 324$ W induced by the sum of the voltage droop and the frequency droop is coherent with the theoretical computation (taking into account the physical system error margin of ± 20 W on the power output of the converters):

- $\Delta P_{f-droop} = \frac{P_{pu}}{f_{pu}} \cdot \frac{\Delta f_2}{k_{f,pu}} = \frac{3000}{50} \cdot \frac{50-49.736}{0.025} = 633.6$ W.
- $\Delta P_{v-droop} = \frac{P_{pu}}{v_{dc,pu}} \cdot \frac{\Delta v_{dc2}}{k_{v,pu}} = \frac{3000}{400} \cdot \frac{400-363}{-0.82} = -330.4$ W.
- $\Delta P_{VSC2} = \Delta P_{f-droop} + \Delta P_{v-droop} = 303.2$ W

Even though the value of the frequency-droop parameter is set at 0.025 p.u./p.u., the effective frequency droop is: $k_{f,effective} = \frac{P_{pu}}{f_{pu}} \frac{\Delta f_2}{\Delta P_{VSC2}} = \frac{3000}{50} \frac{50-49.736}{317} = 0.04997 \approx 0.05$ p.u./p.u. In order to fulfil the engagement with the TSO, the frequency-droop parameter has been corrected according to (6.11) so that the effective frequency droop is actually equal to the contractual value agreed with the TSO.

Comparison between the four scenarii

Figure 6.16 recalls the DC voltage of the VSC 2 as well as the frequency of the AC grid it is connected to, for the four tests described above, hence allowing an easier comparison between the four scenarii.

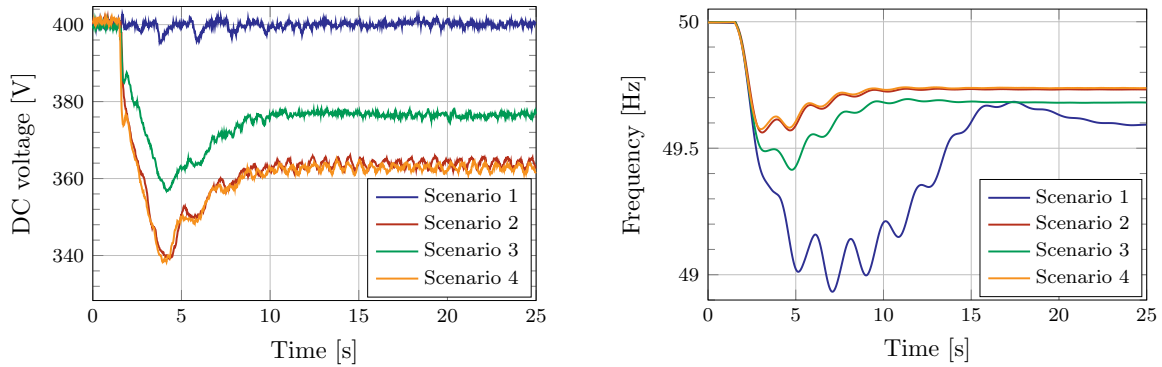


Figure 6.16: Comparison of the DC voltage of the VSC 2 and the frequency of the AC grid 2 for the four scenarii.

It can be observed that, when the VSC is only equipped with a voltage-droop controller (scenario 1, in blue in Figure 6.16), the DC voltage is not affected by the AC event while the frequency of the AC grid shows a greater nadir, a greater steady-state deviation and a longer settling time than for the other scenarii. In return, when the VSC 2 is only equipped with a frequency-droop controller (scenario 2, in red in Figure 6.16), the DC voltage is greatly impacted by the tripping of a synchronous machine in the AC grid, while the nadir and the steady-state value of the frequency is less impacted than for scenarii 1 and 3. When the VSC 2 is equipped with the dual controller with a contractual frequency-droop parameter of 0.05 p.u./p.u. (scenario 3, in green in Figure 6.16), both the DC voltage and the frequency graphs show an intermediate value by comparison to the first two scenarii. This means the interaction between the two droops prevents the MTDC system from fully participating in the frequency regulation with an effective frequency droop of 0.05 p.u./p.u. This value needs to be corrected according to (6.23) to ensure the correct effective frequency droop while still enabling the VSC to participate in the DC voltage regulation of the DC grid by means of the voltage droop. This is described by the scenario 4 (in orange in Figure 6.16) where both the DC voltage and the frequency of the AC grid fits the behaviour of the graphs of scenario 2, which means that the effective frequency droop actually corresponds to the contractual value of the droop that was agreed with the TSO, yet the converter is

also equipped with a voltage droop to participate in the DC voltage regulation in case of a disturbance on the DC grid.

The comparison between scenario 2 and scenario 4 shows quasi-identical results. This means the use of a dual controller with a corrected frequency-droop parameter allows the converter to negate the undesired effect of the voltage droop when the AC grid actually needs frequency support. Yet, in case of a DC event, the voltage droop is present to allow the converter to participate in the DC voltage regulation. This is explained by the fact that the converter dynamics are much faster than the rate of change of frequency (which is usually capped at 0.5 Hz/s). As a result, the MTDC system has no impact on the AC network frequency outside of the effect of the frequency droop.

6.5 Chapter Conclusion

After reviewing the basic functioning of the voltage droop and the frequency droop for VSC-HVDC converters, this chapter discussed the use of a dual controller using both droops at the same time. The coupling between the two droops was pointed out and a theoretical study showed that this coupling makes it necessary to correct the frequency-droop parameter in order to comply with the TSO requirements.

Simulations using the software EMTP-RV[®] and experimental results using the L2EP mock-up of an MTDC system showed the impact of the voltage droop on the frequency droop after an AC event and validated the corrected value of the frequency-droop parameter obtained in the theoretical study as well as the dynamic frequency-droop parameter, allowing the converter to comply with the TSO exigences despite the unintended interactions between the two droops.

The dual controller is a viable alternative to single-droop controllers since it offers the advantages of the two droops at the same time, thus a more reliable system. However, the interactions between the AC grids and the DC grid must not be overlooked since they degrades the efficiency of both droops.

While this chapter covers the interaction between AC and DC grids in the event of an AC fault, the assumption that the DC voltage variation is identical at every node of the DC grid is not valid any longer in the event of a DC fault such as a converter outage. Future work needs to be done in this direction.

Chapter 7

Conclusions and Future Perspectives

Restlessness is discontent – and discontent is the first necessity of progress. Show me a thoroughly satisfied man – and I will show you a failure.

– T. Edison in *The Diary and Sundry Observations of Thomas Alva Edison* (1948).

Let the future tell the truth and evaluate each one according to his work and accomplishments. The present is theirs; the future, for which I really worked, is mine.

– N. Tesla on patent controversies regarding the invention of Radio and other things, as quoted in *A Visit to Nikola Tesla* by Dragislav L. Petkovi in *Politika* (April 1927).

7.1 Conclusions

The electric transmission system is evolving to meet the new energy challenges of the day: the share of intermittent renewable energy in the global electricity generation is rising, polluting conventional generation units are being shut-down, the energy consumption is still growing and the world's population is increasingly urbanised and live in congested areas. The AC transmission system of the 20th century, while completely adequate at the time, is now in needs of new means of electricity transportation that can effectively transmit bulk power over either very long distances or via underground and undersea cables. HVAC is not the answer and the most feasible solution to this issue is the HVDC technology. This is why the number of point-to-point HVDC transmission systems is booming worldwide. In some geographical areas, DC reinforcements, extensions and AC zone interconnections may then lead to a Multi-Terminal HVDC (MTDC) grid in the future, which would allow more flexibility of power dispatch location, optimized assets between wind power and trade transfer capability, smoothed wind power fluctuations, frequency support to onshore grids and more overall reliability.

However, several challenges need to be tackled before MTDC becomes the norm. These include: an efficient modelling of MTDC systems, the perfect understanding of the system behaviour, the testing and maturing of a proficient global control strategy, the elaboration of fast protection schemes, the development of effective DC breakers and the standardisation of equipments between the different manufacturers. This thesis addressed the first three challenges by: (a) proposing a model of both a standard 2-level VSC and an MMC as well as their respective control, and furnishing a methodology for a Matlab[®] routine able to automatically generate the state-space model of any MTDC system independently of its topology; (b) understanding MTDC system dynamics and behaviours by performing a modal analysis on their state-space representations and analysing the eigenvalues; (c) designing the gain of a proposed global control technique and testing its behaviour in both EMT simulations and physical system experimentations.

Contributions of the thesis structured by chapters

- Chapter 4 accounted for the linearisation of the Average Value Models (AVMs) of both the 2-level VSC and the MMC which were derived in Chapter 3. It also described the methodology that led to the acquisition of their respective state-space representations. The state-space models of the two VSC technologies were then validated by the study of an HVDC link (both with 2-level VSCs

and MMCs) whose behaviour were compared with the EMT simulations of more detailed models. An in-depth modal analysis highlighted the dynamics of the two systems (with the two technologies) by analysing their eigenvalues using the participation factors and by visualizing their trajectories for a sweep of the time constant of the DC voltage controller. The results were then compared and the additional dynamics of the MMC-based HVDC link were emphasised and explained. Additionally, a control strategy variant of the MMC-based HVDC link, where both converters shares their energy with the DC bus, was studied. The system dynamics were compared with the MMC-based HVDC link where only the master converter shares its energy with the DC bus. This highlighted the fact that in the first case, the HVDC link behaves in a similar fashion as a classical VSC-based HVDC link (with a natural coupling between the DC voltage and the DC current), while in the second case, the DC current is controlled as an independent variable because the energy stored in the flying capacitors of the SMs is then fully independent from the DC bus voltage level (this can lead to a more volatile DC voltage behaviour).

- Chapter 5 described the voltage-droop control strategy that is presumably the most suitable control technique to regulate the power flows and the DC voltage of an MTDC system. Then, the chapter proposed a methodology that processes the previous converter state-space representations and inserts them in a Matlab[®] routine able to automatically generate the state-space model of any MTDC system independently of its topology. The study of 5-terminal, MMC-based HVDC system in pentagon shape was then achieved by means of another in-depth modal analysis which led to the identification of interaction modes that play a deciding role in the DC voltage and DC current dynamics. The modal analysis also permitted to exclude a range of voltage-droop parameters that led to unstable operations of the MTDC system. The state-space model of the 5-terminal system was finally used to design the voltage-droop parameter of the converters by performing a Singular Value Decomposition (SVD) study, ensuring that the resulting interval of voltage-droop parameters prevents the MTDC system from bypassing a $\pm 5\%$ DC voltage deviation constraint, both in transient and in steady state. Additionally, the impact of the cable model of the DC lines on the results of the SVD analysis was also assessed.
- Chapter 6 proposed an additional controller for MTDC systems. This controller, called the frequency-droop controller, is to be used in combination with the

voltage-droop controller of the converters of an MTDC system. It enables a converter to participate in the frequency regulation of the AC network it is connected to, in similar fashion as conventional generation units support the AC grid frequency in the event of a disturbance. The power deviations generated by both the voltage and the frequency droop as well as their mutual interaction are mathematically quantified. EMT simulations using the software EMTP-RV[®] corroborate the theory and confirm the proper functioning of the proposed controller. Finally, physical experimentations on the L2EP Lille MTDC mock-up of the European project *Twenties* validate the use of the controller.

Reflection on the main findings of the thesis

The modal analyses performed on the HVDC transmission systems of this thesis significantly improved the understanding of HVDC systems dynamic properties. It also shed light on the principal modes of the systems, namely, the ones corresponding to the power flows in the DC grid and responsible for the HVDC transmission system stability, and the ones which are to the main drivers behind the DC voltage dynamic behaviour. The evolution of these modes during a sweep of the voltage-droop parameter then offered some valuable information on the system variables compartment such as undesired oscillations on the DC voltage or DC current after a power reference step or a disturbance. However, it can be difficult to discern which modes really have an impact on the variables of the system and which modes do not. Additionally, the participation factors are to be handled with caution as they can lead to false interpretation, especially in HVDC systems where the converters possess several cascading control loops that interact with each other and with the other converters of the system.

The SVD analysis permitted the frequency response analysis of an MTDC system. More specifically, it allowed the study of the system dynamic behaviour with regard to the quantification of a DC voltage deviation constraint in the frequency domain. This SVD analysis led to a set of acceptable voltage-droop parameters that allow the system to comply with this maximum DC voltage deviation constraint both in steady-state (static point of view) and during transient (dynamic point of view). In this sense, the SVD tool and the modal analysis perfectly complement one another as they give a complete and thorough understanding of the system dynamic behaviour and of the dangerous modes of the system with regards to either the overall system stability or the compliance of the system to a given constraint, something that cannot be achieved by the sole simulations of EMT programs. However, one has to keep in mind that the results of the SVD study can be very conservative, and certain constraints can be

relaxed for a short period in real-life system in order to loosen the restrictions on the parameters of the system. Moreover, the work of this thesis showed that the cable model of the DC lines plays a significant impact in the SVD results validity and that the fitted PI section of a cable gives the most accurate results.

Finally, the proposed dual controller, that acts simultaneously as a voltage-droop and a frequency-droop controller, proved to be a simple yet efficient way for the converters of an MTDC system to participate in the onshore grids' frequency regulation while also regulating the DC voltage of the HVDC transmission system. Both the EMT simulations and the experimental tests on the *Twenties* project mock-up confirmed the theory developed in this thesis behind this dual controller. The simplicity of this dual control is commendable, yet it yields interactions between the two droops that need to be taken into account when selecting the frequency-droop parameter. Another approach to avoid these interactions would be to activate only one droop at a time depending on the disturbance affecting the system. However, since the DC voltage dynamics depend on the voltage-droop parameters of all the converters of the DC grid, deactivating one voltage droop impacts the dynamic DC voltage behaviour of the system as well as the steady-state DC voltage deviation.

7.2 Future Work

To further assess the potential and limitation of VSC-based transmissions, and especially with the MMC technology, a number of additional studies and applications constitute, to the author opinion, a very interesting consortium of future research topics or improvements of the current work. They are structured by chapters:

- Chapter 3
 - Compare the simplified MMC model derived in this chapter to other relatively simple models of the literature (but only to models that can easily be linearised and put in state-space form, i.e. AVMs that do not have any incorporated algorithm such as a BCA).
 - Study the non-energy based MMC control strategies that are starting to sprout in the literature [1, 113, 91], acquire a state-space model of the non-energy based control strategies, and compare their behaviours to the energy-based control strategy of this thesis.
- Chapter 4

- Use more advanced linear control theory tools (such as the sensitivity matrix) to better understand the origins of the system eigenvalues.
 - Analyse the impact of the system key physical components (such as the capacitor values of the SMs of the MMCs or the capacitive elements of the DC cable) on the behaviour of the eigenvalues of the system.
 - Perform a modal analysis on an HVDC link with MMCs controlled with a non-energy based command and compare it to the current modal analysis.
 - Investigate in which scenario should the MMCs of the DC link share their energy with the DC bus with regard to the master-slave control strategy and the system performances.
 - Replace the infinite AC buses by the state-space models of non-ideal AC networks and study their interaction with the HVDC system by means of a modal analysis. Investigate what would be the influence of an AC disturbance on the system's behaviour. Study the impact on the power flows if the HVDC link is embedded in an AC network (as for the INELFE transmission between France and Spain).
- Chapter 5
 - Assess the impact of different cable lengths on the system dynamics and stability.
 - Investigate the impact of different values of the voltage-droop parameter of the converters of an MTDC system on the SVD results.
 - Compare the dynamic performances of the MTDC system between different type of existing voltage-droop controllers.
 - Investigate in which scenario should the MMCs of the MTDC system share their energy with the DC bus by studying the impact of such a control strategy on the voltage droop of the converters and thus on the DC voltage dynamics.
 - Look into the results of the SVD method applied to other variables than just the DC voltages and the DC currents of the converters (such as the maximum allowed stored energy deviation of an MMC, especially when the converter is sharing its energy with the DC bus).
 - Replace the infinite AC buses by the state-space models of non-ideal AC networks and study their interaction with the MTDC system, and the impact

on the SVD results. More particularly, investigate how a disturbance in one AC network can affect the other AC networks connected together via the MTDC system.

- Chapter 6
 - Compare the behaviour of other frequency-droop controller proposed in the literature with the one proposed in this work.
 - Improve the proposed controller with the notion of virtual inertia achieved by the power electronics of the converter [55].
 - Investigate the impact of this controller on the stored energy of an MMC. In particular, investigate the possibility of participating in the AC grid frequency regulation without affecting the DC grid by drawing on the MMC (limited) stored energy reserve.

Bibliography

- [1] a. J. Far, A. and Jovcic, D. (2015). Circulating current suppression control dynamics and impact on MMC converter dynamics. In *PowerTech, 2015 IEEE Eindhoven*, pages 1–6.
- [2] ABB (2004). Special Project Collection, Three Gorges. Technical Brochure. Available online: [hyperlink](#).
- [3] ABB (2006). Brazil-China-India meeting on HVDC and Hybrid Systems, planning and Engineering Issues. Online presentation. Available online: [hyperlink](#).
- [4] ABB (2011a). North-east agra. connecting remote generation. Technical brochure. Available online: [hyperlink](#).
- [5] ABB (2011b). Tesla vs Edison: the war of currents. Online website. Available online: [hyperlink](#).
- [6] ABB (2015a). HVDC Classic - Thyristor valve projects. Reference list. Technical brochure. Available online: [hyperlink](#).
- [7] ABB (2015b). HVDC Light - The original VSC technology. Reference list. Technical brochure. Available online: [hyperlink](#).
- [8] Akkari, S., Dai, J., Petit, M., and Guillaud, X. (2015a). Coupling between the frequency droop and the voltage droop of an AC/DC converter in an MTDC system. In *PowerTech, 2015 IEEE Eindhoven*, pages 1–6.
- [9] Akkari, S., Dai, J., Petit, M., and Guillaud, X. (2016a). Interaction between the voltage-droop and the frequency-droop control for multi-terminal HVDC systems. *IET Generation, Transmission Distribution*, 10(6):1345–1352.
- [10] Akkari, S., Dai, J., Petit, M., Rault, P., and Guillaud, X. (2015b). Small-signal modelling for in-depth modal analysis of an MTDC system. In *Electrical Power and Energy Conference (EPEC), 2015 IEEE*, pages 233–238.
- [11] Akkari, S., Petit, M., Dai, J., and Guillaud, X. (2014). Modélisation, simulation et commande des systèmes VSC-HVDC multi-terminaux. In *Symposium de Génie Électrique (SGE14)*.
- [12] Akkari, S., Petit, M., Dai, J., and Guillaud, X. (2015c). Interaction between the Voltage-Droop and the Frequency-Droop Control for Multi-Terminal HVDC Systems. In *AC and DC Power Transmission, 11th IET International Conference on*, pages 1–7.

- [13] Akkari, S., Prieto-Araujo, E., Dai, J., Gomis-Bellmunt, O., and Guillaud, X. (2016b). Impact of the DC Cable Models on the SVD Analysis of a Multi-Terminal HVDC System. In *Power Systems Computation Conference (PSCC), 2016*, pages 1–6.
- [14] Andersen, B. R., Xu, L., and Wong, K. T. G. (2001). Topologies for VSC transmission. In *AC-DC Power Transmission, 2001. Seventh International Conference on (Conf. Publ. No. 485)*, pages 298–304.
- [15] Asplund, G. (2008). Electric transmission system in change. In *IEEE Power Electronics Specialists Conference, Rhodes*.
- [16] Bahrman, M. P. (2008). HVDC transmission overview. In *Transmission and Distribution Conference and Exposition, 2008. T x00026;D. IEEE/PES*, pages 1–7.
- [17] Bahrman, M. P. and Johnson, B. K. (2007). The ABCs of HVDC transmission technologies. *IEEE Power and Energy Magazine*, 5(2):32–44.
- [18] Baliga, B. J. (2008). *Fundamentals of Power Semiconductor Devices*. Springer Science + Business Media, LCC.
- [19] Baliga, B. J. (2011). *Advanced High Voltage Power Device Concepts*. Springer Science + Business Media, LCC.
- [20] Beerten, J. and Belmans, R. (2012). Modeling and Control of Multi-Terminal VSC HVDC Systems. *Energy Procedia*, 24:123–130.
- [21] Beerten, J., D’Arco, S., and Suul, J. (2015). Cable Model Order Reduction for HVDC Systems Interoperability Analysis. In *AC and DC Power Transmission, 11th IET International Conference on*, pages 1–10.
- [22] Beerten, J., D’Arco, S., and Suul, J. A. (2016a). Frequency-dependent cable modelling for small-signal stability analysis of VSC-HVDC systems. *IET Generation, Transmission & Distribution. Special Issue: Selected Papers from the 11th IET International Conference on AC and DC Power Transmissions (ACDC 2015)*, 10:1370–1381.
- [23] Beerten, J., Diaz, G. B., D’Arco, S., and Suul, J. A. (2016b). Comparison of Small-Signal Dynamics in MMC and Two-Level VSC HVDC Transmission Schemes. In *Energycon 2016*.
- [24] Bergna Diaz, G., Suul, J., and D’Arco, S. (2015). Small-signal state-space modeling of modular multilevel converters for system stability analysis. In *Energy Conversion Congress and Exposition (ECCE), 2015 IEEE*, pages 5822–5829.
- [25] Chaudhuri, N. and Chaudhuri, B. (2013). Adaptive Droop Control for Effective Power Sharing in Multi-Terminal DC (MTDC) Grids. *Power Systems, IEEE Transactions on*, 28(1):21–29.
- [26] Chaudhuri, N., Majumder, R., and Chaudhuri, B. (2013). System Frequency Support Through Multi-Terminal DC (MTDC) Grids. *Power Systems, IEEE Transactions on*, 28 No. 1(1):347–356.

- [27] Chester Daily Times (1880). Local Intelligence. Newspaper, vol.7, NO. 1031. Available online: [hyperlink](#).
- [28] CIGRÉ. Colloquium - HVDC and Power Electronics: Enhancing the Transmission Networks (2011). HVDC and Power Electronics projects in Australia and New Zealand. Technical brochure. Available online: [hyperlink](#).
- [29] CIGRÉ WG 04 of Study Committee 14 (DC Links) (1987). Compendium of HVDC schemes throughout the world. Technical brochure No. 003. Available online: [hyperlink](#).
- [30] CIGRÉ WG 14-28 (2003). Active filters in HVDC applications. Technical Brochure No. 223. Available online: [hyperlink](#).
- [31] CIGRÉ WG B4-37 (2005). VSC transmission. Technical brochure. Available online: [hyperlink](#).
- [32] CIGRÉ WG B4-46 (2010). Voltage Source Converter (VSC) HVDC for Power Transmission - Economic Aspects and Comparison with other AC and DC Technologies. Technical brochure. Available online: [hyperlink](#).
- [33] Cole, S. (2010). *Steady state and dynamic modelling of VSC HVDC systems for power system simulation*. PhD thesis, Katholieke Universiteit, Leuven.
- [34] Dai, J., Akkari, S., and Petit, M. (2013). Commande en tension dans un réseau HVDC. *Revue 3EI*, 73:pp15–20.
- [35] D’Arco, S., Suul, J., and Molinas, M. (2014). Implementation and analysis of a control scheme for damping of oscillations in VSC-based HVDC grids. In *Power Electronics and Motion Control Conference and Exposition (PEMC), 2014 16th International*, pages 586–593.
- [36] Delarue, P., Gruson, F., and Guillaud, X. (2013). Energetic macroscopic representation and inversion based control of a modular multilevel converter. In *Power Electronics and Applications (EPE), 2013 15th European Conference on*, pages 1–10.
- [37] Despouys, O. (2012). Offshore DC grids: Impact of topology on power flow control. In *AC and DC Power Transmission (ACDC 2012), 10th IET International Conference on*, pages 1–6.
- [38] Dierckxsens, C., Srivastava, K., Reza, M., Cole, S., Beerten, J., and Belmans, R. (2012). A distributed DC voltage control method for VSC MTDC systems. *Electric Power Systems Research*, 82(1):54 – 58.
- [39] Du, C. (2007). *VSC-HVDC for Industrial Power Systems*. PhD thesis, Chalmers University of Technology, Göteborg, Sweden.
- [40] Edison Tech Center (2014). Arc lamps. Resources. Available online: [hyperlink](#).
- [41] Egea-Alvarez, A., Beerten, J., Van Hertem, D., and Gomis-Bellmunt, O. (2012). Primary and secondary power control of multiterminal HVDC grids. In *AC and DC Power Transmission (ACDC 2012), 10th IET International Conference on*, pages 1–6.

- [42] Elkhorne, J. L. (1967). The Fabulous Drone. *73* magazine. Available online: [hyperlink](#).
- [43] Eriksson, R., Beerten, J., Ghandhari, M., and Belmans, R. (2014). Optimizing DC Voltage Droop Settings for AC/DC System Interactions. *Power Delivery, IEEE Transactions on*, 29(1):362–369.
- [44] European Network of Transmission System Operators for Electricity (2010). Ten-Years Network Development Plan 2010-2020. Technical report, entsoe. Available online: [hyperlink](#).
- [45] European Wind Energy Association (2009). Oceans of Opportunity – Harnessing Europe’s largest domestic energy resource. Technical report, EWEA.
- [46] Fazel, S. S., Bernet, S., Krug, D., and Jalili, K. (2007). Design and Comparison of 4-kV Neutral-Point-Clamped, Flying-Capacitor, and Series-Connected H-Bridge Multilevel Converters. *IEEE Transactions on Industry Applications*, 43(4):1032–1040.
- [47] Flourentzou, N., Agelidis, V., and Demetriades, G. (2009). VSC-Based HVDC Power Transmission Systems: An Overview. *Power Electronics, IEEE Transactions on*, 24(3):592–602.
- [48] Freytes, J. (2015). Interoperability between different Modular Multilevel Converters connected to a MTDC grid. First year phd report, Laboratoire d’électrotechnique et d’électronique de puissance de Lille (L2EP).
- [49] Freytes, J., Akkari, S., Dai, J., Rault, P., Gruson, F., and Guillaud, X. (2016a). Small-Signal State-Space Modeling of an HVDC Link with Modular Multilevel Converters. In *2016 IEEE 17th Workshop on Control and Modeling for Power Electronics (COMPEL)*.
- [50] Freytes, J., Papangelis, L., Saad, H., Rault, P., Cutsem, T. V., and Guillaud, X. (2016b). On the Modeling of MMC for Use in Large Scale Dynamic Simulations. In *19th Power Systems Computation Conference (PSCC 2016)*.
- [51] Freytes, J., Rault, P., Gruson, F., Colas, F., and Guillaud, X. (2016c). Dynamic impact of MMC controllers on DC voltage droop controlled MTDC grids. In *2016 IEEE 17th Workshop on Control and Modeling for Power Electronics (COMPEL)*.
- [52] Froehlich, F. E. and Kent, A. (Retrieved 10 September 2012). *The Froehlich/Kent Encyclopedia of Telecommunications*, volume Volume 17. Books.google.com. Available online: [hyperlink](#).
- [53] Gnanarathna, U. N., Gole, A. M., and Jayasinghe, R. P. (2011). Efficient Modeling of Modular Multilevel HVDC Converters (MMC) on Electromagnetic Transient Simulation Programs. *IEEE Transactions on Power Delivery*, 26(1):316–324.
- [54] Gonzalez-Longatt, F., Roldan, J., and Rueda, J. (2013). Impact of DC control strategies on dynamic behaviour of multi-terminal voltage-source converter-based HVDC after sudden disconnection of a converter station. In *PowerTech (POWERTECH), 2013 IEEE Grenoble*, pages 1–6.

- [55] Guan, M., Pan, W., Zhang, J., Hao, Q., Cheng, J., and Zheng, X. (2015). Synchronous Generator Emulation Control Strategy for Voltage Source Converter (VSC) Stations. *IEEE Transactions on Power Systems*, 30(6):3093–3101.
- [56] Gustavsen, B. (2006). Improving the pole relocating properties of vector fitting. *IEEE Transactions on Power Delivery*, 21(3):1587–1592.
- [57] Gustavsen, B. and Semlyen, A. (1999). Rational approximation of frequency domain responses by vector fitting. *IEEE Transactions on Power Delivery*, 14(3):1052–1061.
- [58] Hagiwara, M. and Akagi, H. (2008). PWM control and experiment of modular multilevel converters. In *Power Electronics Specialists Conference, 2008. PESC 2008. IEEE*, pages 154–161.
- [59] Haileselassie, T., Torres-Olguin, R., Vrana, T., Uhlen, K., and Undeland, T. (2011). Main grid frequency support strategy for VSC-HVDC connected wind farms with variable speed wind turbines. In *PowerTech, 2011 IEEE Trondheim*, pages 1–6.
- [60] Haileselassie, T. and Uhlen, K. (2010). Primary frequency control of remote grids connected by multi-terminal HVDC. In *Power and Energy Society General Meeting, 2010 IEEE*, pages 1–6.
- [61] Jacobson, B., Karlsson, P., Asplund, G., Harnefors, L., and Jonsson, T. (2010). VSC-HVDC transmission with cascaded two-level converters. In *CIGRÉ 2010, WG B4-110*.
- [62] Jonnes, J. (2004). *Empires Of Light: Edison, Tesla, Westinghouse, And The Race To Electrify The World*. Random House Trade Paperbacks.
- [63] Jovicic, D. and Jamshidifar, A. A. (2015). Phasor Model of Modular Multilevel Converter With Circulating Current Suppression Control. *IEEE Transactions on Power Delivery*, 30(4):1889–1897.
- [64] Kaura, V. and Blasko, V. (1996). Operation of a phase locked loop system under distorted utility conditions. In *Applied Power Electronics Conference and Exposition, 1996. APEC '96. Conference Proceedings 1996., Eleventh Annual*, volume 2, pages 703–708 vol.2.
- [65] Klooster, J. W. (2009). *Icons of Invention: The Makers of the Modern World from Gutenberg to Gates*. ABC-CLIO.
- [66] Kocar, L., Mahseredjian, J., and Olivier, G. (2008). Weighting Method for Transient Analysis of Underground Cables. *Power Delivery, IEEE Transactions on*, 23(3):1629–1635.
- [67] Kundur, P. (1994). *Power System Stability and Control*. McGraw-Hill, Inc.
- [68] Lathrop, G. P. (1890). Talks with edison. Harper's magazine, Vol. 80. Available online: [hyperlink](#).

- [69] Lesnicar, A. and Marquardt, R. (2003). An innovative modular multilevel converter topology suitable for a wide power range. In *Power Tech Conference Proceedings, 2003 IEEE Bologna*, volume 3, pages 6 pp. Vol.3–.
- [70] Liu, C.-C., (UCD), L. H., Finney, S., Adam, G. P., Curis, J.-B., Despouys, O., Prevost, T., Moreira, C., Phulpin, Y., and Silva, B. (2011). Preliminary Analysis of HVDC Networks for Off-Shore Wind Farms and Their Coordinated Protection. Status report for the european commission deliverable: D5.1, Twenties European Project.
- [71] Liu, S., Xu, Z., Hua, W., Tang, G., and Xue, Y. (2014). Electromechanical Transient Modeling of Modular Multilevel Converter Based Multi-Terminal HVDC Systems. *IEEE Transactions on Power Systems*, 29(1):72–83.
- [72] Marquardt, R. (2011). Modular Multilevel Converter topologies with DC-Short circuit current limitation. In *Power Electronics and ECCE Asia (ICPE ECCE), 2011 IEEE 8th International Conference on*, pages 1425–1431.
- [73] Martinez Sanz, I., Chaudhuri, B., and Strbac, G. (2014). Frequency changes in AC systems connected to DC grids: Impact of AC vs. DC side events. In *PES General Meeting | Conference Exposition, 2014 IEEE*, pages 1–5.
- [74] Najmi, V., Nazir, M. N., and Burgos, R. (2015). A new modeling approach for Modular Multilevel Converter (MMC) in D-Q frame. In *Applied Power Electronics Conference and Exposition (APEC), 2015 IEEE*, pages 2710–2717.
- [75] Papangelis, L., Guillaud, X., and Cutsem, T. V. (2015). Frequency support among asynchronous AC systems through VSCs emulating power plants. In *AC and DC Power Transmission, 11th IET International Conference on*, pages 1–9.
- [76] Park, R. H. (1929). Two-reaction theory of synchronous machines generalized method of analysis-part I. *Transactions of the American Institute of Electrical Engineers*, 48(3):716–727.
- [77] Perez-arriaga, I. J., Verghese, G. C., and Schweppe, F. C. (1982). Selective Modal Analysis with Applications to Electric Power Systems, PART I: Heuristic Introduction. *IEEE Transactions on Power Apparatus and Systems*, PAS-101(9):3117–3125.
- [78] Pourbeik, P., Bahrman, M., John, E., and Wong, W. (2006). Modern countermeasures to blackouts. *IEEE Power and Energy Magazine*, 4(5):36–45.
- [79] Prieto-Araujo, E. (2016). *Power converter control for offshore wind energy generation and transmission*. PhD thesis, Universitat Politècnica de Catalunya, Departament d’Enginyeria Elèctrica.
- [80] Prieto-Araujo, E., Bianchi, F., Junyent-Ferré, A., and Gomis-Bellmunt, O. (2011). Methodology for Droop Control Dynamic Analysis of Multiterminal VSC-HVDC Grids for Offshore Wind Farms. *Power Delivery, IEEE Transactions on*, 26(4):2476–2485.

- [81] Prieto-Araujo, E., Egea-Alvarez, A., Fekri, S., and Gomis-Bellmunt, O. (2015). DC voltage droop control design for multi-terminal HVDC systems considering AC and DC grid dynamics. *Power Delivery, IEEE Transactions on*, PP(99):1–1.
- [82] Ramadan, H. S. M. (2012). *Non-Linear Control and Stabilization of VSC-HVDC Transmission Systems*. PhD thesis, Supélec, Gif-Sur-Yvette.
- [83] Ramos-Leanos, O., Naredo, J., Mahseredjian, J., Dufour, C., Gutierrez-Robles, J., and Kocar, I. (2012). A Wideband Line/Cable Model for Real-Time Simulations of Power System Transients. *Power Delivery, IEEE Transactions on*, 27(4):2211–2218.
- [84] Rault, P. (2014). *Dynamic Modeling and Control of Multi-Terminal HVDC Grids*. PhD thesis, Laboratory L2EP, University Lille Nord-de-France.
- [85] Rault, P., Colas, F., Guillaud, X., and Nguefeu, S. (2012). Method for small signal stability analysis of VSC-MTDC grids. In *Power and Energy Society General Meeting, 2012 IEEE*, pages 1–7.
- [86] Rault, P., Guillaud, X., Colas, F., and Nguefeu, S. (2013). Investigation on interactions between AC and DC grids. In *PowerTech, 2013 IEEE Grenoble*, pages 1–6.
- [87] Ravemark, D. and Normark, B. (2005). Light and invisible. Underground transmission with HVDC Light. ABB review. Available online: [hyperlink](#).
- [88] Réseau de Transport d'Électricité (RTE) (2012). L'interconnexion électrique france-angleterre: Une renovation au service de la fiabilité. Press release. Available online: [hyperlink](#).
- [89] Réseau de Transport d'Électricité (RTE) (2015). Nouvelle interconnexion électrique France-Espagne. Press release. Available online: [hyperlink](#).
- [90] Rohner, S., Bernet, S., Hiller, M., and Sommer, R. (2010). Modulation, Losses, and Semiconductor Requirements of Modular Multilevel Converters. *Industrial Electronics, IEEE Transactions on*, 57(8):2633–2642.
- [91] Saad, H. (2015). *Modélisation et simulation d'une liaison HVDC de type VSC-MMC*. PhD thesis, École Polytechnique de Montréal.
- [92] Saad, H., Dennetière, S., Mahseredjian, J., Delarue, P., Guillaud, X., Peralta, J., and Nguefeu, S. (2014). Modular Multilevel Converter Models for Electromagnetic Transients. *Power Delivery, IEEE Transactions on*, 29(3):1481–1489.
- [93] Saad, H., Guillaud, X., Mahseredjian, J., Dennetière, S., and Nguefeu, S. (2015). MMC Capacitor Voltage Decoupling and Balancing Controls. *IEEE Transactions on Power Delivery*, 30(2):704–712.
- [94] Samimi, S., Gruson, F., Guillaud, X., and Delarue, P. (2015). Control of DC bus voltage with a Modular Multilevel Converter. In *PowerTech, 2015 IEEE Eindhoven*, pages 1–6.

- [95] Sarlette, A., Dai, J., Phulpin, Y., and Ernst, D. (2012). Cooperative frequency control with a multi-terminal high-voltage DC network. *Automatica*, 48(12):3128 – 3134.
- [96] Scherer, M., Schlipf, D., and Sattinger, W. (2011). Test for primary control capability (Version 1.1). Technical report, Swissgrid Ltd.
- [97] Sellick, R. L. and Åkerberg, M. (2012). Comparison of HVDC Light (VSC) and HVDC Classic (LCC) site aspects, for a 500MW 400kV HVDC transmission scheme. In *AC and DC Power Transmission (ACDC 2012), 10th IET International Conference on*, pages 1–6.
- [98] Setreus, J. and Bertling, L. (2008). Introduction to HVDC Technology for Reliable Electrical Power Systems. In *Probabilistic Methods Applied to Power Systems, 2008. PMAPS '08. Proceedings of the 10th International Conference on*, pages 1–8.
- [99] SIEMENS (2007). Siemens connects Majorca to power grid on the Spanish mainland – HVDC link for higher security of power supply and increased system stability. Press release. Available online: [hyperlink](#).
- [100] SIEMENS (2008). HVDC Plus. Basic and Principle of Operation. Technical brochure. Available online: [hyperlink](#).
- [101] SIEMENS (2011). High voltage direct current transmission - proven technology for power exchange. Technical brochure. Available online: [hyperlink](#).
- [102] Silva, B., Moreira, C., Seca, L., Phulpin, Y., and Peas Lopes, J. (2012). Provision of Inertial and Primary Frequency Control Services Using Offshore Multiterminal HVDC Networks. *Sustainable Energy, IEEE Transactions on*, 3(4):800–808.
- [103] Skogestad, S. and Postlethwaite, I. (2007). *Multivariable Feedback Control, Analysis and Design*. John Wiley & Sons.
- [104] Teeuwsen, S. P. (2009). Simplified dynamic model of a voltage-sourced converter with modular multilevel converter design. In *Power Systems Conference and Exposition, 2009. PSCE '09. IEEE/PES*, pages 1–6.
- [105] Tesla, N. (1904). *Experiments With Alternate Currents of High Potential and High Frequency*. The Book Tree. Available online: [hyperlink](#).
- [106] Tesla, N. (1905). The Transmission of Electrical Energy Without Wires as a Means for Furthering Peace. *Electrical World and Engineer* magazine. Available online: [hyperlink](#).
- [107] Tesla, N. (1919). My Inventions. Chapter 5 : The Influences That Shape Our Destiny. Available online: [hyperlink](#).
- [108] Tesla, N. (1935). A Machine to End War. *Liberty* magazine. Available online: [hyperlink](#).

- [109] The European Commission (2014). Renewable energy: Processing towards the 2020 target. Communication from the Commission to the European Parliament and the Council.
- [110] The World Bank (2011-2015). Access to electricity (% of population). Online website. Available online: [hyperlink](#).
- [111] Trinh, N. T., Zeller, M., Wuerflinger, K., and Erlich, I. (2016). Generic Model of MMC-VSC-HVDC for Interaction Study With AC Power System. *IEEE Transactions on Power Systems*, 31(1):27–34.
- [112] Tu, Q. and Xu, Z. (2011). Impact of Sampling Frequency on Harmonic Distortion for Modular Multilevel Converter. *IEEE Transactions on Power Delivery*, 26(1):298–306.
- [113] Tu, Q., Xu, Z., and Zhang, J. (2010). Circulating current suppressing controller in modular multilevel converter. In *IECON 2010 - 36th Annual Conference on IEEE Industrial Electronics Society*, pages 3198–3202.
- [114] Vrana, T. K., Zeni, L., and Fosso, O. B. (2012). Active Power Control with Undead-Band Voltage & Frequency Droop for HVDC Converters in Large Meshed DC Grids. In *EWEA Conference, Copenhagen*.
- [115] Weimers, L. (1998). HVDC Light: A New Technology for a Better Environment. *IEEE Power Engineering Review*, 18(8):19–20.
- [116] Working Group B4.52 (2013). HVDC Grid Feasability Study. Technical report, [cigré](#). Available online: [hyperlink](#).
- [117] Yazdani, A. and Iravani, R. (2006). A unified dynamic model and control for the voltage-sourced converter under unbalanced grid conditions. *IEEE Transactions on Power Delivery*, 21(3):1620–1629.
- [118] Zhang, L. (2010). *Modeling and Control of VSC-HVDC Links Connected to Weak AC Systems*. PhD thesis, Royal Institute of Technology, School of Electrical Engineering, Electrical Machines and Power Electronics.

Appendix A

Parameters of the HVDC Transmission Systems Used Throughout this Thesis

A.1 HVDC Link with VSCs

The HVDC link used in Chapter 4 (Sections 4.2.3 and 4.4.1) is recalled in Figure A.1. The base values used in the per unit system are described in Table A.1. The converter parameters are listed in Table A.2. The DC line has a length of 300 km. The cable model is recalled in Figure A.2 and its parameters in Table A.3.

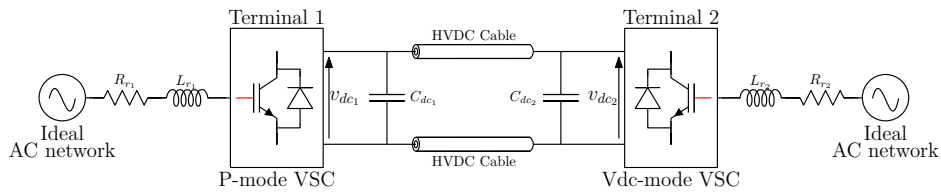


Figure A.1: Configuration of a VSC-based HVDC link.

	Active Power P_b	Power Factor $\cos \phi$	AC Voltage $U_{b,ac}$	Frequency f_b	DC Voltage $V_{b,dc}$
Base Value	1 GW	1	230 kV	50 Hz	640 kV

Table A.1: Base values used for the Per Unitage.

$R_r = 12.21 \cdot 10^{-5}$ p.u. (0.0125 Ω)			$L_r = 0.3$ p.u. (97.8 mH)			$C_{dc} = 195.31$ μ F		
PLL			AC Current Loop			DC Voltage Loop		
1 ms			10 ms			60 ms		

Table A.2: VSC component values and control loops response times.

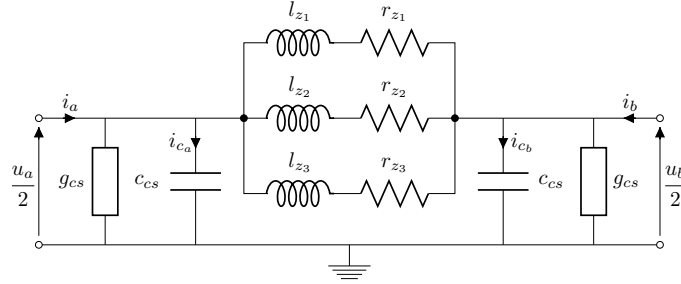


Figure A.2: Fitted PI-section of a cable [21, 22].

$r_{z1} = 1.1724 \cdot 10^{-1}$ Ω /km	$l_{z1} = 2.2851 \cdot 10^{-4}$ H/km
$r_{z2} = 8.2072 \cdot 10^{-2}$ Ω /km	$l_{z2} = 1.5522 \cdot 10^{-3}$ H/km
$r_{z3} = 1.1946 \cdot 10^{-2}$ Ω /km	$l_{z3} = 3.2942 \cdot 10^{-3}$ H/km
$g_{cs} = 7.6333 \cdot 10^{-11}$ S/km	$c_{cs} = 1.9083 \cdot 10^{-7}$ F/km

Table A.3: Component values of the fitted PI cable.

A.2 HVDC Link with MMCs

The HVDC link used in Chapter 4 (Sections 4.3.3 and 4.4.2) is recalled in Figure A.3. The MMC model type 3 is recalled in Figure A.4. The base values used in the per unit system are still described by Table A.1. The converter parameters are listed in Table A.4. The DC line still has a length of 300 km. The cable model is recalled in Figure A.2 and its parameters are recalled in Table A.3.

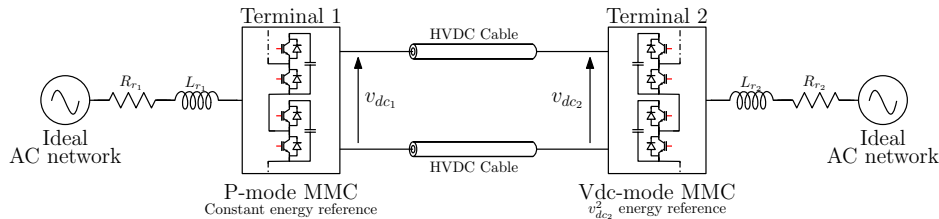


Figure A.3: Configuration of an MMC-based HVDC link.

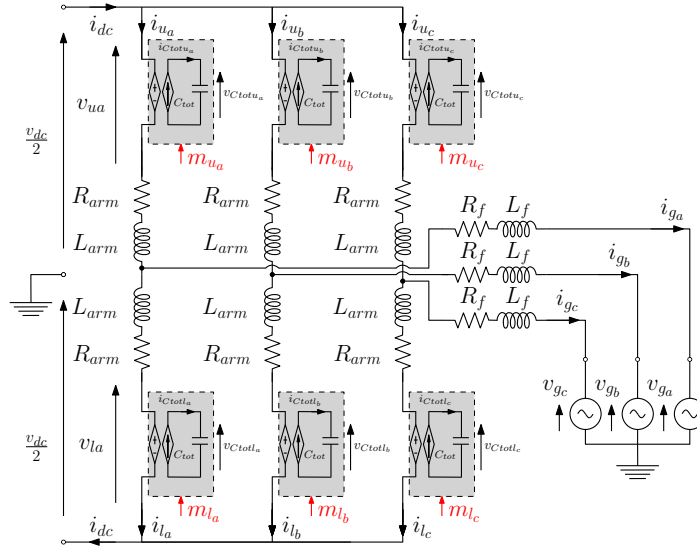


Figure A.4: Detailed representation of the AAM of an MMC.

$R_f = 0.005$ p.u. (0.512 Ω)	$L_f = 0.18$ p.u. (58.7 mH)	$R_{arm} = 0.01$ p.u. (1.024 Ω)	$L_{arm} = 0.15$ p.u. (48.9 mH)
400 SMs	$C_{SM} = 13.02$ mF	$C_{arm} = 32.55$ μ F	$C_{eq,MMC} = 195.31$ μ F
PLL	AC Current Loop	DC Current Loop	DC Voltage Loop
1 ms	10 ms	4 ms	60 ms
			Stored Energy Loop
			40 ms

Table A.4: MMC component values and control loops response times.

A.3 MTDC with VSCs

The MTDC system used in Chapter 6 is recalled in Figure A.5. The initial operating point and the droop parameters are described by Table A.5. The base values used in the per unit system are described by Table A.6. The converter parameters are listed in Table A.7. The DC lines lengths are described in Figure A.5a. Their cable model is the one of a PI section. The AC grid 1 is described by Tables A.9, A.10, A.11, A.12 and A.13.

Converter	1	2	3	4	5
P_g^* (p.u.)	0.667	0.667	-0.167	-0.540	-0.667
k_v (p.u./p.u.)	-0.05	-0.05	-0.05	$-\infty$	$-\infty$
k_f (p.u./p.u.)	0.05	∞	∞	∞	∞

Table A.5: Initial operating point.

	Active Power	Power Factor	AC Voltage	Frequency	DC Voltage
	P_b	$\cos \phi$	$U_{b,ac}$	f_b	$V_{b,dc}$
Numerical Value	300 MW	0.8	230 kV	50 Hz	640 kV

Table A.6: Base values used for the Per Unitage.

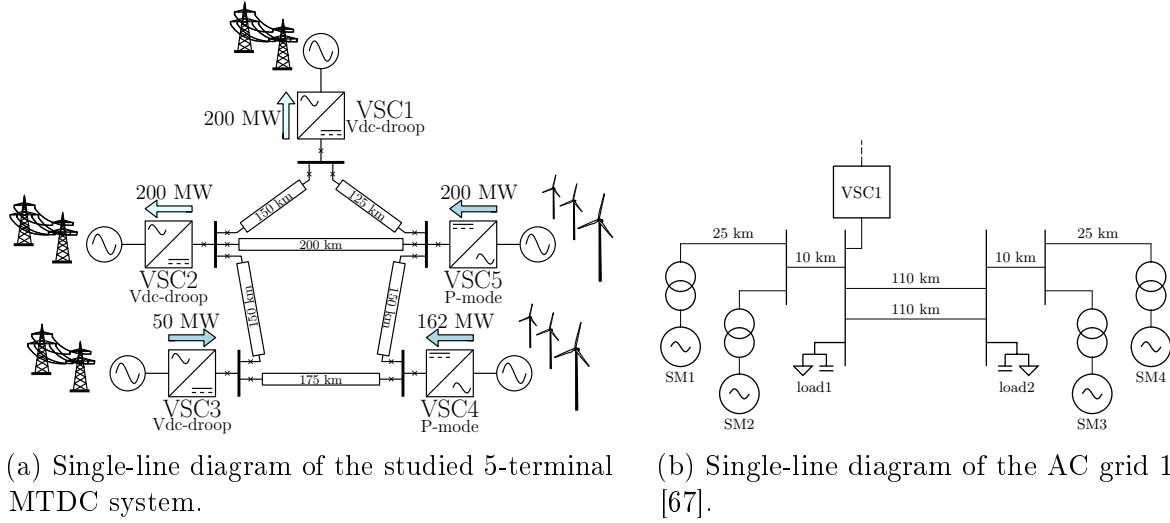


Figure A.5: Single-line diagrams of the considered system.

$R_r = 12.21 \cdot 10^{-5}$ p.u. (0.0125 Ω)				$L_r = 0.3$ p.u. (97.8 mH)	$C_{dc} = 195.31$ μ F	$k_{v_{1,2,3}} = 0.05$ p.u./p.u.
PLL	Inner Loop	Outer Loops				
1 ms	10 ms	100 ms				

Table A.7: VSC component values and control loops response times.

$$r = 5.347 \text{ m}\Omega/\text{km} \quad l = 3.740 \text{ mH}/\text{km} \quad c = 0.247 \text{ }\mu\text{F}/\text{km} \quad i_{\max} = 2265 \text{ A}$$

$$g = 6.207\text{E-}8 \text{ S}/\text{km}$$

Table A.8: DC cable data.

$$r = 20 \text{ m}\Omega/\text{km} \quad l = 0.853 \text{ mH}/\text{km} \quad c = 0.0135 \text{ }\mu\text{F}/\text{km} \quad i_{\max} = 3000 \text{ A}$$

Table A.9: AC OHL data.

AC grid 1 short-circuit ratio: 5.0

Generator	G1	G2	G3	G4
P_e (MW)	300	300	300	300

Table A.10: AC grid 1 generator power outputs.

Load	1	2
Consumption (MW)	700	700
Consumption (MVAR)	-50	-50

Table A.11: AC grid 1 loads.

$$\begin{array}{lll}
 S_N = 500 \text{ MVA} & V_N = 20 \text{ kV} & H = 6.5 \text{ s} \\
 X_d = 1.8 \text{ pu} & X_q = 1.7 \text{ pu} & X_l = 0.2 \text{ pu} \\
 X'_d = 0.3045 \text{ pu} & X'_q = 0.5747 \text{ pu} & X_0 = 0.129 \text{ pu} \\
 T'_{d0} = 9.636 \text{ pu} & T'_{q0} = 0.54 \text{ pu} & R_a = 0.002 \text{ pu} \\
 T''_{d0} = 0.0359 \text{ pu} & T''_{q0} = 0.0533 \text{ pu} &
 \end{array}$$

Table A.12: Generator data.

$$\begin{array}{lll}
 V_{1N} = 20 \text{ kV} & V_{2N} = 230 \text{ kV} & S_N = 500 \text{ MVA} \\
 X = 0.15 \text{ pu} & R = 0 \text{ pu} &
 \end{array}$$

Table A.13: Transformer data.

A.4 MTDC with MMCs

The MTDC system used in Chapter 5 is recalled in Figure A.5. The initial operating point and the droop parameters are described by Table A.14. The base values used for the Per Unitage are the ones of Table A.1. The converter parameters are the ones of Table A.2. The DC lines lengths are described in Figure A.5a. Their cable model is the fitted PI of Figure A.2.

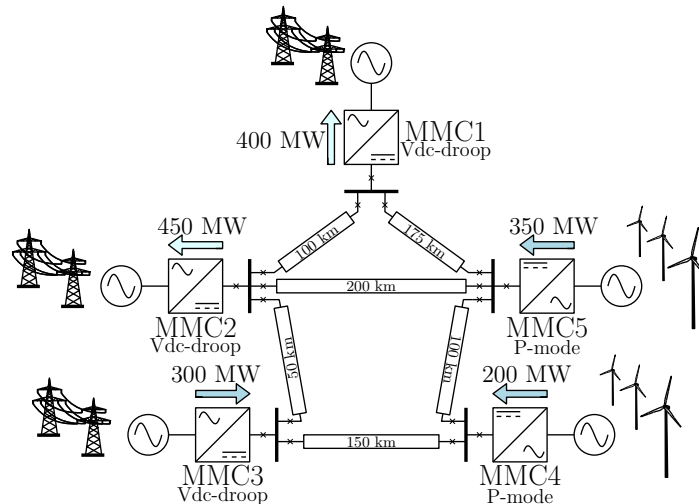


Figure A.6: Topology of the MTDC system.

Converter	1	2	3	4	5
P_g^* (p.u.)	0.40	0.45	-0.30	-0.20	-0.35
k_v (p.u./p.u.)	-0.05	-0.05	-0.05	$-\infty$	$-\infty$

Table A.14: Initial operating point.

Appendix B

Direct-Quadrature-Zero (or dq0) Transformation

The direct-quadrature-zero (or dq0) transformation is a mathematical transformation of a fixed reference frame into a rotating reference frame which simplifies the analysis of three-phase circuits. The dq0 transform used in this thesis is hardly different from the transform first proposed in 1929 by Robert H. Park [76] (hence the other name of the dq0 transform: Park transform). In the case of balanced three-phase circuits, application of the dq0 transform reduces the three AC quantities to two DC quantities. Simplified calculations can then be carried out on these DC quantities before performing the inverse transform to recover the actual three-phase AC results. The Clarke transform (see Figure B.1a) allows the projection of the three-phase quantities onto a stationary two-axis reference frame:

$$\begin{bmatrix} v_\alpha \\ v_\beta \\ v_0 \end{bmatrix} = \frac{2}{3} \begin{bmatrix} 1 & -\frac{1}{2} & -\frac{1}{2} \\ 0 & \frac{\sqrt{3}}{2} & -\frac{\sqrt{3}}{2} \\ \frac{1}{2} & \frac{1}{2} & \frac{1}{2} \end{bmatrix} \begin{bmatrix} v_a \\ v_b \\ v_c \end{bmatrix} \quad (\text{B.1})$$

where v_a , v_b and v_c are the three-phase voltage quantities in the abc reference frame, and v_α and v_β are the corresponding voltage quantities in the $\alpha\beta$ reference frame when $\varphi = 0$.

The rotating $dq0$ reference frame is the rotation of the $\alpha\beta$ reference frame at the angular velocity ω (rad/s), i.e. the angle between the d -axis and the α -axis is $\theta = \omega t$

(rad):

$$\begin{bmatrix} v_d \\ v_q \\ v_0 \end{bmatrix} = \begin{bmatrix} \cos \theta & \sin \theta & 0 \\ \sin \theta & -\cos \theta & 0 \\ 0 & 0 & 1 \end{bmatrix} \begin{bmatrix} v_\alpha \\ v_\beta \\ v_0 \end{bmatrix} \quad (\text{B.2})$$

It is to be noted that the direction of the q -axis is deliberately chosen opposite to its usual direction. This leads to a simpler expression of the reactive power, as illustrated below.

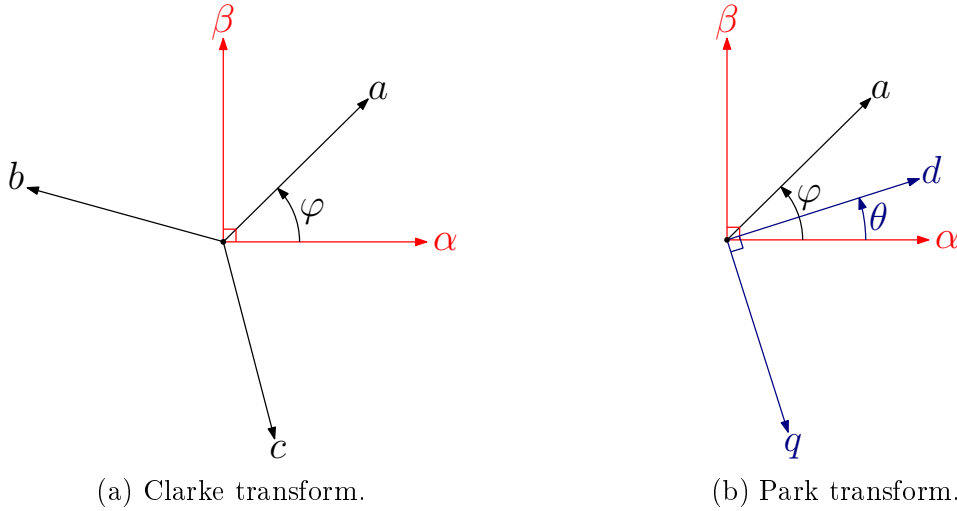


Figure B.1: Clarke and Park transforms.

The abc to $dq0$ transformation matrix \mathbf{T} and its inverse matrix ($dq0$ to abc matrix) \mathbf{T}^{-1} result from (B.1) and (B.2):

$$\begin{bmatrix} v_d \\ v_q \\ v_0 \end{bmatrix} = \mathbf{T} \begin{bmatrix} v_a \\ v_b \\ v_c \end{bmatrix} = \frac{2}{3} \begin{bmatrix} \cos \theta & \cos(\theta - \frac{2\pi}{3}) & \cos(\theta + \frac{2\pi}{3}) \\ \sin \theta & \sin(\theta - \frac{2\pi}{3}) & \sin(\theta + \frac{2\pi}{3}) \\ \frac{1}{2} & \frac{1}{2} & \frac{1}{2} \end{bmatrix} \begin{bmatrix} v_a \\ v_b \\ v_c \end{bmatrix} \quad (\text{B.3})$$

$$\begin{bmatrix} v_a \\ v_b \\ v_c \end{bmatrix} = \mathbf{T}^{-1} \begin{bmatrix} v_d \\ v_q \\ v_0 \end{bmatrix} = \begin{bmatrix} \cos \theta & \sin \theta & 1 \\ \cos(\theta - \frac{2\pi}{3}) & \sin(\theta - \frac{2\pi}{3}) & 1 \\ \cos(\theta + \frac{2\pi}{3}) & \sin(\theta + \frac{2\pi}{3}) & 1 \end{bmatrix} \begin{bmatrix} v_d \\ v_q \\ v_0 \end{bmatrix} \quad (\text{B.4})$$

The same transformations can be applied to the three-phase current quantities:

$$\begin{bmatrix} i_d \\ i_q \\ i_0 \end{bmatrix} = \mathbf{T} \begin{bmatrix} i_a \\ i_b \\ i_c \end{bmatrix} \quad (\text{B.5})$$

$$\begin{bmatrix} i_a \\ i_b \\ i_c \end{bmatrix} = \mathbf{T}^{-1} \begin{bmatrix} i_d \\ i_q \\ i_0 \end{bmatrix} \quad (\text{B.6})$$

The active and reactive power, as well as the amplitude of the AC voltage are then computed in the reference $dq0$ frame as:

$$P_g = v_d i_d + v_q i_q \quad (\text{B.7})$$

$$Q_g = v_d i_q + v_q i_d \quad (\text{B.8})$$

$$v = \sqrt{v_d^2 + v_q^2} \quad (\text{B.9})$$

Appendix C

Controller Tuning

C.1 Inner Current Loops Controller Tuning

The Proportional Integral (PI) controller of the AC current loop has the following form in the s-domain:

$$C_i(s) = k_{p,i} + \frac{k_{i,i}}{s} \quad (\text{C.1})$$

The AC current control loop presented in Chapter 3 (Figure 3.8 in Section 3.2.2), is such that the d - and q -axis currents are decoupled, and each current is regulated via a PI controller. The transfer functions of the AC currents and their respective references are the same for both axes. For instance, the d -axis current control loop transfer function is:

$$\frac{i_{g,d}}{i_{g,d}^*}(s) = \frac{1 + \frac{k_{p,i}}{k_{i,i}}s}{1 + \frac{k_{p,i} + R_r}{k_{i,i}}s + \frac{L_r}{k_{i,i}}s^2} \quad (\text{C.2})$$

Similarly, the transfer function of the DC current of an MMC and its reference (Figure 3.24 in Section 3.3.2) is:

$$\frac{i_{dc}}{i_{dc}^*}(s) = \frac{1 + \frac{k_{p,dc}}{k_{i,dc}}s}{1 + \frac{k_{p,dc} + R_{eq}^{dc}}{k_{i,dc}}s + \frac{L_{eq}^{dc}}{k_{i,dc}}s^2} \quad (\text{C.3})$$

The controller gains $k_{p,i}$ and $k_{i,i}$ are then tuned using the pole placement method: the denominator of the transfer function is compared to a second-order characteristic equation whose dynamics are known:

$$P(s) = 1 + \frac{2\zeta}{\omega_n}s + \frac{1}{\omega_n^2}s^2 \quad (\text{C.4})$$

where ζ is the damping ratio and ω_n is the undamped natural frequency (rad/s) of the system response.

Figure C.1 shows a step response of the transfer function $1/P(s)$ for two different values of the damping ratio and for a 5% settling time of 10 ms (i.e. the system response definitively enters the $\pm 5\%$ error band around the final value after a 10 ms time period). The damping ratio determines how much the system overshoots (or oscillates) as the response transitions to steady state. The undamped natural frequency determines how fast the system oscillates during any transient response and is linked to the system dynamics. As illustrated by Figure C.1, a damping ratio of 0.7 gives an overshoot slightly below 5% and hence leads to the shortest 5% response time for a given ω_n , corresponding to $t_{r,5\%} \approx \frac{3}{\omega_n}$, while a damping ratio of 1 gives no overshoot and a $t_{r,5\%} \approx \frac{5}{\omega_n}$.

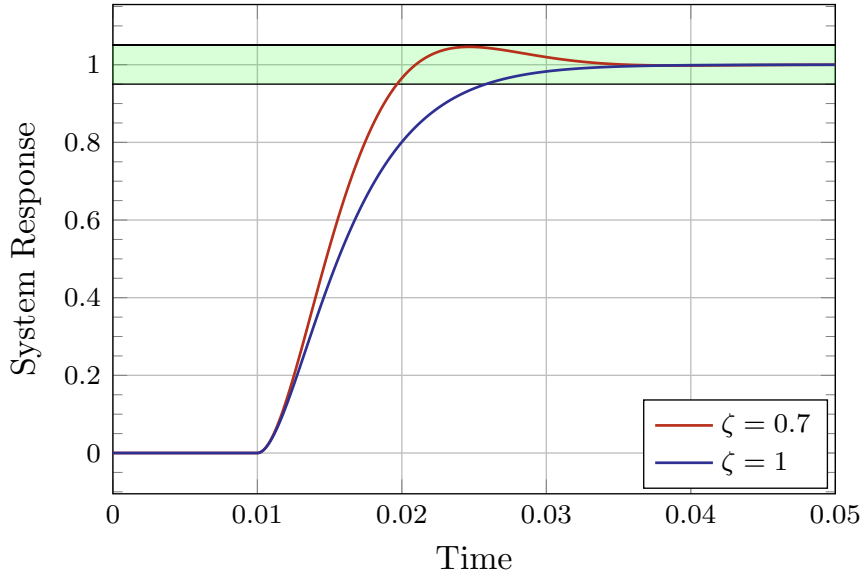


Figure C.1: System response to a step for different values of the damping ratio but for the same ω_n . The $\pm 5\%$ error band is represented in green.

The gains of the PI controller of the current loops are tuned for the current transfer function characteristic polynomial of (C.2) and (C.3) to fit the desired polynomial of (C.4):

$$\begin{cases} k_{i,i} = \omega_n^2 L_r \\ k_{p,i} = 2\zeta\omega_n L_r - R_r \end{cases} \quad (\text{C.5})$$

$$\begin{cases} k_{i,dc} = \omega_n^2 L_{eq}^{dc} \\ k_{p,dc} = 2\zeta\omega_n L_{eq}^{dc} - R_{eq}^{dc} \end{cases} \quad (\text{C.6})$$

C.2 DC Voltage Loop Controller Tuning

The PI controller of the DC voltage loop has the following form:

$$C_{v_{dc}}(s) = k_{p,v_{dc}} + \frac{k_{i,v_{dc}}}{s} \quad (\text{C.7})$$

To avoid any possible interferences between the cascaded control loops, the response time of the outer control loops must be much longer than the one of the inner control loops (it is typically chosen 10 times slower). Under these conditions, the dynamics of the inner control can be neglected when computing the transfer function of the variable controlled by the considered outer controller. Hence, by considering the capacitor $C_{dc,eq}$ which represents the equivalent capacitor of the converters and the DC grid, the DC voltage transfer function is characterised by:

$$\frac{v_{dc}}{v_{dc}^*}(s) = \frac{1 + \frac{k_{p,v_{dc}} s}{k_{i,v_{dc}}}}{1 + \frac{k_{p,v_{dc}} s}{k_{i,v_{dc}}} + \frac{C_{dc,eq}}{k_{i,v_{dc}}} s^2} \quad (\text{C.8})$$

which leads to the tuning of the PI gains such that:

$$\begin{cases} k_{i,v_{dc}} = \omega_n^2 C_{dc,eq} \\ k_{p,v_{dc}} = 2\zeta\omega_n C_{dc,eq} \end{cases} \quad (\text{C.9})$$

Appendix D

State-Space Association Routine

Section D.1 describes the theoretical principle behind the state-space association routine. Section D.2 specifies the methodology used in the Matlab[®] routine to automatically generate the state-space model of the complete system from the individual state-space model of each subsystem.

D.1 State-Space Association Theoretical Principle

This section describes the acquirement of the state-space model of a system via the state-space association of two subsystems whose inputs and outputs are partially connected (i.e. some of the inputs of subsystem 1 correspond to some of the outputs of subsystem 2 and vice-versa).

Let us consider the state-space model of the two individual subsystems of a system (i.e. the state-space combination of the two subsystems without taking into account any possible connection between the inputs and the outputs of the subsystems):

$$\begin{cases} \frac{d}{dt}X_{ol} = A_{ol} \cdot X_{ol} + B_{ol} \cdot U_{ol} \\ Y_{ol} = C_{ol} \cdot X_{ol} + D_{ol} \cdot U_{ol} \end{cases} \quad (\text{D.1})$$

where

$$X_{ol} = \begin{bmatrix} X_1 \\ X_2 \end{bmatrix}; \quad U_{ol} = \begin{bmatrix} U_1 \\ U_2 \end{bmatrix}; \quad Y_{ol} = \begin{bmatrix} Y_1 \\ Y_2 \end{bmatrix}$$

and

$$A_{ol} = \begin{bmatrix} A_1 & 0 \\ 0 & A_2 \end{bmatrix}; \quad B_{ol} = \begin{bmatrix} B_1 & 0 \\ 0 & B_2 \end{bmatrix}; \quad C_{ol} = \begin{bmatrix} C_1 & 0 \\ 0 & C_2 \end{bmatrix}; \quad D_{ol} = \begin{bmatrix} D_1 & 0 \\ 0 & D_2 \end{bmatrix}$$

Let us now assume that some of the new system inputs are connected to some of the outputs (closed-loop). Those inputs are considered as *internal inputs* while the inputs that are not connected to any output are considered as *external inputs*.

$$U_{ol} = U_{int} + U_{ext} \quad (D.2)$$

with:

$$U_{int} = M_{int} \cdot Y_{ol}; \quad U_{ext} = M_{ext} \cdot U_{ol}$$

where M_{int} is called the *interconnection matrix* (or *feed-back matrix*) since it interconnects some of the outputs to the inputs, and M_{ext} corresponds to external inputs that are not linked to the outputs of the system (i.e. M_{ext} gives the information on which inputs of the subsystems are external inputs of the new system).

The relationship between all the inputs U_{ol} and all the outputs Y_{ol} can then be expressed by:

$$U_{ol} = M_{int} \cdot Y_{ol} + M_{ext} \cdot U_{ol} \quad (D.3)$$

Injecting (D.3) in (D.1) yields:

$$\begin{cases} \frac{d}{dt} X_{ol} = A_{ol} \cdot X_{ol} + B_{ol} \cdot M_{int} \cdot Y_{ol} + B_{ol} \cdot M_{ext} \cdot U_{ol} \\ Y_{ol} = (I - D_{ol} \cdot M_{int})^{-1} \cdot (C_{ol} \cdot X_{ol} + D_{ol} \cdot M_{ext} \cdot U_{ol}) \end{cases}$$

which gives, with $E_{ol} = (I - D_{ol} \cdot M_{int})^{-1}$,

$$\begin{cases} \frac{d}{dt} X_{ol} = (A_{ol} + B_{ol} \cdot M_{int} \cdot E_{ol} \cdot C_{ol}) \cdot X_{ol} + (B_{ol} + B_{ol} \cdot M_{int} \cdot E_{ol} \cdot D_{ol}) \cdot M_{ext} \cdot U_{ol} \\ Y_{ol} = E_{ol} \cdot C_{ol} \cdot X_{ol} + E_{ol} \cdot D_{ol} \cdot M_{ext} \cdot U_{ol} \end{cases} \quad (D.4)$$

of the form:

$$\begin{cases} \frac{d}{dt} X_{cl} = A_{cl} \cdot X_{cl} + B_{cl} \cdot U_{cl} \\ Y_{cl} = C_{cl} \cdot X_{cl} + D_{cl} \cdot U_{cl} \end{cases} \quad (D.5)$$

Hence, by identification, and according to (D.5), the matrices of the closed-loop state-space model are given by:

$$\begin{aligned} X_{cl} &= X_{ol} \\ U_{cl} &= U_{ext} = M_{ext} \cdot U_{ol} \\ Y_{cl} &= Y_{ol} \end{aligned} \quad (D.6)$$

and

$$\begin{aligned}
 A_{cl} &= (A_{ol} + B_{ol} \cdot M_{int} \cdot E_{ol} \cdot C_{ol}) \\
 B_{cl} &= (B_{ol} + B_{ol} \cdot M_{int} \cdot E_{ol} \cdot D_{ol}) \\
 C_{cl} &= E_{ol} \cdot C_{ol} \\
 D_{cl} &= E_{ol} \cdot D_{ol}
 \end{aligned} \tag{D.7}$$

D.2 Routine Methodology for State-Space Interconnection

The state-space model of the complete MTDC system is built step by step by a Matlab[®] routine whose methodology is as follows:

1. The user specifies the converter technology (standard 2-level VSC or MMC), the converter control strategies (which outer loops for which converter) and the converter parameters (such as the controller gains or the inductance value of the phase reactor), the HVDC grid topology (radial or meshed shape and DC line lengths) the DC cable models (classical PI, fitted PI, etc...) and the MTDC system operating point (power output of each converter), and then starts the routine.
2. The routine checks if each user request is conform with the routine protocol, and a load-flow algorithm generates the actual initial operating point (power and DC voltage) of each converter of the MTDC system from the specified topology of the HVDC grid and the desired cable model.
3. The routine assembles an open-loop state-space model (see (D.1)) for each subsystem (i.e. for each converter and for the HVDC grid), in accordance with the pre-built templates of the elementary blocks (i.e. the converter physical model, the PLL, the inner current loop, the outer loops, the cable model, etc...)
4. An algorithm generates the interconnection matrices between the inputs and outputs of the open-loop state-space models of the subsystems (see (D.3)).
5. The closed-loop state-space model of each subsystem (i.e. the converters and the DC grid) is generated from their open-loop state-space model and the interconnection matrices, as described by (D.6) and (D.7).
6. This time, the routine generates the interconnection matrices between the inputs and outputs of the *closed*-loop state-space models of the subsystems.

7. The closed-loop state-space model of the complete MTDC system is generated from the subsystem state-space models and the interconnection matrices, as described by (D.6) and (D.7).
8. The final state-space model of the MTDC system is obtained by simplifying the closed-loop state-space model (deleting variable doubles and internal inputs).

The Matlab[®] routine protocol is summarised by Figure D.1.

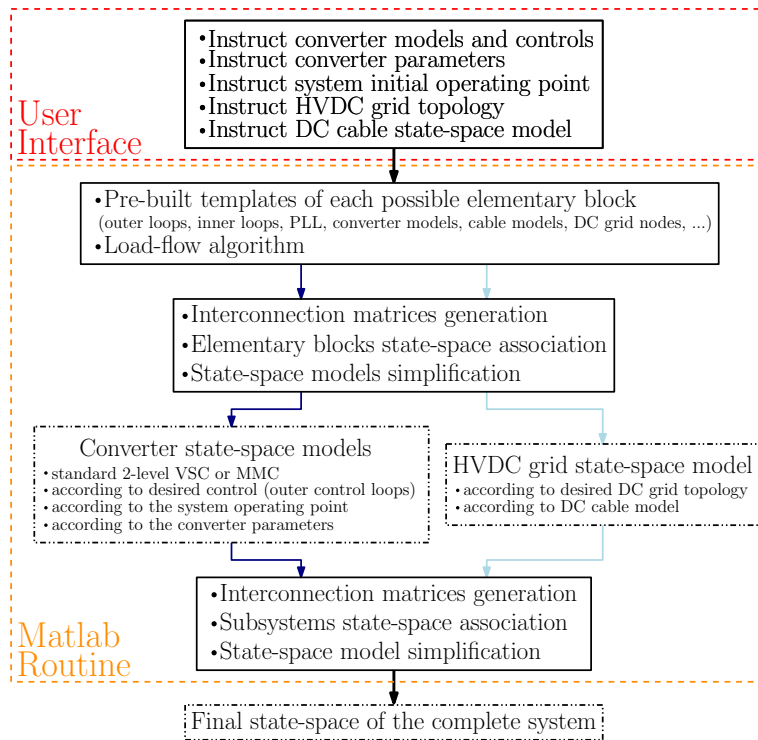


Figure D.1: State-space generation routine overview.

Title: Control of a multi-terminal HVDC (MTDC) system and study of its interactions with the AC grids

Keywords: Control, High Voltage Direct Current (HVDC), Modal analysis, Modelling, Multi-terminal HVDC (MTDC), Simulation, Singular Value Decomposition (SVD), State-space

HVDC transmission systems are largely used worldwide, mostly in the form of back-to-back and point-to-point HVDC, using either thyristor-based LCC or IGBT-based VSC. With the recent deployment of the INELFE HVDC link between France and Spain, and the commissioning in China of a three-terminal HVDC transmission system using Modular Multi-level Converters (MMCs), a modular design of voltage source converters, the focus of the scientific community has shifted onto the analysis and control of MMC-based HVDC transmission systems.

In this thesis, the average value models of both a standard 2-level VSC and an MMC are proposed and the most interesting difference between the two converter technologies –the control of the stored energy in the MMC– is emphasised and explained. These models are then linearised, expressed in state-space form and validated by comparing their behaviour to more detailed models under EMT programs. Afterwards, these state-space representations are used in the modelling of HVDC transmission systems, either point-to-point or Multi-Terminal HVDC (MTDC). A modal analysis is performed on an HVDC link, for both 2-level VSCs and MMCs. The modes of these

two systems are specified and compared and the independent control of the DC voltage and the DC current in the case of an MMC is illustrated. This analysis is extended to the scope of a 5-terminal HVDC system in order to perform a stability analysis, understand the origin of the system dynamics and identify the dominant DC voltage mode that dictates the DC voltage response time. Using the Singular Value Decomposition method on the MTDC system, the proper design of the voltage-droop gains of the controllers is then achieved so that the system operation is ensured within physical constraints, such as the maximum DC voltage deviation and the maximum admissible current in the power electronics. Finally, a supplementary droop –the frequency-droop control– is proposed so that MTDC systems also participate to the onshore grids frequency regulation. However, this controller interacts with the voltage-droop controller. This interaction is mathematically quantified and a corrected frequency-droop gain is proposed. This control is then illustrated with an application to the physical converters of the *Twenties* project mock-up.

Titre: Contrôle d'un système multi-terminal HVDC (MTDC) et étude des interactions entre les réseaux AC et le réseau MTDC

Mots clés: Analyse modale, Commande, Décomposition en Valeurs Singulières (SVD), High Voltage Direct Current (HVDC), Modélisation, Multi-terminal HVDC (MTDC), Représentation d'état, Simulation

La multiplication des projets HVDC de par le monde démontre l'engouement toujours croissant pour cette technologie de transport de l'électricité. La grande majorité de ces transmissions HVDC correspondent à des liaisons point-à-point et se basent sur des convertisseurs AC/DC de type LCC ou VSC à 2 ou 3 niveaux. Les travaux de cette thèse se focalisent sur l'étude, le contrôle et la commande de systèmes HVDC de type multi-terminal (MTDC), avec des convertisseurs de type VSC classique ou modulaire multi-niveaux.

La première étape consiste à obtenir les modèles moyens du VSC classique et du MMC. La différence fondamentale entre ces deux convertisseurs, à savoir la possibilité pour le MMC de stocker et de contrôler l'énergie des condensateurs des sous-modules, est détaillée et expliquée. Ces modèles et leurs commandes sont ensuite linéarisés et mis sous forme de représentations d'état, puis validés en comparant leur comportement à ceux de modèles de convertisseurs plus détaillés à l'aide de logiciels de type EMT. Une fois validés, les modèles d'état peuvent être utilisés afin de générer le modèle d'état de tout système de transmissions HVDC, qu'il soit point-à-point ou MTDC. La comparaison d'une liaison HVDC à base de VSCs classiques puis de MMCs est alors réalisée. Leurs valeurs propres sont étudiées et comparées, et les

modes ayant un impact sur la tension DC sont identifiés et analysés. Cette étude est ensuite étendue à un système MTDC à 5 terminaux, et son analyse modale permet à la fois d'étudier la stabilité du système, mais aussi de comprendre l'origine de ses valeurs propres ainsi que leur impact sur la dynamique du système. La méthode de décomposition en valeurs singulières permet ensuite d'obtenir un intervalle de valeurs possibles pour le paramètre de "voltage droop", permettant ainsi le contrôle du système MTDC tout en s'assurant qu'il soit conforme à des contraintes bien définies, comme l'écart maximal admissible en tension DC. Enfin, une proposition de "frequency droop" (ou "statisme"), permettant aux convertisseurs de participer au réglage de la fréquence des réseaux AC auxquels ils sont connectés, est étudiée. Le frequency droop est utilisé conjointement avec le voltage droop afin de garantir le bon fonctionnement de la partie AC et de la partie DC. Cependant, l'utilisation des deux droop génère un couplage indésirable entre les deux commandes. Ces interactions sont mathématiquement quantifiées et une correction à apporter au paramètre de frequency droop est proposée. Ces résultats sont ensuite validés par des simulations EMT et par des essais sur la plate-forme MTDC du laboratoire L2EP.

